Reconstructing past flow rates of southern component water masses using sedimentary ^{231}Pa/^{230}Th

Benjamin J. Hickey

Thesis submitted to the University of Oxford
for the degree of Doctor of Philosophy
December 2010

Department of Earth Sciences
and University College,
University of Oxford

Supervised by Prof. Gideon Henderson
and Dr. Alex Thomas

“The farther backward you can look,
the farther forward you are likely to see.”
- Sir Winston Churchill

Abstract

Reconstructing past flow rates of southern component water masses using sedimentary ^{231}Pa/^{230}Th

Benjamin J. Hickey

This thesis uses the paleoceancirculation proxy ^{231}Pa/^{230}Th, coupled with water mass tracers δ^{13}C and εNd, to reconstruct circulation histories for southern source waters masses in the South Atlantic, in addition to North Atlantic Deep Water (NADW) far from its source, for the last ~25 kyrs.

Downcore ^{231}Pa/^{230}Th records from a suite of cores along a depth transect in the Argentine Basin show distinct differences with depth, suggesting that ^{231}Pa/^{230}Th ratios in sediments are reflective of conditions in only the bottom most waters. This indicates the importance of consideration of changes in water mass distribution when interpreting ^{231}Pa/^{230}Th records. Opal and particle flux data from these cores show little correlation with ^{231}Pa/^{230}Th values meaning that changes in ^{231}Pa/^{230}Th cannot be explained by a local composition or particle flux effect and are instead likely to be reflecting changes in circulation.

A core bathed by Antarctic Intermediate Water (AAIW) throughout the last 25 kyrs (GeoB 2107, 1045 m), has relatively high ^{231}Pa/^{230}Th values (0.075) during the Holocene and distincly lower values (0.055) at the LGM suggesting faster AAIW transport during the last glacial. At greater depths, ^{231}Pa/^{230}Th, δ^{13}C and εNd data in core GeoB 2109 (2504 m) indicate a change in both circulation and water mass distribution on glacial-interglacial timescales, with moderate flow of Antarctic Bottom Water (AABW) at the LGM being replaced by more vigorous flow of NADW during the Holocene.

On millenial timescales, ^{231}Pa/^{230}Th values in deep cores GeoB 2109 and GeoB 2112 (4010 m) indicate enhanced production of AABW during northern hemisphere stadials, when variations in ^{231}Pa/^{230}Th records are of opposite sign between hemispheres, supporting a possible bipolar seesaw relationship in deep water formation between hemispheres. These data indicate that the ^{231}Pa/^{230}Th proxy can be used to reconstruct past flow rates of multiple water masses in the Argentine Basin and provide evidence that southern source water masses play a dynamic counterpart to NADW formation on abrupt as well as glacial-interglacial timescales.

Extended Abstract

Reconstructing past flow rates of southern component water masses using sedimentary ^{231}Pa/^{230}Th

Benjamin J. Hickey

The use of ^{231}Pa/^{230}Th sedimentary records to reconstruct past rates of ocean circulation have to date focused primarily on the North Atlantic, where increases in ^{231}Pa/^{230}Th have been observed to coincide with periods of abrupt cooling, suggesting a possible link between reorganizations in past deep water production in the North Atlantic and northern hemisphere climate. Antiphasing of climate records between hemispheres during the last glacial has been explained by a “bipolar seesaw” theory in which deep water formation occurs more vigorously in one hemisphere at a time, drawing heat from the tropics to the high latitudes of that hemisphere. To test this theory, and to improve our understanding of past flow rates of southern source waters in the Atlantic more generally, four cores from the Argentine Basin were assessed for ^{231}Pa/^{230}Th, coupled with water mass proxies δ^{13}C and εNd, for the past ~25 kyrs. This allows for reconstruction of the past flow rates and distribution of southern water masses AAIW and AABW in addition to NADW far from its source on glacial-interglacial as well as millenial timescales.

^{231}Pa/^{230}Th ratios are observed to be below the production ratio in all four cores throughout the last 25 kyrs, indicating that the proxy is sensitive to changes in circulation and export productivity in the Argentine Basin. The four study cores show distinctly different downcore ^{231}Pa/^{230}Th records for the last ~25 kyrs, suggesting that ^{231}Pa/^{230}Th in sediment is set by flow conditions of only the bottom most water mass.

This result stresses the importance of considering possible changes in water mass distribution when interpreting downcore ^{231}Pa/^{230}Th records.

The potential influence of composition and flux of scavenging particles on ^{231}Pa/^{230}Th were assessed by measuring biogenic silica and evaluating past changes in particle flux by ^{230}Th normalization. Total particulate fluxes are found to correlate strongly with lithogenic inputs (average r^2 = 0.73), which in turn are observed to be strongly controlled by sea level, reflecting the close proximity of the shallower study cores to the Brazilian continental shelf. The high fluxes of lithogenic material to the sediment appears to have little impact on ^{231}Pa/^{230}Th ratios with particle fluxes showing no significant correlation with ^{231}Pa/^{230}Th across all four study cores (average r^2 =0.003). Opal fluxes in the Argentine Basin were found to be low in comparison to other ocean regions where opal fluxes have been observed to show a strong control on sediment ^{231}Pa/^{230}Th. Furthermore, ^{230}Th normalized opal fluxes are observed to show no significant correlation with ^{231}Pa/^{230}Th across all core samples in the Argentine Basin (average r^2 = 0.001). Given the lack of a local control of both opal and particle fluxes on ^{231}Pa/^{230}Th, changes in ^{231}Pa/^{230}Th in the study area are inferred to mainly reflect lateral advection of Pa related to changes in deep water circulation.

Downcore ^{231}Pa/^{230}Th values in core GeoB 2107 (1048 m), a core located within AAIW for the last 25 kyrs, are significantly lower at the LGM than during the Holocene. Given the lack of evidence for a local or far field control on ^{231}Pa/^{230}Th, these results are best be explained by an increase in AAIW circulation at the LGM, consistent with paleoceanographic and modeling evidence of a more prominent AAIW during glacial times. Rapid circulation at intermediate depths is also observed in North Atlantic sediments relative to less vigorous flow of AABW below at the LGM, as indicated by relatively high $^{231}Pa/^{230}Th$ values in deep cores from both the Argentine Basin and the North Atlantic. The LGM pattern of circulation is opposite to that observed during the Holocene, when relatively low $^{231}Pa/^{230}Th$ values are observed at depth in both hemispheres, reflecting vigorous renewal of NADW at depth in contrast to higher $^{231}Pa/^{230}Th$ values observed in intermediate depth cores. This suggests the operation of two distinctly different modes of circulation in the Atlantic on glacial-interglacial timescales. A transition from glacial to interglacial circulation mode is observed to take place at ~11 ka in GeoB 2109 (2504 m), when $^{231}Pa/^{230}Th$, $\delta^{13}C$ and εNd all indicate the replacement of AABW with a more vigorous flow of NADW at mid depths in the Argentine Basin. This is consistent with the core of northern source waters in the southwest Atlantic deepening from ~1600 m at the LGM to 2500 m in the Holocene, as deduced from a compilation of $\delta^{13}C$ data from Brazilian margin cores (Curry and Oppo, 2005).

On millennial timescales, there is evidence for increasing formation of AABW in the Argentine Basin during Heinrich Stadials (HS) 1 and 2 and the Younger Dryas, when $^{231}Pa/^{230}Th$ values are observed to decrease significantly in cores GeoB 2109 and GeoB 2112. Minimum $^{231}Pa/^{230}Th$ values in these southern cores are observed to occur when maximum $^{231}Pa/^{230}Th$ values are observed in deep North Atlantic sediments, suggesting a possible inverse coupling of deep water production between hemispheres. This is consistent with observations of an increased presence of southern source waters in the North Atlantic during northern hemisphere stadials (e.g. Roberts et al., 2009).

A significant (~1000 years) delay between warming in Antarctica and minimum ^{231}Pa/^{230}Th values is observed in deep core records from the Argentine Basin during HS2. This observation, coupled with the more synchronous and abrupt nature of changes in Greenland temperature and ^{231}Pa/^{230}Th values in North Atlantic sediments suggests that perturbations in deep water production of NADW/GNAIW, possibly related to meltwater discharges from northern hemisphere ice sheets, are responsible for triggering reorganizations in deep water mass circulation between hemispheres.

Acknowledgements

First and foremost I would like to thank my supervisor Gideon Henderson for all his support and supervision throughout my time at Oxford. It was a pleasure to work with you and so many wonderful people within your research group over the past few years. I would also like to thank my co-supervisor Alex Thomas, who proved to be an invaluable source of information in and out of the lab.

Despite taking nearly four years to finish, my lab work would not have been nearly as efficient without the help of many lab technicians in the department, with special thanks to Steve Wyatt, Jeremy Hyde and Cees-Jan de Hoog. Thanks also to Linda Reynard and Josh West who were always happy to help when called upon and to Steve Moreton at the NERC radiocarbon facility for providing radiocarbon analysis of my samples.

I also owe a debt of gratitude to all those who collaborated on this project. These include fellow students Cesar Negre, Paul Carter and James Rae who all shared in the experience of investigating the history of deep ocean circulation change in the South Atlantic. In addition I'd like to thank Cristiano Chiessi at the University of Bremen for providing invaluable sample material and data in support of this research. I particularly appreciated your enthusiasm for my data, even when unclear as to what it meant! It was a pleasure working with you all.

I must also thank Kevin Burton and Ian Hall for examining this thesis and providing many useful comments, corrections and discussion in my viva.

Finally I would like to thank my friends and family for all their support, and especially Diane for her extraordinary patience and understanding.

This research was gratefully supported by the Natural Environmental Research Council (NERC).

Contents *page*

Chapter 1: Ocean circulation and climate

Chapter 2: The ^{231}Pa/^{230}Th Proxy

Chapter 3: Regional setting and core selection

Chapter 4: Analytical techniques

Chapter 5: Core chronology

Chapter 6: Particulate fluxes, Uranium and water mass proxy data

Chapter 7: ^{231}Pa/^{230}Th data

List of Figures *page*

List of Tables *page*

List of abbreviations

(…/…)	Activity ratio
a/ka	Years/kilo years
AABW	Antarctic Bottom Water
AAIW	Antarctic Intermediate Water
ACC	Antarctic Circumpolar Current
ACR	Antarctic Cold Reversal
AMS	Accelerator Mass Spectrometry
B-A	Bolling Allerod
BP	Before Present
Cal	Calendar
CDW	Circumpolar Deep Water
cps	counts per second
$\delta^{13}C$	Stable carbon isotope $^{13}C/^{12}C$ ratio
$\delta^{18}O$	Stable oxygen isotope $^{18}O/^{16}O$ ratio
$\delta^{234}U$	$[(^{234}U/^{238}U) -1] \times 1000$
D-O	Dansgaard-Oeschger
λ	Decay constant
d.p.m	disintegrations per minute
εNd	Neodymium isotope $^{143}Nd/^{144}Nd$ ratio
et al	*et alli* (and others)
$F_{Th/Pa}$	Fractionation factor between Thorium and Protactinium
GISP	Greenland Ice Sheet Project
GNAIW	Glacial North Atlantic Intermediate Water
HS1, HS2..	Heinrich Stadial 1, 2…
ITCZ	Inter-Tropical Convergence Zone
K_d	Distribution coefficient
LGM	Last Glacial Maximum
MC-ICPMS	Multiple Collector Inductively Coupled Plasma Mass Spectrometer
mg	milligram 10^{-3}g
μg	microgram 10^{-6}g

MOC	Meridional Overturning Circulation
ng	nanogram 10^{-9}g
NADW	North Atlantic Deep Water
$(^{231}Pa/^{230}Th)_{xs,0}$	$^{231}Pa/^{230}Th$ activity ratio, excess and decay corrected
ppb	parts per billion
ppm	parts per million
PF	Polar Front
s.d	standard deviation
σ	Standard error from the mean
$t_{1/2}$	Half life
THC	Thermohaline circulation
YD	Younger Dryas

Chapter 1: Introduction

Overview

This chapter sets the scene for the research conducted in this thesis by providing a brief introduction to the global ocean overturning circulation, its influence on modern climate, and how circulation in the Atlantic was different during the last glacial. Possible modes of circulation associated with different climate states are discussed followed by an introduction to the concept of the bipolar seesaw and a brief review of previous studies of past circulation in the southern hemisphere.

1.1 Global ocean circulation

Today there is increasing debate in society about the possibility of climate change resulting from rising concentrations of greenhouse gases in the atmosphere. To help understand how earth's climate may change in the future we must continue to research how and why it has varied in the past. This thesis concentrates on investigating past changes in ocean circulation in order to improve our understanding of the role of the oceans in Earth's climate system and better constrain potential future changes in circulation as a result of increasing atmospheric CO_2.

The oceans are a critical component of the Earth's climate system, storing roughly 1000 times as much heat, and 50 times as much carbon, as the atmosphere (e.g. Sigman and Boyle, 2000; Sabine et al., 2004). Covering just over 70% of the Earth's surface, the oceans receive a significantly larger portion of the Sun's incoming solar radiation than the land. Due to the spherical nature of the Earth, this solar heating is distributed unevenly over the planets surface, with the tropics receiving more heat from the sun than polar regions. Heat energy from the tropics is transported towards the poles via the atmosphere and by ocean circulation. The high specific heat capacity of water (4186 Jkg^{-1} K^{-1} for water at 15^{o}C vs. 1005-1030 Jkg^{-1} K^{-1} for dry-wet air (Osborne et al., 1939)) and the ability of the oceans to circulate make them highly effective at distributing heat around the planet.

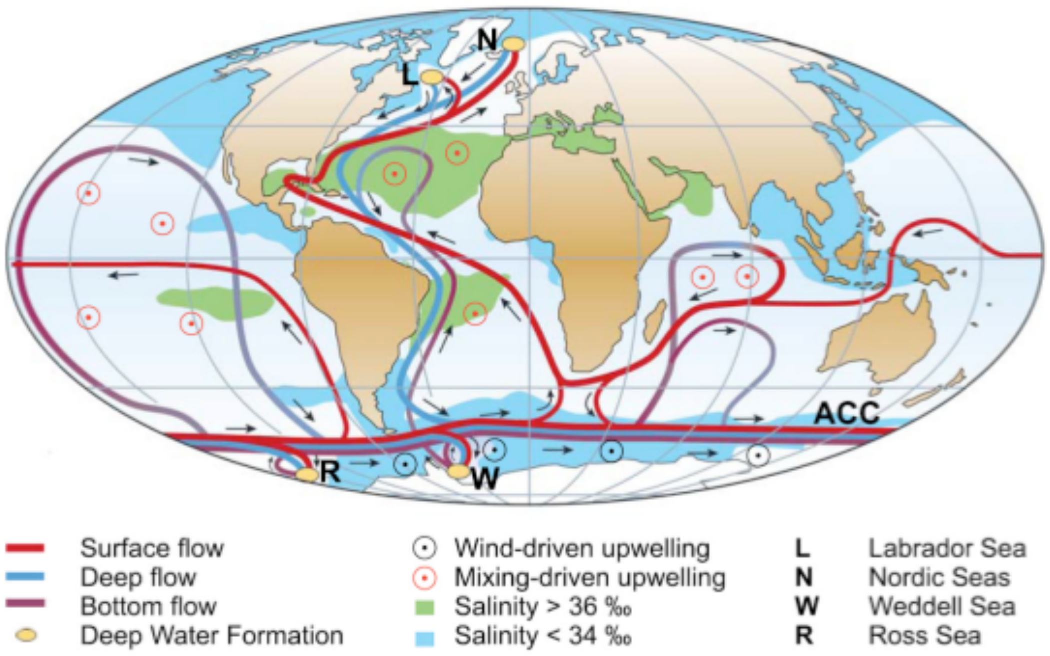

Figure 1.1: Schematic representation of the global ocean conveyor belt system. Principle water mass flow paths are depicted together with regions of deep water formation and upwelling. ACC represents the Antarctic Circumpolar Current. From Rahmstorf (2002).

Modern day global ocean circulation is often described by the Global Ocean Conveyor Belt (Broecker, 1991). The conveyor begins in the North Atlantic where cold surface water sinks to depth and begins a long journey through the deep ocean (Figure 1.1). Initially, it moves southwards at depth in the Atlantic as North Atlantic Deep Water (NADW), where it joins Circumpolar Deep Water (CDW) forming in the

Southern Ocean, and then flows eastward with the Antarctic Circumpolar Current (ACC) before being distributed into the Indian and Pacific oceans.

As deep water does not form at high northern latitudes in the Pacific or Indian Oceans, this input from the Southern Ocean constitutes the dominant deep water supply. In the Pacific Ocean, a strong halocline is formed due to a perennial low salinity surface layer that efficiently prevents sinking of surface water into the interior (Warren, 1983). In the subtropical Indian Ocean, warm surface temperatures maintain a stable density stratification that does not allow for convective overturning (Broecker, 1997). Upwelling of deep water into the surface layer at the northern extension of these two ocean basins is thought to feed the surface return flow into the Atlantic, thus closing the loop of the Ocean Conveyor Belt (the formation and flow paths of the major water masses that make up the ocean conveyor are described more completely in chapter 3 of this thesis).

The conveyor model, although a simplified version of deep ocean circulation, broadly describes the modern thermohaline system. The thermohaline circulation (THC) is so termed because its pattern is influenced significantly by temperature and salinity induced density contrasts in the water column (Stommel, 1961; Rahmstorf 2002). Together, thermohaline and wind driven forcing form a “single integrated circulation system” (Gordan, 1996), often represented by the zonally integrated north-south meridional overtunrning circulation (MOC; Figure 1.2).

In general, the ocean is well stratified, producing a stable water column with cold dense water sitting at depth while warm less dense water sits at the surface. The region where the two water masses meet is marked by a large gradient in temperature, termed the thermocline (Figure 1.2).

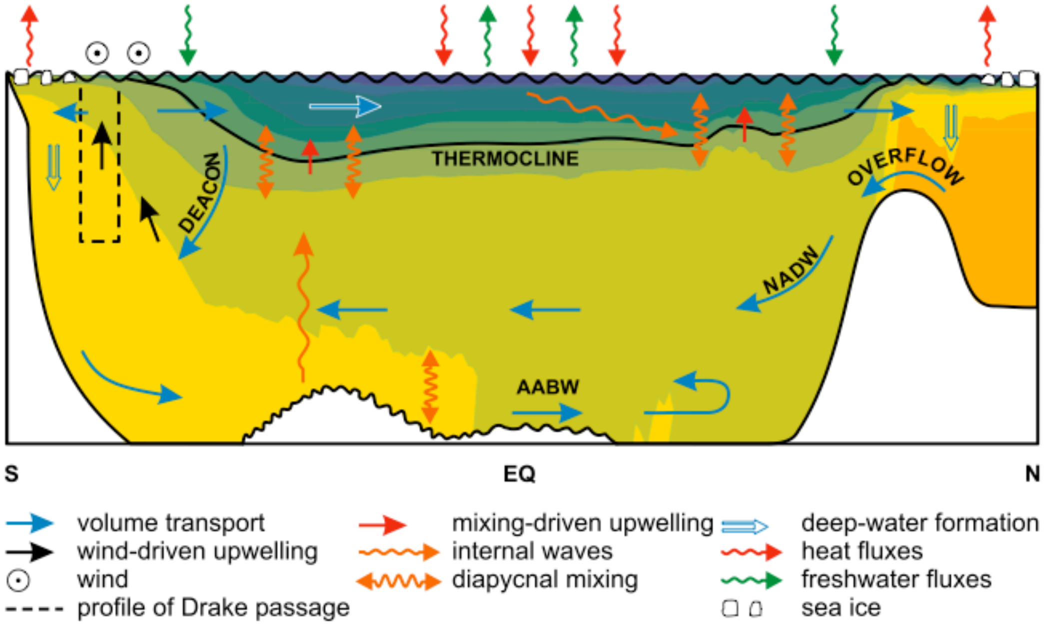

Figure 1.2: Idealized meridional section representing a zonally averaged picture of the Atlantic Ocean. Density stratification is illustrated by colour shading (lightest waters in blue, most dense in orange). Straight arrows represent the MOC. Wind driven upwelling is a consequence of a northward flow of surface water in the Southern Ocean, the Ekman transport, that is driven by strong westerly winds. Mixing along the density gradient, called diapycnal mixing, causes mixing-driven upwelling. Deep water formation occurs in the high northern and southern latitudes, forming North Atlantic Deep Water (NADW) and Antarctic Bottom Water (AABW, see also section 3.4.2). From Kuhlbrodt et al. (2007).

The water above the thermocline is kept warm by solar heating and wind energy mixes this layer to distribute heat across it. The high temperature of this mixed layer keeps it buoyant, preventing vertical mixing. However, there are some regions in the world ocean where surface water can sink to form deep water masses, principle among these are the Labrador and Greenland Seas in the North Atlantic and the Weddell and Ross Seas in the southern ocean (denoted by yellow circles in Figure 1.1). There are also other regions where water can sink due to thermohaline density changes, such as the formation of intermediate waters in the Southern Ocean (discussed in section 3.4) and in the eastern Mediterranean. However, density changes associated with these regions are not sufficient to cause the ventilation of water to the bottom of the major ocean basins.

While THC may be simplistically thought as being driven by formation of deep convecting water masses at high latitudes, modeling studies show that after approximately 1000 years the deep ocean would be filled with cold dense water and circulation would cease (Rahmstorf, 2006). A de-densification mechanism is required to maintain circulation, which takes the form of a downward penetration of heat as a result of turbulent mixing from the winds and tides (e.g. Munk and Wunch 1998). Winds may also help drive ocean circulation more directly, whereby westerly winds over the Southern Ocean create unusually deep upwelling from >2500 m (Toggweiler and Samules, 1995; also see Figure 1.2). Modelling experiments show that both mechanisms are important in driving MOC (Kuhlbrodt et al., 2007) and, as global winds and tides are relatively constant, it is unlikely that deep water circulation could totally shut down for more than a few hundred years (Wunsch, 2003).

1.2 Atlantic meridional overturning circulation and modern climate

In the Atlantic Ocean, an immense quantity of water, equal to a flux of 20 sverdrups (1 Sv = 10^6 m^3 s^{-1}), is transported south at depth from the North Atlantic and replaced at the surface by warm water from the tropics (Broecker, 1991). This Atlantic meridional overturning circulation (AMOC) transports up to 1PW of heat energy to high northern latitudes via the Gulf Stream and the North Atlantic Drift (e.g. Talley, 2003).

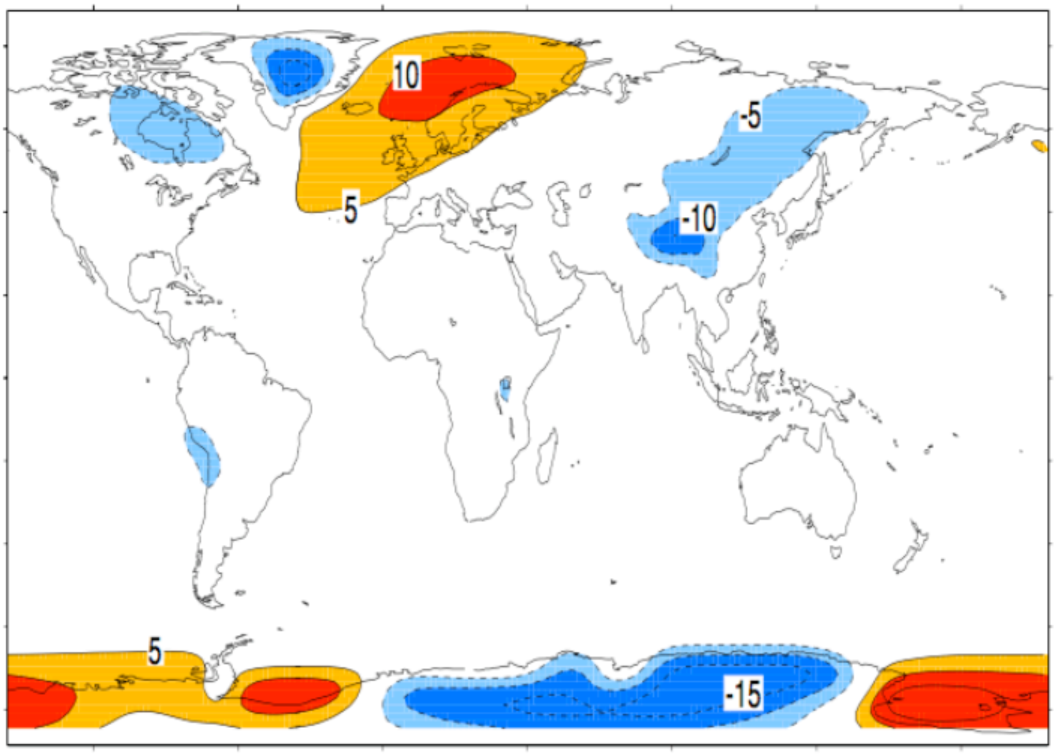

Figure 1.3: Global deviations from the zonal mean temperature. Higher temperatures are associated with deep water formation regions in the North Atlantic around Greenland and in the Weddell and Ross seas of the Southern Ocean. From Rhamstorf (2006).

This heat is released to the atmosphere during deepwater formation in the Labrador and Greenland Seas, warming this region by up to 10°C (Ganachaud and Wunch 2000, Figure 1.3).

Smaller temperature increases relative to the latitudinal mean are observed over deep water formation regions in the Southern Ocean, most notably in the Weddell and Ross Seas. Perturbations to the modern Atlantic MOC that result in reduced rates of deep water formation (e.g. through salinity changes resulting from influx of freshwater at high latitudes) therefore have the potential to impact climate in the North Atlantic and globally.

1.3 Comparisons between modern and glacial Atlantic circulation

Modern day hydrographic profiles of the Atlantic Ocean show that deep-water circulation is dominated by southward flowing NADW, which is readily identifiable as a tongue of nutrient-depleted water extending to depth and as far south as the Southern Ocean (Figure 1.4a). Southern source waters are by comparison limited in extent, with salinity minimum of Antarctic Intermediate Water (AAIW) seen as far north as ~20°N at depths of ~1000 m and the high nutrient water from the Southern Ocean (Antarctic Bottom Water, AABW) penetrating northward beneath NADW to ~40°N.

Nutrient proxies recorded in the calcite of benthic dwelling foraminifera, such as Cd/Ca (e.g. Boyle and Keigwin, 1982; Marchitto and Broecker, 2006) and $\delta^{13}C$ (e.g. Duplessy 1998; Curry and Oppo 2005), in addition to non-biological tracers such as εNd (e.g. Piotrowski et al., 2004), have been used to map water-mass distributions in the past and show a water-mass geometry at the Last Glacial Maximum (LGM) quite different to today (Figure 1.4b). During the last glacial, deep-water production of NADW shallowed to intermediate depths, forming Glacial North Atlantic Intermediate Water (GNAIW; Boyle and Keigwin, 1987). At depths greater than 2 km in the North Atlantic, northern source waters were replaced by nutrient-rich Southern Ocean sourced water at depth, with AABW filling a much greater fraction of the ocean basin relative to today.

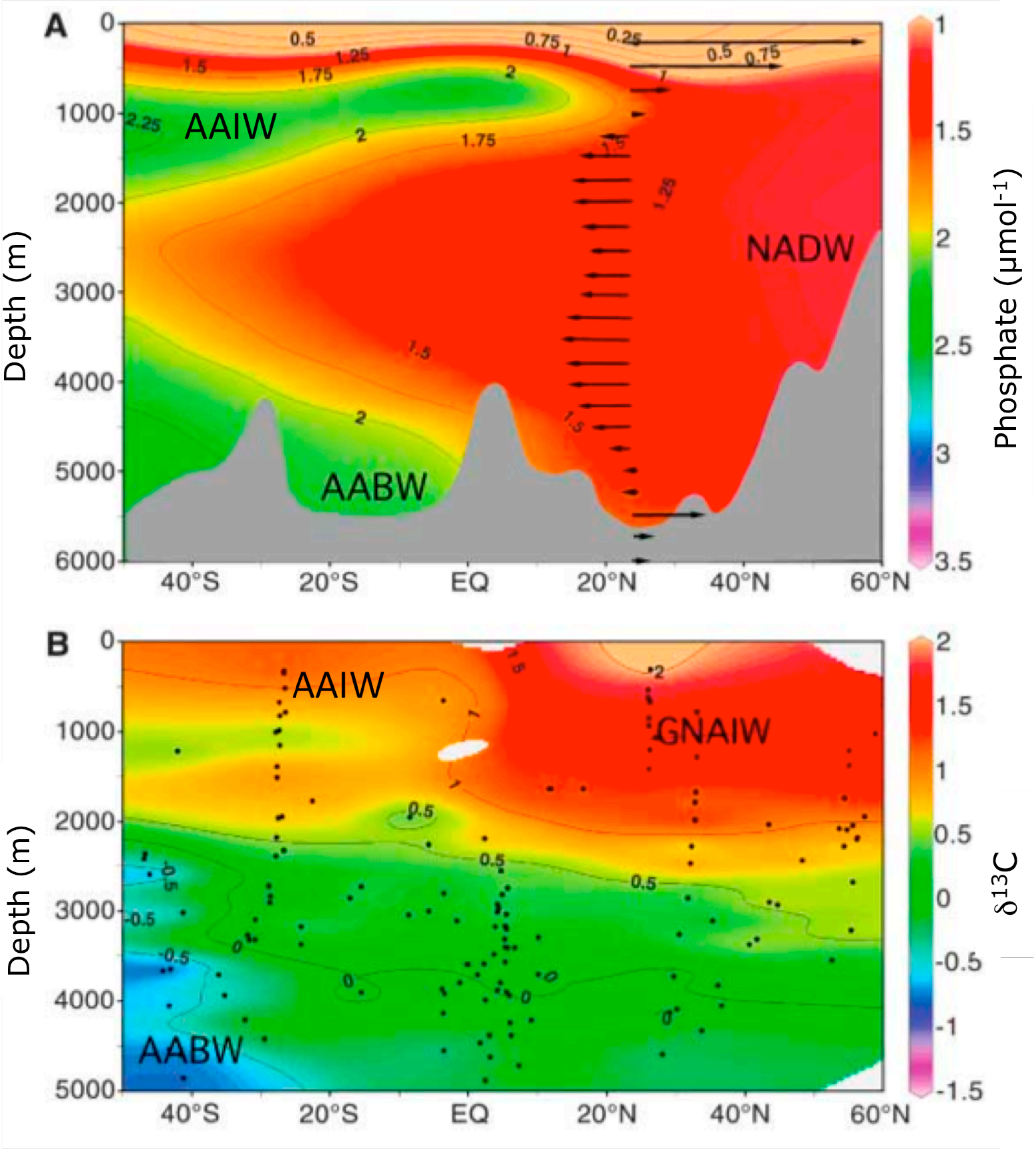

Figure 1.4: Distribution of the major water masses in the western Atlantic Ocean for both a) the modern ocean, based on dissolved phosphate concentrations and b) the Last Glacial Maximum (LGM), based on the carbon isotopic composition of the shells of benthic foraminifera. From Lynch Stieglitz et al., 2007.

The presence of southern sourced AAIW at shallow depths is less well defined at the LGM due to a scarcity of data at intermediate depths in the South Atlantic (Marchitto and Broecker, 2006), although $\delta^{13}C$ data from the Brazilian margin indicate a continued presence of southern source waters at 1000 m at the LGM (Curry and Oppo, 2005), as discussed in chapter 6 of this thesis.

Water mass tracers do not provide information about circulation rates, although the distinct vertical structure seen in nutrient proxies at the LGM must have been maintained by continuous circulation to prevent homogenization by wind and tidal mixing (Wunsch, 2003).

Temperature and salinity were also different at the LGM, with temperatures of deep waters virtually reaching freezing point leading to a circulation controlled by salinity variations (Adkins et al., 2002). In contrast, the modern ocean is dominated by thermal gradients between cold, fresh and dense AABW which underlies warm, salty NADW at all latitudes south of 40^{o}N in the Atlantic.

1.4 Abrupt climate change and reorganizations of Atlantic MOC during the last glacial.

The last glacial and deglacial periods were characterized by millennial scale shifts in global climate. Records from Greenland ice cores (Stuvier and Grootes, 2000) and North Atlantic sediments (e.g. Shackleton et al., 2000) suggest that high latitudes in the Northern Hemisphere were repeatedly subject to large and abrupt fluctuations in temperature, commonly referred to as Dansgaard-Oeschger (D-O) oscillations (Figure 1.5). In the Northern Hemisphere, D-O oscillations take the form of rapid warming, typically over few decades, followed by gradual cooling over hundreds of years (Dansgaard, 1993). These changes occur too frequently and abruptly to be controlled by changes in the orbital cycle of the Earth. Instead, the cause of this climate instability has been attributed to changes in the mode of ocean circulation (e.g. Broecker 2004).

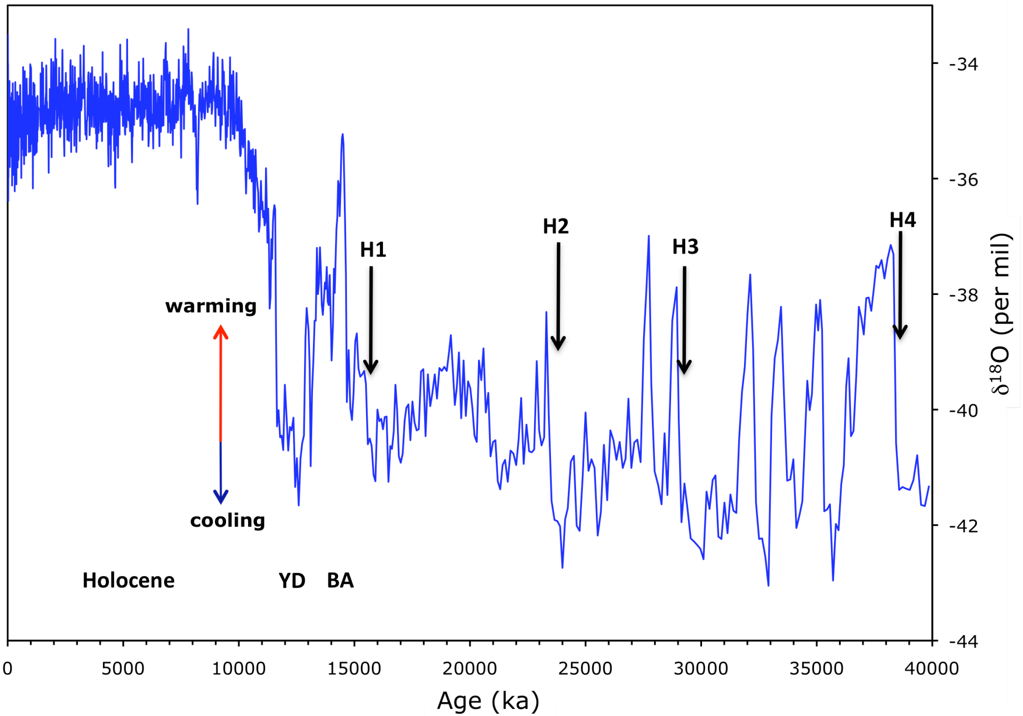

Figure 1.5: Greenland $\delta^{18}O$ data from the GRIP ice core, for the last ~40 kyr displaying the rapid fluctuations in climate (D-O events) that characterized the last glacial. Massive ice rafting episodes known as Heinrich events are depicted (H4-H1) in addition to the Bolling Allerod (BA) and Younger Dryas (YD) intervals. In contrast to the glacial, and deglacial, climate was relatively stable during the Holocene, only punctuated by a brief cold snap at 8.2 ka.

Major reorganizations of the MOC have also been linked to collapses in the Greenland ice sheet, with massive discharges of ice causing the collapse of NADW production and associated heat transport to the high latitudes via surface currents (Broecker, 1994). These so-called Heinrich events, which occur in the cold spells immediately preceeding D-O warmings, are documented as thick layers of ice-rafted debris in marine sediments in the North Atlantic (Hemming, 2004).

Modeling studies (e.g. Ganopolski and Rahmstorf, 2001; Rahmstorf, 2002) suggest that abrupt climate changes that punctuated the glacial are associated with changes between three distinct modes of Atlantic circulation (Sarnthein et al., 1994, Elliot et al., 2002, Figure 1.6).

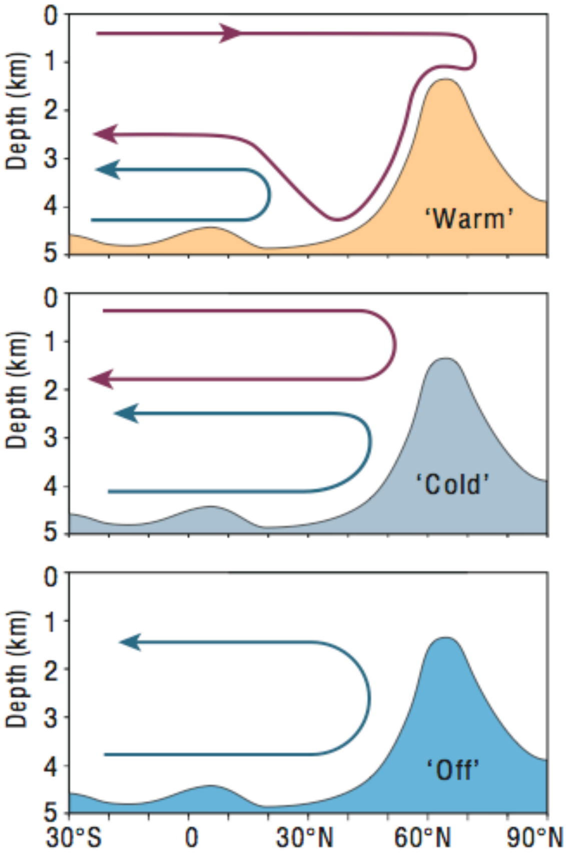

Figure 1.6: Schematic of three ocean circulation modes that prevailed during different times of the last glacial period in the Atlantic. NADW and AABW circulation are shown by purple and blue lines respectively. During the "cold" stadial mode, production of NADW occurs at shallower depths than during the 'warm' circulation mode and south of the shallow sill between Greenland and Scotland, as indicated by the rise in bottom topography at ~60^{o}N. From Rahmstorf (2002).

The rapid warming observed at the end of D-O events in the glacial is associated with a "warm" circulation mode (Figure 1.6) which involves the resumption of deep water formation in the Nordic seas and heat transport to the northern high latitudes via surface currents.

In the "cold" stadial mode, low atmospheric temperatures in the Nordic seas forces convection to shift to the open North Atlantic where NADW forms south of the Greenland-Scotland Ridge, sinking only to intermediate depths. Model simulations suggest that this mode of circulation is stable in a glacial climate (Ganopolski and Rahmstorf, 2001). The occurrence of Heinrich events immediately preceding D-O warmings is likely to have involved a switch from the glacial "cold" mode to an "off" mode (Figure 1.6, Rahmstorf, 2002) where NADW all but ceased due to freshwater inputs derived from melting ice sheets. In both the *cold* and *off* modes NADW is replaced by southern sourced AABW at depths, as observed in Atlantic water mass reconstructions for the LGM (Figure 1.4).

1.5 Anti-phasing of climate records between hemispheres: a Bipolar See-saw?

Comparison of high resolution ice core records from Greenland and Antarctica reveal that temperature fluctuations over Antarctica during the last glacial were more gradual than those observed in Greenland, and were anti-correlated with these northern changes (Blunier and Brook 2001, Figure 1.7).

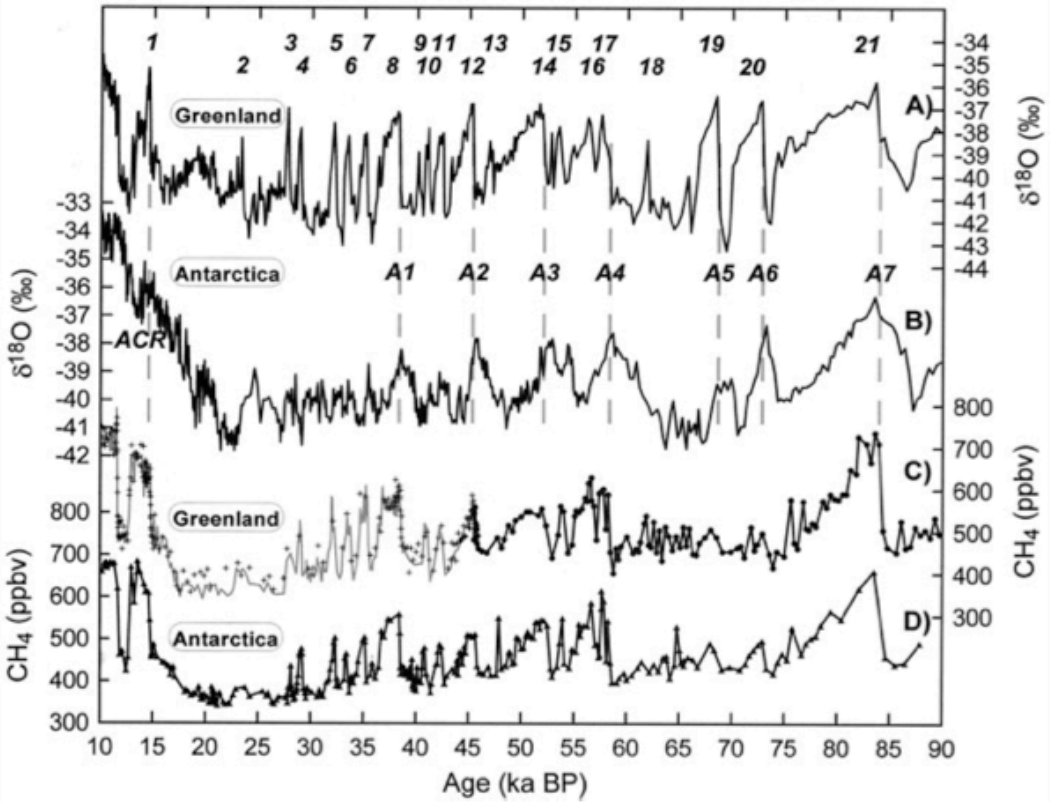

Figure 1.7: Greenland (A) and Antarctica (B) $\delta^{18}O$ records for the past 90 kyr, with timescale synchronized by methane concentrations (C,D). Vertical dashed lines indicate the onset of major Dansgaard-Oeschger events (numbered 1-21). Dashed vertical lines (A1-A7) are used to show times of maximum warming in the south (corresponding to peaks in $\delta^{18}O$ values) coinciding with cooling in the north (minimum $\delta^{18}O$ values). From Blunier and Brook (2001).

More specifically, Antarctic temperatures are observed to increase gradually while Greenland temperatures were decreasing or constant and the termination of Antarctic warming was coincident with the onset of rapid warming in Greenland.

This anti-phasing of climate records between hemispheres has been explained by a mechanism known as the bi-polar seesaw (Broecker, 1998). In this mechanism, deep-water formation occurs more vigorously in one hemisphere than the other, drawing heat from the tropics to the high latitudes in one hemisphere at a time (Stocker, 1998**).** The location of vigorous deep-water formation is thought to oscillate from north to south causing climate changes that are out of phase in the two hemispheres. As discussed above, deep water production in the high latitudes of the North Atlantic currently drives heat transport northward in surface currents from the tropics, allowing reductions in NADW formation to cool the high latitudes of the northern hemisphere and warm the south (Clark et al., 2002). The accuracy of this seesaw mechanism as the cause of abrupt change is supported by an increasing body of evidence which demonstrates that changes in North Atlantic ocean circulation occur synchronously with changes in Greenland temperature (e.g. McManus et al., 2004, Gherardi et al., 2005, discussed in more detail in chapter 2 of this thesis).

The classical bipolar seesaw model predicts an anti-phase relationship between hemispheres, with no time lag. However, the ice core synchronizations of Blunier and Brook (2001) show a time lag between abrupt cooling in Greenland and warming in Antarctica of ~1500 years. A thermal “bipolar seesaw” model has been proposed by Stocker and Johnsen (2003) in which a southern heat reservoir - thought to be the Southern Ocean - is used to account for the significant lag time of southern hemisphere warming in response to a switch off of NADW formation. It is also possible that changes in atmospheric circulation, perhaps driven by changes in the North Atlantic, are responsible for the southern hemisphere response. Significant changes in the position of the Inter-Tropical Convergence Zone (ITCZ) has been predicted in models (Chiang et al., 2003) and observed in speleotherm records (e.g. Wang et al., 2004) and could therefore account for the bipolar temperature change.

Warming over Greenland and Antarctica may also be the direct result of heat released to the atmosphere from deep water formation as discussed above (Figure 1.3). Broecker (1998) suggested, on the basis of atmospheric radiocarbon concentrations, that heat released due to increased AABW formation in the Southern Ocean was important in warming Antarctica during the Younger Dryas, when deep water production in the north was thought to have decreased. At present, however, it is not clear whether ocean circulation changes in the south accompany documented climate changes observed in Antarctica, due to a lack of circulation rate data for southern water masses. Consequently, the bi-polar seesaw, in its true sense of representing antiphase changes in deep-water formation in the two hemispheres, remains an untested hypothesis. Reconstructing past rates of flow of southern water masses in the Argentine Basin would allow for testing of the presently untested southern half of the bipolar seesaw. Furthermore, It is hoped that this research will help improve our understanding of the relationship between ocean circulation and climate, potentially enabling us to better constrain climate scenarios for the future.

1.6 Reconstructions of past ocean circulation in the Southern Hemisphere

As discussed above, tracers such as $\delta^{13}C$ (e.g. Duplessy et al., 1984) Cd/Ca (e.g. Boyle, 1986) and Nd isotopes (e.g. Rutberg et al., 1998) have been used to investigate changes in the distribution of water masses in the past. However, it is the rate of circulation of these water masses that controls heat and carbon transport and hence is of critical importance for assessing the influence of ocean circulation on Earth's climate. Proxies used to reconstruct past flow rates include ^{14}C measurements on planktic and benthic foraminifera to estimate deep water renewal rates (e.g. Adkins et al., 1998), measurements of the mean grain size of the sortable silt (e.g. McCave and Hall 2006), stable-isotope geostrophy (e.g. Lynch-Stieglitz et al., 2006) and sedimentary $^{231}Pa/^{230}Th$ (e.g. Yu et al., 1996).

Studies of past southern hemisphere circulation are few in comparison to those in the north. Hall et al. (2001) investigated flow speeds of the deep western boundary current (DWBC) for the past 1.2 Ma by measuring the mean grain size of sortable silt from sediments east of New Zealand. Using this sortable silt palaeocirculation proxy coupled with foraminiferal $\delta^{13}C$ data, Hall et al. (2001) found evidence for intensified deep Pacific Ocean inflow during glacial periods, possibly due to an increase in production of AABW.

Pahnke et al. (2003) produced a record of $\delta^{18}O$ and Mg/Ca ratios from planktonic foraminifera in sediments from the southwest Pacific to assess surface water hydrographic changes (sea surface temperature $\delta^{18}O$ of sea water) over the past 340,000 years. Data from interglacial core sections were observed to closely correlate with Antarctic climate, whilst glacial core sections displayed higher variability than seen in Antarctic ice cores, implying climate de-coupling between mid and high southern latitudes during glacial times due to an enhanced circulation of the Antarctic Circumpolar Current. In a separate study using sediments from the same location, Pahnke and Zahn (2005) used benthic $\delta^{13}C$ in conjunction with benthic and planktic $\delta^{18}O$ records to infer greater production of AAIW during episodes of northern hemisphere cooling, suggesting that AAIW has significant potential as a dynamic component in interhemispheric deep water formation.

As discussed in more detail in chapter 2 of this thesis, Thomas et al. (2007) observed near constant $^{231}Pa/^{230}Th$ ratios in sediments off Madagascar across the last glacial-interglacial cycle, suggesting that there has been little or no change in the inflow of AABW to the Indian Ocean during the last 140 ka, in contrast to changes in deep circulation thought to occur in other ocean basins.

The research presented in this thesis aims to add to these studies of past southern hemisphere circulation records through reconstruction of past flow rates of southern sourced water masses in the South Atlantic using the sedimentary $^{231}Pa/^{230}Th$ palaeocirculation proxy.

Chapter 2: The ^{231}Pa/^{230}Th proxy

Overview

This thesis focuses on the use of ^{231}Pa/^{230}Th ratios in ocean sediment as a proxy for past ocean circulation. The ^{231}Pa/^{230}Th ratio is more formally expressed as (^{231}Pa/^{230}Th)$_{xs,0}$ where brackets are used to represent the activity ratio of ^{231}Pa to ^{230}Th. The xs,0 subscript is used to indicate that values represent excess ^{231}Pa and ^{230}Th activities which have been corrected for ^{231}Pa and ^{230}Th supported by uranium isotopes present in the sediment mineral lattices and decay corrected to the time of deposition (as described in section 7.2). For simplicity, this expression will subsequently be written in this text as ^{231}Pa/^{230}Th.

This chapter gives a brief overview of the production of ^{231}Pa and ^{230}Th in the water column and discusses the major controls on the sedimentary ^{231}Pa/^{230}Th ratio: particle composition, particle flux and ocean circulation. The use of ^{231}Pa/^{230}Th to investigate past changes in oceanographic processes both in and outside the North Atlantic is then discussed from a historical perspective. At the end of the chapter, a brief introduction to the use of εNd and δ^{13}C isotopes as water mass tracers is also given as these will be used to complement ^{231}Pa/^{230}Th data in this study.

2.1 Production of Pa and Th in seawater

The radioisotopes ^{231}Pa ($t_{1/2}$ = 32.5 kyrs) and ^{230}Th ($t_{1/2}$ = 75.2 kyrs) are produced in seawater by radioactive decay of dissolved parent isotopes ^{235}U and ^{234}U respectively:

$$^{235}\text{U} \xrightarrow{\alpha} {}^{231}\text{Th} \xrightarrow{\beta} {}^{231}\text{Pa} \rightarrow \ldots\ldots {}^{207}\text{Pb} \tag{2.1}$$

$$^{238}\text{U} \xrightarrow{\alpha} {}^{234}\text{Th} \xrightarrow{\beta} {}^{234}\text{Pa} \xrightarrow{\beta} {}^{234}\text{U} \xrightarrow{\alpha} {}^{230}\text{Th} \rightarrow \ldots\ldots {}^{206}\text{Pb} \tag{2.2}$$

Uranium isotopes behave conservatively in oxygenated seawater, forming stable and soluble uranyl carbonate ions. Consequently uranium has a long residence time in the oceans of approximately 400,000 years (Dunk et al., 2002), resulting in the isotopic concentration of uranium being homogenous throughout the oceans (Chen et al., 1986). Subsequently, ^{231}Pa and ^{230}Th are produced, from the decay of their respective parent uranium isotopes (equations 2.1, 2.2), at a constant production activity ratio, (β^{Pa},/ β^{Th}) of 0.093 throughout the ocean (equation 2.3):

$$\left({}^{231}\text{Pa}/{}^{230}\text{Th}\right) = \frac{\beta\left({}^{231}\text{Pa}\right)}{\beta\left({}^{230}\text{Th}\right)} = \frac{2.33\times10^{-3}\,\text{dpm m}^{-3}\ \text{yr}^{-1}}{2.52\times10^{-3}\,\text{dpm m}^{-3}\ \text{yr}^{-1}} = 0.093 \tag{2.3}$$

Protactinium and thorium are significantly less soluble than uranium and are rapidly removed from seawater by adsorption onto settling particles (Anderson et al., 1983). This scavenging process results in the accumulation of excess, or unsupported, ^{230}Th and ^{231}Pa in the underlying sediment. The process of adsorption onto falling particles and subsequent desorption leads to an increase of ^{231}Pa and ^{230}Th concentrations at depth in the water column (Figure 2.1). This process, known as reversible scavenging, takes place because of the sinking of particles to depths with different Pa and Th concentrations and because ^{231}Pa and ^{230}Th remain in an exchangeable form on particle surfaces (Bacon and Anderson, 1982).

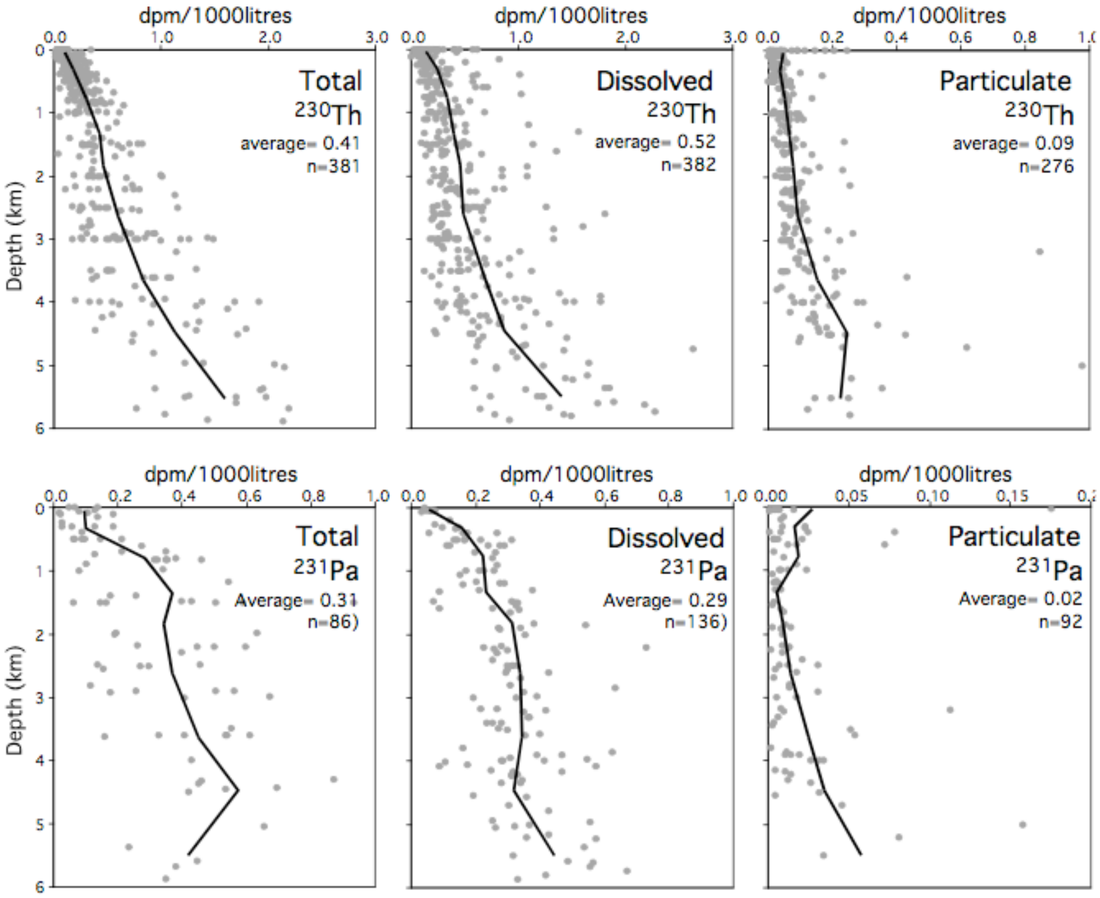

Figure 2.1: A compilation of water column profiles of total, dissolved and particulate phases for ^{230}Th (top) and ^{231}Pa (bottom), with average profiles shown by black lines. From Henderson and Anderson (2003).

The concentration of Th in the water column is greater than ^{231}Pa due to its more abundant parent isotope ^{238}U. ^{230}Th is also more abundant than ^{231}Pa in the particulate phase due to its greater particle reactivity. The less efficient scavenging of dissolved ^{231}Pa gives it a relatively longer ocean residence time of approximately 120 years while that of dissolved ^{230}Th is approximately 30 years (Henderson and Anderson, 2003). These residence times are orders of magnitude shorter than the half lives of ^{231}Pa and ^{230}Th, meaning radioactive decay in the water column is a negligible factor for sedimentary ^{231}Pa/^{230}Th. In addition, the half life of the shorter lived ^{231}Pa ($t_{1/2}$ = 32.5 kyrs) implies that the use of ^{231}Pa/^{230}Th as a valid proxy for ocean processes is restricted to the last 150 kyrs (i.e. ~5 half lives, e.g. Yu e al., 1996).

2.2 The influence of particle composition and particle mass flux on sedimentary ^{231}Pa/^{230}Th

The degree to which ^{230}Th is preferentially scavenged relative to ^{231}Pa is dependent on the composition of scavenging particles in seawater (e.g. Henderson and Anderson, 2003).

Partition coefficients (K_d) are used to describe the equilibrium partitioning of a species between the dissolved and particulate phase for a given particle type (equation 2.4):

$$K_d^{231Pa} = \frac{^{231}Pa_{particulates}}{^{231}Pa_{water}} K_d^{230Th} = \frac{^{230}Th_{particulates}}{^{230}Th_{water}} \qquad (2.4)$$

Typical values for equilibrium partition coefficients for ^{231}Pa and ^{230}Th on carbonate and opal (Table 2.1) are high, reflecting the fact that ^{231}Pa and ^{230}Th adhere to particle surfaces very strongly. However, most ^{231}Pa and ^{230}Th exist in the dissolved phase due to the low concentration of particles in seawater.

	Opal	Carbonate
Kd (^{230}Th) g/g	5.5×10^5	1.0×10^6
Kd (^{231}Pa) g/g	1.67×10^6	2.5×10^5

***Table 2.1*:** Typical partition coefficients for ^{230}Th and ^{231}Pa. From Siddall et al. (2005).

The differential removal of ^{231}Pa and ^{230}Th from the water column for a given particle composition is expressed in terms of the ratio of their partition coefficients, as a fractionation factor (F), (equation 2.5):

$$F_{\left({}^{230}Th/{}^{231}Pa\right)} = \frac{K_d^{\,230}{}^{Th}}{K_d^{\,231}{}^{Pa}} = \frac{\left(\dfrac{{}^{230}Th}{{}^{231}Pa}\right)_{particulates}}{\left(\dfrac{{}^{230}Th}{{}^{231}Pa}\right)_{water}} \qquad (2.5)$$

Partition coefficients for ^{231}Pa and ^{230}Th as a function of particle composition have been determined experimentally through measurement of nuclide concentrations in particles collected in sediment traps and in the water above them (e.g. Chase et al., 2002).

Whilst the precise nature of particle type dependence is still controversial (e.g. Chase and Anderson, 2004; Luo and Ku, 2004; Siddall et al., 2005), there is a clear tendency for F(^{230}Th/^{231}Pa) to decrease with increasing opal content and increase with increasing carbonate content (Chase et al., 2002, Figure 2.2).

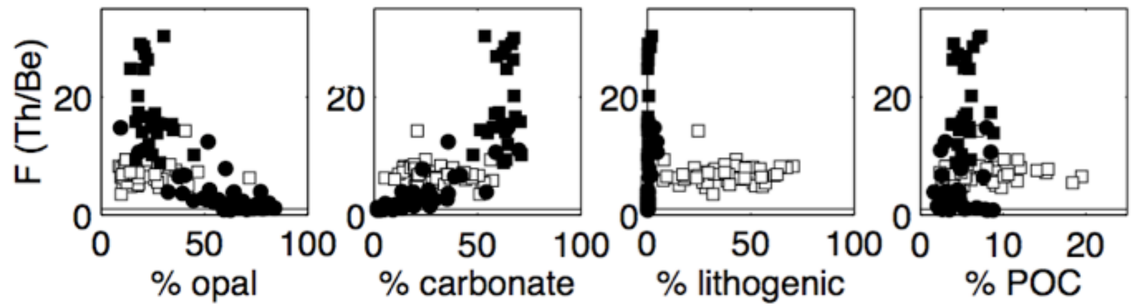

Figure 2.2: Fractionation factor (^{230}Th/^{231}Pa) as a function of particle composition (Chase et al., 2002).

In fact, Chase et al. (2002) report that, due to the lack of relationship between the fractionation factor and the percentage of lithogenic or particulate organic carbon (POC), the fractionation between ^{231}Pa and ^{230}Th in seawater depends primarily on the balance between the two biogenic components opal and carbonate, rather than on the absolute contribution of biogenic versus lithogenic fluxes.

In open-ocean regions and particularly in oligotrophic areas where organisms with carbonate shells dominate, fractionation factors are high (typically $F \approx 10$), reflecting the high proportion of carbonate in the biogenic fraction. Preferential scavenging of ^{230}Th relative to ^{231}Pa in open ocean regions leads to dissolved ^{231}Pa/^{230}Th of 0.3 to 0.4 (i.e. greater than the production ratio of 0.093) and correspondingly low ^{231}Pa/^{230}Th of 0.03-0.04 in sediments underlying these waters (Henderson and Anderson, 2003).

In regions of biological productivity where the composition of scavenging particles is dominated by opal, such as in the Southern Ocean, particles essentially do not fractionate between ^{231}Pa and ^{230}Th ($F \approx 1$). This is due to the strong affinity of opal for ^{231}Pa and also to the weaker affinity of opal for ^{230}Th, relative to other particle types. In such regions, sedimentary ^{231}Pa/^{230}Th is typically greater than the production ratio of 0.093 reflecting the higher seawater values caused by ^{230}Th removed elsewhere (Yu et al., 1996, Figure 2.3).

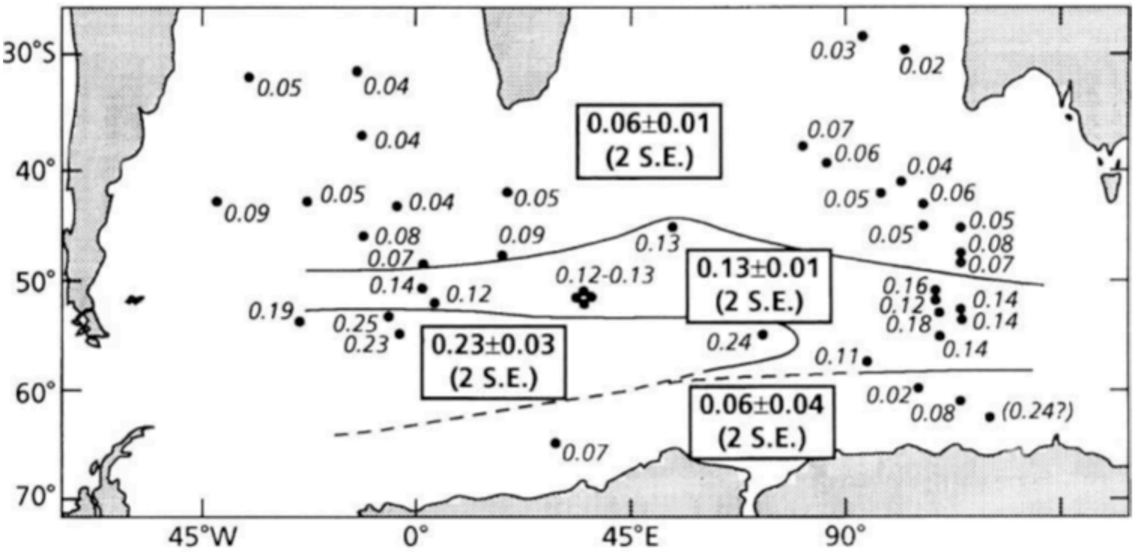

Figure 2.3: Distribution of $^{231}Pa/^{230}Th$ ratios in Southern Ocean Holocene sediments (Yu et al., 1996). Note that, for significant regions of the Southern Ocean the ratio is higher than the production ratio (0.093) due to scavenging of Pa by the opal rich particulate flux.

Further evidence for a strong influence of particle composition and particularly the presence of opal on sedimentary $^{231}Pa/^{230}Th$ ratios comes from Holocene sediment in the Northern Rockall trough (Hall et al., 2006) and from several cores in the western tropical Atlantic (Bradtmiller et al., 2009) where downcore $^{231}Pa/^{230}Th$ profiles show a high correlation with opal concentrations. Whilst opal production is clearly a strong modulator of sedimentary $^{231}Pa/^{230}Th$, it is important to note that estimations of past opal concentrations in marine surface waters is confounded by the many factors that can influence the efficiency of opal preservation in sediments (e.g. Lippold et al., 2009).

In addition to the control on $^{231}Pa/^{230}Th$ fractionation by particle composition, the scavenging efficiency of Pa and Th is greater in regions of high particle flux due to the higher surface area available to Pa and Th for scavenging (Kumar et al., 1993). Past changes in particle flux can be evaluated by ^{230}Th normalization (as described in section 6.2 of this thesis). Using this technique, data collected from sediment traps have indicated a positive correlation between ^{231}Pa/^{230}Th and mass flux of particles in the water column (Lao et al., 1993; Kumar et al., 1995).

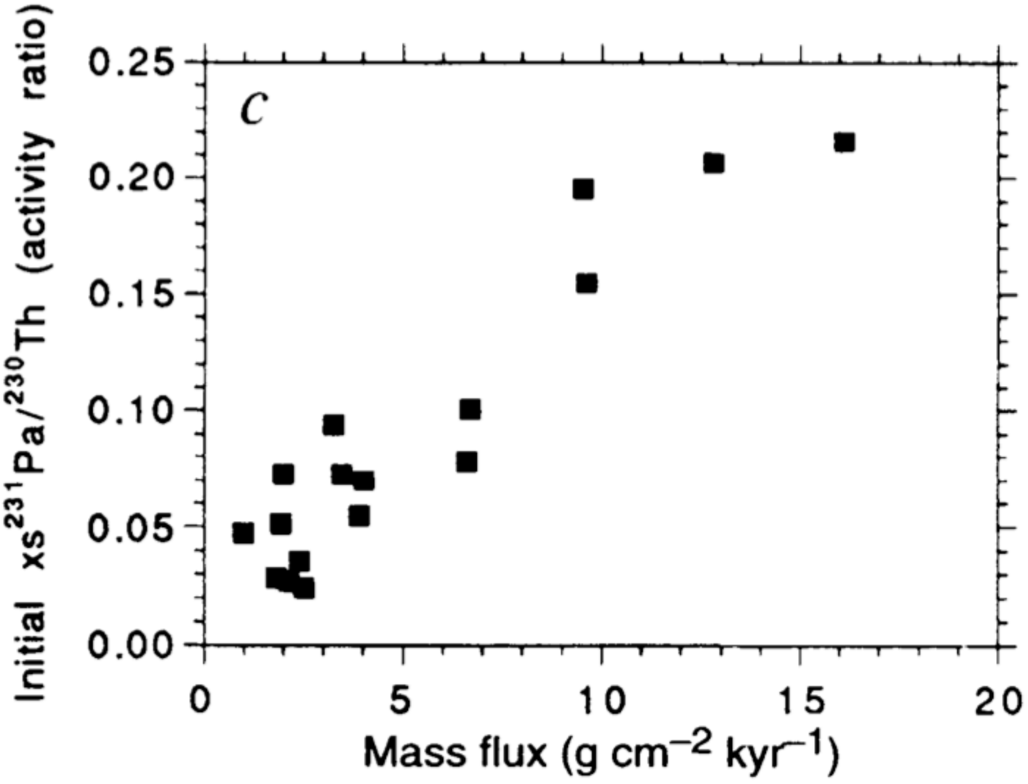

Figure 2.4: ^{231}Pa/^{230}Th ratios plotted against mean annual mass flux of particles collected in sediment traps from the South Atlantic (Kumar et al. 1995)

This relationship was initially relied on to use ^{231}Pa/^{230}Th ratios to reconstruct past productivity (e.g. Kumar et al., 1993, section 2.5), though subsequent realization of the importance of opal for ^{231}Pa/^{230}Th fractionation undermines the use of sediment ^{231}Pa/^{230}Th as a proxy for paleo particle flux.

Enhanced scavenging of Pa occurs at ocean margins due to the combined effects of high particle mass flux and high concentrations of opal in surface waters. The combination of these effects, known as boundary scavenging, involves the lateral transport of Pa to coastal areas by diffusive processes before being scavenged to the sediment (e.g. Anderson and Bacon, 1983**)**. Causes for the increased scavenging in the near-shore environment include greater particulate flux from rivers and coastal erosion and enhanced bio-productivity due to upwelling (Luo et al., 2004).

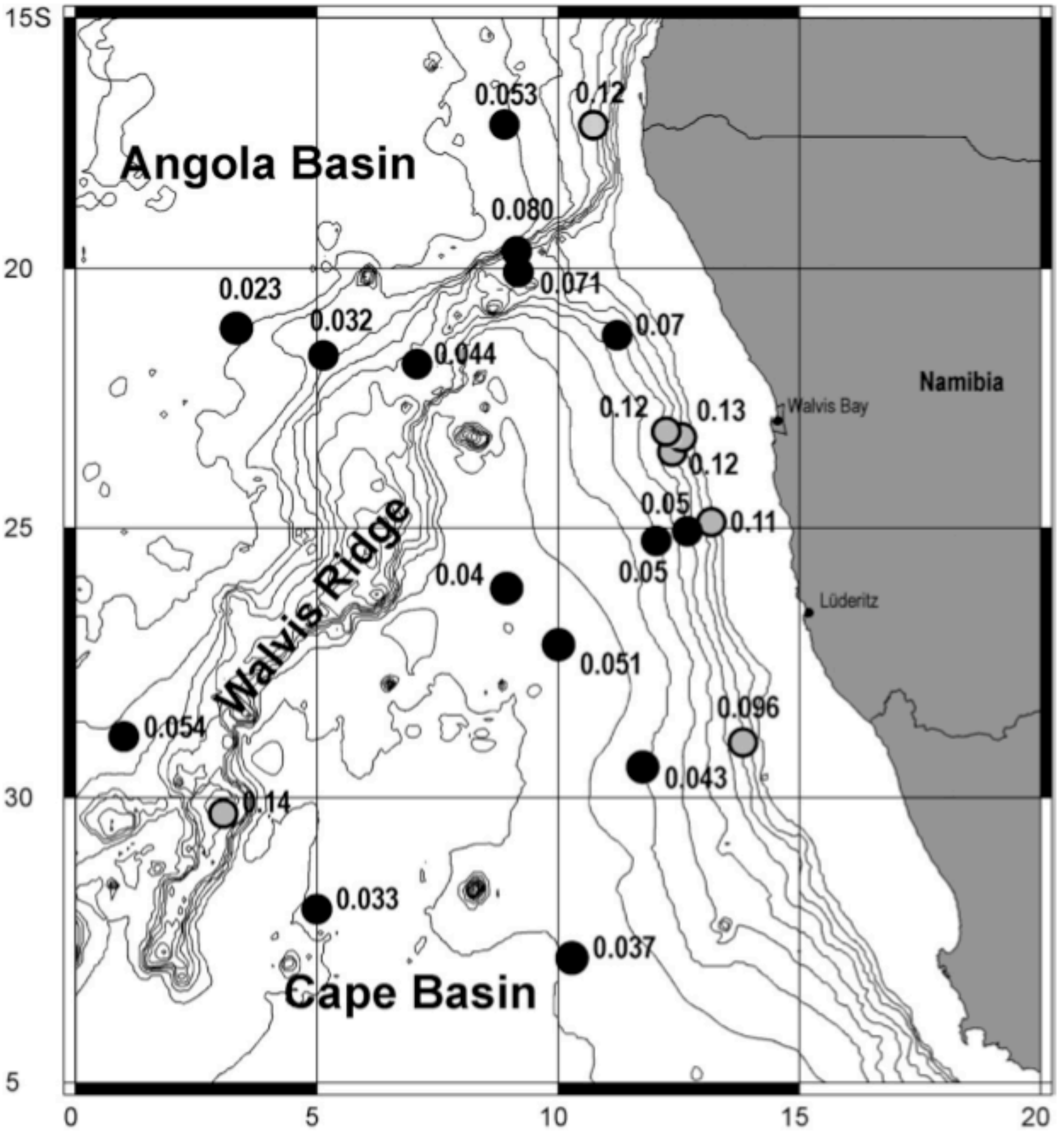

Figure 2.5: ^{231}Pa/^{230}Th ratios in surface sediments off the Namibian coast: grey circles are ^{231}Pa/^{230}Th ratios higher than the production rate of these isotopes in the water column (0.093), black circles are ^{231}Pa/^{230}Th ratios lower than the production ratio. From Scholten et al. (2008).

An example of such boundary scavenging is provided by Scholten et al. (2008), who document evidence for boundary scavenging in upwelling regions off the west coast of Africa, where ^{231}Pa/^{230}Th in surface sediments is observed to decrease with distance from the Namibian coast (Figure 2.5). This is thought to reflect enhanced removal of Pa due to higher particle flux and greater opal production with proximity to the coastline. However, boundary scavenging is generally weakly expressed in the Atlantic in comparison to other ocean basins with longer water mass residence times (Moran et al., 2001) because waters are advected southward and out of the basin before significant lateral diffusion of ^{231}Pa to the margins can occur.

2.3 The use of ^{231}Pa/^{230}Th as a proxy for past ocean circulation

The use of ^{231}Pa/^{230}Th to assess past circulation rates relies on the difference in solubility of Pa and Th. As described in section 2.2, Pa is slightly more soluble than Th and therefore has longer residence time in the water column. Consequently, ^{231}Pa is more strongly advected by ocean circulation than ^{230}Th and can be transported laterally over longer distances and away from the site of sediment deposition.

The ^{231}Pa/^{230}Th preserved in sediments can therefore be used as a proxy for measuring past rates of ocean circulation in ocean regions where water mass residence times are shorter or on the same order of magnitude as the scavenging time of ^{230}Th and ^{231}Pa (Scholten et al., 1995). Higher rates of meridional overturning circulation in the past would result in greater Pa export from the North Atlantic to the Southern Ocean and in lower ^{231}Pa/^{230}Th ratios in the underlying sediments of the North Atlantic. In contrast, a stagnant water mass will reach a state where the ^{231}Pa/^{230}Th of the underlying sediments in the North Atlantic is equal to the production ratio in the water column of 0.093.

In the North Atlantic today, deep water formation combined with rapid advection is responsible for exporting approximately 50-70% of ^{231}Pa and only 10% of ^{230}Th produced in the water column to the southern ocean (Yu et al., 1996). Consequently modern Atlantic sediments north of 50°S have a mean ^{231}Pa/^{230}Th significantly lower than the natural production ratio of 0.093 (Yu et al., 1996). On reaching the Southern Ocean, the excess ^{231}Pa exported from the North Atlantic is scavenged by opal in regions of high biological productivity, leading to sedimentary ^{231}Pa/^{230}Th ratios in excess of the production ratio (Figure 2.6, Henderson 2002).

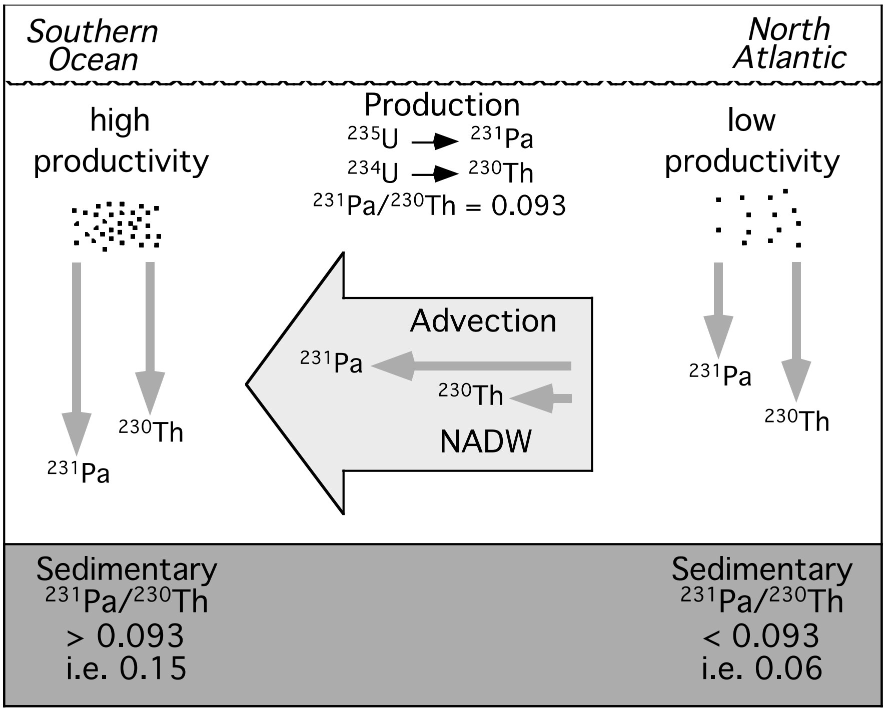

Figure 2.6: Relative ^{231}Pa/^{230}Th ratios in the north Atlantic and Southern Ocean resulting from southward advection of Pa with NADW. Taken from Henderson (2002).

2.4 Reconstructing past variations in North Atlantic MOC using ^{231}Pa/^{230}Th

The use of ^{231}Pa/^{230}Th as a paleocirculation proxy was first applied by Yu et al., (1996) to assess changes in the flow rate of NADW between the last glacial and the Holocene. Similar sedimentary ^{231}Pa/^{230}Th ratios in the Southern Ocean between the Last Glacial Maximum and the Holocene were at first used to indicate little change in the overall strength of the Atlantic MOC between these periods. This result conflicted with previous water mass studies that had demonstrated that less of the Atlantic was influenced by NADW during glacial times (e.g. Duplessy et al., 1998; Boyle and Keigwin, 1982). However, later modeling studies found that ^{231}Pa/^{230}Th in the Southern Ocean is relatively insensitive to changes in ocean circulation due to the high opal productivity in this region which results in high ^{231}Pa/^{230}Th regardless of the rate of NADW flow (Marchall et al., 2000).

The timeslices of Yu et al. (1996) were followed by the first continuous high resolution palaeorecord of ^{231}Pa/^{230}Th in a study by McManus et al. (2004). In this study, changes in deep-water formation during the past ~20 kyrs were assessed by analysis of a high accumulation rate core (OCE326-GGC5; 33°42'N, 57°33'W, 4,550 m) in the deep western subtropical Atlantic (Figure 2.7). The sedimentary ^{231}Pa/^{230}Th record in core GCC5 is marked by large changes in ^{231}Pa/^{230}Th during the deglacial, whose timing suggest rapid, large scale oscillations in MOC that occurred in concert with regional climatic variations as observed in Greenland ice core isotope records (Figure 2.7). Specifically, ^{231}Pa/^{230}Th ratios from the Bermuda Rise are observed to increase soon after ~19 ka toward the production ratio of 0.093 at ~17.5 ka and remain above 0.08 until ~15 ka.

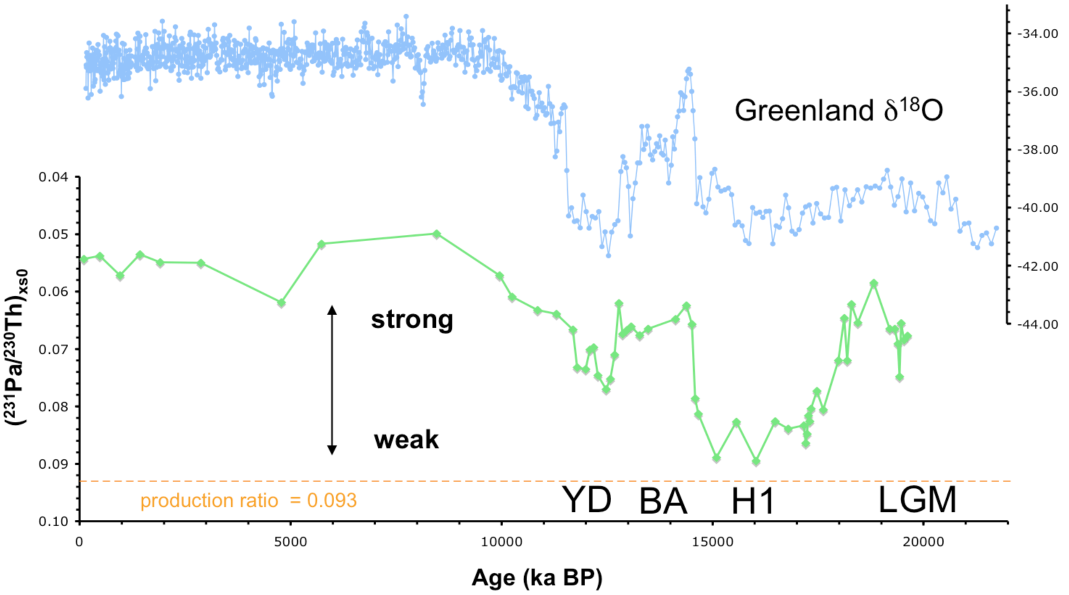

Figure 2.7: ^{231}Pa/^{230}Th ratios (green) from the Bermuda Rise (core GGC5) after McManus et al (2004). GISP oxygen isotope data is shown in blue (data taken from NGDC). Dashed orange line is used to indicate the natural ^{231}Pa/^{230}Th production ratio (0.093).

These high ^{231}Pa/^{230}Th ratios were interpreted by McManus et al. (2004) as reflecting a nearly total shutdown of the MOC that lasted for more than 2000 years. This inferred collapse of deep ocean circulation is thought to be linked to the onset of the Heinrich-1 (H1) iceberg rafting event (at ~17.5 ka). The Heinrich-1 stadial was followed by an abrupt decrease in ^{231}Pa/^{230}Th and subsequent inferred reinvigoration of MOC during the dramatic warming of Bolling-Allerod (at ~15 ka). A further abrupt increase in ^{231}Pa/^{230}Th, implying a partial reduction in MOC, occurs at 12.7 ka coinciding with the beginning of the Younger Dryas cold event.

The results of McManus et al. (2004) have been supported by subsequent studies from the Iberian Margin (Gherardi et al., 2005) and the northeast Atlantic (Gherardi et al., 2009) in which similarly high ^{231}Pa/^{230}Th ratios were observed during H1 and the Younger Dryas (YD). The similarities in the ^{231}Pa/^{230}Th records from the Iberian margin and the Bermuda Rise record suggests that sedimentary ^{231}Pa/^{230}Th ratios record basin-wide changes in deep water circulation in the North Atlantic (Siddall et al., 2005).

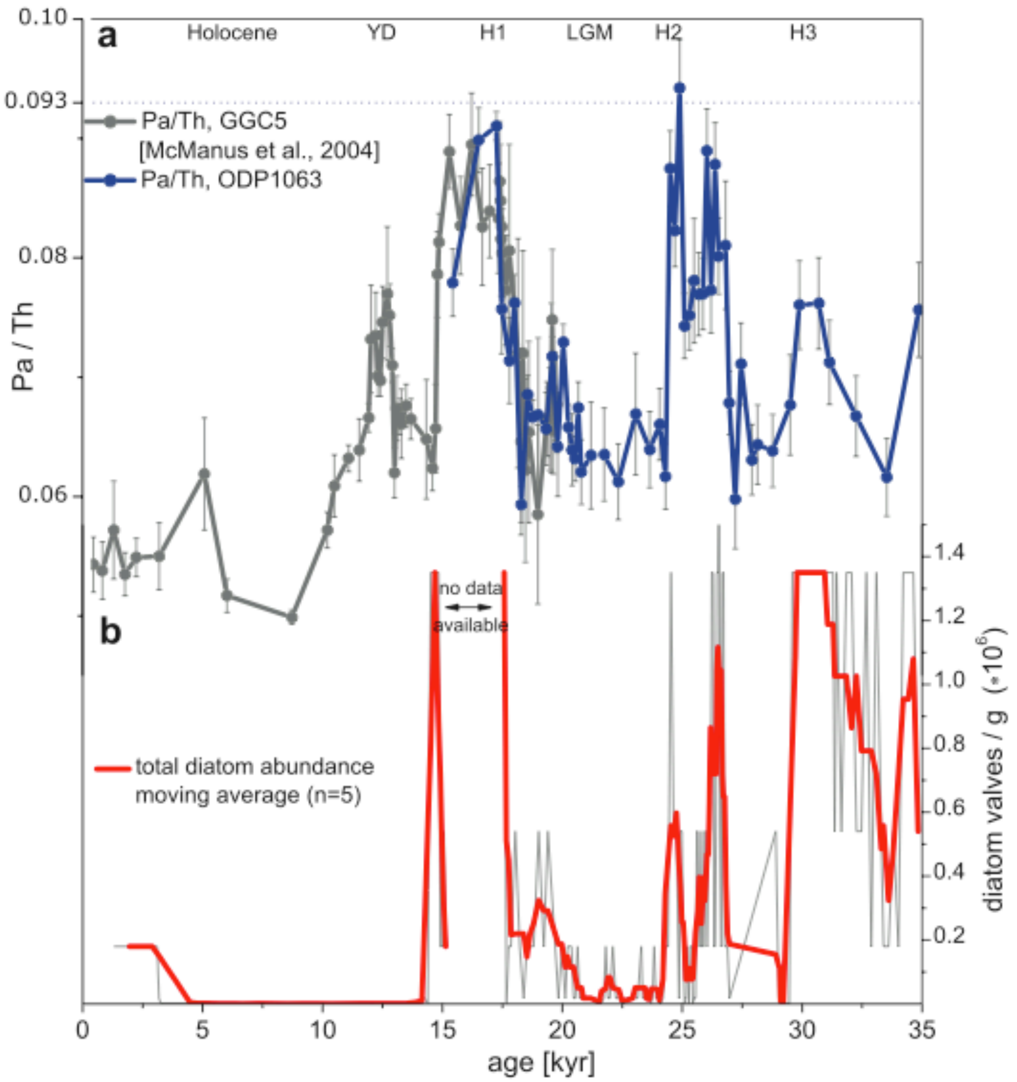

Figure 2.8: **a)** ^{231}Pa/^{230}Th ratios from Bermuda Rise cores ODP1063 (blue, Lippold et al., 2009) and GGC5 (grey, McManus et al., 2004). **b)** Total diatom abundance in core ODP1063 (grey: original data, red: smoothed data). From Lippold et al., 2009.

The ^{230}Th normalized sediment flux records in each of the aforementioned studies did not show significant changes in particle flux at any of these sites, suggesting that changes in these ^{231}Pa/^{230}Th records are likely to be mainly due to changes in circulation (Siddall et al., 2005). However, further research by Lippold et al. (2009)

found a significant correlation between diatom concentration and $^{231}Pa/^{230}Th$ ratios in core ODP 1063 (33° 41'N, 57° 37'W, 4,584 m) close to the location of core GGC5, suggesting that particle composition may have a strong control on $^{231}Pa/^{230}Th$ ratios in North Atlantic sediments, most notably during Heinrich stadials (Figure 2.8).

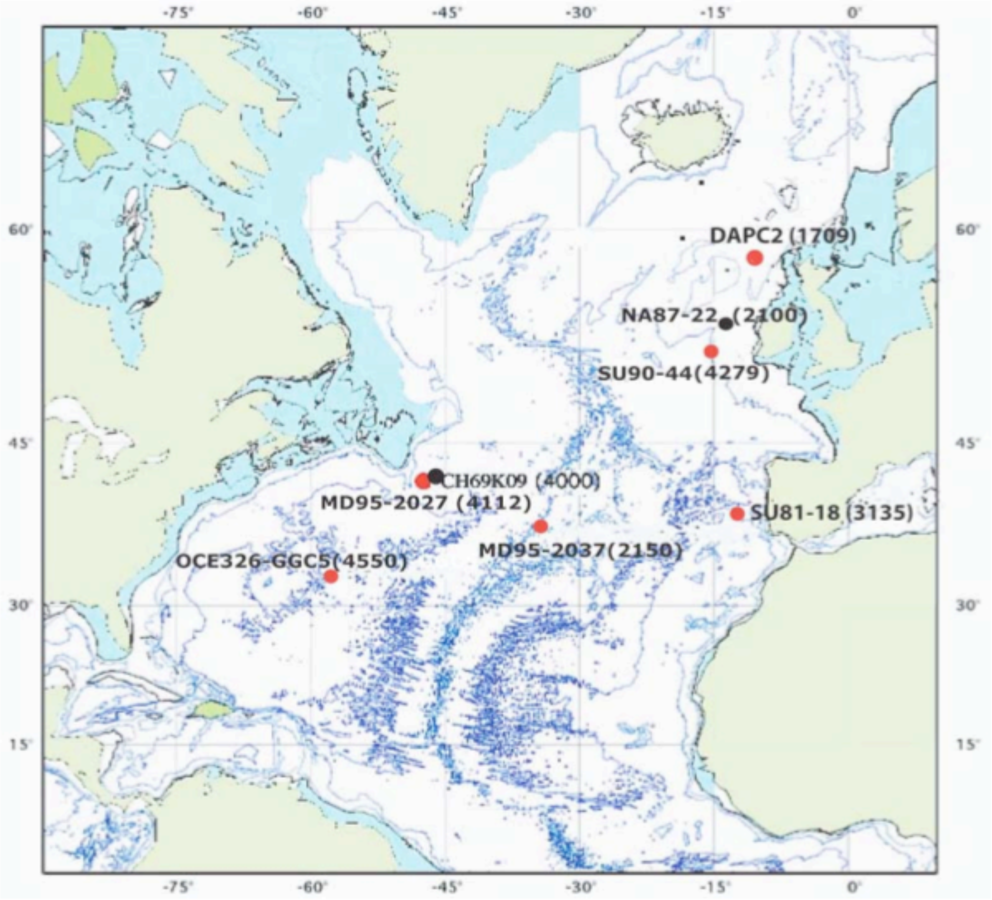

Figure 2.9: Map of north Atlantic showing locations of cores used in Gherardi $^{231}Pa/^{230}Th$ compilation study (red circles) and sites of cores used for stratigraphic correlations (black circles). From Gherardi et al. (2009).

Gherardi et al. (2009) compiled $^{231}Pa/^{230}Th$ ratios from six North Atlantic sediment cores ranging in depth from ~2-4.5 km to investigate the evolution of the geometry and rate of formation of deep waters in the North Atlantic for the last ~25 kyrs (Figure 2.9). These records included three previously published records from McManus et al. (2004), Gherardi et al. (2005) and Hall et al. (2006). Average sedimentary ^{231}Pa/^{230}Th ratios for each core were calculated for five major time slices (Heinrich-1 (H1), Younger Dryas (YD), Bolling-Allerod (BA), Holocene and the LGM) and plotted versus depth (Figure 2.10).

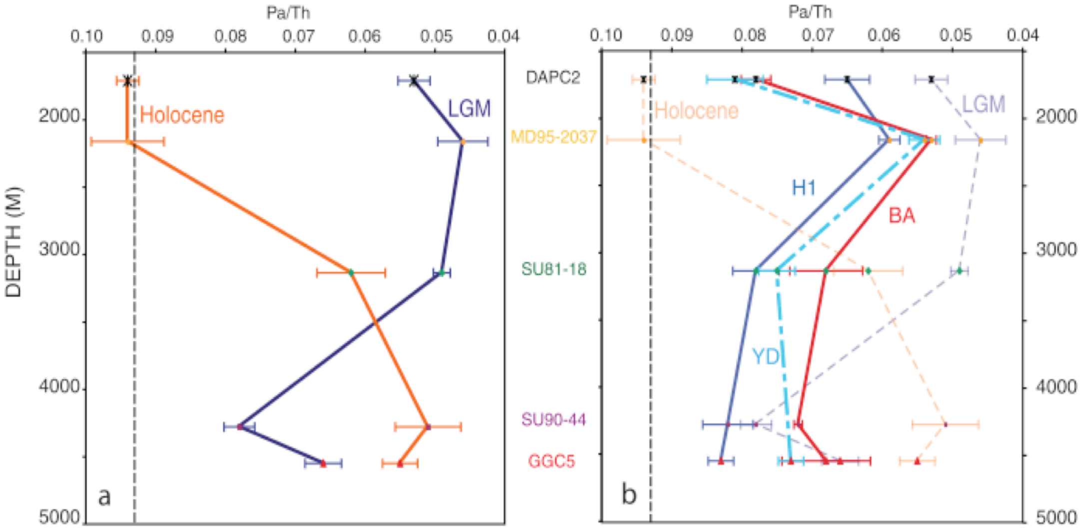

Figure 2.10: Sedimentary ^{231}Pa/^{230}Th time slices versus water depth from North Atlantic sediments (Gherardi et al. 2009). a) LGM (solid dark blue) versus Holocene (orange) time slice. b) H1 (solid blue), BA (red) and YD (dashed light blue). The ^{231}Pa/^{230}Th natural production ratio (0.093) is shown using a black vertical dashed line.

Results from the time slice profiles show that Holocene ^{231}Pa/^{230}Th ratios decrease with depth (Figure 2.10a), indicating vigorous export of deep waters consistent with our understanding of modern Atlantic Ocean circulation. In contrast, ^{231}Pa/^{230}Th ratios at the LGM indicate that GNAIW drove a rapid overturning circulation down to depths of 3000 m, below which circulation was much slower than today, as indicated by higher ^{231}Pa/^{230}Th. The very different ^{231}Pa/^{230}Th profiles observed for the Holocene and LGM is consistent with the differences between Holocene and glacial circulation modes previously inferred from nutrient proxies (e.g. Curry and Oppo, 2005) as discussed in chapter 1.

The timeslice from H1 (Figure 2.10b), shows relatively high ^{231}Pa/^{230}Th ratios at depth indicating reduced deep water renewal rates, whereas significantly lower ^{231}Pa/^{230}Th ratios at 2000 m suggests there was still an active overturning cell that was exporting ^{231}Pa from the North Atlantic at this time. ^{231}Pa/^{230}Th values during the Bolling-Allerod period, commonly thought to have a circulation mode similar to the modern ocean, indicate lower deep water renewal than during the Holocene although greater than during H1. The circulation characteristics of the YD appear to be intermediate between those of H1 and BA.

Hall et al. (2006) argue that the high ^{231}Pa/^{230}Th ratios recorded in core DAPC2 during the Holocene are the result of high opal concentrations in particulate fluxes to the sediment in the Rockall trough. Others have suggested that the ^{231}Pa/^{230}Th signal in some North Atlantic records may be caused by high opal concentrations (Keigwin and Boyle, 2008). However, a similar level of opal abundance to DAPC2 is observed in core MD95-2037 during the glacial, with little apparent influence on the ^{231}Pa/^{230}Th signal, casting doubt on this explanation (Gherardi et al. 2009).

2.5 The use of ^{231}Pa/^{230}Th outside of the North Atlantic

Early studies of sedimentary ^{231}Pa/^{230}Th ratios outside of the North Atlantic focused on the use of ^{231}Pa/^{230}Th as a paleo productivity proxy in the Southern Ocean. Kumar et al. (1993) used ^{231}Pa/^{230}Th records from cores located north and south of the modern day Antarctic Polar Front (APF) to investigate spatial variations in particle flux and biologic productivity over the last ~150 kyrs. Kumar et al. (1993) observed that high ^{231}Pa/^{230}Th ratios occurred during interglacial periods south of the APF

(Figure 2.11a) whilst during glacial periods high ^{231}Pa/^{230}Th was found north of the APF (Figure 2.11b).

Assuming ^{231}Pa/^{230}Th to reflect mainly changes in mass flux, regardless of the composition of settling particles, Kumar et al. (1993) interpreted these ^{231}Pa/^{230}Th records as reflecting an a northward shift in the zone of high biological productivity during glacial periods due to an increase of Southern Ocean sea-ice cover.

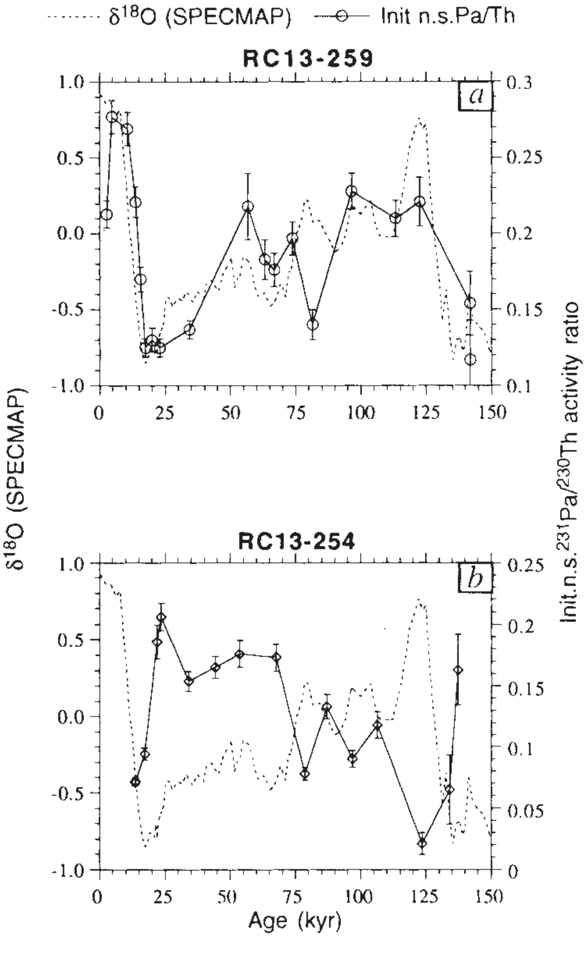

Figure 2.11: Decay corrected ^{231}Pa/^{230}Th ratios in sediments from **(a)** core RC13-259 located south of the present position of the Antarctic Polar Front (APF) and **(b)** RC 13-254 located north of the APF. The SPECMAP δ^{18}O record (dashed line) is shown to illustrate glacial-interglacial cycles over this time interval (Kumar et al. 1993). The pattern of variability north and south of the APF are opposite to one another with ^{231}Pa/^{230}Th ratios well below the production ratio (0.093) observed during interglacials north of the APF and ^{231}Pa/^{230}Th ratios a factor of three greater than the production ratio observed during interglacials south of the APF.

Subsequent work investigating the control of particle composition on ^{231}Pa/^{230}Th (e.g. Chase et al., 2002) found that opal concentrations have a significant influence on

$^{231}Pa/^{230}Th$ (as discussed in section 2.2). However, because high particle flux regions tend to be dominated by diatoms (opal) it is often difficult to separate the influences of both particle flux and particle composition on sedimentary $^{231}Pa/^{230}Th$ ratios in regions of high particle flux.

Pa and Th water column profiles for the southwest Indian Ocean, produced by Thomas et al. (2006) indicate that waters flowing from the Southern Ocean (AABW) are depleted in Pa relative to other water masses (Figure 2.12). This was attributed to scavenging of Pa as waters flow northwards through the opal belt at ~50°S.

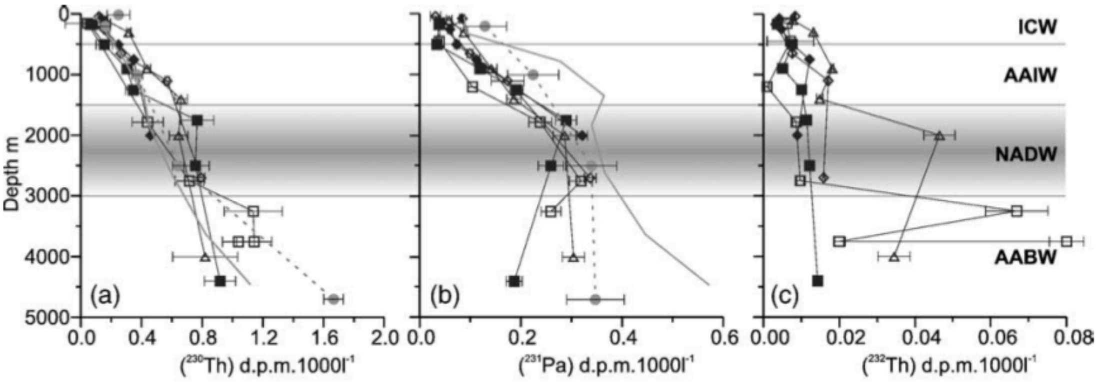

Figure 2.12: Water column results from the southwest Indian Ocean showing profiles through the water column for a) ^{230}Th; b) ^{231}Pa and c) ^{232}Th. A depletion in Pa relative to overlying waters and globally averaged data (thick grey line) is observed in AABW. From Thomas et al. (2006).

This result has important implications for the study of sedimentary $^{231}Pa/^{230}Th$ in ocean regions where sediments are bathed by southern sourced water masses. For example, enhanced scavenging of Pa in southern sourced water masses flowing through the opal belt would result in $^{231}Pa/^{230}Th$ ratios below the production ratio at core sites in the Argentine Basin. $^{231}Pa/^{230}Th$ ratios below the production ratio are likely to be sensitive to changes in circulation and export productivity and can therefore potentially be used to reconstruct the past circulation of AABW in the South Atlantic.

The observation of water masses with distinct Pa values in a single water column also raised the question of which water mass controls sedimentary ^{231}Pa/^{230}Th values. A common assumption in interpretation of sedimentary ^{231}Pa/^{230}Th ratios from the North Atlantic has been that they represent average flow conditions through the entire water column. This assumption has been tested in a recent study by Thomas et al. (2006). Using a simple 1D model to assess the depth at which Pa and Th last equilibrate in the water column before reaching the sediment, Thomas et al. (2006) found that Pa and Th exported to the ocean bottom last equilibrate with waters within ~1000 m of the seafloor as a consequence of increasing Pa and Th concentration with depth. The sedimentary ^{231}Pa/^{230}Th ratio is therefore thought to reflect the flow rate of only the deepest water mass, rather than averaging flow across the entire water column. This finding suggests that southern component waters may act as a potential modulator of sedimentary ^{231}Pa/^{230}Th in the North Atlantic, given the evidence of northward intrusion of southern waters during cold periods (e.g. Boyle and Keigwin, 1987; Curry and Oppo, 2005).

Thomas et al. (2007) measured ^{231}Pa/^{230}Th in sediments from a deep core east of Madagascar to assess past flow-rates of AABW into the Indian Ocean over the last glacial-interglacial cycle. ^{231}Pa/^{230}Th ratios were found to be nearly constant at 0.055 throughout this period, significantly lower than the production ratio of 0.093, indicating that the proxy is sensitive to changes in circulation and sediment fluxes at this site. The consistent value suggests there has been no change in the inflow of

AABW to the Indian Ocean during the last 140 ka, in contrast to changes in deep circulation thought to occur in other ocean basins (e.g. Atlantic Ocean)

2.6 Modeling the response of ^{231}Pa/^{230}Th to changes in Atlantic MOC

General Circulation Models (GCM's) are able to reproduce the main features of global ^{231}Pa/^{230}Th in sediments (Siddall et al., 2005) and have recently been used to examine the potential changes in sedimentary ^{231}Pa/^{230}Th with a shutdown of NADW formation (Siddall et al., 2007). Figure 2.13(A) shows modeled ^{231}Pa/^{230}Th ratios representing modern day AMOC circulation scenario with core top ^{231}Pa/^{230}Th data (in circles) shown for comparison.

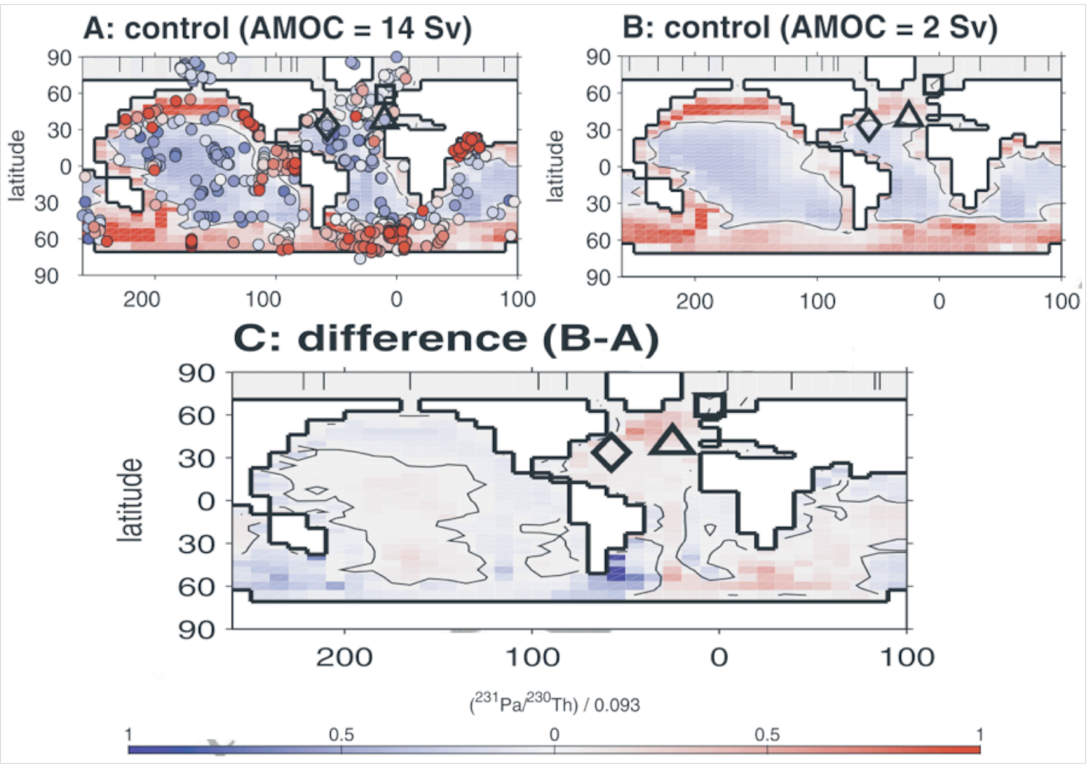

Figure 2.13: Model simulation of surface sedimentary ^{231}Pa/^{230}Th. For **(a)** the control simulation of the present day surface sedimentary ^{231}Pa/^{230}Th (AMOC-on, 14 Sv), as given by Siddall et al. (2005). Observations are shown as colored circles**. (b)** Modled surface sedimentary ^{231}Pa/^{230}Th for the AMOC-off state (2 Sv). **(c)** The difference in modeled surface sedimentary ^{231}Pa/^{230}Th between the AMOC-on and AMOC-off states. The diamond marks the location of core GGC5 from McManus et al. (2004) and the triangle that of core SU81-18 from Gherardi et al. (2005). Adapted from Siddall et al. (2007).

Open ocean regions can be seen to have relatively low ^{231}Pa/^{230}Th as a result of their low particle flux and predominance of carbonate (as discussed in section 2.1). The model run for a collapsed or reduced state of AMOC (Figure 2.13(B)) shows that Pa is scavenged to sediments in regions of high particle flux. The influence of boundary scavenging and particle flux is more fully expressed in the Pacific and Indian Oceans due to the relatively short residence time of Atlantic waters. The difference in surface sedimentary ^{231}Pa/^{230}Th between AMOC on and off states (Figure 2.13(C)) is most pronounced in the North Atlantic. However, there is also a significant reduction in ^{231}Pa/^{230}Th observed in the SW Atlantic due to changes in circulation of southern source waters in this region. This model result hints at a possible seesaw like behavior in circulation strength of northern and southern water masses in the southwest Atlantic.

2.7 Water mass tracers complimentary to ^{231}Pa/^{230}Th

This section briefly describes the use of εNd in Fe-Mn precipitates and δ^{13}C in benthic foraminifera as water mass tracers in the ocean. These proxies will be used to complement ^{231}Pa/^{230}Th data in this study, in helping to reconstruct the evolution of water mass geometry in the Argentine Basin over the last ~25 kyrs.

2.7.1 Stable carbon isotopes

Paleoceanographic studies of stable carbon isotopes focus on the ratio of ^{13}C to ^{12}C in the tests of bottom dwelling (benthic) foraminifera, which is reported as relative deviation from a standard, Vienna Pee Dee Belemnite (Coplen 1996):

$$\delta^{13}\mathrm{C}(‰) = \left[\frac{\left({}^{13}\mathrm{C}/{}^{12}\mathrm{C}_{sample}\right) - \left({}^{13}\mathrm{C}/{}^{12}\mathrm{C}_{standard}\right)}{\left({}^{13}\mathrm{C}/{}^{12}\mathrm{C}_{standard}\right)} \right] \times 1000 \qquad (2.6)$$

During photosynthesis, marine phytoplankton preferentially take up the lighter isotope of carbon, ^{12}C, causing enrichment of ^{13}C in the dissolved carbon of surface waters (Park and Epstein 1960). The strong preferential uptake of ^{12}C causes marine phytoplankton to form organic matter with δ^{13}C values which are -20 to -23 ‰ lower than ambient seawater (e.g. Hoefs, 2003). When the ^{13}C depleted organic matter sinks and decomposes, nutrients and CO_2 enriched in ^{12}C are released causing a decrease in the δ^{13}C of seawater at depth.

Greater surface productivity will therefore cause an increase in the gradient between ^{13}C enrichment in surface waters and ^{13}C depletion in deep waters. In addition, the longer a water mass spends at depth with organic matter raining into it, the more enriched in ^{12}C and nutrients it becomes. Therefore, newly formed deepwaters, such as NADW, have high δ^{13}C values and are nutrient poor where as poorly ventilated deep waters such as AABW have relatively low δ^{13}C and are nutrient rich.

As carbon behaves as a conservative element in the ocean, changes in δ^{13}C of deep waters may arise from mixing of waters with different isotopic compositions and from remineralisation of organic matter in the deep ocean (Curry et al., 1998). Hence, δ^{13}C of benthic foraminifera can be used as a tracer of past water mass distribution in the ocean.

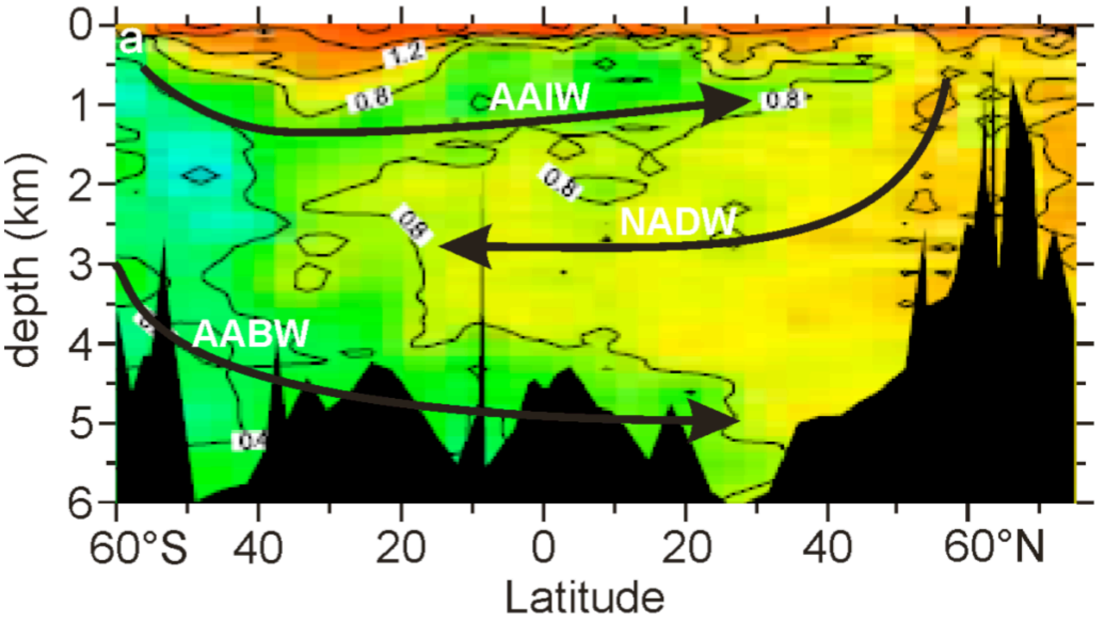

Figure 2.14: $\delta^{13}C$ distribution in the modern western Atlantic, showing the distinctly high $\delta^{13}C$ signature of AAIW relative to NADW and AABW. Adapted from Curry and Oppo (2005).

However, the $\delta^{13}C$ of seawater can also be influenced by carbon isotope fractionation during air-sea exchange. At the ocean-atmosphere interface, carbon dioxide equilibrates with the atmosphere. Given sufficient time at the surface, surface water will tend towards equilibrium, exchanging ^{12}C for ^{13}C with the atmosphere. The efficiency of the equilibrium reaction is dependent on both the time any one parcel of water spends in contact with the atmosphere and on the sea surface temperature, with oceanic carbon becoming more enriched in ^{13}C relative to the atmospheric value by about 0.1‰ per degree of cooling (Mook et al., 1974). High wind speeds increase exchange rates, bringing the dissolved inorganic carbon $\delta^{13}C$ closer to equilibrium with the atmosphere (e.g. Broecker and Maier-Reimer, 1992). Due to the greater mobility of $^{12}CO_2$, the direction of carbon dioxide flux also influences the air-sea exchange signature, imparting a negative surface ocean air-sea exchange signature in regions of CO_2 invasion and a positive exchange signature in regions of CO_2 evasion

(Lynch-Stieglitz et al., 1995). These factors can lead to significant changes in the preformed signature of a water mass that are independent of changes in nutrient content. For example, AAIW is characterized by an extremely positive $\delta^{13}C$ value as a result of surface waters spending a prolonged period in contact with the atmosphere prior to its formation in the cold, windy Southern Ocean.

At the LGM, the air-sea exchange signature of $\delta^{13}C$ in AAIW is thought to have been significantly different due to several reasons. In particular, reduced ventilation of the Southern Ocean, due to increased sea ice (Moore et al., 2000, Stephen and Keeling 2000) and surface water stratification (Francois et al., 1997; Toggweiler, 2006) along with a reversal in the direction of CO_2 flux (e.g. Sigman and Boyle, 2000) would reduce the $\delta^{13}C$ signature in AAIW (Mook et al., 1974; Lynch-Stieglitz and Fairbanks, 1994; Lynch-Stieglitz et al., 1995). Additionally, shoaling of northern source waters at the LGM (discussed in chapter 6 of this thesis) resulted in mixing of AAIW with an increased component of GNAIW, which had aged along its flow path from the North Atlantic to the South Atlantic, further reducing the $\delta^{13}C$ signature in AAIW (Oppo and Horowitz, 2000; Came et al., 2003).

In addition to variations in the isotopic composition of seawater, the $\delta^{13}C$ recorded in benthic foraminifera can also vary by species. This is due to different species having different microhabitat preferences, with some species (e.g. *Cibicidoides*) living on or near the sediment surface and others (e.g. *Uvigerina*) living within the sediments. The infaunal species *Uvigerina* show depleted $\delta^{13}C$ relative to the $\delta^{13}C$ DIC of bottom waters that, in general, reflect the magnitude of the pore-water depletions. The epifaunal species *Cibicidoides* tend to have the smallest isotopic offset relative to bottom waters (Lynch-Stieglitz 2003). However, in areas of high productivity, benthic foraminifera living above the sediment may also experience δ^{13}C depletion due to calcification within a layer of phytodetritus resulting from the high supply of organic material to the sediments (Mackensen et al., 1993).

2.7.2 Neodymium isotopes

The use of neodymium isotopes in paleoceanography focuses on the ratio of the radiogenic isotope ^{143}Nd to the stable isotope ^{144}Nd, the former being produced by the alpha decay of ^{147}Sm ($t_{1/2} \sim 1.06 \times 10^{11}$ years). Due to the long half-life of ^{147}Sm, geological variations in ^{143}Nd/^{144}Nd values are very small. To facilitate interpretation and presentation of Nd isotopic data, an epsilon notation, εNd, is used which normalizes the ^{143}Nd/^{144}Nd value of a geologic sample to that of a chondritic uniform reservoir (CHUR) representing the bulk Earth, in parts per ten thousand (DePaolo and Wasserburg, 1976):

$$\varepsilon\mathrm{Nd} = \left[\frac{\left(\frac{^{143}\mathrm{Nd}}{^{144}\mathrm{Nd}}\right)\mathit{sample}}{\left(\frac{^{143}\mathrm{Nd}}{^{144}\mathrm{Nd}}\right)\mathit{CHUR}} - 1\right] \mathrm{x}\ 10{,}000 \qquad (2.7)$$

with CHUR having a present day value of 0.512638 (Jacobsen and Wasserburg, 1980).

The ^{143}Nd/^{144}Nd ratio in a given lithology results from different initial Sm and Nd concentrations acquired during mineral formation. Sm, is a more compatible element than Nd and is consequently partitioned into the mantle during partial melting of the silicate earth, where as Nd is partitioned into the crust. Old continental rocks which contain relatively low concentrations of Sm are therefore characterized by low ^{143}Nd/^{144}Nd ratios and very negative, nonradiogenic εNd values. In contrast, younger mantle-derived rocks such as arc terranes and mid-ocean ridge basalts have higher initial Sm concentrations and are characterized by higher ^{143}Nd/^{144}Nd ratios and more radiogenic εNd values. These εNd values are imprinted on seawater through weathering and erosion of the continents, and the use of εNd as a water mass tracer stems from the geographic distribution of the continents with different lithologies and ages (Lynch-Stieglitz 2003). More specifically, the Nd isotopic composition of an individual deep water mass is derived from the composition of dissolved, and to a lesser extent suspended materials draining into the source regions of that water mass (Goldstein and Jacobsen, 1988; Elderfield et al., 1990).

The geographically distinct εNd isotope ratios in bottom water and Fe-Mn precipitates (Figure 2.15), vary from values as high as εNd~ 0 in the Pacific to εNd < -20 in the Labrador Sea (Piotrowski et al., 2004). In the North Atlantic, NADW forms as dense waters from the Nordic Sea, with a εNd value of ~-9, flow southward and mix with sinking waters from the Labrador Sea with a surface εNd as low as -26, resulting in NADW having a εNd signature of ~-14 (Piepgras and Wasserburg, 1987). The low εNd values in the North Atlantic reflect the addition of Neodymium from the predominantly old continental derived detrital material where as the high Pacific values reflect the influence of recent volcanic activity (Lynch-Stieglitz, 2003).

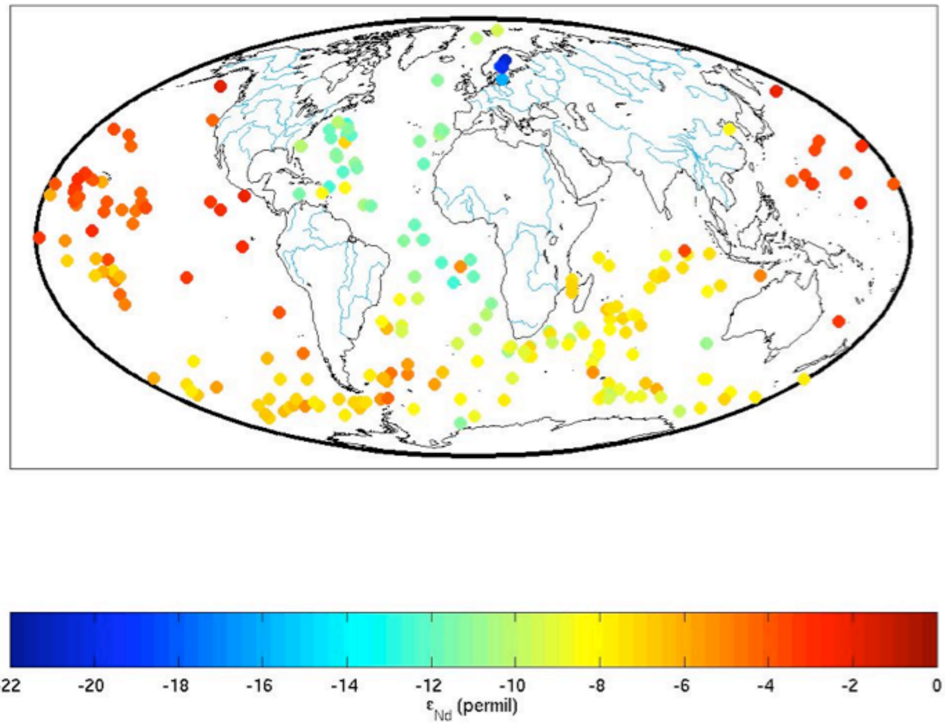

Figure 2.15: The modern distribution of Nd isotopes in deep water from Fe-Mn crust top data. From Frank 2002.

Water column profiles show that water masses conserve the Nd isotopic fingerprints of their source regions over long transport paths. In the modern Atlantic Ocean, the NADW Nd isotope signature (εNd~-14) can be traced into the South Atlantic and the Antarctic Bottom Water signature (εNd~-7 to -9) can be traced northward (Figure 2.15). In regions where there is active mixing between water masses, such as the Atlantic and Southern Oceans, the seawater and Fe-Mn precipitates have intermediate values (Frank, 2002). Neodymium isotope ratios are unaffected by biological cycling in the ocean but there are both sources and sinks of Neodymium beneath the sea surface particularly at the sediment-water interface where it is precipitated in metallic crusts.

Given the documented stability of both the Pacific (Abouchami et al., 1997) and Atlantic (Van de Flierdt et al., 2006) εNd end-members through the LGM to Holocene, any changes in the southern εNd end-member are thought to relate only to the relative input of northern and southern sourced waters to the circum-polar ocean (Piotrowski et al., 2004, Pahnke et al., 2008). During periods of reduced North Atlantic overturning (such as the Younger Dryas and Heinrich Stadial 1), the southern end-member has been observed to become more radiogenic (Goldstein et al., 2007, Pahnke et al., 2008). This finding has been interpreted as due to a decreased contribution of northern component water to CDW. In contrast, less radiogenic values during the Holocene and LGM reflect an increased presence of northern component waters in the form of NADW and GNAIW respectively (Goldstein et al., 2007).

2.8 Summary

Changes in ^{231}Pa/^{230}Th through time, as recorded by marine sediments, document variations in the processes and factors controlling the fractionation between Th and Pa in the water column. Principle among these are particle mass flux and composition of scavenging particles in addition to rate of flow. It is therefore essential to consider possible biases resulting from changes in particle flux and composition at any core site before interpreting sedimentary ^{231}Pa/^{230}Th profiles in terms of circulation changes. This can be achieved by measuring biogenic silica and evaluating past changes in particle flux by ^{230}Th normalization.

The model result of Thomas et al. (2006) indicating that ^{231}Pa/^{230}Th ratios are set by the bottom most water mass is particularly relevant to this study in which ^{231}Pa/^{230}Th sedimentary records will be produced from a suite of cores at different depths in the Argentine Basin, a region modeling studies have shown to be sensitive to changes in AMOC. This will allow for reconstruction of circulation changes in both northern (NADW) and southern source water masses (AAIW, AABW), as identified using existing $\delta^{13}C$ and Nd data, over the past 25 kyrs, a time period encompassing the last deglaciation and the major abrupt climate changes associated with it (H1, YD).

Chapter 3: Regional setting and core selection

3.1 Regional setting: SE Brazilian Continental Margin

This study is based on the analysis of sediment cores from the southeast Brazilian continental margin and in the Argentine Basin of the southwest Atlantic Ocean, between 27°S to 29°S (Figure 3.1).

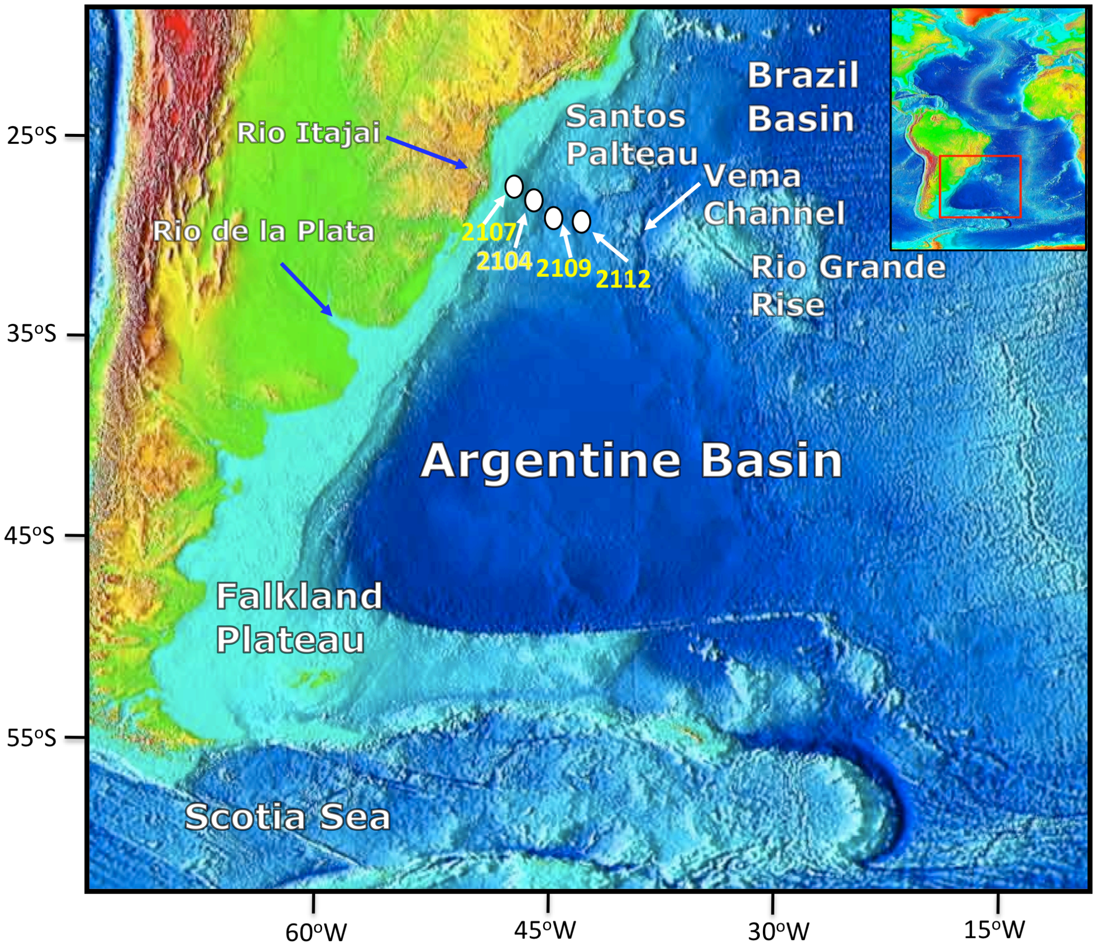

Figure 3.1: Bathymetry of the southwest Atlantic Ocean showing location of sample cores on the Brazilian continental margin. Major rivers are indicated by blue arrows. Flow paths of surface currents and deep water masses in South Atlantic are shown in Figures 3.2 and 3.4 respectively. Adapted from Rae (2008).

The Rio Grande Rise and Santos Plateau separate the Argentine Basin from the Brazil Basin to the north. Deep water flows from the south and into the Brazil Basin via the

Vema Channel, which separates the Rio Grande Rise from the Santos Plateau and the continental slope (Figure 3.1).

Ocean sediments in this region range from coarse bioclastic carbonates on the inner continental shelf to foraminiferal ooze on the outer shelf and slope, with deep sea sediments being dominated by clays below approximately 4000 m water depth (Mollenhauer et al. 1993). The supply of terrestrial sediments to the Brazilian margin core sites utilized in this study are sourced from the Rio Itajai, which drains part of the South Brazilian coastal mountains and lowlands (Heil, 2006).

3.2 Core selection

A number of cores from the Argentine Basin were available for sampling as listed in Table 3.1.

Core	Lat. Long. °S, °W	Depth (m)	Core Repository
GeoB6211	32.51, 50.24	657	MARUM
GeoB6212	32.69, 50.10	1010	MARUM
GeoB2107	27.18, 46.45	1048	MARUM
GeoB6213	33.17, 49.56	1502	MARUM
GeoB2104	27.29, 46.37	1503	MARUM
GeoB2109	27.91, 45.88	2504	MARUM
GeoB6340	44.92, 58.10	2785	MARUM
GeoB2110	28.65, 45.52	3008	MARUM
GeoB2819	30.85, 38.34	3435	MARUM
GeoB1312	31.67, 29.66	3436	MARUM
GeoB1309	31.67, 28.67	3963	MARUM
GeoB2112	29.07, 43.22	4010	MARUM
GeoB1306	35.21, 26.76	4058	MARUM
RC28-28	37.05, 39.97	4945	LDEO
RC28-27	45.72, 49.16	5550	LDEO
RC28-20	45.75, 49.16	5556	LDEO

Table 3.1: A selection of available cores from the Argentine Basin. Cores are archived at the Center for Marine and Environmental Sciences (MARUM) at Bremen University and the Lamont Doherty Earth Observatory (LDEO) at Columbia University.

Four sediment cores were selected for ^{231}Pa/^{230}Th analyses: GeoB 2104, 2107, 2109 and 2112 (Table 3.2). These cores span water depths from 1045 m (GeoB 2107) to 4010 m (GeoB 2112), a range that allows for characterization of each of the major water masses observed in the modern southwest Atlantic Ocean (Figure 3.3).

Core	**Location**	**Depth (m)**	**Modern water mass**	**Sedimentation rate (cm kyr^{-1})**
GeoB 2107	27.18°S, 46.45°W	1048	AAIW	~7
GeoB 2104	27.29°S, 46.37°W	1503	AAIW	~7
GeoB 2109	27.91°S, 45.88°W	2504	NADW	~4
GeoB 2112	29.07°S, 43.22°W	4010	AABW	~1

Table 3.2: Details of Brazilian margin cores selected for ^{231}Pa/^{230}Th analysis. All cores were sampled from the Center for Marine and Environmental Sciences (MARUM), Bremen. Further details regarding core chronology and sample intervals are presented in chapter 5 of this thesis.

In addition to sampling each of the major water masses, these cores were carefully selected for the following reasons:

1. Quality and availability of sample material: All sample cores were deemed to be in a good condition on visual inspection at the MARUM core repository in Bremen. For the most part, these cores were not heavily sampled which meant that extra sample material would likely be available if required (e.g. for replica measurements). According to original cruise reports, sedimentation rates in at least the shallower cores were high enough to obtain data records at a resolution sufficient to observe changes in ocean processes on millennial timescales.

2. Existence of complimentary proxy data: Previous work on each of these four cores provided a wealth of existing data complementary to ^{231}Pa/^{230}Th. All existing data from the cores used in this study is summarized in section 3.5 of this chapter.

3. Proximity of cores to one another: The selection of cores in close proximity to one another offers potential to establish an age model for the deepest core, GeoB 2112 (4010 m), which, due to its greater depth, would likely have an insufficient mass of carbonate required for ^{14}C dating. Chronologies of shallower cores, based on ^{14}C ages, might be extrapolated to depth by correlation of existing XRF data. Furthermore, as discussed in chapter 2, particle flux and composition are geographically highly variable, so sampling cores from the same oceanographic region, deposited under similar sedimentary conditions, would help in assessing the influence of ocean circulation versus particle flux and composition on sedimentary ^{231}Pa/^{230}Th.

3.3 Modern day hydrography in the southwest Atlantic

The surface circulation pattern along the Brazilian margin is dominated by the Brazil Current, which flows south over the GeoB core sites, and the northward flowing Malvinas (or Falkland) Current. These two surface currents meet at the Brazil Malvinas Confluence to the south of the study area (Figure 3.2).

Deep water circulation in the Argentine Basin is characterized by the interplay between several water masses (Figure 3.3). Warm South Atlantic central waters are observed at shallow depths down to 500 m**.** From 500 m to 1200 m Antarctic Intermediate Water (AAIW) is distinctive by its relatively low salinity levels (Table

3.3). Core GeoB 2107 (at 1048 m) is located in the main body of AAIW today, whilst GeoB 2104, located at 1503 m, is at the lower limit of AAIW in the transition zone to underlying UCDW and NADW.

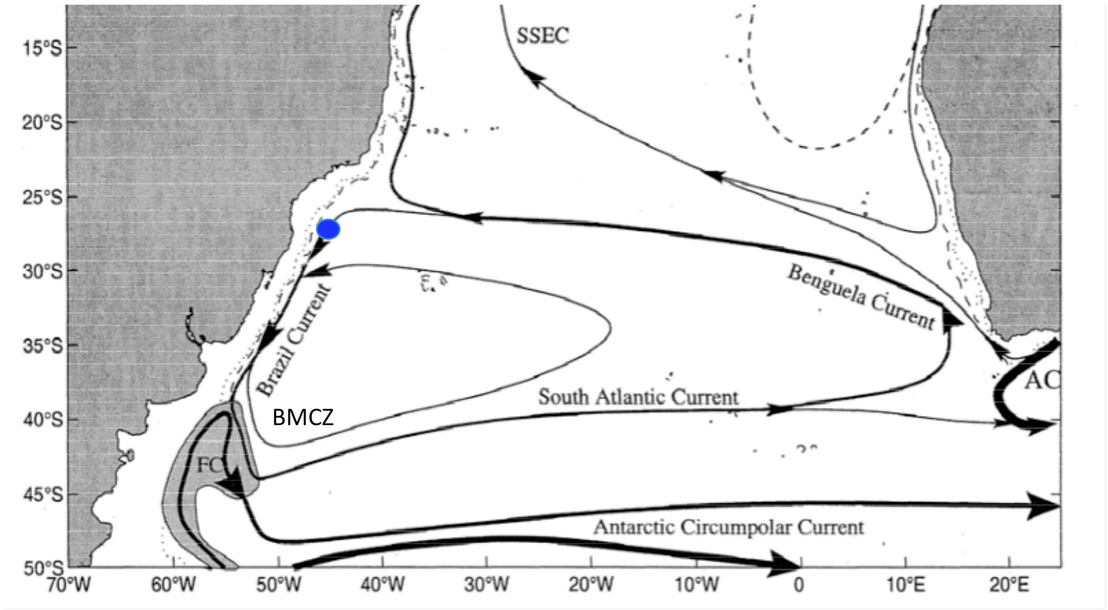

Figure 3.2: Oceanographic map showing the major surface currents in the southwest Atlantic. The blue circle is used to denote the approximate location of GeoB cores used in this study. Also shown are the Malvinas or Falkland current (FC), the Southern South Equatorial Current (SSEC), the Brazil Malvinas Confluence Zone (BMCZ) and the Antarctic Circumpolar Current (ACC). Adapted from Strammer and England, 1999).

North Atlantic Deep Water (NADW), distinguished by its low nutrient content is found between 1500 m and 3500 m water depth, bisecting upper and lower circumpolar deep waters. GeoB 2109 (2504 m) is located within the modern day core of NADW. Below NADW, nutrient rich AABW fills the basin from depths between 3500 m and 4000 m to the ocean floor. GeoB 2112 (4010 m) is located within the transition zone between modern day AABW and NADW.

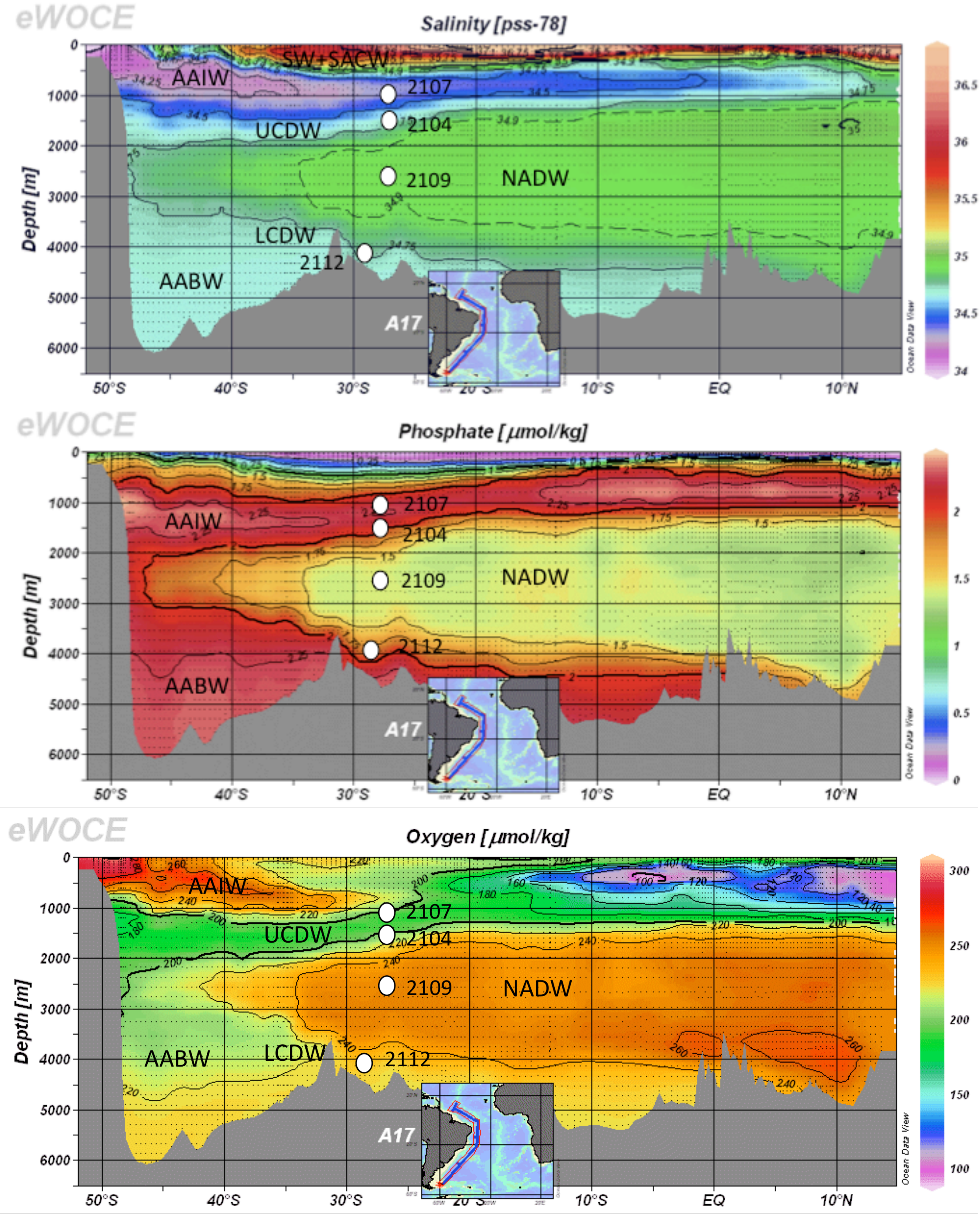

Figure 3.3: Salinity, phosphate and oxygen profiles showing the various water masses in the southwest Atlantic today. Adapted from eWOCE transect data (http://www.ewoce.org/gallery/). A tongue of AAIW, identified by its low salinity content, lies immediately below high salinity Surface Water (SW) and South Atlantic Central Water (SACW) and above oxygen poor UCDW. NADW, identified by its high oxygen and salinity content, can be seen splitting UCDW and LCDW. The distinctive salinity and nutrients of AABW fill the South Atlantic Basin. White circles mark the approximate location of the four sample GeoB cores utilized in this study.

In total, more than 10 water masses can be distinguished along the western boundary of the South Atlantic (e.g. Reid et al., 1997) but these may be grouped into six main units (Table 3.3).

Water mass	Depth (m)	Characteristics	Formation
Surface Water	0-300	High salinity (36.5-36.75)	In tropics/sub-tropics
South Atlantic Central Water (SACW)	300-550	High salinity (35.5-36.5), 5-20°C	In sub-tropical gyre
Antarctic Intermediate Water (AAIW)	550-1300	Salinity min (34.2-34.5), O_2 max, temperature max (4°C)	In Antarctic Convergence Zone and SE Pacific
Upper Circumpolar Deep Water (UCDW)	1300-1500	Low salinity (34.5-34.7), low O_2, temperature ~2°C, high nutrients	Old deep water that peels off Antarctic Circumpolar Current
North Atlantic Deep Water (NADW)	1500-3500	High salinity (34.75-34.9), high O_2, low nutrients	Subduction of north flowing surface waters in Labrador, Norwegian seas.
Lower Circumpolar Deep Water (LCDW)	~3500-4000	High salinity (34.6-34.75), low O_2, low nutrients, low temperature (~0.5°C)	As for UCDW
Antarctic Bottom Water (AABW)	>4000	Salinity (34.6-34.7), low temperature (~0°C), high nutrients	From CDW round Antarctica and Weddell and Ross seas

Table 3.3: characteristics of the major water masses in the southwest Atlantic. References: Strammer and England 1999; Arz et al., 1999; Reid et al., 1999 and Oppo and Horowitz 2000.

3.4 Formation and circulation of intermediate and deep water masses

The following section briefly describes the formation and flow paths of the major water masses observed in the southwest Atlantic today.

3.4.1 North Atlantic Deep Water (NADW)

In the North Atlantic, warm and saline surface waters travel northward via the Gulf Stream and the North Atlantic Drift. As this water flows northward it becomes increasingly cold and saline due to heat exchange with the atmosphere and net evaporation. These changes in temperature and salinity make the surface waters more dense and prone to sinking, although vertical convection is inhibited by a strong thermocline. This stratification can be overcome during storm events, when surface divergence and increased vertical mixing disrupts the thermocline, allowing surface waters to sink (Gascard and Clarke, 1983).

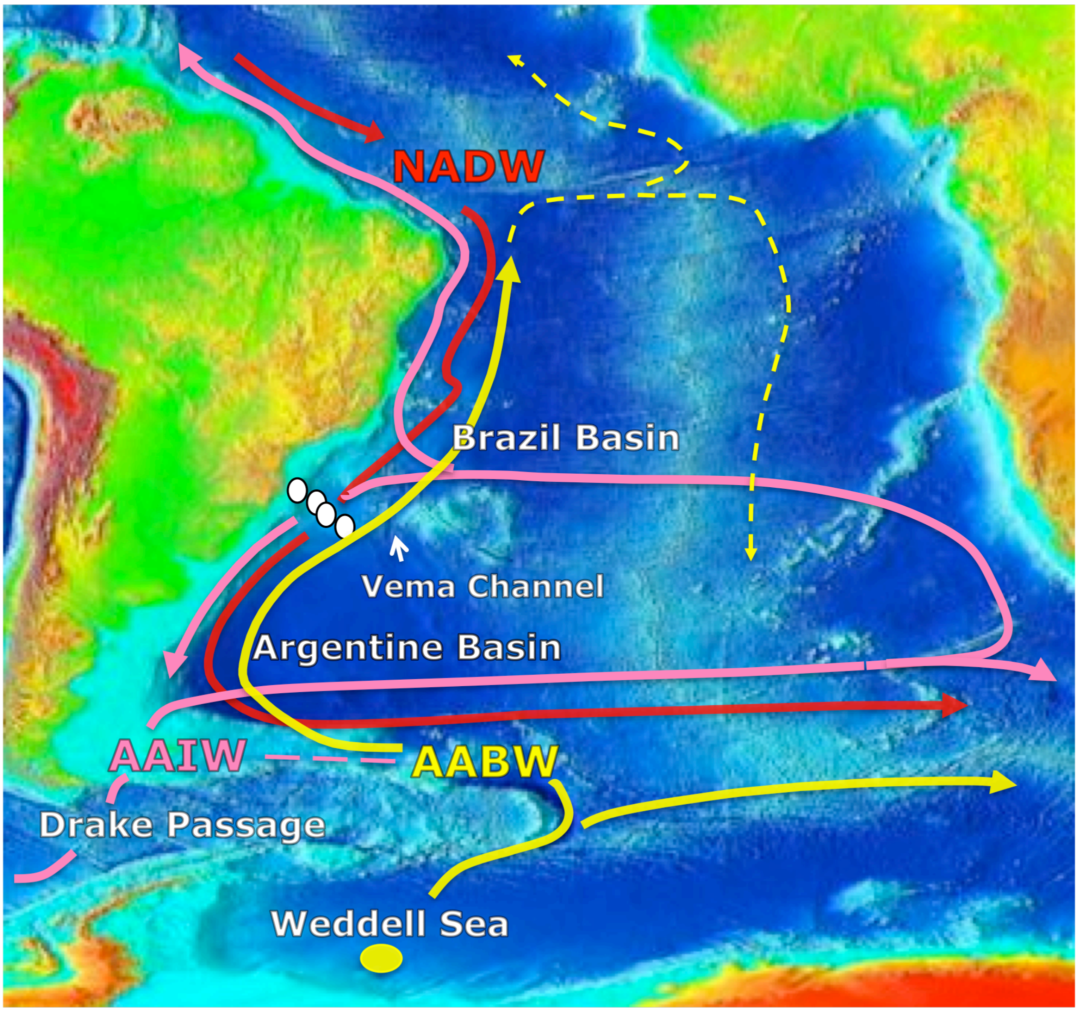

Figure 3.4: Map of the South Atlantic showing the major flow paths of NADW (red), AABW (yellow) and AAIW (pink). A yellow circle is used to indicate a formation region of AABW and white circles indicate the approximate location of GeoB cores used in this study. The pink horizontal dashed line marks the approximate location of AAIW formation in the southwest Atlantic (shown in Figure 3.5) which combines with AAIW that has formed in the southeast Pacific and enters the Atlantic via the Drake Passage.

The sinking of dense and highly saline waters in the Norwegian, Greenland and Labrador Seas combine to form NADW (e.g. Colling et al., 2001). Sinking to a depth of 2000-4000 m, this water mass flows south across the Atlantic as a deep western boundary current. It is clearly distinguished by its low nutrient, high oxygen and high salinity levels (Figure 3.3). In the South Atlantic, the vertical extent of NADW decreases and there is an increasing prominence of AAIW above and AABW below. NADW passes along the coast of South America between 20^{o}S and 50^{o}S before turning eastward across the south Atlantic as part of the ACC (Figure 3.4). The high salinity of NADW can be traced into the Southern Ocean as it mixes with CDW and also into the Pacific and Indian oceans where it spreads northward towards the equator (Reid et al., 1994).

3.4.2 Antarctic Bottom Water

AABW is formed in the Southern Ocean around the coast of Antarctica, particularly in the Weddell and Ross Seas. It is formed from circumpolar deep waters that upwell in the Antarctic Divergence region (Figure 3.5). Upon upwelling, these waters experience Ekman transport of the surface layer (depth to which wind penetrates) due to wind forcings. In the Southern Hemisphere, Ekman transport acts at a 90 degree angle to the left of the surface motion (e.g. Colling et al., 2001). Consequently, the East Wind Drift (Figure 3.5), flowing counter clockwise around Antarctica, is pushed south and the clockwise flowing ACC is pushed towards the equator. The surface waters flowing toward Antarctica lose heat and moisture to the cold and dry atmosphere. This effect is enhanced by cold catabatic winds blowing off the Antarctic land mass (Parish, 1998). In addition, surface waters increase in salinity due to sea ice formation, causing them to cool and densify before sinking down the continental rise of Antarctica, forming a thick layer of AABW (Warren, 1981; Reid et al., 1989).

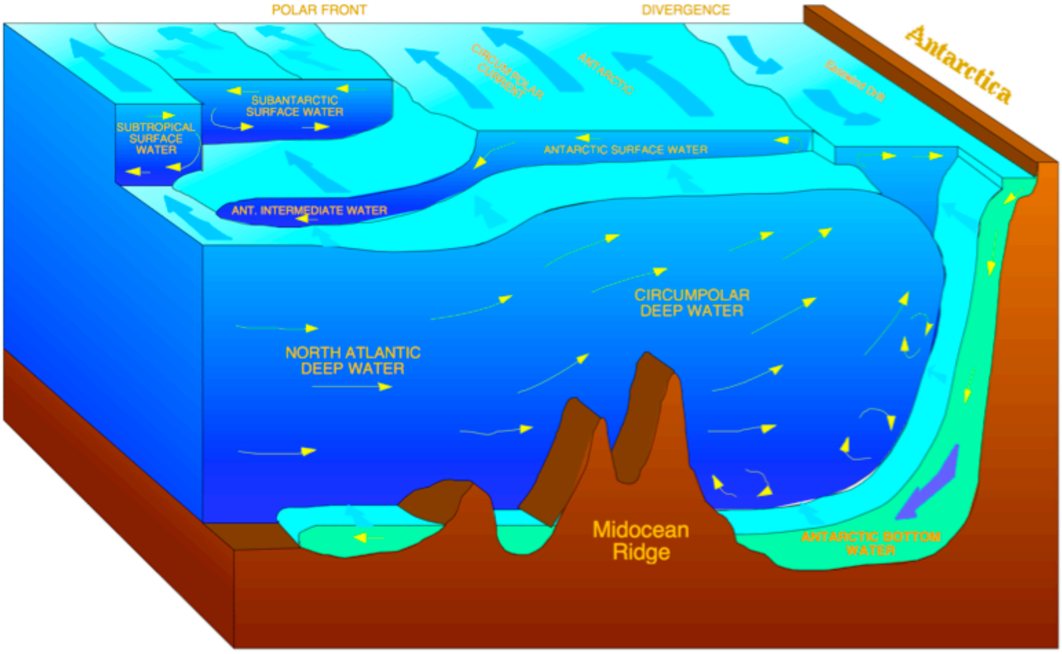

Figure 3.5: Water mass bodies of the Southern Ocean. Source: Hanes Grobe, Alfred Wegener Institute for Polar and Marine research, Bremerhaven, Germany (2000).

AABW spreads throughout the Southern Ocean by mixing with the overlying waters of the ACC and from there flows into the rest of the world ocean. It is characterized by low temperature (-1 to 0^{o}C), low salinity and high nutrients (Table 3.3). It is the densest water mass in the world ocean and therefore is often the deepest water mass in ocean basins. The movement of AABW in the Atlantic, Indian and Pacific Oceans is restricted by seafloor topography, with ridges acting as barriers and deep fracture zones and channels acting as conduits (Stramma and England, 1999). In the Argentine Basin, AABW enters through gaps in the Falkland Ridge to the South and spreads to fill the deep basin before exiting to the north through the Vema channel (Figure 3.4).

3.4.3 Circumpolar deep water (CDW)

CDW originates in the Southern Ocean as a result of mixing of AABW with northern source waters – i.e. NADW (Orsi et al., 1999). CDW is a large mass of fresh, oxygen poor and nutrient-rich water. It circulates eastward around Antarctica as part of the ACC and returns to the Atlantic through the Drake Passage. In the Argentine Basin CDW encounters NADW flowing from the north and splits into an upper (UCDW) and lower branch (LCDW). LCDW is characterized by a salinity maximum and nutrient minima derived from NADW (Table 3.3). UCDW is characterized by an oxygen minimum and nutrient maxima, with sources in the Indian and Pacific Oceans (Reid et al., 1989).

3.4.4 Antarctic Intermediate Water (AAIW)

AAIW is formed at the ocean surface in the Antarctic Convergence Zone (AACZ) near the Antarctic Polar Front (e.g. Garabato et al., 2009) currently located between 50°S and 60°S (Figure 3.5). Upwelling CDW in the Antarctic Divergence region flows towards the equator due to Ekman transport of the ACC. Persistent precipitation at the polar lows (60°S) along with an influx of melt water decreases the overall salinity of the original CDW, forming Antarctic Surface Waters, such as Subantarctic Mode Water (SAMW) (Maamaatuaiahutapu et al., 1999). SAMW is specifically formed by deep winter mixing of surface waters in the Subantarctic Zone immediately north of the Polar Front (McCartney, 1977). These surface waters continue to flow north until they encounter warmer ‘Subantarctic Water’ at the AACZ (Figure 3.5). Here they begin to sink due to thier greater density, forming AAIW, which is sandwiched between warmer South Atlantic Central Water above and colder, more saline NADW below (Lutjeharms, 1985). An additional component of AAIW forms from upwelling of CDW at the Polar Front in the Southeast Pacific. This water enters the Atlantic through the Drake Passage and joins AAIW formed in the Atlantic at the AACZ (Reid et al. 1989).

Together with AABW, AAIW is transported into all ocean basins by the ACC, which flows clockwise around Antarctica. The movement of AAIW is less restricted than AABW by topographic barriers, although the depth to which it can penetrate is limited due to its relatively low salinity and high temperature. In the South Atlantic, AAIW is injected into the subtropical gyre in the Falkland Current loop and at the Brazil Malvinas (or Falkland) Confluence Zone (BMCZ; Boebel et al. 1999; Figure 3.2) and is carried east with the South Atlantic Current. AAIW splits to the east of the mid-Atlantic Ridge where is meets Aguhlas Water, with one branch joining the Benguela Current and the other continuing into the Indian Ocean. Upon reaching South America, AAIW bifurcates near the Santos Plateau between 25-30°S with a southward component flowing over the sample core sites and a northward component flowing as the North Brazil western boundary current. North of 20°S AAIW properties gradually erode due to warming and diapycnal upwelling into thermocline waters (You, 2001), although traces of AAIW can be followed as far north as ≈ 60°N (Tsuchiya, 1989).

3.5 Existing core data

All but the deepest of the cores used in this thesis have existing $\delta^{18}O$ and $\delta^{13}C$ data, collected by Dr Stefan Mulitza and Cristiano Chiessi at the University of Bremen, Germany. These $\delta\ ^{18}O$ stratigraphies provide a first estimate of the ages of sediments in the cores, and of the sedimentation rates, by correlation with the global benthic $\delta\ ^{18}O$ curve of Lisiecki and Raymo (2005, Figure 5.11). No stable-isotope data were available for the deepest core, GeoB 2112, due to the lack of carbonate present in ocean sediments at this depth.

Core	**Depth (m)**	**$\delta^{18}O$**	**$\delta\ ^{13}C$**	**XRF**	**^{14}C ages**
GeoB 2107	1048	Every cm resolution on *U. perigrina and every 5 cm C. wullerstorfi*	Every cm resolution on *U.peringria* and *C. wuellerstorfi*	Fe, Ca, Ti counts (every cm)	8 ages on G. Saculifer
GeoB 2104	1503	Every 5 cm resolution on *U. perigrina*	Every 5 cm resolution on *U. perigrina*	Fe and Ca counts (every cm)	-
GeoB 2109	2504	Every 5 cm resolution on *U. perigrina* and *G. truncatuloides*	Medium resolution on *G.ruber* and *C. wuellerstorfi*	-	-
GeoB 2112	4010	-	-	Fe, Ca, Ti counts (every cm)	-

Table 3.4: Summary of existing data for each of the GeoB cores selected for sampling.

3.6 Core sampling

The four GeoB cores selected for sample analysis were collected by the *RV Meteor* during the 1993 METEOR cruise 23/2. These cores are stored at the MARUM Center For Marine and Environmental Sciences at the University of Bremen and sampled on site with help from James Rae (Oxford), Paul Carter (Bristol) and Cristiano Chiessi (Bremen).

Individual cores were sealed in plastic containers and wrapped tightly in cling film to prevent mould growth. Each core was visually inspected for sampling suitability. A brief physical description for each sample core was recorded in the original cruise report, as summarized below:

GeoB 2104 (1045 m): The sediments in the upper 2 m are light olive brown to grey mud-bearing foraminferal nannofissil ooze. Below 2 m the core consists of grey pelagic clays without apparent structure.

GeoB 2107 (1503 m): Sediments are very homogenous with respect to colour and lithology. The top 10 cm consist of dark grayish brown to grey clay-bearing foraminiferal nanofossil ooze. The remainder of the core is grey to dark grey foraminifera and nannofossil bearing pelagic clay.

GeoB 2109 (2504 m): Comprises alternations between carbonate rich (calcareous pelagic clay) and carbonate poor (pelagic clay) sections. Colour varies between light grey and grayish brown with intensively green colured layers in the pelagic clay.

GeoB 2112 (4010 m): Sediments are homogenous with respect to lithology and color. Thicker calcareous clay sections alternate with thin layers of foraminifer and nanofossil bearing pelagic clay.

Individual samples were taken from these cores at 5 cm intervals in GeoB 2104, 2107 and 2109 and at 1 cm intervals in GeoB 2112 (due to the lower sedimentation rate in this core) using 5 cm^3 plastic scoops. The exact depth of each sample from the core top was carefully recorded. Holes created by the sampling process were filled using polystyrene foam to prevent slumping. Each core was then re-sealed with cling film, capped and returned to the core repository to be stored under refrigerated conditions.

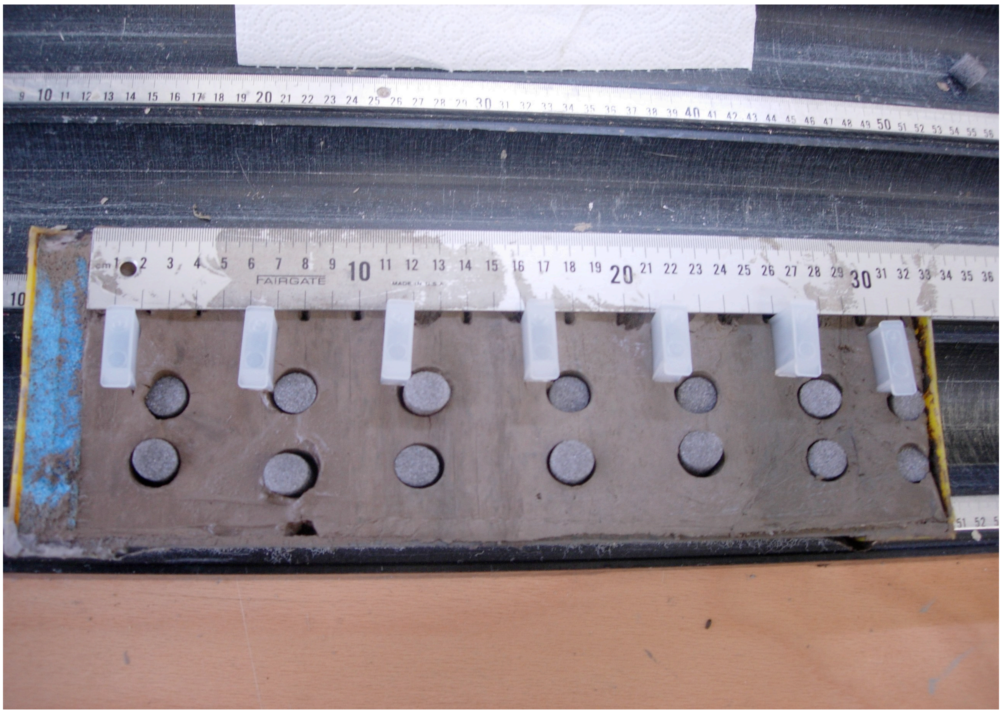

Figure 3.6: Photo of a section of core GeoB-2107 being sub sampled. Samples were taken at 5 cm intervals using 5 cm^3 plastic scoops with a width of 1 cm. Pieces of circular grey foam mark the location of previously sampled material which has been filled to prevent slumping.

A total of 108 individual sediment samples from the four GeoB cores were placed into sealed plastic bags and transferred to the Earth Sciences department at the University of Oxford where they were stored in a cool dry place in preparation for sample analysis.

Chapter 4: Analytical techniques

Overview

This chapter includes the methods and techniques used for all laboratory work and sample analysis done as part of this thesis. This includes the preparation of a ^{233}Pa spike, sample chemistry and analysis by multi-collector inductively coupled plasma mass spectrometry (MC-ICPMS). Corrections associated with mass spectrometric biases and data uncertainties are discussed. Also included are methods for measurement of opal, trace metals and preparation of samples for radiocarbon dating. For completeness, the method used for the analysis of Nd isotopes performed by collaborators at Bristol University is also included in this chapter.

4.1. Overview of Pa, Th and U analysis

The analytical procedure for the measurement of Pa, U and Th in sediment involved sample digestion, the manufacture of a ^{233}Pa spike, U-Th-Pa separation using anion-exchange resin and measurement of these element concentrations and isotope ratios by MC-ICPMS.

The sediment digestion procedure is based on a method developed by Steve Wyatt and adapted by Alex Thomas at Oxford (Thomas, 2006). Due to the very low concentrations of ^{231}Pa and ^{230}Th in ocean sediment, all sample chemistry was carried out under clean laboratory conditions. All laboratories were pressurized with HEPA filtered air, preventing airborne particulate contaminants from entering. Laminar flow hoods used for column chemistry were kept under neutral pressure, preventing flow of contaminants into the hoods and removing chemical vapours. Tyvec suits, latex gloves, goggles and lab clogs were worn at all times for safety reasons and to reduce contamination.

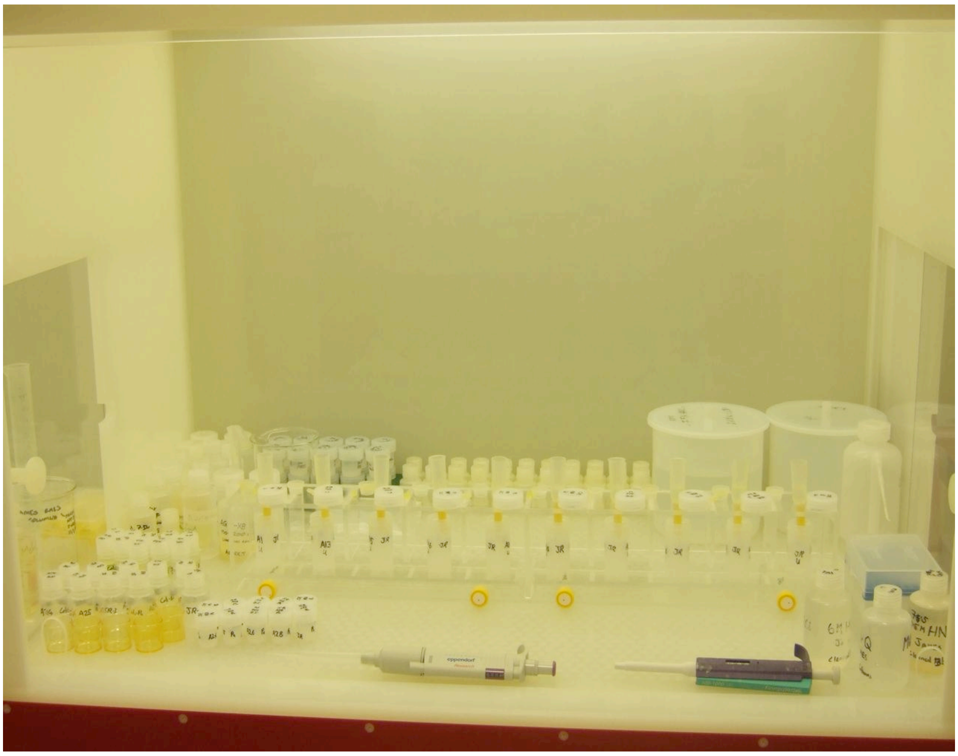

Figure 4.1: Photo showing laminar flow hood and materials used in column chemistry.

4.2 Beaker cleaning and sample preparation

Teflon sample beakers were cleaned by refluxing overnight with strong acids (2M HCL, 7.5M HNO_3, 6M HCL + 0.05M HF) at 120^{o}C. Between reflux steps beakers were rinsed thoroughly using milli-Q deionized water (18 mOhm). Reagent bottles and columns were also cleaned in this way prior to use.

Samples selected for $^{231}Pa/^{230}Th$ analysis were dried overnight in an oven at 90°C to remove moisture. Individual samples were then lightly crushed using a pestle and mortar. Approximately 0.1 g of dried sediment was weighed into cleaned 30 ml Teflon beakers using a Satorius Genius ME balance, accurate to 10^{-4}g. Sample weights were measured by recording differences in beaker weights before and after each sample was placed into the sample beaker. For each sample mass an average of three readings were taken. A few drops of milli-Q H_2O was used to dampen each sample immediately after weighing to prevent loss of powdered sediment from the beaker.

4.3 Sediment dissolution

To remove carbonates, 4 ml of 7.5M HNO_3 was added to each sample, with the first 2 ml of acid added drop wise to reduce potential sample loss from violent fizzing as the carbonate component reacted. Beakers were capped and refluxed overnight at 120 °C.

$$\mathrm{CaCO_3 + 2HNO_3 \rightarrow Ca(NO_3)_2 + H_2O + CO_2} \qquad (4.1)$$

Sample solutions were dried down and redissolved in 4 ml of Aqua Regia ($3HNO_3$:1HCl) taking care to add HCl drop wise to the nitric acid. Aqua Regia acts as a very strong oxidizing agent, due to the nitrosyl chloride produced (equation 4.2).

$$\mathrm{3HNO_3 + HCl \rightarrow NOCl + 2NO_2 + 2H_2O + O_2} \qquad (4.2)$$

Oxidation of nitrosyl chloride produces chlorine (equation 4.3), which removes organic matter from solution.

$$O_2 + 2NOCl \rightarrow 2NO_2 + Cl_2 \qquad (4.3)$$

Samples were then refluxed again overnight at 150°C before being dried down to incipient dryness.

To digest silicates, a mixture of 4 ml 7.5M HNO_3 and 1 ml 0.05M concentrated (27M) HF was added to each sample solution, together with a few drops of perchloric acid. The mixture was refluxed at 150°C overnight before being heated to incipient dryness.

$$SiO_2 + 4HF \rightarrow 4SiF_4 + 2H_2O \qquad (4.4)$$

The addition of HF effectively breaks Si-O bonds. However, this can lead to the formation of insoluble fluorides. These fluorides are converted to nitrates whenever HNO_3 is added during dissolution steps.

$$MF_2 + HNO_3 \rightarrow M(NO_3) + 2HF \qquad (4.5)$$

Adding perchloric acid and drying down at a high temperature (~150 °C) helps to drive this reaction to completion, ensuring all HF is evaporated. This procedure was performed in a fume hood equipped with a scrubber to remove any condensed perchloric acid from the exhaust piping.

This dissolution process was repeated several times until no remaining solids were visible in solution. Samples were then redissolved in 4 ml of 7.5M HNO_3, ready for spiking. Complete dissolution was often only achieved once the total volume of solution was increased to 8 ml due to the partial insolubility of some nitrates.

4.4 Standards and spikes

4.4.1 Isotope dilution

The ability of the MC-ICPMS to measure more than one isotope at the same time allows for very accurate measurements of isotope ratios, as any variation in plasma intensity will affect both isotopes similarly.

This feature is exploited using a technique know as ‘isotope dilution’ in which a known mass of a calibrated spike solution is added to a sample and equilibrated. The ratio of spike isotope to sample isotope in this mixture is measured and from this the amount of sample isotope can be calculated (e.g. McClaren et al.,1987).

The measured ratio of spike and natural isotopes, R_M, can be described by the addition of spike, S and natural, N, ratio:

$$R_M = \frac{A_N + A_S}{B_N + B_S} \tag{4.6}$$

where A and B are the number of moles of each isotope. As the number of moles of an isotope is the same as the number of moles of the element (M) multiplied by the atomic abundance of the isotope (%), the expression can be written as:

$$R_M = \frac{M_N \times \%A_N + M_S \times \%A_S}{M_N \times \%B_N + M_S \times \%B_S} \tag{4.7}$$

which can be rearranged to give:

$$M_N = M_S \times \frac{\%A_S - R_M \times \%B_S}{R_M \times \%B_N - \%A_N} \tag{4.8}$$

The above expression can be rewritten to give the mass of the natural isotopes, using the fact that mass (P) = number of moles (M) x atomic weight (W):

$$P_N = \frac{P_S \times W_N}{W_S} \times \frac{\%A_S - R_M \times \%B_S}{R_M \times \%B_N - \%A_N} \tag{4.9}$$

Assuming the composition of the spike is known, the number of natural atoms of each isotope can now be calculated. If the spike contains some of the sample isotope of interest then this must be corrected for when calculating the number of natural atoms in the sample. This can be done by subtracting the number of atoms of this isotope in the spike, as determined by calibration against a standard of known concentration, from the total number of atoms of this isotope measured in the sample.

4.4.2 U and Th spike

It is necessary to add approximately the same mass of spike isotope to each sample as the mass of the isotope of interest in that sample. This minimizes any uncertainty due to non-linearity of small isotope beams during mass spectrometric measurement of the isotope ratio. It is therefore necessary to use a mixed spike of U and Th so that the concentrations of ^{236}U and ^{229}Th can best be matched to the ratio of U and Th typical in samples of ocean sediment. Furthermore, a mixed spike containing both ^{236}U and ^{229}Th reduces the time involved in spiking each sample, and the associated weighing errors from calculations. Both ^{236}U and ^{229}Th are contained within the "Oxford Carbonate spike" prepared and calibrated against secular equilibrium standards by Robinson et al. (2002) and recalibrated by Thomas et al. (2009).

	^{229}Th	**^{236}U**
Oxford Carbonate Spike (g/g)	2.43494×10^{-10}	9.09591×10^{-8}
Oxford Dilute Water Spike (g/g)	3.882143×10^{-16}	4.369682×10^{-11}
mass (amu)	229.031755	236.045562
decay constant (a^{-1})	8.77×10^{-5}	2.96×10^{-8}

Table 4.1: Table to show the composition of the mixed ^{229}Th and ^{236}U spikes: The Oxford 'Carbonate' spike and dilute water spike, as calibrated by Robinson et al. (2002).

4.4.3 ^{233}Pa spike

^{231}Pa is the only naturally occurring long-lived isotope of Pa. As a spike for Pa, we use the second longest lived isotope, ^{233}Pa with a half-life of 26.967 days (Usman and MacMahon, 2000). The ^{233}Pa spike is prepared by milking of its parent isotope ^{237}Np, which is not found naturally but is formed as a waste product of the nuclear industry. ^{237}Np decays to ^{233}Pa via alpha emission:

$$^{237}\mathrm{Np} \xrightarrow{\alpha} {}^{233}\mathrm{Pa} \xrightarrow{\beta} {}^{233}\mathrm{U} \rightarrow \ldots {}^{208}\mathrm{Pb} \qquad (4.10)$$

$\mathbf{t_{1/2}}$ (^{237}Np)=2.14×10^6 yrs

$\mathbf{t_{1/2}}$ (^{233}Pa)=26.97 days

As ^{237}Np decays, the concentration of its radioactive daughter ^{233}Pa increases until secular equilibrium is reached between the two isotopes.

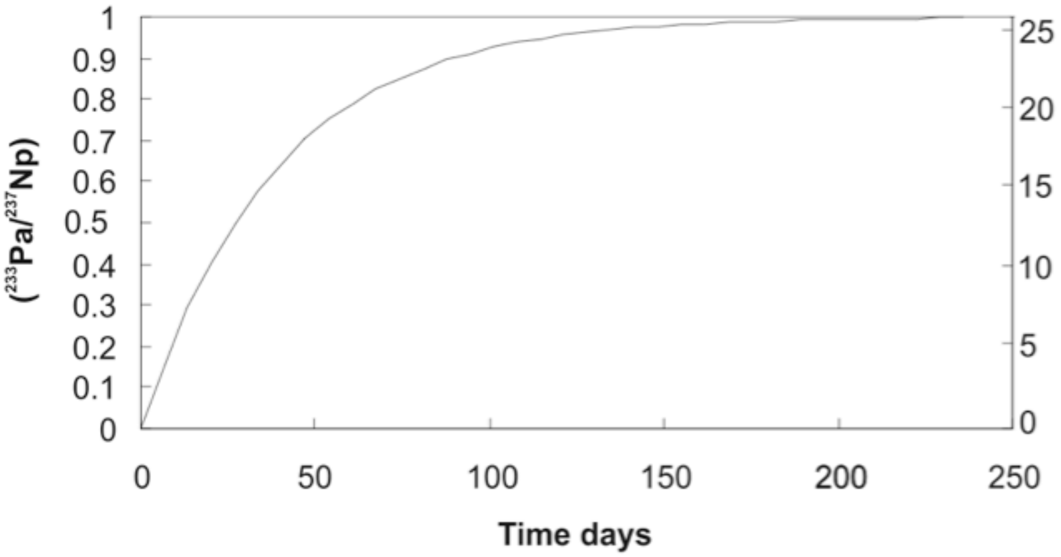

Figure 4.2: The increase in (^{233}Pa/^{237}Np) during ingrowth to secular equilibrium of a ^{237}Np solution with no initial ^{233}Pa. Also shown is the amount of ^{233}Pa produced from a ^{237}Np solution containing 750 μg of ^{237}Np (from Thomas, 2006).

Once ^{233}Pa has been chemically separated from the ^{237}Np solution, the ^{237}Np solution must be left for at least three months to allow enough ^{233}Pa to grow in before another milking can usefully be performed.

4.4.4. The ^{237}Np-^{233}Pa separation procedure

The separation procedure of ^{233}Pa from ^{237}Np is taken from Regolus et al. (2004) and is based on the high affinity of Pa to silica in 7.5 M HNO_3 while Np, U and Th do not adhere and are washed from the column. Subsequent use of HNO_3 with trace HF solubilises Pa and removes it from the silica.

The Np-Pa separation procedure was carried out in a clean lab designated for 'hot' chemistry (Figure 4.3) and adhering to all UK and EU laws for handling of radioactive substances. Radioactivity levels were monitored using a gamma counter and a DP6RA 2019 alpha and beta monitor. Radioactivity counts on all equipment were checked against background levels and logged on a daily basis during chemistry.

Figure 4.3: Photo showing the clean lab hood designated for 'hot' chemistry and materials used for the Np-Pa separation procedure.

4.4.5 ^{237}Np - ^{233}Pa column preparation

A silica gel column was prepared by first degassing approximately 30 mls (enough for four columns) of MERCK "Silica Gel 60" resin using a glass bell jar under vacuum for several hours. It was important that any trapped air bubbles were removed from the resin to ensure the columns did not get blocked during the elution passes. The degassed resin was then washed several times using Milli-Q H_2O and 8M HNO_3. 5 ml of cleaned, degassed silica resin was then loaded onto a 7 ml Bio-rad column which was then sealed before being centrifuged inside a larger tube filled with water to ensure any remaining air is expelled from the column. A further three columns were prepared in this way so that four columns were available for the milking procedure.

4.4.6 ^{237}Np - ^{233}Pa column chemistry

The Np solution, stored in 8M HNO_3 and trace HF was dried down on a hot plate at 120°C, with a few drops of $HCLO_4$ added to help drive off the trace HF. The Np was loaded onto the first silica gel column in 5 ml 8M HNO_3 and washed on with a further 5 ml 8M HNO_3. The load and wash solutions were collected from the column and monitored to check for the absence of ^{233}Pa by gamma spectrometry. 2x 35 ml of 8M HNO_3 was then added to the column using a funnel to wash ^{237}Np and ^{233}U from the column. This wash was returned to the original bottle and stored safely for the next milking. The Pa was then collected with 1x 30 ml 7.5M HNO_3 + 0.05M HF and 1x 30 ml 7.5M HNO_3 + 0.1 M HF. The strength of the HF used was critical: too weak and the Pa remained on the column, too strong and the HF started to dissolve the silica gel which blocked the column resulting in very long elution times and introduces Si into the Pa fraction which must be removed by fuming with HF. The column and all washes were monitored using a Geiger counter to check for ^{233}Pa recovery. Good separation of Pa from Np was important as any Np left in the Pa spike will continue to form ^{233}Pa meaning that the concentration of ^{233}Pa will no longer be a simple function of the decay constant of ^{233}Pa:

$$^{233}\mathrm{Pa}{=}^{233}\mathrm{Pa}_0 e\left(-\lambda 233\mathrm{Pa}_t\right) + {}^{237}\mathrm{Np}_0\left(1 - e\left(-\lambda 237\mathrm{Np}_t\right)\right) \qquad (4.11)$$

To achieve a sufficient separation of Pa and Np the Pa solution was cleaned by repeating the same separation procedure twice more using an extra 35 ml of HNO_3 to wash out Np for the second and third columns. All HF was driven off between each column by fuming with $HCLO_4$. All aliquots containing Np were combined and evaporated to a smaller volume, then made up with ~30 ml 7.5M HNO_3 + 0.05M HF and stored for the next milking separation.

The ^{237}Np/^{233}Pa atom ratio of the Pa spike was measured using a Thermo-Finnigan MAT element 2 sector field ICPMS. Prior to measurement, a small drop of the concentrated Pa solution was pipetted onto a square piece of aluminium foil, dried down and monitored for alpha and beta counts. A reading of 0 alpha counts was required to ensure Np levels were sufficiently low for mass spectrometer analysis.

10 μl of the Pa solution was then taken and transferred to a 6 ml Teflon beaker, to which was added ~1 ml of 7.5N HNO_3 and a few drops of $HCLO_4$. This was then fumed to drive off any HF. This sub-sample of the Pa was diluted to 1 ml in a centrifuge tube, which was then measured by ICP-MS for all unit masses 229 to 238.

A ^{237}Np/^{233}Pa atom ratio <30 in the milked Pa spike is sufficient to require only one calibration of ^{233}Pa following milking (Regelous et al., 2004). After three passes through silica gel columns the ^{237}Np/^{233}Pa ratio was typically between 30-100 and after a fourth column pass the ratio was ~1. By increasing the volume of nitric acid added to the first three columns, the ^{237}Np/^{233}Pa ratio was typically <30 after the third column pass. If separation was not sufficient then the contents of the Pa beaker were treated as if it were the initial Np solution and the entire process was repeated, making sure to fume the Pa solution with $HCLO_4$ to remove the HF before adding it to the next column. If Np/Pa separation was sufficient (Np/Pa <30) then the Np was stored by reducing the volume, and then adding 7.5N HNO_3 and trace HF, before transferring to its Teflon bottle. The Pa solution, once fumed with $HClO_4$, was made up with 7.5N HNO_3 and 0.5N HF, allowed to cool and transferred to a spike bottle to use in sample analysis.

Separation of the ^{233}U that ingrows from ^{233}Pa was also important as calibration and use of the spike assumes zero initial ^{233}U. The ^{233}Pa/^{233}U ratio has been measured in prepared spikes at $2x10^6$, which is sufficiently high to assume zero initial ^{233}U in the spike.

4.4.7 ^{233}Pa spike calibration

The ^{233}Pa spikes were calibrated by MC-ICPMS against a known ^{236}U spike after approximately five months once all ^{233}Pa had decayed to ^{233}U. This approach allows the ^{233}Pa concentrations to be measured from ^{236}U/^{233}U, eliminating the effect of elemental fractionation within the mass spectrometer. Any ^{231}Pa impurities stemming from the ^{237}Np solution were quantified during an initial calibration soon after milking and later confirmed from the final calibration. These were corrected for when calculating sample ^{231}Pa concentrations as described in section 4.7.

date spike made	made by	date of final calibration	sample batch	^{233}Pa (fg/g)	2 S.E.	^{231}Pa (fg/g)	2 S.E.
06-Mar-07	A.T	21-Dec-07	1	419.47	4.34	8.55	0.29
10-Jul-07	B.H	21-Dec-07	2,3	1222.72	5.33	66.37	1.39
07-Jun-08	B.H	17-Jul-09	4,5,6	1036.74	23.50	11.85	0.58
06-Oct-08	B.H	17-Jul-09	7,8	745.86	3.99	3.63	0.24
03-Jun-09	B.H	03-Dec-09	9,10,11	698.36	3.39	2.71	0.18
09-Jul-09	A.T	03-Dec-09	12	1349.42	5.79	3.73	0.17

Table 4.2: Concentrations of ^{233}Pa (and ^{231}Pa impurities) in the six ^{233}Pa spikes produced as part of this thesis work. Initials A.T and B.H stand for Alex Thomas and Ben Hickey respectively.

4.4.8 Spike additions

Approximately 10 drops (~0.1g) of ^{229}Th-^{236}U carbonate spike and 0.5-1 ml of ^{233}Pa spike were added to dissolved sample solutions. A Sartorius Genius ME balance, accurate to 10^{-4}g was used to record all spike masses. The amount of ^{233}Pa spike added to each sample depended on the approximate concentration of ^{231}Pa in the sediment, aiming for a measured ^{233}Pa/^{231}Pa ratio of 1.0. Samples were then refluxed overnight and heated to incipient dryness with $HCLO_4$. This was done to ensure full equilibration of spike and sample and to drive off HF from the ^{233}Pa spike. The sample solution was then converted to nitrate from with 4 mls 7.5M HNO_3, in preparation for column chemistry.

4.5 Pa-Th-U separation

Pa, Th and U were separated from the sample matrix and each other by column chromatography, adapting the procedure described in Edwards et al. (1986). This process is important to accurately measure Pa, U and Th on the mass spectrometer without clogging the nebuliser with matrix solids. Element separation also minimizes abundance sensitivity and molecular interference from large beams, such as ^{232}Th and ^{232}ThH^{+} onto ^{231}Pa and ^{233}Pa and removes any ingrown ^{233}U from the ^{233}Pa spike that formed since milking.

4.5.1 Separation procedure

10 ml Biorad columns were loaded with Dowex Biorad AG1-X8 anion exchange resin (100-200 mesh) that had been cleaned with repeated 10 ml washes of Milli-Q,

and 7.5M HNO_3. 4 ml of 7.5M HNO_3 was added to each column before being loaded with dissolved sample solutions. Acids were added drop wise to each column to prevent remixing of elements into the reservoir and minimize re-suspension of resin.

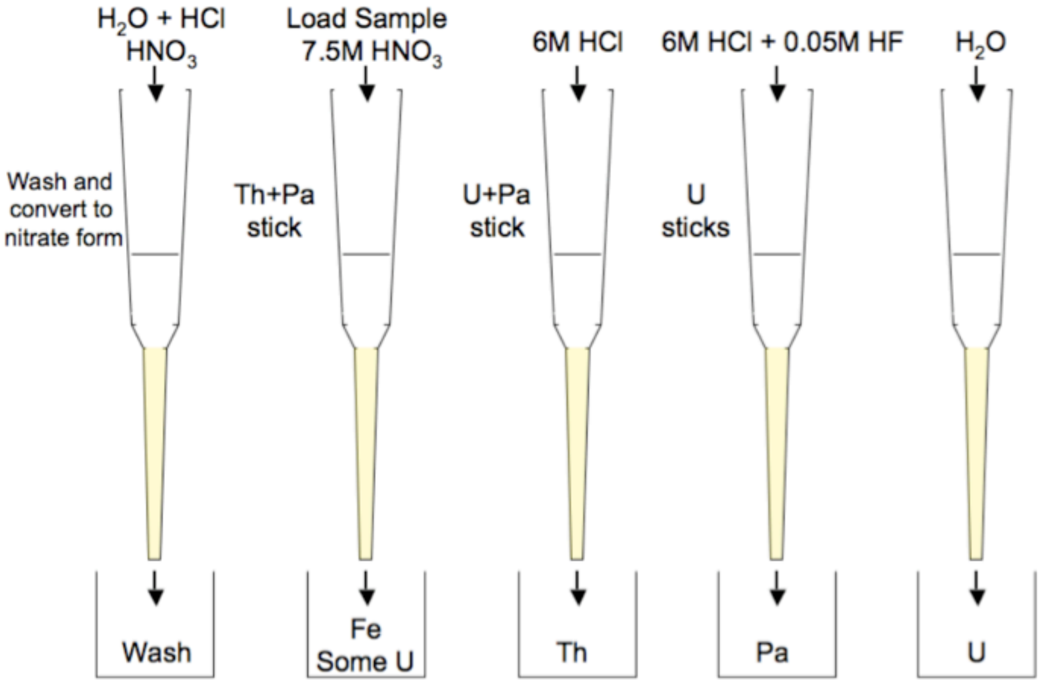

Figure 4.4: Schematic of column chemistry used in the U-Th-Pa separation process. Resin is indicated in yellow (from Rae, 2007).

To ensure a clean Pa fraction, the first Pa cut was dried down, redissolved in 4 ml 7.5M HNO_3 and given a second column pass. The additional Pa column pass improves Pa/Th separation, reducing the interference of ^{232}Th hydrides to the ^{233}Pa beam during measurement. The Pa fraction was collected in original sample beakers to improve yields, as Pa can have an affinity for Teflon. Due to the relatively short half-life of ^{233}Pa it is important to accurately record the time of the final separation of Pa and U. This is taken to be the time of the final column pass. Once separated from U, the ^{233}Pa spike will continue to decay and produce daughter ^{233}U (159 ka half life). As this daughter has the same mass as ^{233}Pa, the $233^+/231^+$ should not change after separation. Although the ionisation efficiencies of U and Pa have been shown to be similar (Choi et al., 2001) the Pa fraction was measured as soon as possible after chemical separation to minimize potential fractionation of ^{233}Pa and ^{233}U during ionisation.

Finally, Pa, Th and U fractions were reduced to a single drop and redissolved in 1 ml of 2% HNO_3 in preparation for analysis by MC-ICPMS.

4.6. Mass spectrometry

U, Th and Pa were measured on a Nu instruments Multi Collector Inductively Coupled Mass Spectrometer (MC-ICPMS). The use of MC-ICPMS allows for highly accurate and precise measurements of isotope ratios after correction for mass bias, ion counter gain, molecular interferences, abundance sensitivity and machine drift (as described in section 4.8).

Prior to the main sample run, diluted aliquots of the U and Th fractions were used to check solution concentrations of ^{238}U and ^{232}Th. This was done to optimize beam intensities and to ensure standard concentrations were approximately equal to sample concentrations, reducing biases that can result from variations in beam size.

Samples were loaded into the auto sampler and introduced to the mass spectrometer using a Nu Instruments desolvating nebuliser with an uptake rate of ~100 μl min^{-1}, being ionized by the ~8000 k plasma. The ions are accelerated through the sampler and skimmer cones by a high voltage (~4 kV) before entering an electrostatic and magnetic sector and arriving at an array of 12 Faraday collectors and three ion counters.

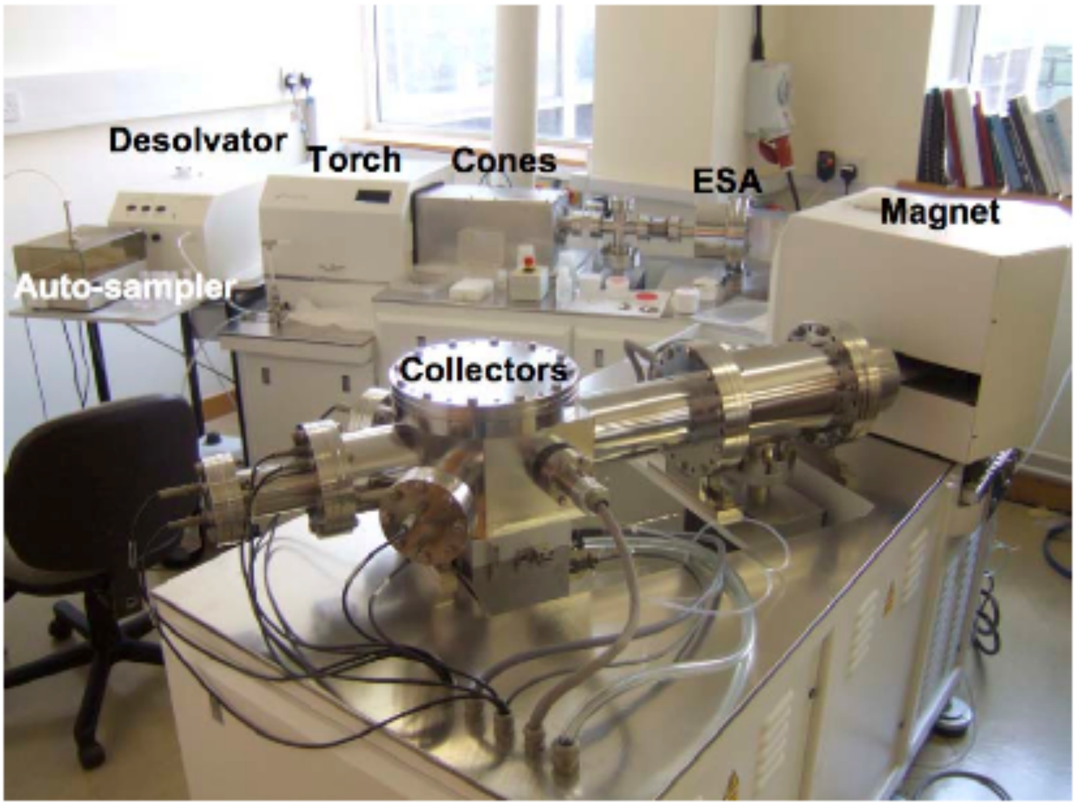

Figure 4.5: The Nu-instruments Multi-Collector Inductively Coupled Plasma Mass Spectrometer (MC-ICPMS) used for sample analysis.

Ion counters are used for low abundance isotopes and can detect the arrival of a single ion, while Faraday cups measure the beam current as a voltage passing across a resistor, and require beams of ~100,000 ions per second to provide precise values. The maximum voltage that can be recorded on one of the Faraday collectors is 10V. Above this limit isotope beam signals are invalid and readings from other collectors become unreliable.

Uranium was measured statically with ^{238}U, ^{236}U and ^{235}U focused in Faraday collectors and ^{234}U in an ion counter (step 4, Table 4.3). Each sample was bracketed with a measurement of CRM-145 uranium standard (step 5, Table 4.3) measured as a dummy sample, to correct mass bias, abundance sensitivity and ion counter gain (described in section 4.8).

	Step	F(+6)	F(+4)	F(+3)	F(+2)	F(+1)	AXIAL	F(-1)	F(-2)	IC(-3)	F(-4)	IC(-5)	F(-6)	IC(-7)	F(-8)
Protactinium	1				238		236	235		233	232	231			
Thorium	2		238			235			232		230	229			
	3			238			235					230	229		
Uranium	4					238		236	235	234					
CRM 145 mass bias	5					238			235						
CRM 145 gain corr.	6						238			235	234				
(Pa and Th)	7								238			235	234		

Table 4.3: The ion counter and Faraday cup collector configurations for Pa, Th and U analysis. F = Faraday collector IC = ion counter. Numbers refer to their mass relative to the axial collector.

Following each standard measurement, a repeated wash of 2% HNO_3 and 10% HNO_3 was required to ensure all standard solution was washed out before the next sample solution was measured. A test was first carried out to estimate wash out time, which varies depending on the gas flow rate of the nebuliser. The total wash out time used was approximately three times the time taken for a beam to reduce to 1% of its original intensity after the sipper is taken from the standard and placed into the 2% HNO_3 wash. Due to the ion counters on the Nu Instruments MC-ICPMS being spaced two mass units apart, Thorium was measured in two steps (steps 2 and 3, Table 4.3) to allow both ^{230}Th and the spike isotope ^{229}Th to be measured in ion counters. The ^{230}Th/^{229}Th ratio is corrected for variations in beam intensity between steps 2 and 3 by normalizing to ^{235}U in each step. No gain correction was required for the ^{230}Th/^{229}Th ratio due to the fact that each isotope was measured in the same ion counter. Mass bias and ion counter gain (for the ^{232}Th/^{230}Th and ^{232}Th/^{229}Th ratios) were corrected for by sample bracketing with U standard CRM 145 (steps 5 and 7, Table 4.3). As with U, a measurement of 2% HNO_3 was made following each standard measurement to ensure sufficient wash out of Th between samples. Due to the high concentration of ^{232}Th in sediment samples, the Th cut was diluted before the main run to ensure that the ^{232}Th beam did not exceed the 10 V limit of a Faraday cup and that the concentration between samples and standards was approximately equal.

Protactinium was measured in a static step, with both ^{233}Pa and ^{231}Pa collected in ion counters IC(-3) and IC(-5) respectively (step1, Table 4.3). Ion counter gain and mass bias were assessed by bracketing samples with U standard CRM 145, setting ^{235}U sequentially into each ion counter (steps 6 and 7) and then a Faraday collector (step 5). The affect of abundance sensitivity from $^{232}ThH^+$ on ^{233}Pa as well as molecular interference from ^{232}Th was assessed by measuring a ^{232}Th standard run as a sample (step1) between Pa sample measurements. As this Th standard contained no Pa, all measured signal masses at 233 and 231 were the result of these affects and were later corrected for in the raw Pa data. For each element, samples were measured in blocks of ~30 x10 second integrations and standards were typically measured in blocks of 5 x 10 second integrations.

4.7 Corrections for mass spectrometric biases

4.7.1 Mass bias

The transfer of ions from the ion source in a plasma ionization mass spectrometer is significantly dependent on the mass of the ions. Heavy ions are preferentially transferred into the mass spectrometer. This mass bias is thought to be due to the fact that when charged ions pass through a confined space their positive charges repel one another out of the central ion beam. Lighter ions are deflected further by this repulsion resulting in the central ion beam becoming enriched in heavier ions.

This mass bias effect was corrected for by bracketing sample measurements with measurements of a standard of known isotopic ratio (^{238}U /^{235}U) and correcting for all biases by normalizing the samples to this ratio, so that:

$$\varepsilon = \left(\frac{^{238}\mathrm{U}/^{235}\mathrm{U}}{137.88} - 1 \right) / 3 \tag{4.12}$$

where ε is mass bias per atomic unit. 137.88 is taken as the natural and uniform value of ^{238}U/^{235}U (Stirling et al., 2005). Recent work has demonstrated small natural variations in this ratio (Bopp et al., 2009) but these variations are too small to affect the results of analysis in this thesis.

This correction assumes that the mass bias effect is linear at high atomic numbers and is the same for U, Th and Pa. This has been demonstrated for U and Th on the Nu instrument (Mason and Henderson 2010) and is likely to be so for Pa.

4.7.2 Ion counter gain

The difference between the response of an ion counter relative to that of the same ion beam in a Faraday cup is known as the ‘ion counter gain’ and is corrected by dividing the measured intensity by this number:

$$Gain = \frac{Intensity_{IC}}{Intensity_{Faraday}} \tag{4.13}$$

External measurements of the gain are made by measuring the $^{238}U/^{235}U$ ratio sequentially with a ^{235}U beam centered firstly in each ion counter and then in a Faraday collector. Gains on the ion counters during analysis reported here were typically 75-80% for IC(-3) and 80-85% for IC (-5) and were assessed between each sample measurement. Typical uncertainty on the gain measurements were 0.7-0.9% (2 s.e).

4.7.3 Abundance sensitivity and molecular interference

As a beam of ions travels through the mass spectrometer a small proportion of the ions interact with gaseous atoms due to the imperfect vacuum. Some ions are slowed by these interactions and have lower energy than is typical for ions of their mass. Consequently, when the magnet deflects the beam, these ions of lower energy are deflected more and appear as a low mass tail on isotope peaks. This abundance sensitivity becomes a significant contribution to measurements of isotopes in small concentrations in the same solution as an isotope of relatively much greater concentration and slightly greater mass. For example, a major source of abundance sensitivity on ^{231}Pa measurements is from the larger ^{232}Th beam.

In addition, molecules may be formed when the sample is introduced the plasma, often by interaction with water. The most significant molecular interference is from $^{232}ThH^{+}$ due to the large beam size of ^{232}Th relative to $^{233}Pa,U$. The effect of abundance sensitivity and molecular interference are corrected from the $^{233}Pa/^{231}Pa$

ratio using a measurement of a ^{232}Th standard containing no Pa in between sample measurements. Typical contributions from abundance sensitivities and molecular interference were 5 x10^{-7} cps on 231 and 5 x 10^{-6} cps on 233 . These were equivalent to 0.3% and 0.1% of the actual values for the 233 and 231 beams respectively.

$$^{233}\mathrm{Pa}/^{231}\mathrm{Pa}_{cor} = \frac{^{233}\mathrm{Pa}_{meas} - {}^{232}\mathrm{Th}_{meas} \times \left(233^{+}/^{232}\mathrm{Th}\right)_{std}}{^{231}\mathrm{Pa}_{meas} - {}^{232}\mathrm{Th}_{meas} \times \left(231^{+}/^{232}\mathrm{Th}\right)_{std}} \tag{4.14}$$

To help reduce the effect of abundance sensitivity, the central ion counter (IC-5) is equipped with an energy filter that only allows ions through to the detector that have the same energy as those accelerated by the high voltage at the front of the machine.

4.8 Blanks and Uncertainties

A full procedural blank was run with each batch of samples to correct for sample contamination introduced during sample preparation (Table 4.4).

Sample batch	^{230}Th (fg)	% blank	^{232}Th (pg)	% blank	^{231}Pa (fg)	% blank	^{238}U (ng)	% blank
JR_run3	*174*	*3.88*	149	0.02	3.72	3.61	1.02	0.57
run 1	*262*	*3.10*	214	0.02	5.67	2.85	4.19	1.86
run 2	1.56	0.02	554	0.04	32.2	12.56	2.49	0.61
run 3	2.69	0.02	255	0.03	29.6	11.10	0.47	0.30
run 4	1.81	0.04	340	0.04	1.71	1.36	0.11	0.06
run 5	3.3	0.04	170	0.02	2.92	1.40	0.1	0.03
run 6	*0*	*0*	*0*	*0*	1.35	0.70	0.07	0.03
run 7	6.06	0.08	208	0.02	1.49	0.66	0.06	0.02
run 8	56	0.50	1356	0.13	1.62	0.52	0.95	0.42
run 9	5.99	0.04	202	0.02	1.89	0.56	0.33	0.18
run 10	4.82	0.03	183	0.02	1.8	0.56	0.11	0.06
run 11	4.69	0.04	195	0.02	0.68	0.24	0.09	0.04
run 12	5.6	0.07	635	0.10	4.21	1.43	0.17	0.13
average	9.25	0.09	371.75	0.04	6.84	2.89	0.78	0.33

Table 4.4: Blanks of the major isotopes measured in each sample run. Values in italics were subjectively removed from the mean. Th blanks for run 6 were set to 0 due to negative readings for this sample blank in the Th run.

The percentage blanks are highest for ^{231}Pa. Due to the relatively low concentration of Pa in sediments, this high blank is most likely the result of cross contamination between samples, possibly during vigorous evaporation steps. Blanks could therefore be reduced by greater physical separation of samples during chemical dissolution steps. Blanks for ^{230}Th are noticeably higher in JR_run3 and run1. This may be the result of increase cross contamination resulting from two people (James Rae and the author) using the same hood to dissolve sediments from different sample batches (JR-run3 and run1) over the same period of time.

Standard errors were converted from standard deviations by dividing by the square root of the number of measurements, n:

$$\sigma = \frac{\mathrm{s.d}}{\sqrt{n}} \tag{4.15}$$

Standard errors were propogated through corrections assuming that uncertainties in each correction are independent of each other. In this way, errors were summed quadratically, such that:

$$\sigma_y^2 = \left(\frac{\partial y}{\partial a}\right)\sigma_a^2 + \left(\frac{\partial y}{\partial b}\right)\sigma_b^2 + \ldots \tag{4.16}$$

Where a and b are independently measured variables of which y is a function and σ is the standard error. This can be simplified for simple addition or subtraction of individual errors to:

$$\sigma_y = \sqrt{\sigma_a^2 + \sigma_b^2 + \ldots} \tag{4.17}$$

and:

$$\sigma_y = \sqrt{\left(\frac{\sigma_a}{a}\right)^2 + \left(\frac{\sigma_a}{b}\right)^2 + \ldots} \tag{4.18}$$

for simple multiplication and division. In complex cases, such as the propagation through Pa spike addition, each variable has its error added and subtracted in turn and the corrected error calculated by summing these values quadratically.

2 S.E	$(^{238}\mathrm{U})$	$(^{232}\mathrm{Th})$	$(^{230}\mathrm{Th})$	$(^{230}\mathrm{Th})_{\mathrm{lith}}$	$(^{230}\mathrm{Th})_{\mathrm{auth}}$	$(^{230}\mathrm{Th})_{\mathrm{xs0}}$
absolute	0.0003	0.007	0.014	0.004	0.000	0.013
%	0.01%	0.39%	0.60%	0.37%	0.38%	0.92%
	$(^{231}\mathrm{Pa})$	$(^{231}\mathrm{Pa})_{\mathrm{lith}}$	$(^{231}\mathrm{Pa})_{\mathrm{auth}}$	$(^{231}\mathrm{Pa})_{\mathrm{xs0}}$	$(^{231}\mathrm{Pa}_{\mathrm{xs}}/^{230}\mathrm{Th}_{\mathrm{xs}})_0$	
absolute	0.005	0.000	0.001	0.006	0.004	
%	3.57%	0.37%	0.38%	6.08%	6.56%	

Table 4.5: Summary of the average internal errors for the isotopes of interest and on the lithogenic and authigenic Pa and Th components for samples from core GeoB 2107. Standard errors were propogated through corrections to give the final error for $(^{231}\mathrm{Pa}/^{230}\mathrm{Th})_{\mathrm{xs}}0$. All sample errors are listed in data tables 7.1-7.8 in the appendix at the end of this thesis.

The largest contribution to the final $(^{231}\mathrm{Pa}/^{230}\mathrm{Th})_{\mathrm{xs}}0$ error comes from the error associated with the $\mathrm{Pa}_{\mathrm{xs}}0$ component (Table 4.5). A relatively minor impact on the final error comes from $^{230}\mathrm{Th}$ component whilst errors associated with $^{232}\mathrm{Th}$ and $^{238}\mathrm{U}$ are only associated with small corrections and are of less significance.

The relatively high errors on Pa derive mainly from the raw measurement due to low concentration of Pa in samples and also the gain correction, with both Pa isotopes being measured in gain counters. No error is applied to the blank correction as this is assumed to be constant between samples of the same batch.

4.9 Total particulate trace metal concentrations

Following complete dissolution of sediment (as described in section 4.2) and prior to sample spiking, a 2 ml cut of sample solution was pipetted into cleaned 2 ml centrifuge tubes in preparation for trace metal analysis. Sample Teflon beakers were weighed before and after the cut was taken in order to calculate the % mass of solution removed. 30 microlitres of each sample cut was then added to 1 ml of Indium 500 ppb spike solution in cleaned 15 ml polypropylene tubes and topped up to 15 ml with 2% HNO_3.

All trace metal elements were measured on a Thermo-Finnigan MAT element 2 sector field ICPMS, coupled with an Aridus desolvation unit, run with help from Cees-Jan de Hoog and Andrew Mason. The x 20 dilution factor of 0.1 g of sediment into a 2 ml cut, followed by a x 500 dilution of 30 microlitres into 15 ml, represented a total dilution factor of 10,000. Such a large dilution factor was necessary to keep concentrations of major ions at sufficiently low levels when samples were analysed on the mass spectrometer.

Trace element data was first normalized to Indium concentrations and then blank corrected. For a given trace element of interest (specifically Fe, Ca, Ba), concentrations were determined by calibration against a multi element standard run at a suitable range of concentrations expected in ocean sediment, accounting for the sample dilution. Final concentrations for each element were determined after correcting for mass spectrometer drift and a dilution factor of 10,000.

4.10 XRF element intensities

At intervals of 1 cm, GeoB cores 2107, 2104 and 2112 were analyzed for bulk sediment chemistry using an X-ray fluorescence (XRF) core scanner. All core analysis was conducted at the University of Bremen by Dr. Cristiano Chiessi. The XRF core scanner generates an X-ray beam which is directed onto the surface of a split sediment core over a 1 cm^2 area. The incident X-ray increases the energy levels in the atoms of the sediment core, resulting in the emission of an electron from the inner shell of each atom. The vacancy in the inner shell is instantly filled by an electron from the outer shell of each atom, resulting in a release of radiation. As the wavelength of the emitted radiation is element specific (Potts, 1987), the measurement of the wavelength spectrum allows for the calculation of XRF element intensities. XRF intensities give estimates of the concentrations of analysed elements but do not allow for calculation of these concentrations. Therefore, only relative changes in XRF element intensities are significant (Heil, 2006).

4.11 Opal concentrations

4.11.1 Sample preparation

Sample preparation for opal measurements were carried out using a protocol adapted from Mortlock and Froehlich (1989). Approximately 50 mg of dried sediment for each sample was weighed into 50 ml polypropylene centrifuge tubes. 5 ml of 10% H_2O_2 was pipetted into each tube to break down organic matter and after 30 minutes an additional 5 ml of 1 M HCL was added to dissolve carbonates. The sample tubes were then capped and sonicated in a water bath at room temperature for 30 minutes.

20 ml of deionized milli-Q water was added to each sample tube, which were then centrifuged at 4,500 rpm for 6 minutes. Each sample tube was then carefully decanted to discard the supernatant and placed in an oven overnight at 60°C to remove moisture. 40 ml of 2 M Na_2CO_3 was added to each tube, which were capped, shaken vigorously and sonicated for 20 minutes. Sample tubes were then placed into a constant temperature water bath at approximately 85°C in order to digest all silica present in the sediments. At 2 hour intervals, sample tubes were shaken and sonicated for 5 minutes before being returned to the water bath. After a total of 5 hours the tubes were immediately centrifuged for 6 minutes at 4,500 rpm. Approximately 20 ml of the supernatant liquid was transferred to polyethylene vials and stored for future analysis as below.

4.11.2 Photo spectrometer analysis

Opal analysis was performed using the colorimetric Heteropoly Blue Method adapted from Koroleff (1983). 9.3 ml of milli-Q water was added to cleaned polypropylene tubes, together with 0.1 ml of sample solution and 0.2 ml of molybdate reagent. This mixture was shaken and left for 5 minutes. 0.2 ml of citric acid and 0.2 ml of amino acid were added to the sample mixture and left for another hour. Silic acid reacts with molybdate in the presence of acids to form silcomolybdic acid, which is then reduced to a blue colour by an amino naphtol sulfonic acid for low concentrations of silica. The sample mixtures were transferred to spectrophotometer cells and measured using a Hac Lange DR2800 spectrophotometer. Sample readings were calibrated using a silica standard of known concentration. A blank milli-Q solution was used to bracket every sample measurement to account for possible machine drift between sample readings.

Typical data errors were assessed by measurement of several replica samples from each core and standard deviations calculated using repeat measurements on individual samples. All opal data was converted to sample weight % SiO_2 and converted to opal flux by normalization to ^{230}Th, as described in chapter 6.

4.12 Radiocarbon dating

Planktic foraminifera were picked from the >250 μm fraction of wet-sieved sediment samples. For each sample, the most abundant single species of planktic foraminifera were picked for radiocarbon analysis (Figure 4.6). Mixed planktic species were picked in carbonate-poor samples, in order to obtain a minimum mass of 10 mg of carbonate required for accurate ^{14}C dating.

Picked foraminifera were ultrasonically cleaned in Milli-Q and 2% H_2O_2 for 5 minutes at 80°C. The total mass of carbonate picked for each sample was weighed before being sent to the NERC Radiocarbon Facility where samples were prepared for radiocarbon analysis by Dr. Steve Moreton. Briefly, samples were hydrolysed to CO_2 using 85% orphophosphoric acid at 25°C before being converted to graphite by Fe/Zn reduction. Samples were then analysed for ^{14}C at the SUERC AMS Facility in East Kilbride, Scotland.

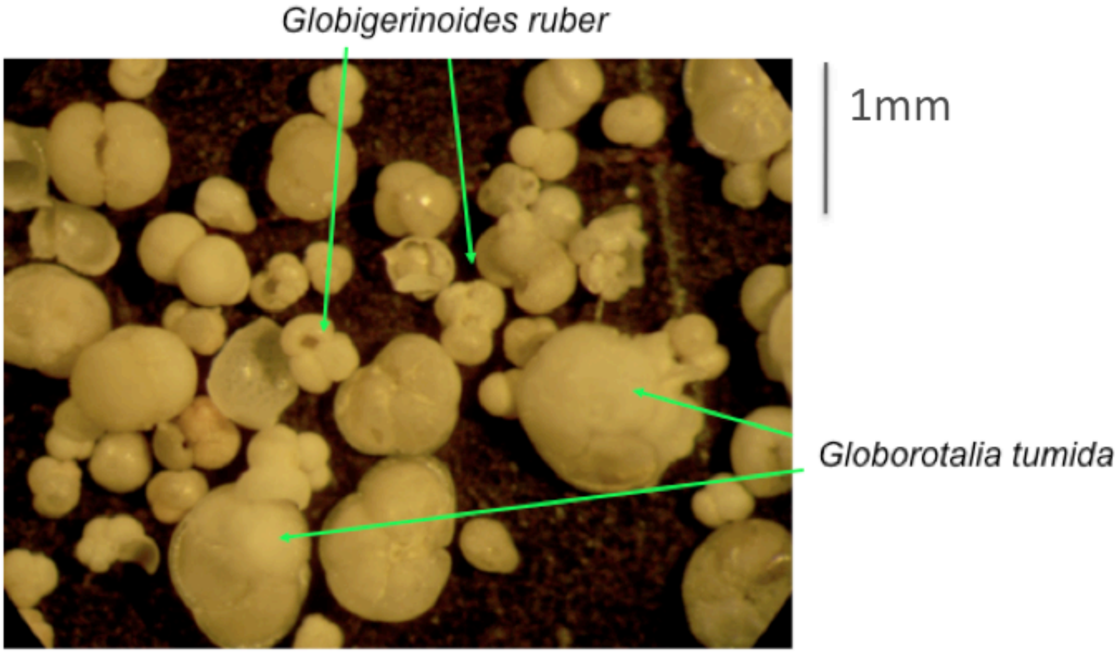

Figure 4.6: Photo showing the major abundant species *Globorotalia tumida* and *Globigerina ruber* in sediment samples from cores GeoB 2104 and GeoB 2109.

For samples of foraminifera, ^{14}C ages have to be corrected for the reservoir effect (Bard, 1988). In the upper ocean, surface waters mix with upwelled deep waters, which are depleted in ^{14}C. Therefore, upper ocean organisms yield ^{14}C ages that are too old. This artificial aging is referred to as the reservoir effect, which on average amounts to 400 years in the world's oceans (Bard, 1988). For the Argentine Basin core samples used in this study, radiocarbon ages were corrected for a reservoir age of 318 years (data source http://calib.qub.ac.uk/marine).

Finally, radiocarbon ages were calibrated to calendar years BP using the "Fairbanks0107" calibration curve extending from 0 to 55,000 years BP (Figure 4.7, Fairbanks et al. 2005). For comparison, calendar ages were also calculated using the calibration curve "Intcal04" and were found to be within error of the calendar ages produced using the "Fairbanks0107" calibration curve. Calendar ages are reported in years before present (yr BP). However, they are dated relative to the year 1950 rather than relative to the present because nuclear bomb testing significantly increased the amount of ^{14}C in the atmosphere after 1950 (Stuvier and Polach, 1977).

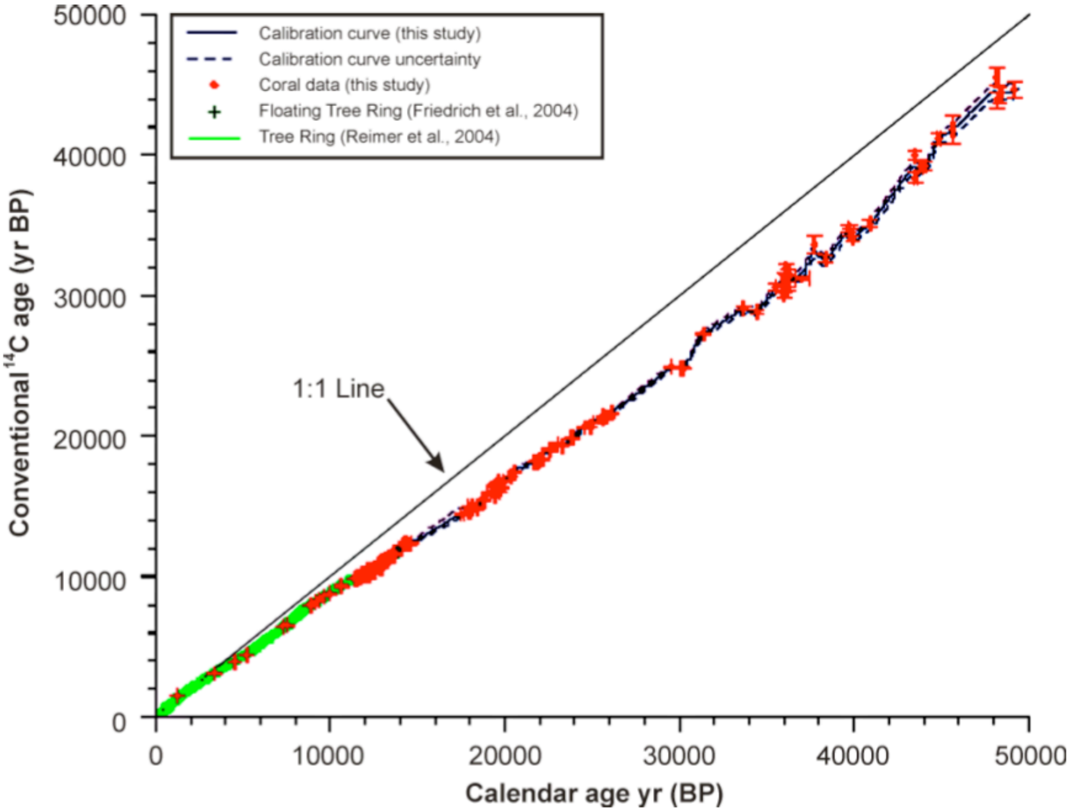

Figure 4.7: Calibration curve for the conversion of ^{14}C ages to calendar ages (Fairbanks et al., 2005). The calibration of ^{14}C ages to calendar ages is required due to variations in the concentration of ^{14}C in the atmosphere over the past 50 ka. Calendar ages are obtained directly by dendrochronology and varve chronology as well as by U/Th dating of corals and speleotherms (e.g. Chiu et al., 2005; Wang et al., 2001).

4.13 Neodymium Isotopes

The following method was used for Nd isotopes analysis by Paul Carter at Bristol University and is taken from Carter (2009).

The chemical separation procedure involved the grinding of ~0.1g bulk sediment per sample, which was then decarbonated using sodium acetate buffered acetic acid, rinsed multiple times, and subjected to 3 hrs of leaching using an acetic acid-hydroxylamine hydrochloride (HH) solution to separate the Fe-Mn oxide fraction, following previously used techniques (e.g. Piotrowski, 2004). The Fe-Mn fraction was centrifuged and decanted to remove any particulate matter, before being dissolved in strong acid. The supernatant was then split into a bulk element fraction and a Nd isotopic fraction.

A number of variants of the acetic acid-HH solution have been used in recent studies, summarised in Gutjahr et al. (2007). Due to previously identified issues with the leaching of easily exchangeable volcanics from southwest Atlantic sediments, recommendations have been made to use weaker leaching solutions on these sediments (Piotrowski, 2004). The recommended solution of Gutjahr et al. (2007) and a 10x diluted version, were tested here on samples from GeoB 2107. The recommended solution of Gutjahr et al. (2007) comprises: 0.05 M hydroxylamine hydrochloride- 15% acetic acid- 0.02 M Na-EDTA, which is buffered to pH 4 with NaOH and shaken for 3 hours. The weaker solution comprises: 0.005 M hydroxylamine hydrochloride - 1.5% acetic acid - 0.002 M Na-EDTA, also buffered to pH 4 with NaOH and shaken for 3 hours.

The two leachate solutions were found to produce significant differences in εNd, ^{87}Sr/^{86}Sr and Al/Nd for the same samples of core GeoB 2107 (Carter 2009, chapter 6), with downcore results showing an offset to more radiogenic εNd values when a weaker leachate solution was used. Gutjahr et al. (2007) argue that the Al/Nd ratio of the leachate fraction can be used as the best measure of potential contamination, as

Al/Nd values in leachates are comparable to those of Fe-Mn crusts when no leaching of the detrital phase has occurred. The Al/Nd ratios of samples from GeoB 2107 were found to be consistently lower for the ‘weak leach’ samples relative to their ‘strong leach’ counterpart from the same depth in core. On this basis, all εNd data presented in this thesis has been acquired using the ‘weak leach’ solution.

Chapter 5: Core chronology

5.1 Introduction

The age models for the cores used in this study were based primarily on multiple radiocarbon measurements on planktonic foraminifera and on bulk sediment for samples that lacked sufficient levels of foraminifera required for radiocarbon dating. A large number of ^{14}C ages were required because of the non-uniform sedimentation rate from these cores as determined from existing $\delta^{18}O$ stratigraphy and in order to place down-core records onto a robust timescale to allow their comparison with other records, particularly with the ice-cores and North Atlantic $^{231}Pa/^{230}Th$ records.

All radiocarbon dates were measured at the NERC Radiocarbon Laboratory, East Kilbride, Scotland as part of this thesis research with the exception of those for GeoB 2107 which were a pre existing data set measured at the Leibniz-Laboratory for Radiometric dating and Isotope Research, University of Kiel, Germany. The method used for sample preparation for radiocarbon analysis is described in section 4.12. In each core the ages of samples between radiocarbon dates were determined by linear interpolation. As discussed in section 4.12, radiocarbon ages were uniformly corrected for a reservoir age of 318 years (source: http://calib.qub.ac.uk/marine) and converted to calendar ages using the calibration program of Fairbanks et al. (2005). All planktonic foraminifera were picked from the >250 μm fraction of wet-sieved sediment except for core GeoB 2107 (see section 5.2). Sample integration times were calculated by dividing the width of the plastic scoops used to sample the cores (1 cm) by the average sedimentation rate for each core.

5.2 GeoB 2107 age model

The age model of GeoB 2107 (1045 m) was developed by Heil (2006) and is based on eight calibrated radiocarbon ages spanning the last ~25 kyr (Table 5.1). Analysis was performed on the mono specific species *Globigenroides sacculifer* sized between 200 µm and 450 µm. All radiocarbon ages for this core were measured at the Leibniz-Laboratory for Radiometric dating and Isotope Research, University of Kiel, Germany.

Depth in core (cm)	lab ID	Foramiferal Species	^{14}C age (yr BP)	Calendar Age (yr BP)
3	KIA 14534	G.*Sacculifer*	1590 ± 30	1120 ± 47
33	KIA 14533	G.*Sacculifer*	5340 ± 40	5670 ± 44
63	KIA 14532	G.*Sacculifer*	8995 ± 55	9580 ± 37
73	KIA 14530	G.*Sacculifer*	11890 ± 80	13390 ± 97
103	KIA 14528	G.*Sacculifer*	13030 ± 80	14990 ± 135
148	KIA 22409	G.*Sacculifer*	19100 ± 130	22340 ± 129
163	KIA 14525	G.*Sacculifer*	19810 ± 150	23160 ± 154
178	KIA 22408	G.*Sacculifer*	24250 ± 200	28790 ± 261

Table 5.1: Radiocarbon ages for GeoB2107. Results are reported as conventional radiocarbon years (relative to AD 1950).

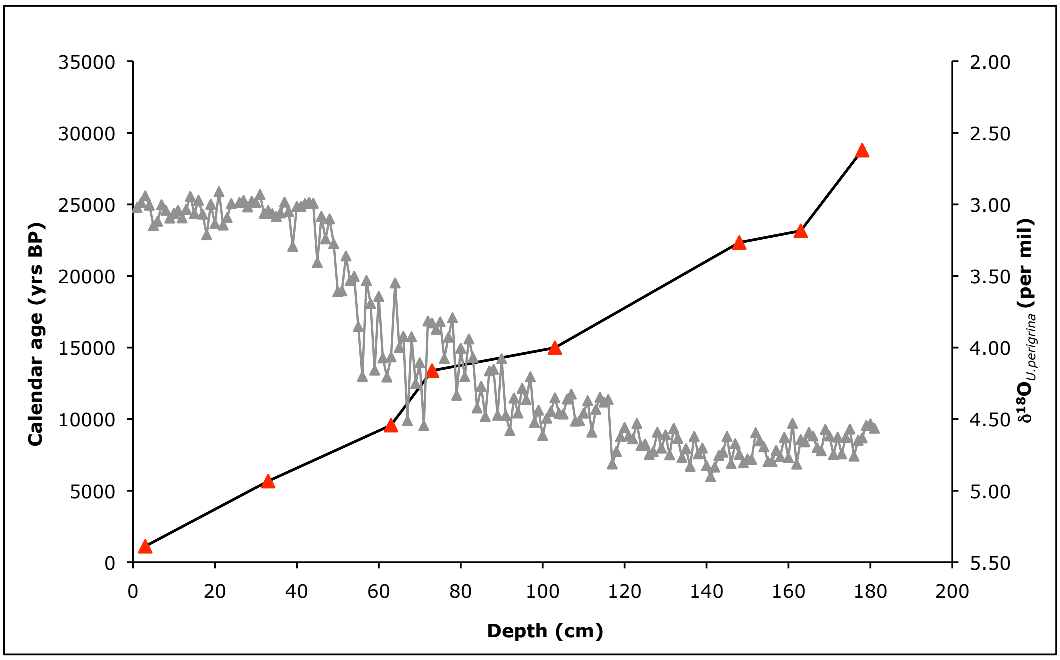

Figure 5.1: Age model for GeoB 2107. Red triangles denote calibrated radiocarbon ages.

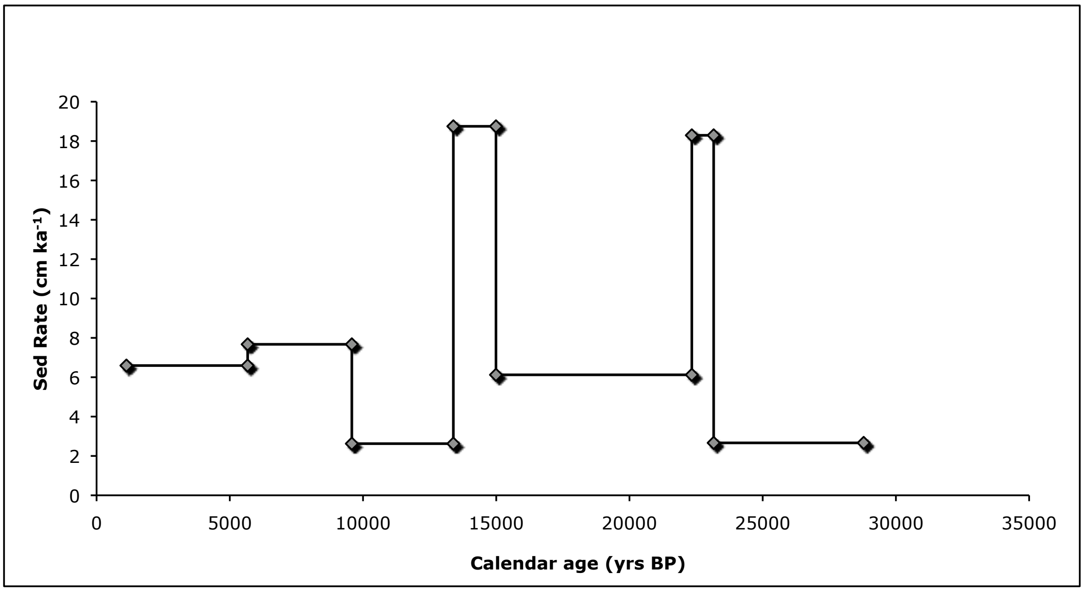

Figure 5.2: Sedimentation rate for GeoB 2107.

The sedimentation rate for GeoB 2107 averages 7 cm ka^{-1} for the duration of the Holocene and much of the deglacial with a maximum rate of ~19 cm ka^{-1} observed from 14-15 ka and from 22-23 ka. For a sampling interval of 5 cm used for this core, this translates into average time sampling steps of ~0.7 ka, with an average sample integration time of ~140 years.

5.3 GeoB 2104 age model

Radiocarbon ages for GeoB 2104 (1503 m) were initially obtained for four samples of the planktonic foraminifera *Globorotalia tumida*, four samples of the planktonic foraminifera *Globigerina ruber* and one sample from a mixture of these two species. For cores GeoB 2104 and GeoB 2109, the switch from dating *Globorotalia tumida* to *Globigerina ruber* was the result of the increasing abundance of *Globigerina ruber* relative to *Globorotalia tumida* downcore and the need to pick 10 mg of a single species for radiocarbon dating where possible. The age of *Globigerina ruber* was found to be ~570 years older than *Globorotalia tumida* in one sample for which both species were dated (depth 41 cm). An average of the two different radiocarbon ages from the two species was used for this sample depth (41 cm) in the age model for core GeoB 2104 (Figure 5.4). Age reversals were observed in two samples at 76 cm and 121 cm (Table 4.2). The cause of these reversals is unknown, although Came et al. (2003) report similar age reversals in the glacial section of a core in the Argentine Basin measured on the same planktonic species *Globigerinoides ruber* but noted that radiocarbon measurements of benthic foraminifera *Globigerina pachyderma* in the same samples produced glacial ages, suggesting that the observed age reversals from *Globigerinoides ruber* in the deglacial may be false. For this reason, the radiocarbon ages given for the two samples at 76 cm and 121 cm are excluded from the age model for core GeoB 2104 (Figure 5.4).

GeoB 2104 core depth (cm)	AMS lab number	Type of dating	Foramiferal Species	^{14}C age (yr)	Calendar Age (yr)
1	SUERC-23880	AMS ^{14}C on carbonate	*G. tumida*	929 ± 35	598 ± 39
16	SUERC-23881	AMS ^{14}C on carbonate	*G. tumida*	4718 ± 35	4969 ± 75
31	SUERC-23884	AMS ^{14}C on carbonate	*G. tumida*	5615 ± 36	6064 ± 69
41	SUERC-23885	AMS ^{14}C on carbonate	*G. tumida*	6763 ± 38	7376 ± 44
41	SUERC-23886	AMS ^{14}C on carbonate	*G. ruber*	7430 ± 37	7943 ± 28
56	SUERC-23887	AMS ^{14}C on carbonate	*G. ruber*	8548 ± 38	9195 ± 71
67	SUERC-23888	AMS ^{14}C on carbonate	*G. ruber*	11730 ± 40	13262 ± 65
76	SUERC-23889	AMS ^{14}C on carbonate	*G. ruber*	9072 ± 38	9724 ± 79
121	SUERC-23890	AMS ^{14}C on carbonate	mixed species	7281 ± 37	7789 ± 48
157	SUERC-30516	AMS ^{14}C on bulk sediment	-	20072 ± 117	23977 ± 147
72	-	Correlation with 2107 XRF	-	-	14200
74.5	-	Correlation with 2107 XRF	-	-	14730
120.5	-	Correlation with 2107 XRF	-	-	18500

Table 5.2: Radiocarbon ages and age model tie points for GeoB 2104. Results are reported as conventional radiocarbon years (relative to AD 1950).

In order to extend the age model beyond ~13 ka in GeoB 2104, additional tie points were produced by cross correlation of XRF Fe/Ca ratios to the shallower core GeoB 2107 (provided by Chiessi, pers comm. 2009). GeoB 2104 is located immediately downslope of GeoB 2107 on the Brazilian margin and has a greater depth of just 450 m. Due to their close proximity, GeoB 2104 has the same sediment supply as GeoB 2107 and is therefore very likely to have similar bulk sediment chemistry histories.

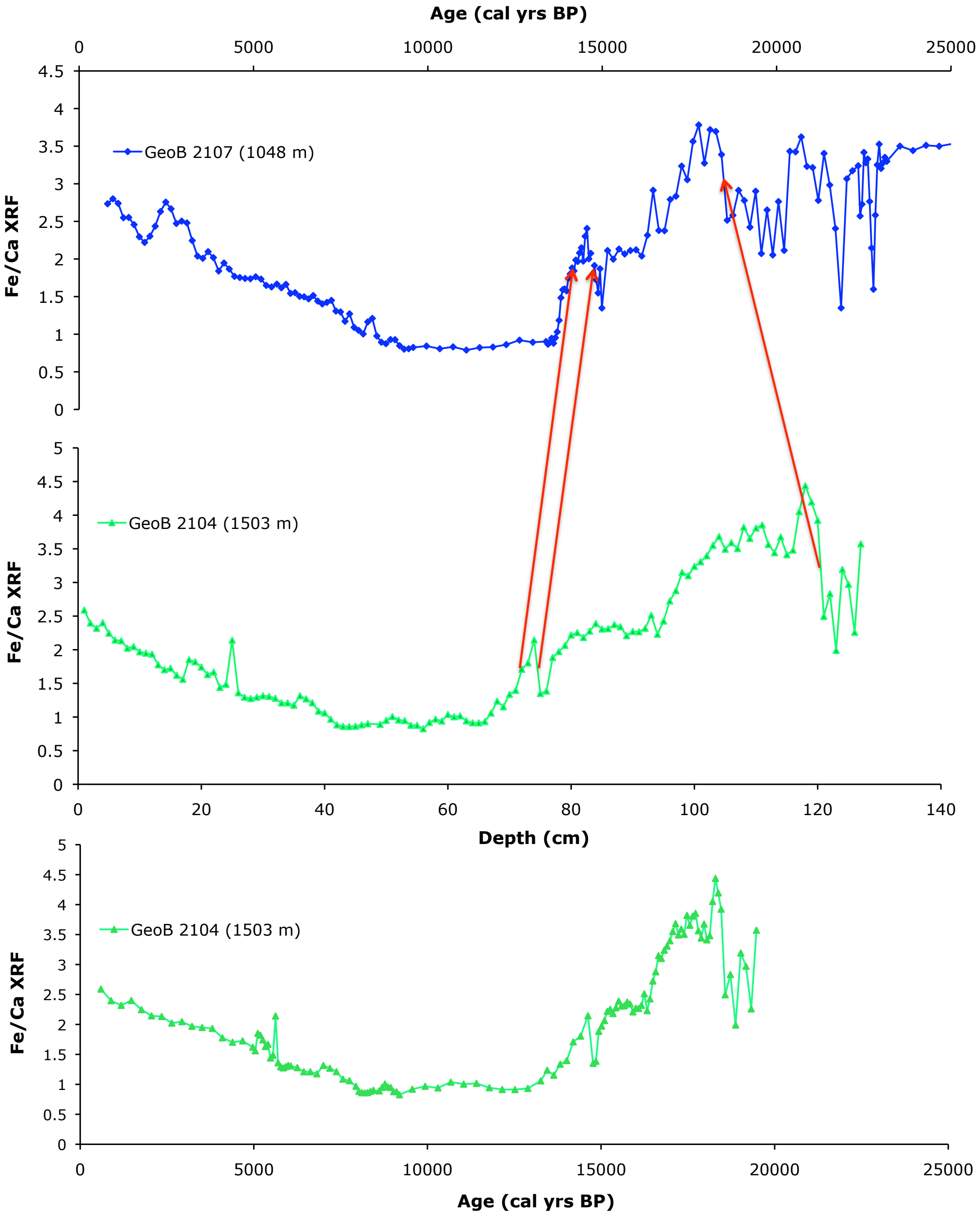

***Figure 5.3*:** Correlation of XRF Fe/Ca ratios between GeoB 2104 and GeoB 2107 used to produce additional age tie points for GeoB 2104. The XRF Fe/Ca ratios for GeoB 2107 and GeoB 2104 are also plotted together against age in section 6.1.7 of this thesis (Figure 6.10).

An additional sample from 157 cm was dated for a bulk sediment radiocarbon age, due to there being an insufficient mass of foraminifera for radiocarbon analysis at this depth in core.

The apparent high variability of sedimentation rates in GeoB 2104 may simply be a function of the uncertainty of radiocarbon and tie point ages used for this age model. Average sedimentation rates are 6.5 cm ka^{-1}. For a sampling interval of 5 cm used for this core, this translates into average time sampling steps of ~0.8 ka, with an average sample integration time of ~150 years.

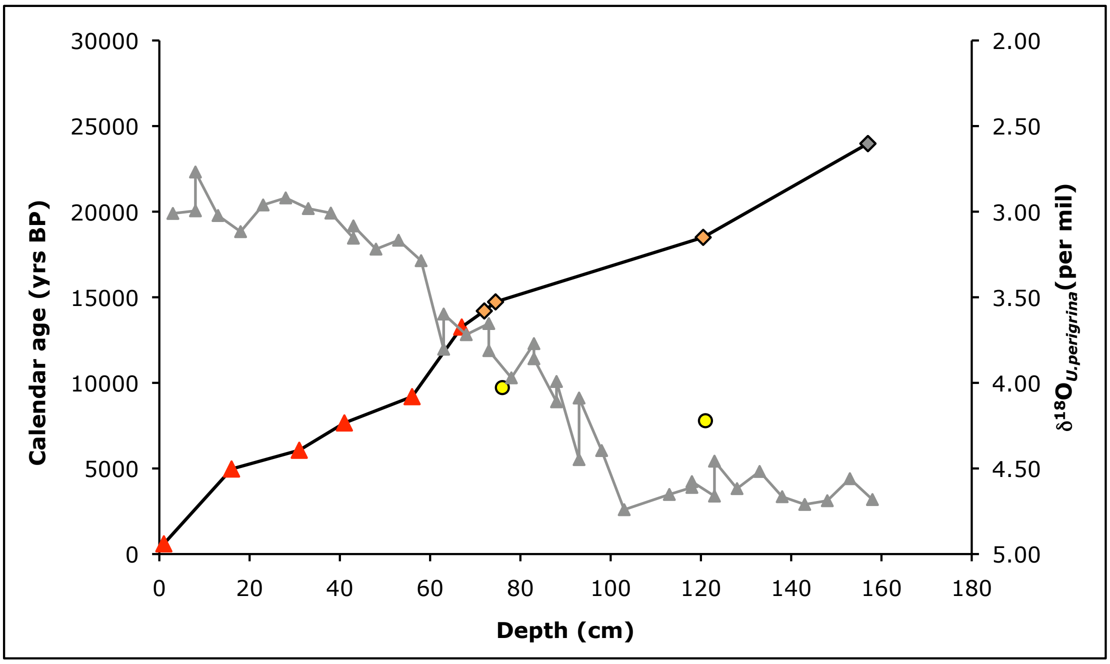

Figure 5.4**:** Age model for GeoB 2104: Combination of calibrated radiocarbon ages (red triangles), bulk sediment radiocarbon ages (grey diamond) and correlation of XRF Fe/Ca ratios with GeoB 2107 (orange diamonds). Two radiocarbon ages (yellow circles) are excluded from the age model as justified in the text.

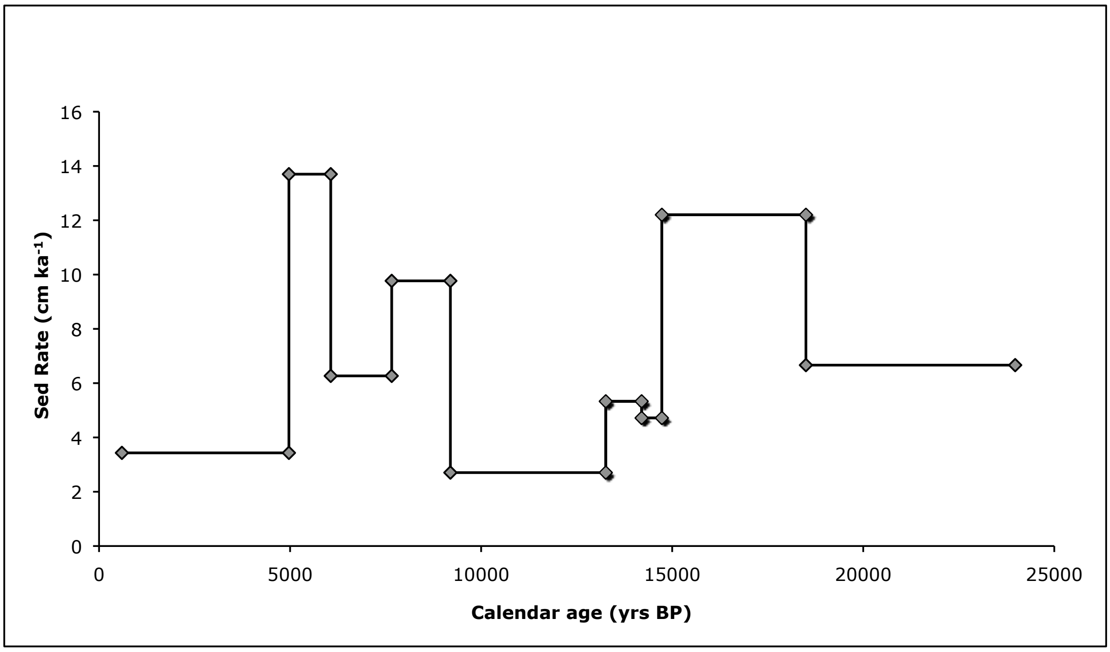

***Figure 5.5*: Apparent sedimentation rate for GeoB 2104.**

5.4 GeoB 2109 age model

The age model for GeoB 2109 (2504 m) is based on nine calibrated radiocarbon ages spanning the last ~30 kyr (Table 5.3). Radiocarbon ages for the upper section of the core were measured on single species *Globorotalia tumida*. The remaining ages were measured on single species *Globigerina ruber*.

GeoB 2109 core depth (cm)	AMS lab number	Type of dating	Foramiferal Species	^{14}C age (yr)	Calendar Age (yr)
1	SUERC-23891	AMS ^{14}C on carbonate	*G. tumida*	1432 ± 37	1011 ± 43
10	SUERC-23895	AMS ^{14}C on carbonate	*G. tumida*	5468 ± 37	5906 ± 34
15	SUERC-23896	AMS ^{14}C on carbonate	*G. tumida*	6890 ± 38	7465 ± 29
15	SUERC-23897	AMS ^{14}C on carbonate	*G. ruber*	8257 ± 35	8769 ± 31
20	SUERC-23898	AMS ^{14}C on carbonate	*G. ruber*	10293 ± 37	11382 ± 89
29	SUERC-23899	AMS ^{14}C on carbonate	*G. ruber*	11086 ± 39	12691 ± 43
34	SUERC-23900	AMS ^{14}C on carbonate	*G. ruber*	11384 ± 40	12929 ± 43
46	SUERC-23901	AMS ^{14}C on carbonate	*G. ruber*	13754 ± 43	15642 ± 118
73	SUERC-23904	AMS ^{14}C on carbonate	*G. ruber*	19813 ± 70	23258 ± 155
113	SUERC-23905	AMS ^{14}C on carbonate	*G. ruber*	26054 ± 133	30946 ± 191

***Table 5.3*: Radiocarbon ages for GeoB2109. Results are reported as conventional radiocarbon years (relative to AD 1950).**

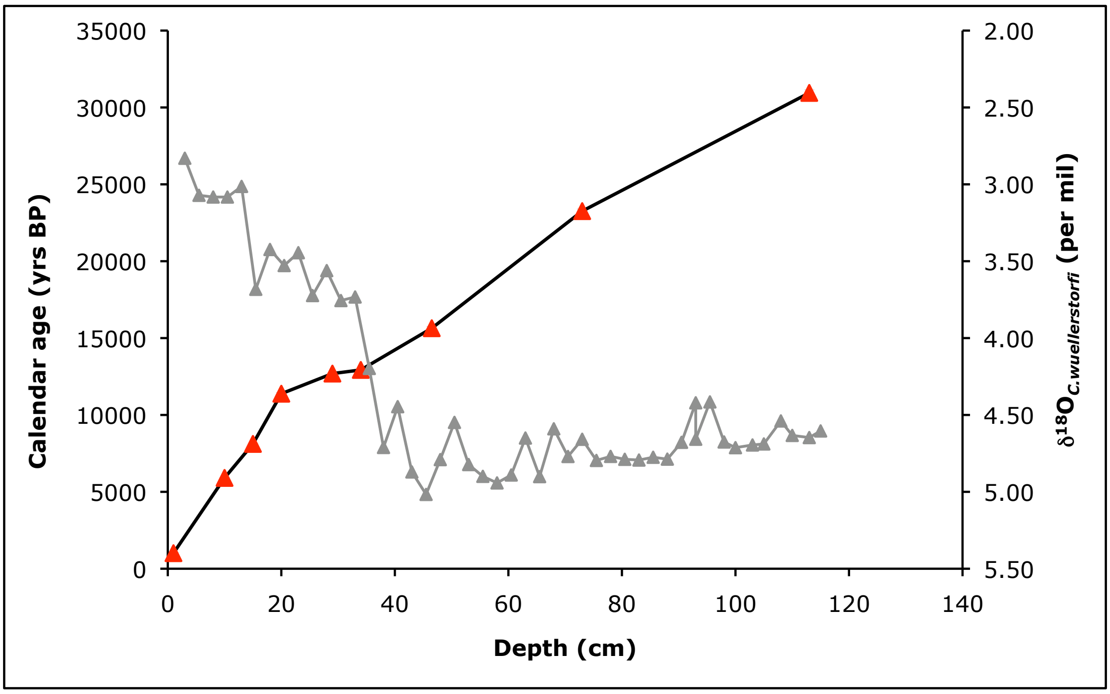

Figure 5.6: Age model for GeoB 2109. Red triangles denote calibrated radiocarbon ages.

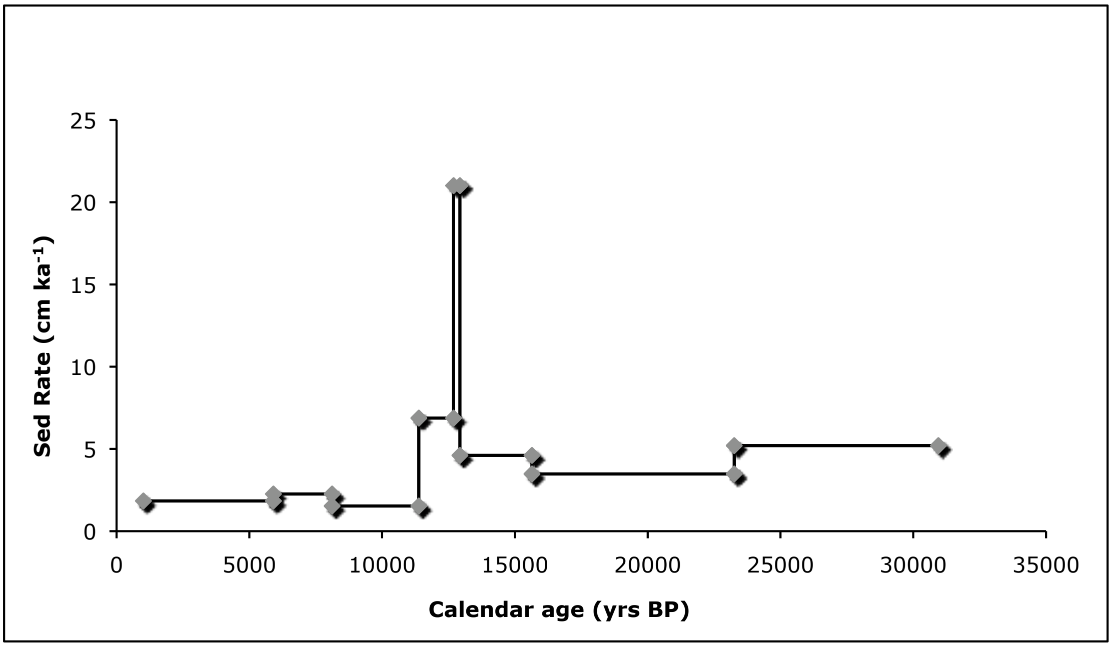

Figure 5.7: Sedimentation rate for GeoB 2109.

The offset in ages between *Globorotalia tumida* and *Globigerina ruber* was assessed by radiocarbon dating of both species in one Holocene sample and found to be ~1300 years at 15 cm depth in core (Table 5.3). An average of the two radiocarbon ages from the two species was used for this sample depth (41 cm) in the age model for core GeoB 2109 (Figure 5.6).

Sedimentation rates average 5 cm ka^{-1} between 30 – 15 ka and are stable throughout the Holocene at ~2 cm ka^{-1}. The peak in sedimentation rate at ~13 ka is unlikely to be real given the uncertainty in radiocarbon ages and the relatively small distance between the two samples at this point in the core. The average sedimentation rate for GeoB 2109 is ~4 cm ka^{-1}. For a sampling interval of 5 cm used for this core, this translates into average time sampling steps of ~1.25 ka, with an average sample integration time of 250 years.

5.5 GeoB 2112 age model

Due to increased carbonate dissolution at depths associated with core GeoB 2112 (4010 m), in common with other cores bathed by AABW, GeoB 2112 was found to have an insufficient mass of foraminifera (i.e. less than 10 μg) needed to produce radiocarbon ages in samples greater than 8 cm depth in core. Consequently, radiocarbon ages were determined from bulk sediments for samples beyond this depth in core (Table 5.4).

To assess the offset between foraminiferal carbonate and bulk sediment radiocarbon ages in GeoB 2112, samples containing both types of material were measured for radiocarbon ages at 3.5 and 7.9 cm depth in core. As stated in section 3.6, core GeoB 2112 was sampled at approximately 1 cm resolution. However, due to the fact that core GeoB 2112 had been previously heavily sampled, it was not possible to sample at exactly 1 cm intervals, resulting in irregular sample depths (appendix Table 7.7).

GeoB 2112 core depth (cm)	AMS lab number	Type of dating	Foramiferal Species	^{14}C age (yr)	Calendar Age (yr)
0.5	SUERC-30506	AMS ^{14}C on bulk sediment	-	4992 ± 35	5398 ± 58
2	SUERC-30499	AMS ^{14}C on carbonate	mixed species	5376 ± 37	5807 ± 63
3.5	SUERC-30500	AMS ^{14}C on carbonate	mixed species	6795 ± 37	7404 ± 33
3.5	SUERC-30507	AMS ^{14}C on bulk sediment	-	7043 ± 39	7585 ± 26
4.8	SUERC-23906	AMS ^{14}C on carbonate	*G. tumida*	6878 ± 35	7456 ± 26
7.9	SUERC-30504	AMS ^{14}C on carbonate	mixed species	9717 ± 38	10622 ± 51
7.9	SUERC-30518	AMS ^{14}C on bulk sediment	-	12205 ± 53	13724 ± 58
10.3	-	Correlation with 2109 Ba/Ca	-	-	16000
11.1	SUERC-30508	AMS ^{14}C on bulk sediment	-	17731 ± 93	20587 ± 125
12.7	SUERC-30509	AMS ^{14}C on bulk sediment	-	17182 ± 85	20035 ± 121
17.6	SUERC-30510	AMS ^{14}C on bulk sediment	-	18540 ± 98	21718 ± 187
20.6	SUERC-30511	AMS ^{14}C on bulk sediment	-	23344 ± 176	27637 ± 243
24.1	SUERC-30514	AMS ^{14}C on bulk sediment	-	26994 ± 275	31960 ± 331
26.7	SUERC-30515	AMS ^{14}C on bulk sediment	-	23990 ± 191	28366 ± 254

Table 5.4: Sample ages of GeoB 2112. Additional tie point (10.3 cm) is provided from correlation of dissolved Ba/Ca data with GeoB 2109.

The offset between foraminiferal carbonate and bulk sediment radiocarbon ages was found to be only 180 years at 3.5 cm depth but approximately 3100 years at 7.9 cm (Table 5.4). The greater offset between the different sample types at 7.9 cm can perhaps be explained by the fact that these samples date from the late deglacial when sea levels were sufficiently low enough to leave the continental shelf exposed. This material could have been exposed on the shelf for some time before being washed into waters bathing the core site. Sea level would have risen enough to flood the shelf by the late deglacial (Niemann 2003, see section 6.3.1) removing the source component of older shelf material in bulk sediment, accounting for the relatively low offset between bulk sediment and carbonate radiocarbon ages from 3.5 cm (at 7.5 ka).

The consistency of this offset further downcore can not be directly determined but it is reasonable to assume that bulk ages are maximum ages and the age model is constructed on that basis (Figure 5.9). Without further age constraints in the glacial it is recognized that the age model beyond the Holocene section of this core has a considerable uncertainty associated with it. An estimate for this uncertainty was calculated by taking an average of the difference between the age model and all bulk sediment radiocarbon ages between the tie point at 10.3 cm (discussed below) and the final bulk sediment radiocarbon age at 26.7 cm. This was found to be approximately 1500 years, and is shown on the age model for this core (Figure 5.9). Any interpretation of data based on this age model must therefore take this uncertainty into account, particularly when assessing possible paleoceanographic changes on millennial timescales (section 7.4.7).

To better constrain the age model for the deglacial section of this core, a further age tie point was derived from cross correlation of Ba/Ca ratios from bulk sediment solutions with the well dated core GeoB 2109 (Figure 5.8). Cross correlation of higher resolution XRF element intensity ratios was not possible because such data was not available for GeoB 2109 and because the shallower cores are geographically too remote to produce an accurate correlation with GeoB 2112. The additional tie point, produced from correlation of a mid-point in the slope of Ba/Ca in GeoB 2112 and GeoB 2109 (Figure 5.8), yields an age of approximately 16 ka at 10.3 cm.

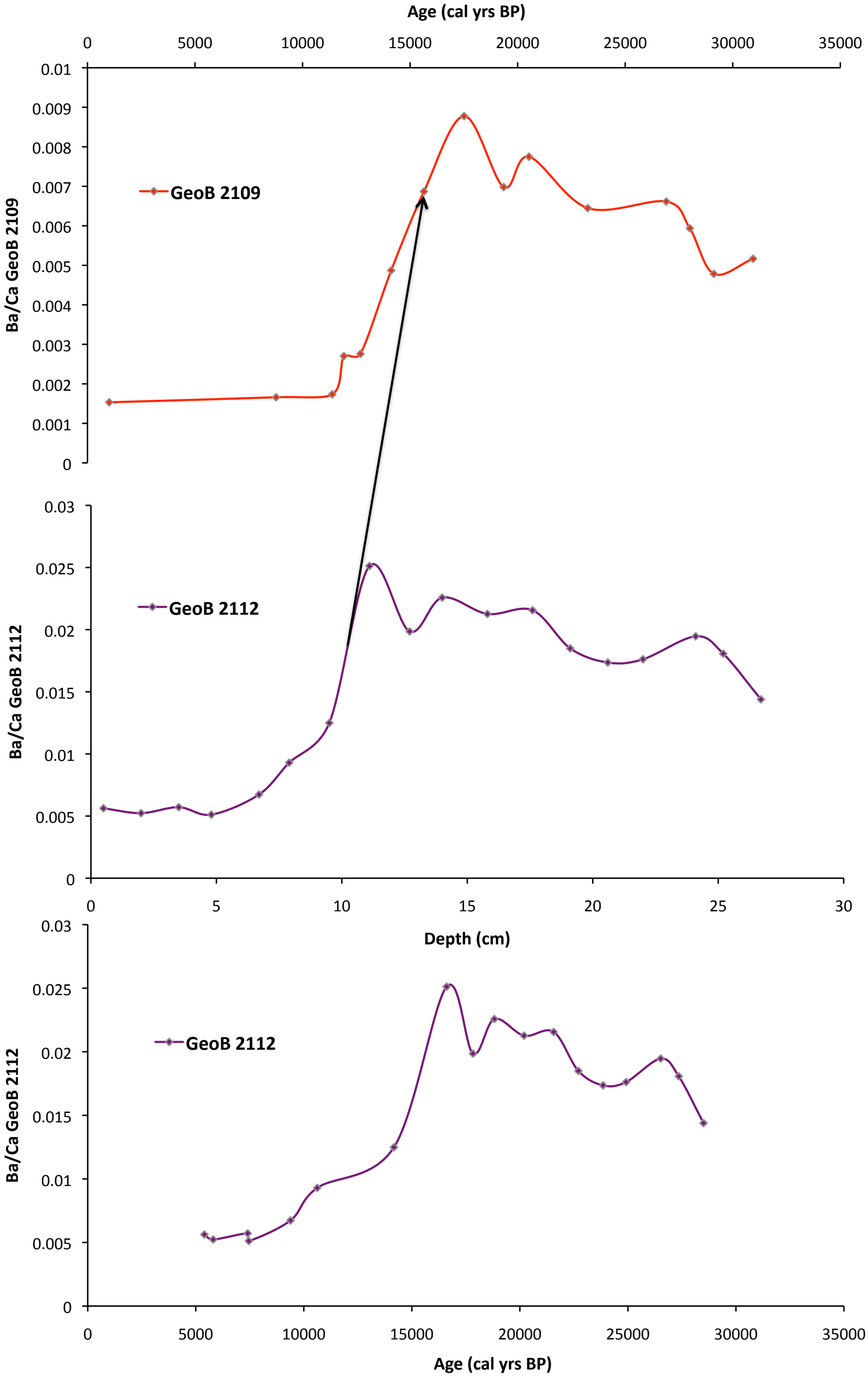

Figure 5.8: Correlation of Ba/Ca ratios in bulk sediment between GeoB 2112 and GeoB 2109 used to produce additional age tie point for GeoB 2112

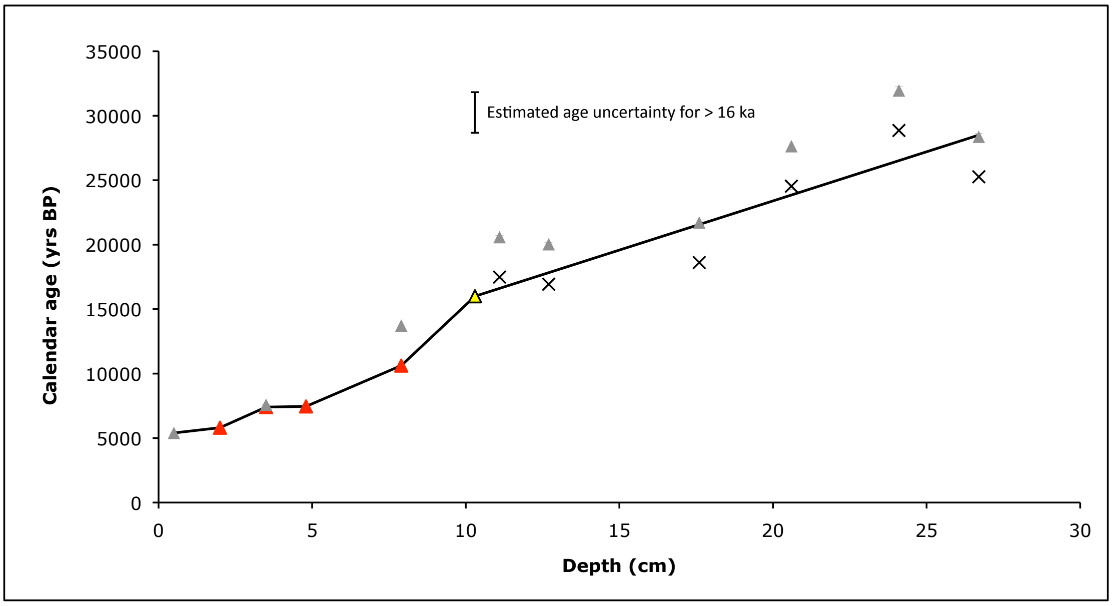

Figure 5.9: Age model for GeoB 2112. Combination of calibrated radiocarbon ages (red triangles), bulk sediment radiocarbon ages (grey triangles) and interpreted offset from bulk sediment radiocarbon ages (grey crosses). Additional tie point from cross correlation of Ba/Ca records with GeoB 2109 is denoted by the yellow triangle. The age error bar at 10.3 cm is shown to indicate the estimated uncertainty (± 1500 years, discussed above) of the age model between linear interpolation of points at 10.3 cm and 26.7 cm.

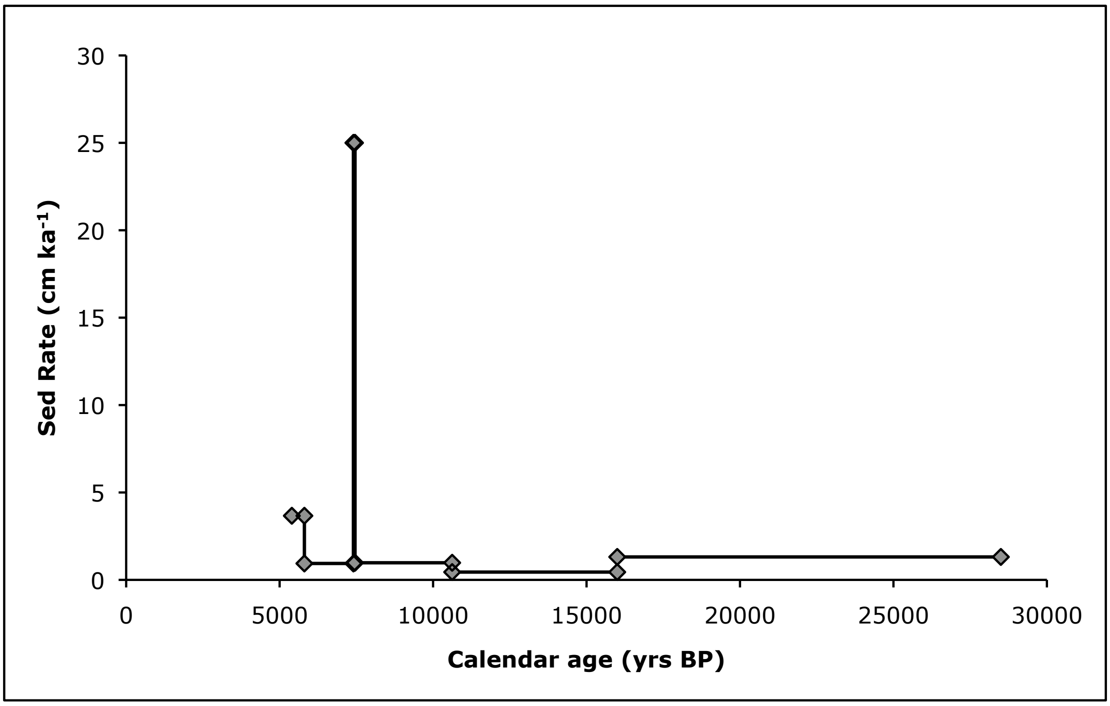

Figure 5.10: Sedimentation rate for GeoB 2112.

Sedimentation rates of 3.5 ka^{-1} are observed between 0.5 – 2 ka. For the remainder of the downcore record, average sedimentation rates are ~1 cm ka^{-1}. This excludes the peak in sedimentation rate at ~7.5 ka which is unlikely to be real given the uncertainty in radiocarbon ages and the relatively small distance between the two samples at this point in the core. For a sampling interval of approximately 1 cm used for this core, this translates into average time sampling steps of ~1 ka, with an average sample integration time of 1000 years.

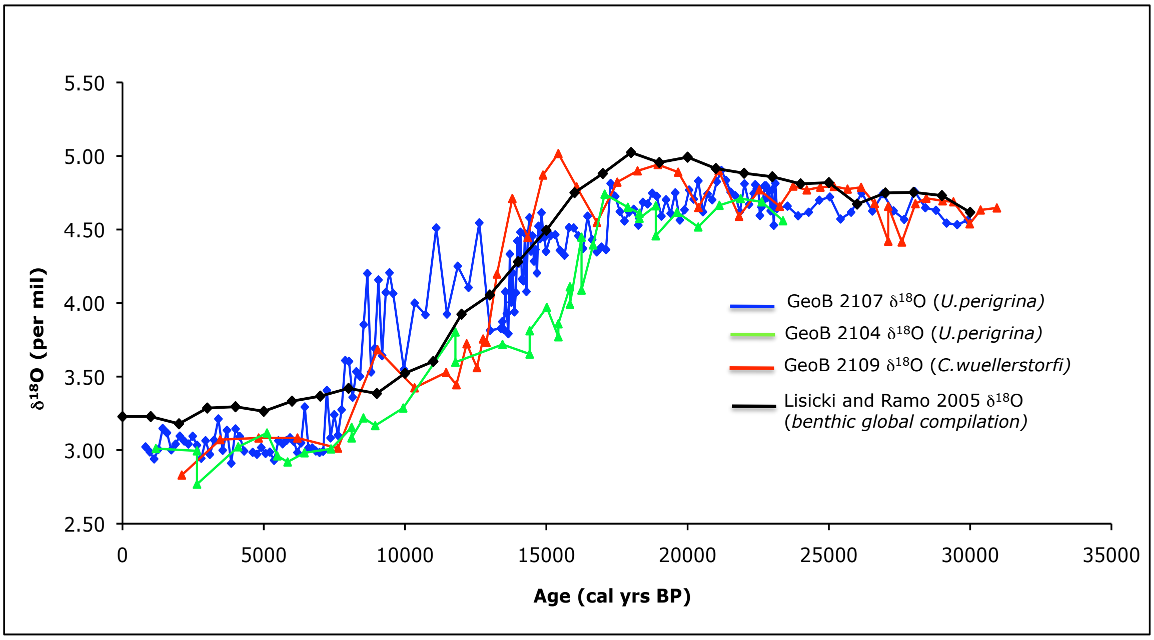

Figure 5.11: Summary age model plot showing benthic δ^{18}O against age for GeoB cores 2107, 2104 and 2109. A stack of 57 globally distributed benthic δ^{18}O records (Lisiecki and Raymo, 2005) is shown for comparison. Although δ^{18}O in the core does not perfectly agree during the whole deglaciation, this may reflect water mass differences, and is reassuring that the start and end of the deglaciation coincide in all cores.

Chapter 6: Particulate fluxes, Uranium and water mass proxy data

Introduction

Variations in local flux of settling particle (due, for instance, to changes in biological productivity) or the composition of settling particles, can strongly influence $^{231}Pa/^{230}Th$ scavenging processes and need to be assessed before any interpretation of $^{231}Pa/^{230}Th$ data in terms of changing ocean circulation can be made (as discussed in chapter 2). In addition to providing this essential backdrop for interpretation of $^{231}Pa/^{230}Th$, proxy assessment of past sediment composition and sedimentary processes offers useful information about the local environment of the Argentine Basin more generally. In this chapter, new results from the Argentine Basin are presented that constrain past particle flux, lithogenic flux, sediment focusing, opal flux, sediment composition, and productivity.

An additional complication in interpreting changes in sedimentary $^{231}Pa/^{230}Th$ ratios in terms of ocean circulation is the need to know the water mass that bathed the measured core in the past so that changes in water mass structure can be taken into account. This is particularly important for the four cores used in this study, which have a depth range of over 3km in the Argentine Basin, spanning several major water masses in the modern ocean today. In this chapter unpublished data for $\delta^{13}C$ and Nd isotopes from two collaborators is described and this data is used to assess the past distribution of water masses in the Argentine Basin.

Data for all cores are presented by proxy type before being discussed collectively in the second section of the chapter. Results are shown graphically here and listed in full in the appendix at the end of this thesis. Derivation of the age models for these cores is given in Chapter 4.

6.1 Sediment processes and composition

6.1.1 Preserved vertical particle flux

Vertical particle flux (*F*v) was calculated by normalization to excess ^{230}Th. This procedure is based on the assumption that the flux of scavenged ^{230}Th to the seafloor is equal to its production rate in the overlying water column (P_{230Th}^{water}). Hence,

$$F_v = \frac{P_{230Th}^{water}}{A_{230Th}^{scav}} = \frac{\beta z}{\left[{}^{230}Th\right]_0} = \frac{\left[{}^{234}U\right]_w \lambda_{230Th} z}{\left[{}^{230}Th\right]_0} \qquad (6.1)$$

where (A_{230Th}^{scav}) is the activity of ^{230}Th in sediments, β is the production rate constant of ^{230}Th in the water column, $\left[{}^{230}Th\right]_0$ is the measured activity of the decay and ingrowth corrected ^{230}Th in the sediment in d.p.m g^{-1}, $\left[{}^{234}U\right]_w$ is the activity of ^{234}U in seawater (2750 d.p.m m^{-3}), λ_{230Th} is the decay constant of ^{230}Th in yr^{-1} and z is the core depth in m, which gives the vertical particle flux (*F*v) in g m^{-2} yr^{-1} (Henderson and Anderson, 2003).

[^{230}Th] and [^{234}U] data GeoB cores 2107, 2104, 2109 and 2112 were assessed for samples spanning the last 30 kyr using the techniques outlined in Chapter 5.

The profiles of vertical particle flux in each of the four cores reveal an overall glacial to interglacial trend of decreasing particle fluxes. Vertical particle flux in GeoB cores 2107, 2104 and 2109 range from ~1.6-2.5 g cm^{-2} kyr^{-1} between 30 – 19 ka and from ~1.1-1.7 g cm^{-2} kyr^{-1} between 8-0 ka (Figure 6.1).

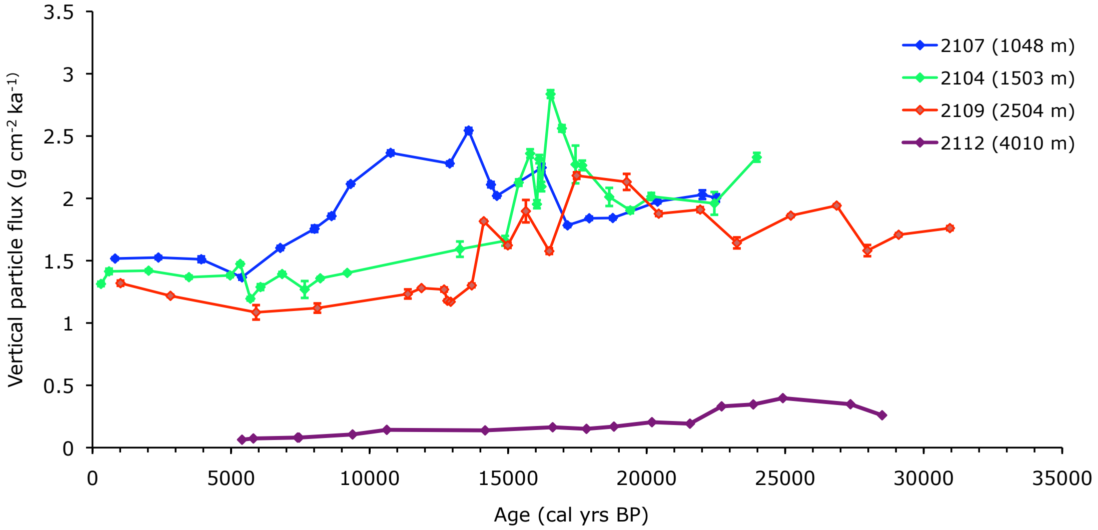

Figure 6.1: ^{230}Th normalized particle fluxes for GeoB 2107, GeoB 2104, GeoB 2109 and GeoB 2112. Errors are within symbol size where not shown.

GeoB 2104 and GeoB 2109 show similar vertical flux histories throughout the record. Both cores show a pronounced decrease in flux between glacial and Holocene times, with the decrease occurring between ~17.5 ka and 13.7 ka, with fluxes dropping from around 3 g cm^{-2} kyr^{-1} to 1.9 g cm^{-2} kyr^{-1} in GeoB 2104 and from 2.3 g cm^{-2} kyr^{-1} to 1.3 g cm^{-2} kyr^{-1} in GeoB 2109. The shallowest core, GeoB 2107, has significantly higher average vertical flux during the late deglacial and early Holocene (2.5 g cm^{-2} kyr^{-1}) in comparison to deeper cores GeoB 2104 (1.4 g cm^{-2} kyr^{-1}) and GeoB 2109 (1.1 g cm^{-2} kyr^{-1}).

GeoB 2112 shows significantly lower particle fluxes than any of the shallower GeoB cores, with fluxes below 0.5 g cm^{-2} kyr^{-1} throughout the ~28 kyr record. The mass flux to this core is highest in the late glacial with maximum values 0.4 g cm^{-2} kyr^{-1} at 26 ka. Flux values are observed to decrease across the deglacial to fluxes less than 0.1 g cm^{-2} kyr^{-1} throughout the Holocene.

6.1.2 Lithogenic flux

The method of ^{230}Th normalization allows calculation not only of the instantaneous sediment flux, but of the vertical rain rate of any sedimentary constituent (F_i) from its weight concentration in the sediment (f_i):

$$F_i = f_i F_v \tag{6.2}$$

This allows for calculation of lithogenic fluxes to the sediment.

Lithogenic fluxes in the study region are influenced by the many drainage basins and rivers of southeast Brazil, in particular the Rio Itajai, the mouth of which is just 270 km from the core site of GeoB 2107 (Heil, 2006). The proportion of terrigenous material in the sediments was inferred from the measured concentration of ^{232}Th, which is of lithogenic origin, assuming a ^{232}Th concentration of 13 ppm in lithogenic material (Rae, 2007). ^{232}Th data was measured using the techniques presented in Chapter 5.

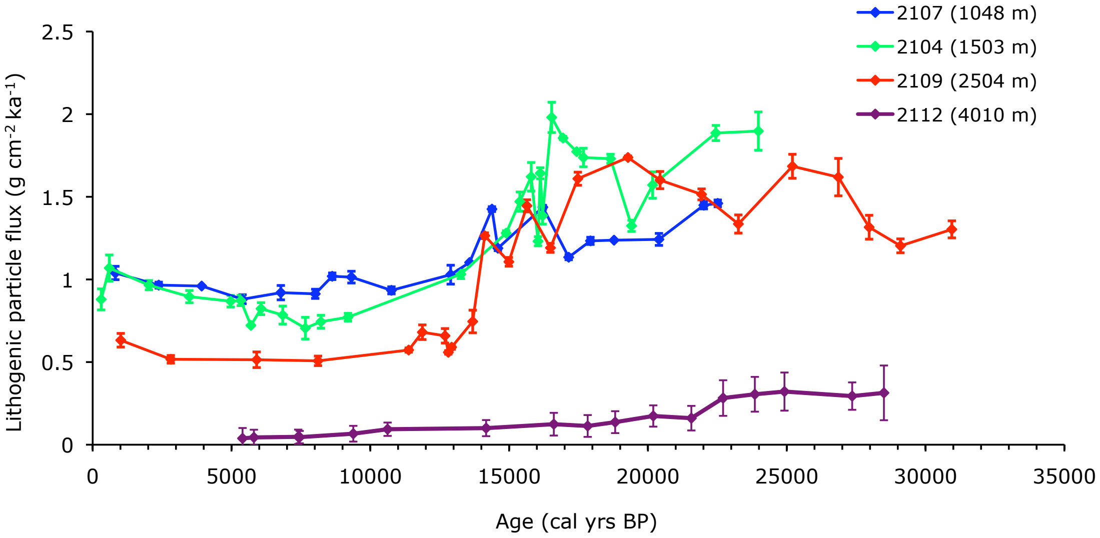

Figure 6.2: ^{230}Th normalized lithogenic fluxes for GeoB 2107, GeoB 2104, GeoB 2109 and GeoB 2112. Errors are within symbol size where not shown.

The lithogenic flux profiles for GeoB 2107, GeoB 2104 and GeoB 2109 all show a significant decrease between glacial and Holocene times with most of the decrease occurring between ~17.5 ka and ~13.5 ka. This step change is most pronounced in GeoB 2109 where values decrease from ~1.7 g cm^{-2} kyr^{-1} at 17.5 ka ~to 0.75 g cm^{-2} kyr^{-1} at 13.7 ka. Lithogenic fluxes are generally constant during the Holocene with fluxes ranging from 1.0-1.1 g cm^{-2} kyr^{-1}, 0.7-1.0 g cm^{-2} kyr^{-1} and 0.5-0.7 g cm^{-2} kyr^{-1} for GeoB 2107, GeoB 2104 and GeoB 2109 respectively. The lithogenic flux records for each core are relatively noisy during the deglacial and LGM and show little correlation between records. However, the range of lithogenic flux remains between 1.2 and 2 g cm^{-2} kyr^{-1} for all cores during this period.

The lithogenic flux profile for GeoB 2112 shows strong similarities with the preserved vertical particle flux, with values distinctly lower than in any of the shallower core records. Maximum lithogenic fluxes are observed in the glacial, averaging 0.3 g cm^{-2} kyr^{-1} between 23 and 30 ka, before decreasing continuously across the deglacial and Holocene to just 0.05 g cm^{-2} kyr^{-1} at 5 ka.

6.1.3 Sediment focusing

The sediment focusing factor (ψ) is used to reconstruct syndepositional sediment redistribution and also provides useful information about near bottom water flow at the core site. The focusing factor is calculated as the amount of decay-corrected ^{230}Th scavenged to the seafloor (A_{230Th}^{scav}) relative to ^{230}Th production in the overlying water column (P_{230Th}^{water}) during a time interval of sediment deposition for a specific core:

$$\psi = \frac{\int_{r_2}^{r_1} A_{230Th}^{scav} dr}{P_{230Th}^{water}} = \frac{\int_{r_2}^{r_1} \left[{}^{230}Th \right]_0 \rho_b dr}{\beta z (t_1 - t_2)} \qquad (6.3)$$

where $\left[{}^{230}Th \right]_0$ is the activity of the decay and ingrowth corrected ^{230}Th in the sediment in d.p.m g^{-1}, r is the depth of the core in m, t is the age of the sediment horizon in yrs, ρ is the density of the sediment in g cm^{-3}, β is the production rate of ^{230}Th in the water column between two dated horizons t_1 and t_2 and z is the water depth of the core in meters (Suman and Bacon, 1989).

For a specific core section, a value of ψ=1 indicates that the sediment has not been affected by syndepositional redistribution, ψ>1 indicates that more ^{230}Th has accumulated in the sediment than is produced in the overlying water column (and therefore presumably that sediment has been focused to the site) and ψ<1 indicates winnowing of sediment from that location. This focusing proxy relies on the assumption that all ^{230}Th formed in the water column is removed to the seafloor with no lateral advection of ^{230}Th in the water column. This assumption has been called into question by some workers (e.g. Lyle et al. 2005) but from chemical observation and modeling appears to be reasonable (e.g. Henderson et al. 1999).

Sediment focusing factors for the four cores of this study are calculated from the ^{230}Th data presented above, and from the age models presented in Chapter 5.

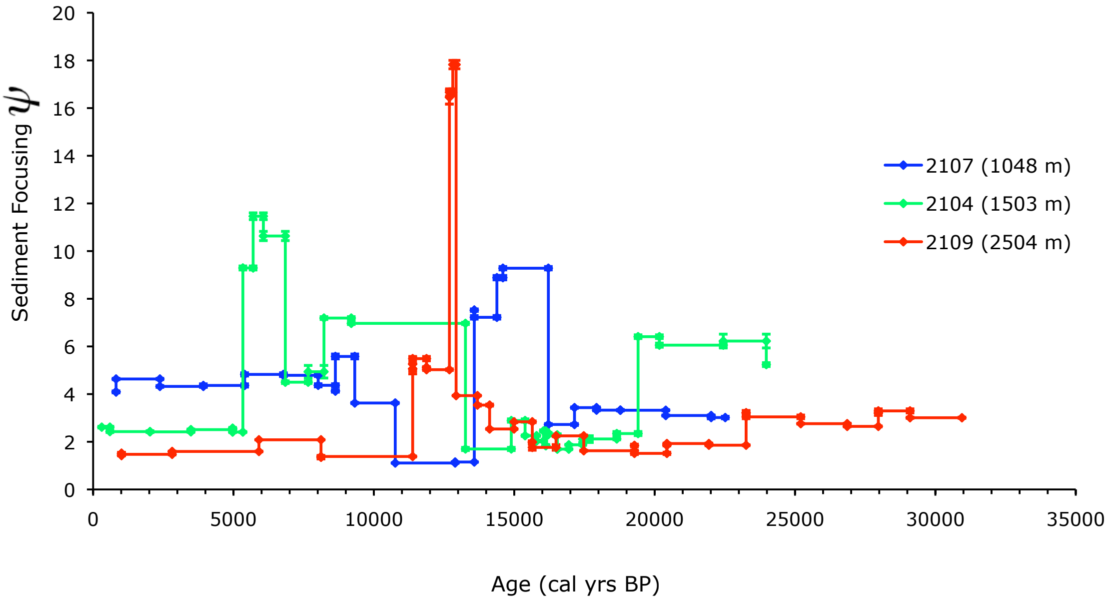

Figure 6.3: Sediment focusing factors for GeoB 2107, GeoB 2104 and GeoB 2109. Errors are within symbol size where not shown.

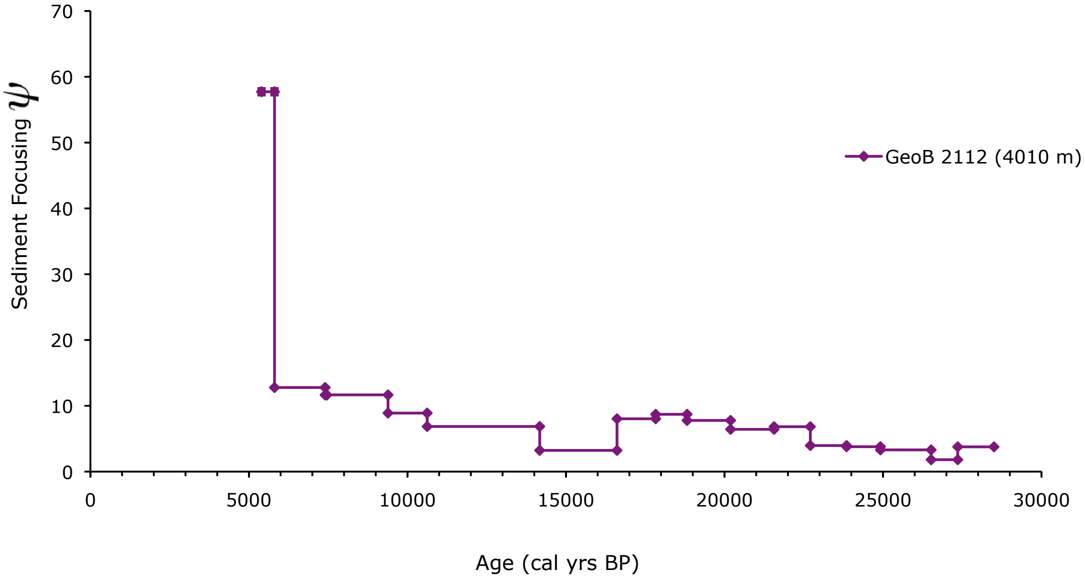

Figure 6.4: Sediment focusing factors for GeoB 2112. Errors are within symbol size where not shown.

The results obtained show distinctly different histories of sediment focusing for all cores used in this study. GeoB 2107 data shows sediment focusing factors to be stable at ψ=~3 between 23-16 ka before peaking at ψ=8 between 16-13.5 ka. Focusing factors in GeoB 2107 then decrease to ψ=~1 between 13.5 ka and 10.5 ka before increasing to ψ=~5 at ~9 ka and are stable at ψ=~4 for the remainder of the Holocene. Several peaks in ψ are seen in the GeoB 2104 record, most noticeably between 24-19.5 ka (ψ=6), 13-8 ka (ψ=7) and 7-5 ka (ψ=~10). GeoB 2109 shows ψ values to increase during the deglacial, with ψ=~1.5 at ~20 ka increasing to ψ=~4 at 13 ka. There is a prominent, isolated peak of ψ=~18 between 12.9-12.8 ka. However, this peak value reduces to ψ=~10 when calculating the focusing factor using the extremes of the age errors between two samples at this depth in core. Focusing factors in GeoB 2109 are observed to be between ψ=2 and ψ=1 throughout the Holocene.

GeoB 2112 shows a gradual increase in focusing factor from ψ=~3 at ~27 ka to ψ=~8 at 16.5 ka before returning to ψ=~3 between 16.5 ka and 14 ka. Focusing factor in GeoB 2112 increases gradually from ψ=~3 at 14 ka to ψ=~13 at ~6 ka. A pronounced change in focusing factor occurs around 6 ka when *ψ* increases from ~13 to ~60. Such large values for ψ at 6 ~ka are most likely due to two samples having similar radiocarbon ages (5.4 and 5.8 ka, Table 5.4) resulting in artificially high sedimentation rates between these samples and consequently high focusing factors.

6.1.4 Opal flux

Opal concentrations in the four GeoB cores were measured using the techniques described in chapter 5 (section 5.11). The data indicates a range of relatively low opal concentrations of 2-4.5 % of the total sediment mass (Figure 6.5) with no clear correlation between any of the core records.

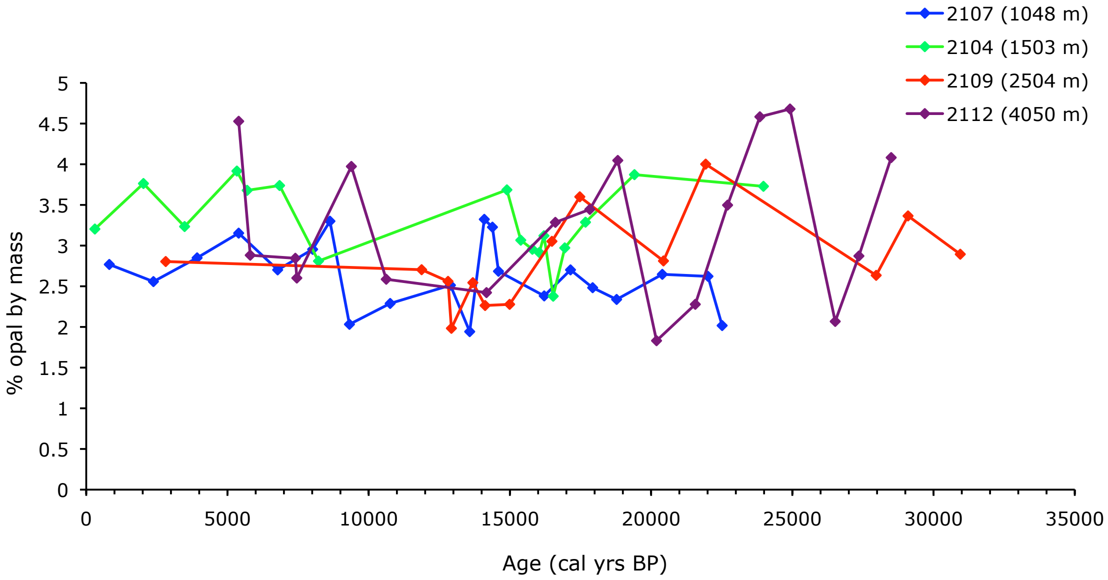

Figure 6.5: Opal concentrations for GeoB 2107, GeoB 2104, GeoB 2109 and GeoB 2112.

This concentration data can be converted to an opal flux by ^{230}Th normalization as in the previous section (Figure 6.6). This produces opal flux profiles with less scatter than opal concentrations The flux of opal in GeoB 2107 show little variation, with values close to an average of 0.55 mg cm^{-2} kyr^{-1} throughout the 30 kyr record.

Cores GeoB 2104 and GeoB 2109 both display highest opal fluxes in the glacial and early deglacial, averaging 80 mg cm^{-2} kyr^{-1} in GeoB 2104 and 70 mg cm^{-2} kyr^{-1} in GeoB 2109 during the LGM. Both cores show a rapid decrease in opal flux across the deglacial between ~17.5 and 13.5 ka before reaching minimum average opal fluxes during the Holocene of 50 mg cm^{-2} kyr^{-1} in GeoB 2104 and 35 mg cm^{-2} kyr^{-1} in GeoB 2109. GeoB 2112 shows comparatively low opal fluxes, averaging 10 mg cm^{-2} kyr^{-1} during the LGM, reaching a maximum of 20 mg cm^{-2} kyr^{-1} at 17 ka before decreasing to 5 mg cm^{-2} kyr^{-1} during the Holocene.

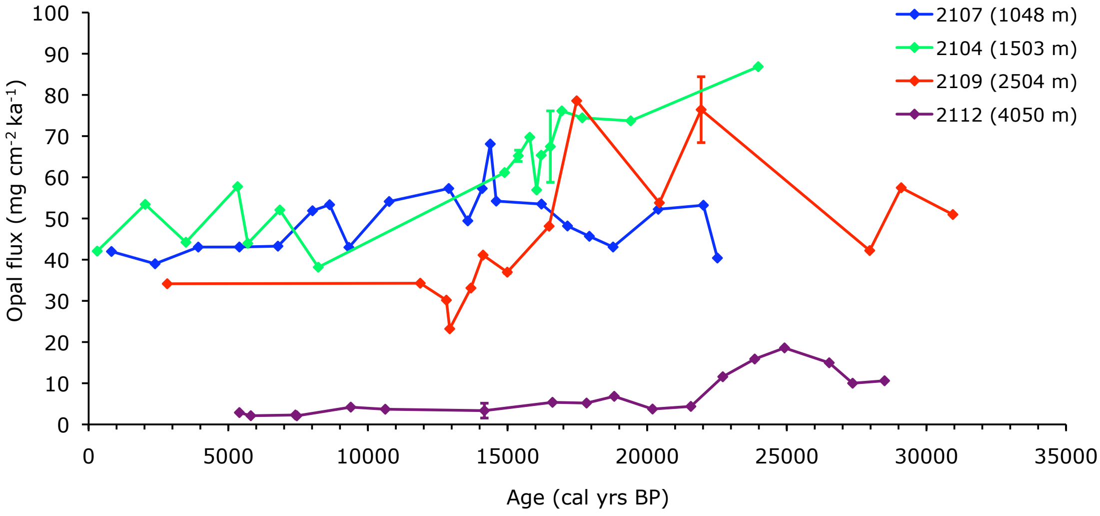

Figure 6.6: ^{230}Th normalized opal fluxes for GeoB 2107, GeoB 2104, GeoB 2109 and GeoB 2112. Errors for the method were calculated on a selection of samples and shown above.

6.1.5 Authigenic Uranium

Authigenic U is formed in sediments which are experiencing reducing conditions due to a depletion of oxygen in the overlying water or to a high flux of organic carbon from the overlying water column (Langmuir, 1978). Anoxic and suboxic conditions are typically found in ocean basins with restricted deep-water circulation and in near shore regions associated with vigorous upwelling and intense biological productivity (Cochran, 1992).

Authigenic uranium can be calculated by subtracting detrital uranium from the total uranium measured in each sample as follows:

$$(^{238}\mathrm{U})_{auth} = (^{238}\mathrm{U})_{meas} - (^{238}\mathrm{U})_{\mathrm{det}} = (^{238}\mathrm{U})_{meas} - (^{232}\mathrm{Th})_{meas}\left(\frac{(^{238}\mathrm{U})}{(^{232}\mathrm{Th})}\right)_{\mathrm{det}} \quad (6.4)$$

where (…) denotes activity and the subscripts

auth = authigenic (insitu ingrowth from U)

meas = measured (total)

det = detrital (continental component)

In this approach, the activity of $^{238}\mathrm{U}_{\mathrm{det}}$ is estimated from the $^{232}\mathrm{Th}_{\mathrm{meas}}$ which is assumed to be entirely of lithogenic origin (Brewer et al, 1980).

U and Th data was measured on the four cores using techniques described in chapter 4 (section 4.6).

The detrital (^{238}U/^{232}Th) ratio was determined for these cores following the approach of Thomas et al. (2007) by plotting (^{238}U/^{232}Th) against δ^{234}U for all cores. The detrital (^{238}U/^{232}Th) is selected as the average of the lowest, and therefore least authigenic, δ^{234}U values. This approach assumes that detrital material has a δ^{234}U value <1 due to alpha-recoil during weathering, while authigenic U has a δ^{234}U initially = 146 because it is derived from seawater with this value.

There is a clear relationship between (^{238}U/^{232}Th) and δ^{234}U in these Argentine cores (Fig 6.7) supporting the use of this approach, and indicating a detrital value of 0.50 for the Argentine Basin. This value lies between values typically used for the Atlantic (0.6) and Southern Ocean (0.4) as shown in Figure 6.7.

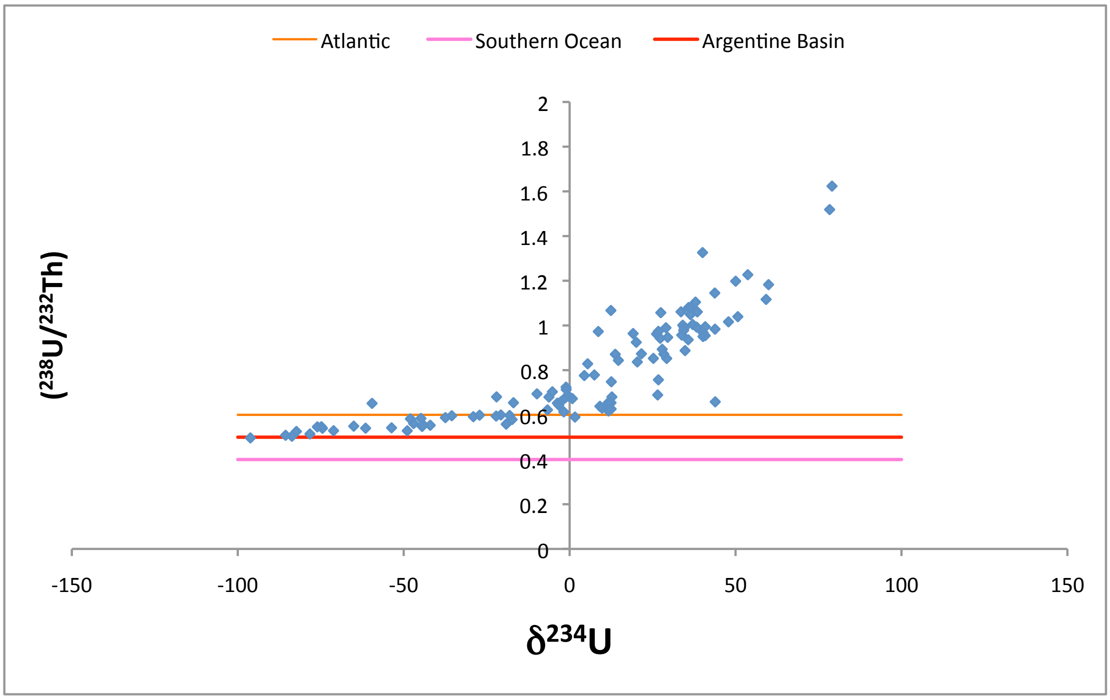

Figure 6.7: Plots of (^{238}U/^{232}Th) against δ^{234}U for cores GeoB 2107, GeoB 2104, GeoB 2109 and GeoB 2112. The lowest δ^{234}U values are typically found near the core top where samples have little authigenic uranium (which has a δ^{234}U of +146 ‰) and retain a low δ^{234}U due to ^{234}U loss from small detrital particles. The red horizontal line represents the detrital (^{238}U/^{232}Th) value selected for the Argentine Basin. The (^{238}U/^{232}Th) values typically used for the Atlantic (0.6) and the Southern Ocean (0.4) are represented by the orange and pink horizontal lines respectively.

Authigenic U concentrations in GeoB 2107 (Figure 6.8) show little variation, ranging between 1.5 ppm and 0.6 ppm from the LGM to 5 ka before decreasing to a minimum of 0.5 ppm near core top. In contrast GeoB 2104 displays significantly more variation in authigenic U concentrations with values increasing gradually from 1.1 ppm at 24 ka to 2.1 ppm at 15.5 ka before increasing rapidly to a peak of 3.1 ppm at 13.3 ka, remaining above 2 ppm until early Holocene. Concentrations steadily decrease in the Holocene towards a minimum value of 0.5 ppm at core top, with an isolated peak of 1.8 ppm at 5.7 ka.

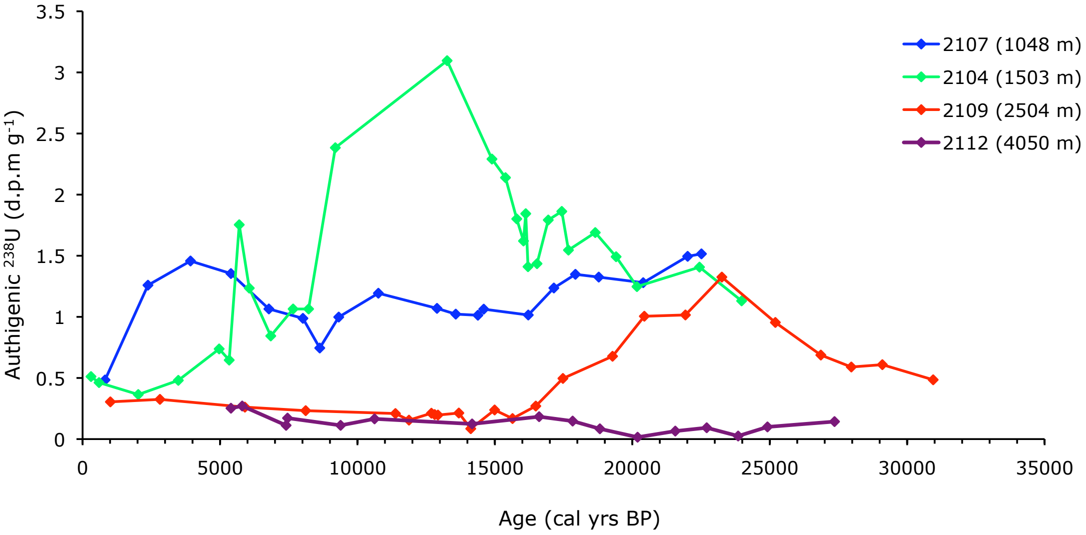

Figure 6.8: Authigenic uranium profiles for cores GeoB 2107, GeoB 2104, GeoB 2109 and GeoB 2112. Errors are within symbol size where not shown.

Authigenic U concentrations in GeoB 2109 increase from 0.5 ppm at 31 ka BP to a maximum of 1.4 ppm centered at 23 ka, with values decreasing to relatively low authigenic U concentrations between 0.2-0.3 ppm throughout the late deglacial and Holocene, concentrations lower than those observed in GeoB 2104 and GeoB 2107 at any time. Concentrations of authigenic U are lowest for core GeoB 2112, with values less than 0.3 ppm observed for the entire downcore record.

6.1.6. Total particulate trace metal ratios

Ratios of trace elements such as Ba/Ca in dissolved sediment solutions can be useful for confirming changes in productivity.

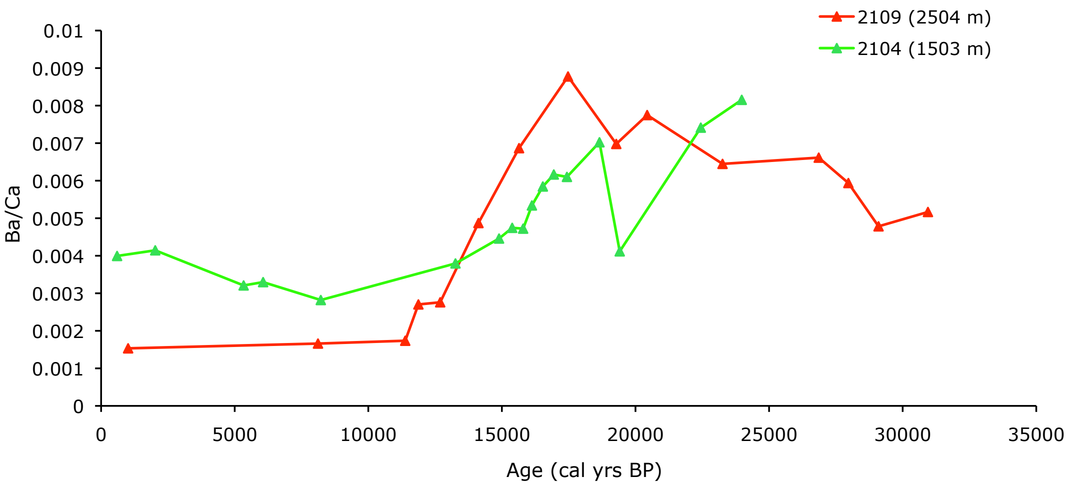

Figure 6.9: Comparison of dissolved Ba/Ca ratios in GeoB 2104 and GeoB 2109.

Dissolved Ba/Ca ratios show a rapid decrease from 0.009 to 0.003 between ~17.5 and ~12.5 ka in GeoB 2109 and from 0.007 to 0.0045 between 18.5 and 15 ka in GeoB 2104. GeoB 2104 Ba/Ca ratios increase gradually during the Holocene from 0.003 to 0.004 between 8 ka and 0.5 ka where as the Ba/Ca ratio appears to be relatively constant during the Holocene for GeoB 2109, though data resolution is too low for detailed comparison.

6.1.7 XRF element intensities

Fe (as well as Ti and K) derives from the weathering of humid tropical soils and therefore represents the terrestrial (siliclastic) fraction of sediment cores on the Brazilian margin (Arz et al., 1998). In contrast, Ca (as well as Sr) mainly occurs in biogenic carbonates such as foraminiferal shells in these cores. The absence of significant Ca in the catchment area of the Rio Itajei (Schobbenhaus et al., 1995) means that the terrestrial fraction does not contain significant amounts of Ca. As Fe represents the terrestrial and Ca the marine source material, the Fe/Ca ratio is suitable for analyzing the ratio of terrestrial versus marine sediment input. Furthermore, as the XRF intensities of Fe and Ca are an order of magnitude higher than those of the other analyzed elements, Fe and Ca XRF intensities allow the most reliable analysis of changes in sediment composition for the cores used in this study.

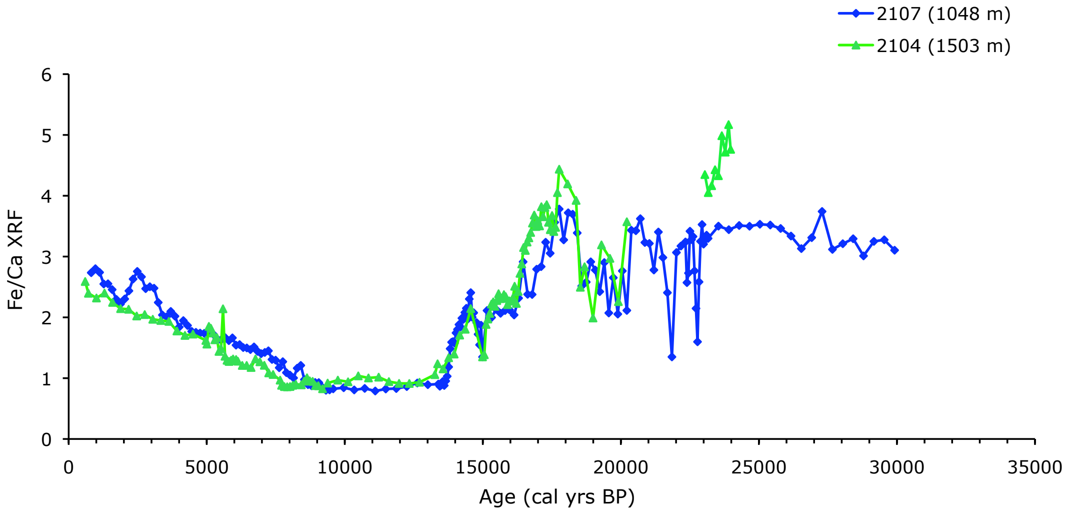

Figure 6.10: XRF Fe/Ca records from cores GeoB 2107 and GeoB 2104.

XRF Fe/Ca ratios in GeoB 2107 show little variability between 30 ka and 23 ka, ranging from ~3.2-3.7 (Figure 6.10). Maximum Fe/Ca ratios of ~5 are observed in GeoB 2104 between 24-23 ka. Fe/Ca data is unavailable for GeoB 2104 between 23-20 ka, when low Fe/Ca values of ~1.5 are observed in GeoB 2107 at ~22.5 ka and 21.5 ka. From ~20 ka to core top, Fe/Ca ratios are almost identical between these two cores. Ratios decrease rapidly in both cores at ~17.5 ka from 4.4 in GeoB 2104 and ~4.0 in GeoB 2107 to minimum values of 0.9 in both cores at 14 ka. From 14 ka to

8.3 ka Fe/Ca ratios remain at 0.9 before increasing continuously to ~2.7 at core top of both GeoB 2104 and GeoB 2107.

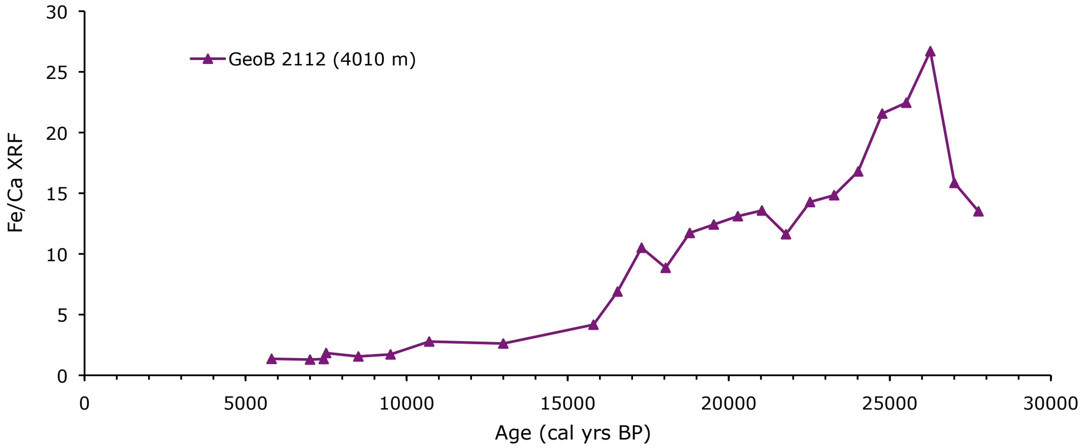

Figure 6.11: XRF Fe/Ca records from cores GeoB 2112.

GeoB 2112 shows higher Fe/Ca values in the glacial than in any of the shallower cores, presumably due to dissolution of carbonate at greater depths. A prominent peak is observed at 26.5 ka with Fe/Ca values decreasing rapidly across the deglacial and into the Holocene.

6.2 Proxies for changes in water mass structure

Two proxies are used to assess the past depth distribution of water masses in the Argentine basin - carbon and neodymium isotopes. An introduction to the use of these proxies is presented in chapter 2, section 2.7.

6.2.1 Stable Carbon Isotopes

Carbon stable isotope data was provided by Cristiano Chiessi at the MARUM Research Institute for Marine Sciences, University of Bremen. Analysis was performed on benthic foraminifera species *Uvigerina perigrina* for cores GeoB 2107 and GeoB 2104, on *Cibicidoides spp.* for GeoB 2107 (measured by Laurence Vidal, CEREGE) and on *Cibicidoides wuellerstorfi* for GeoB 2109 (Figure 6.9). Measurements were made every 5 cm in each core except for GeoB 2107 where *U.peregrina* was measured every cm. No $\delta^{13}C$ measurements were made on core GeoB 2112 (4000m) due to the absence of preserved carbonate at this depth.

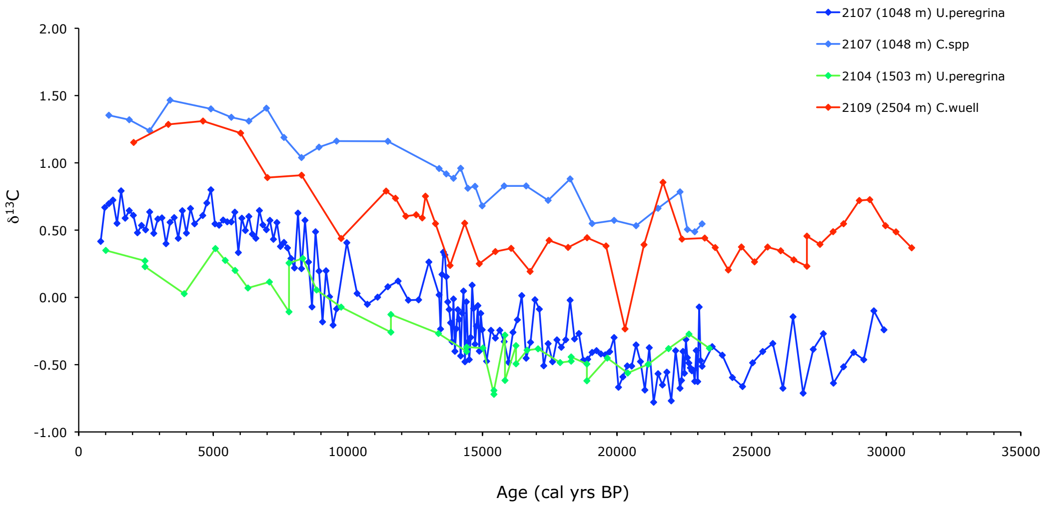

Figure 6.12: Benthic $\delta^{13}C$ records from cores GeoB 2107, GeoB 2104 and GeoB 2109. Derivation of the age models for these cores is given in Chapter 4.

The $\delta^{13}C$ profiles in all cores show a general trend of increasing $\delta^{13}C$ across the deglacial, with minimum $\delta^{13}C$ values observed during the late glacial and maximum $\delta^{13}C$ values in the Holocene (Figure 6.12). $\delta^{13}C$ values for *U. perigrina* from GeoB 2104 and GeoB 2107 show a similar range of $\delta^{13}C$ values which are approximately

1‰ less than the *C. spp.* $\delta^{13}C$ record for GeoB 2107 and the *C.wuellerstorfi* record for GeoB 2109.

$\delta^{13}C$ values in the relatively high resolution record of GeoB 2107 *U.peregrina* display a rapid increase between 14.5 ka and 13.6 ka of ~0.9 ‰. This is followed by a more gradual decrease from 13.6 ka to 9.5 ka (of 0.3 ‰ to 0.2 ‰) before another rapid increase between 9.5 ka and 8.1 ka of ~0.8 ‰. The range of $\delta^{13}C$ values from *C. Spp.* in GeoB 2107 ($\delta^{13}C$ difference between LGM and Holocene = ~0.9 ‰) is noticeably less than seen in the *U.peregrina* record for the same core ($\delta^{13}C$ difference between LGM and Holocene = ~1.6 ‰). $\delta^{13}C$ values for the *U.peregrina* profile of GeoB 2104 are on average 0.2 ‰ lower than GeoB 2107 during the deglacial and 0.4 ‰ lower during the Holocene. A significant increase in $\delta^{13}C$ values in GeoB 2109 occurs at 13.5 ka where values increase from 0.2 ‰ to maximum values of 1.3 ‰ at 7 ka.

6.2.2 Neodymium isotopes

Nd analysis was performed by chemical leaching of Fe-Mn oxyhydroxides in sediments from all cores by Paul Carter at Bristol University using analytical methods briefly summarized in section 4.14.

εNd values (Figure 6.13) range from -3.7 ‰ to -7.9 ‰ for GeoB 2107, -5.9 ‰ to -7.4 ‰ for GeoB 2104, -6.4 ‰ to -8.4 ‰ for GeoB 2109 and -3.8 ‰ to -6.7 ‰ for the deepest core GeoB 2112. Cores GeoB 2107 and GeoB 2104 show excursions to more radiogenic values down core, and all cores except GeoB 2112 are more radiogenic at the LGM and during the deglacial than modern values.

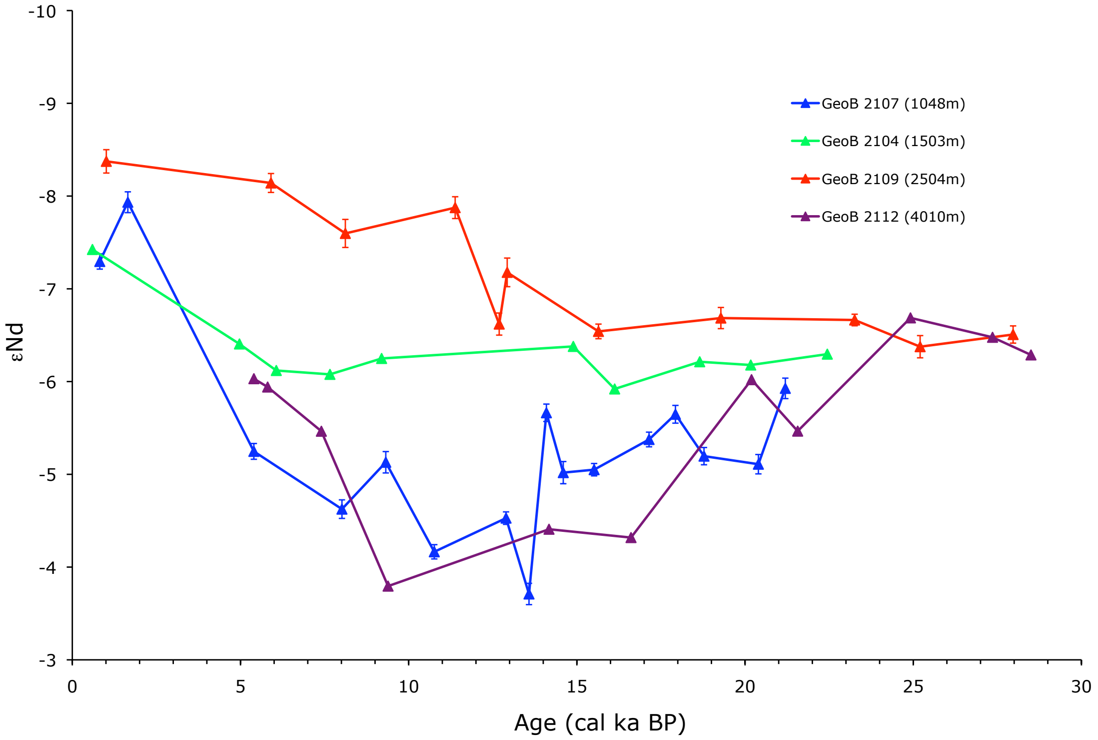

Figure 6.13: εNd records from GeoB cores 2107, 2104, 2109 and 2112.

There are strong similarities observed between GeoB 2107 and GeoB 2112 with both cores showing a broad trough in εNd between 14 ka and 8 ka before a decrease to minimum εNd values in the late Holocene. GeoB 2109 shows stable εNd values during the deglacial around -6.5 ‰ decreasing to -8 ‰ between ~15.5 ka and 11 ka and remaining below -7.5 ‰ throughout the Holocene. GeoB 2104 shows the least variability in Nd of all cores, with values relatively constant at around εNd = -6 between 22 ka and 6 ka, decreasing to -7.5 ‰ at core top.

6.3 Discussion

6.3.1. Variations in particulate fluxes

According to Arz et al. (1999), chemical scavenging in the coastal ocean is likely to have increased at the LGM, with reduced sea levels shifting sediment deposition to the shelf break and increasing sediment fluxes at intermediate depths. This view is supported by the lithogenic flux data, which show maximum lithogenic fluxes in the glacial when sea level was low and minimum lithogenic fluxes during the Holocene. More specifically, peak lithogenic fluxes are observed between ~17.5 ka and 20 ka, in GeoB 2104 and GeoB 2109. These flux peaks are just after or approaching the end of the LGM when sea level would be lowest and shelf exposure at a maximum.

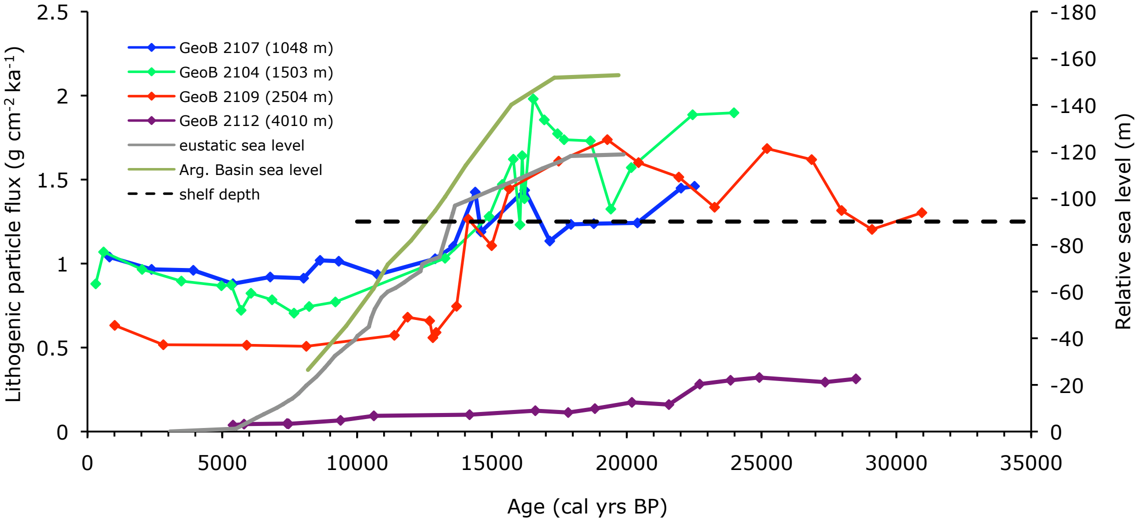

***Figure 6.14*:** Changes in lithogenic flux in GeoB 2107, GeoB 2104 and GeoB 2109 relative to changes in southeast Argentina sea level (Guilderson et al., 2000) and eustatic sea level (Fairbanks and Bard 1990). A horizontal dashed line is used to indicate the approximate depth of the continental shelf between 23°S and 28°S (Heil, 2006).

As sea level begins to rise in response to the melting of ice sheets during the deglaciation, lithogenic fluxes continuously decrease until approximately ~13.5 ka.

This time coincides with the flooding of the Brazilian continental shelf (Niemann 2003, Figure 6.14). Following flooding of the shelf, lithogenic flux is observed to level off before showing a moderate increase from ~8 ka in intermediate depth core GeoB 2104 and from 5.5 ka in GeoB 2107. This may be related to increased runoff and river discharge as a result of a wetter climate during the Holocene (Heil, 2006).

XRF Fe/Ca intensities, which, at shallow core depths, reflect terrestrial inputs to the oceans (see section 6.17), show similar XRF Fe/Ca profiles (Figure 6.10) to lithogenic fluxes in intermediate depth cores GeoB 2104 and GeoB 2107 closest to the coast. In both of these cores Fe/Ca is observed to peak at 18 ka and decrease rapidly until approximately 13.4 ka, consistent with the timing of lithogenic flux decrease in the deglacial.

Lithogenic fluxes in GeoB 2112 are noticeably lower and show less correlation to changes in sea level which is expected given that this core is located significantly further from the coast relative to the shallower cores and should therefore be less sensitive to changes in inputs of coastal material. The pronounced maximum in lithogenic flux in the late glacial record of GeoB 2112 may be related to increased levels of dust transport from Patagonia to Antarctica during the last glacial (Sugden et al., 2009).

The observed changes in lithogenic flux (and XRF Fe/Ca intensities) correlate strongly with changes in vertical particle flux in cores GeoB 2104 ($r^2 = 0.88$, Figure 6.15), GeoB 2109 ($r^2 = 0.94$) and GeoB 2112 ($r^2 = 0.94$). There are some differences between lithogenic and particle flux records in GeoB 2107 ($r^2 = 0.16$), most notably during the late deglacial where particle fluxes are observed to increase (to a maximum of ~2.5 g cm^{-2} kyr^{-1} at ~13.5 ka) despite a decrease in lithogenic fluxes at this time (from 1.55 g cm^{-2} kyr^{-1} at 14.3 ka to 1.2 g cm^{-2} kyr^{-1} at 13.5 ka), suggesting that another factor (e.g. changing biogenic fluxes) may be influencing particle fluxes at the GeoB 2107 core site during this time.

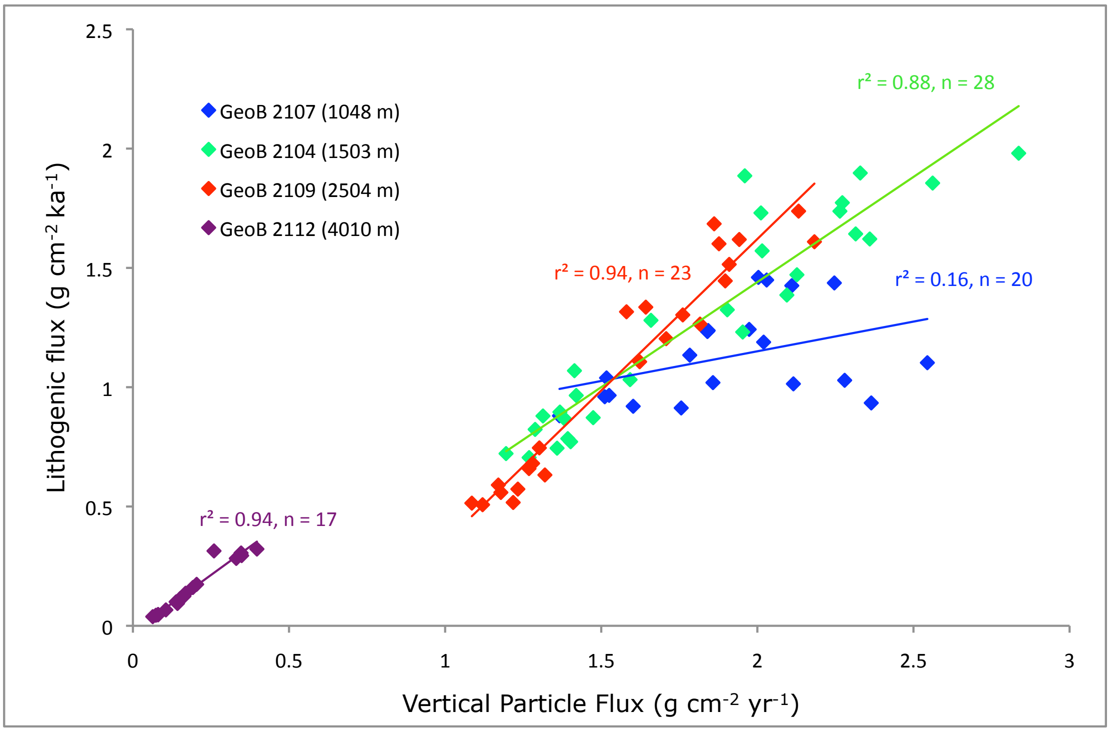

Figure 6.15: Correlation plots between lithogenic and vertical particle flux for cores GeoB 2107, 2104, 2109 and 2112, with r^2 values given to two significant figures for each core.

The overall strong correlation between lithogenic fluxes and preserved vertical particle flux records of GeoB cores in the this study (average $r^2 = 0.73$) suggest that changes in particle flux are mainly driven by terrestrial inputs over these GeoB core sites, related to changes in sea level. This is not unexpected given the proximity of these cores to the South American continent, with lithogenic and particle fluxes generally decreasing with depth (and therefore distance from the coast) when comparing records from all four cores.

6.3.2. Variations in biological productivity

The flux of biogenic particles to the sediment is not by itself a sufficient indicator of past changes in productivity due to the fact that dissolution in the water column and particularly at the sediment-water interface can dramatically modify the biogenic flux signal. For this reason, measurements of authigenic U and Ba/Ca are discussed in addition to opal flux data to assess past changes in productivity in the Argentine Basin.

Peak opal flux values are observed in the glacial for GeoB 2104 (at ~24 ka), GeoB 2109 (at 22 ka) and GeoB 2112 (at 25 ka, Figure 6.6). This data suggests productivity was greater along the Brazilian margin in the late glacial. A northward shift of the Southern Ocean opal belt in the glacial of approximately 5° (Gersonde et al., 2003) may have increased productivity in the southern limb of the subtropical gyre (~40°S) but could not have led to a direct increase in opal flux levels at cores as far north as the latitude of the four study cores between 27°S and 29°S.

Opal flux records correlate well with particle flux records in all GeoB cores with the exception of GeoB 2107 (Figure 6.16), which shows relatively constant opal flux downcore (Figure 6.6). The general decrease in opal flux with core depth (Figure 6.6) is likely related to lower opal preservation with decreasing sedimentation rates (Lippold et al., 2009), with GeoB 2112 having significantly the lowest opal flux as well as the lowest sedimentation rate of all four cores used in this study (see chapter 5).

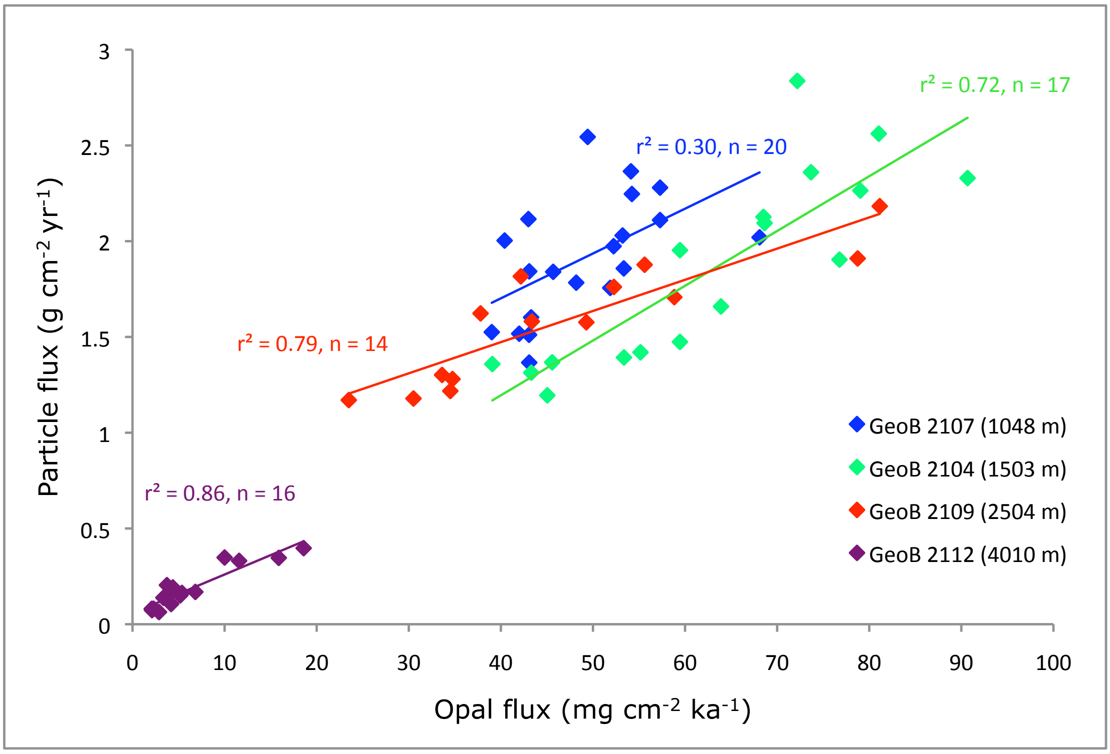

Figure 6.16: Correlation plots between opal flux and particle flux for cores GeoB 2107, GeoB 2104, GeoB 2109 and GeoB 2112, with r^2 values given to two significant figures for each core.

Ba/Ca records for GeoB 2104 and GeoB 2109 (Figure 6.9) both show higher values in the late glacial and early deglacial relative to the Holocene. In comparison to opal flux data (Figure 6.6), GeoB 2104 shows maximum Ba/Ca values to coincide with peak opal flux at ~23 ka. Peaks in Ba/Ca and opal flux data for GeoB 2109 are also observed to coincide around 17 ka. The similarity between Ba/Ca and opal flux records in these two cores support the interpretation from opal flux data that productivity in the Argentine Basin was greater during the late glacial and early deglacial relative to the Holocene.

Downcore authigenic U records are distinctly different in GeoB cores 2107, 2104, 2109 and 2112 (Figure 6.8). A prominent peak is observed between ~14-9 ka GeoB

2104 and in the glacial of GeoB 2109 where as GeoB 2107 shows little variation in authigenic U between 23 ka and 2 ka. Additionally, GeoB 2112 shows significantly lower authigenic U levels than all other cores throughout the last ~28 kyrs. Downcore authigenic U profiles (Figure 6.8) show some similarities to opal flux (Figure 6.6) in cores GeoB 2107 and GeoB 2109 where mean authigenic U and opal flux values are observed to be higher at the LGM than during the Holocene. The prominent peak in authigenic U in GeoB 2104 between 14-9 ka can not be compared with opal flux data due to absence of opal data in GeoB 2104 during this time interval. There is also some similarity between authigenic U and opal flux records in GeoB 2107 with both opal and uthigenic U levels showing little variation downcore, with the exception of a decrease in authigenic U levels at core top.

There is some disparity between authigenic U and opal flux in GeoB 2112, which shows peak opal flux values in the late glacial at a time of a minor decrease in authigenic U. Both opal flux and authigenic U values are significantly lower in GeoB 2112 relative to the three shallower cores.

The similarities between opal flux and authigenic U in cores GeoB 2107, GeoB 2104 and GeoB 2109 suggest that authigenic U levels are influenced mainly by changes in productivity in the Argentine Basin. However, an alternative explanation for the observed variations in authigenic U is that these records are reflecting different levels of ventilation of different water masses at the depths specific to each core. Depleted oxygen levels associated with reduced ventilation would give rise to peaks in authigenic U and can be assessed by comparison with ^{231}Pa/^{230}Th records (discussed in section 7.4.2).

6.3.3. Changes in water mass geometry

According to modern hydrographic transects, cores GeoB 2107 (depth 1048 m) and GeoB 2112 (depth 4010 m) are located within nutrient rich southern component waters AAIW and AABW respectively. GeoB 2104 (depth 1503 m) is positioned on the boundary of AAIW and nutrient poor NADW. GeoB 2109 is positioned within the core of NADW at 2500m (Figure 3.3).

In this section, $\delta^{13}C$ and εNd data from each of the GeoB cores examined in this study will be discussed to assess changes in water mass distribution in the Argentine Basin over the last ~25 kyr. However, before interpreting this data, a number of issues regarding the reliability of both the $\delta^{13}C$ and εNd data to assess water mass changes must first be addressed.

As discussed in section 2.7.1, the benthic species *Cibicidoides* is an epifaunal species living on or near the sediment surface and reflects the $\delta^{13}C$ of dissolved inorganic carbon ($\delta^{13}C_{DIC}$) in waters above the sediment with relatively little offset (Lynch-Stieglitz, 2003). *Uvigerina*, on the other hand is a shallow infaunal species, which lives in the pore waters of sediment where $\delta^{13}C$ of the dissolved inorganic carbon is lower than the overlying water column. Consequently the $\delta^{13}C$ of *Uvigerina* for GeoB 2107 shows significantly lower $\delta^{13}C$ values than the record from *Cibicidoides* from the same core (Figure 6.12). For this reason, the use of $\delta^{13}C$ data to interpret water mass geometry will focus only on the *Cibicidoides* records from GeoB 2107 and GeoB 2109.

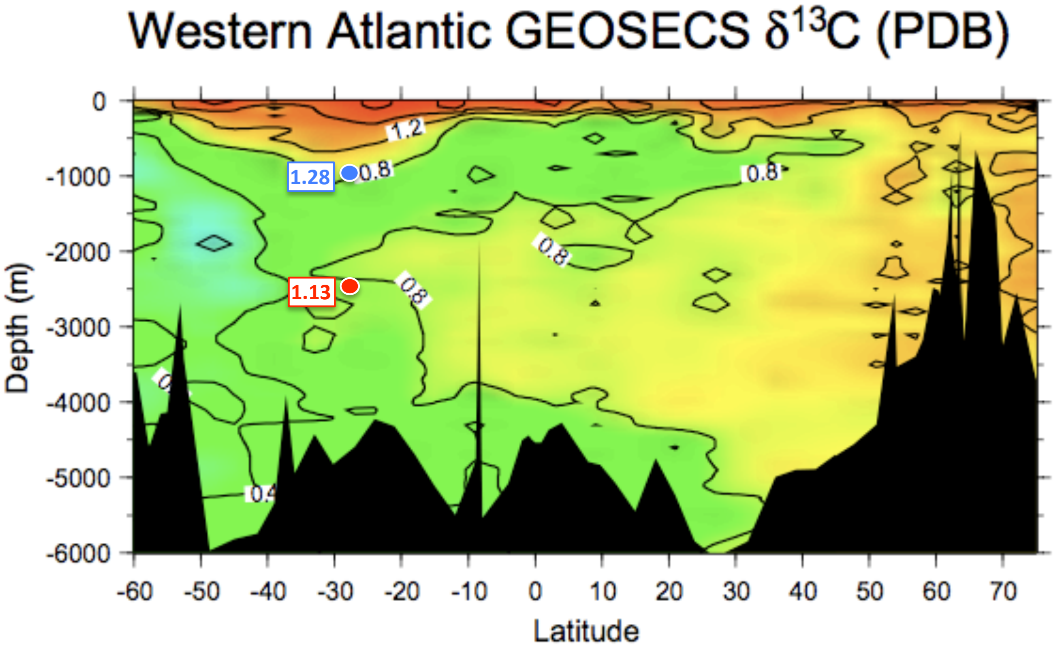

Figure 6.17: The distribution of modern $\delta^{13}C$ in the western Atlantic from Curry and Oppo (2005) after GEOSECS transect data (Kroopnick, 1985). The locations of cores GeoB 2107 (blue circle) and GeoB 2109 (red circle) are displayed, together with their Holocene (0-10 ka) $\delta^{13}C$ mean. The offset between these cores and the GEOSECS transect data is discussed below.

In comparison to modern $\delta^{13}C$ water column data for the southwest Atlantic (Figure 6.17), mean Holocene $\delta^{13}C$ values of GeoB 2107 and GeoB 2109 are observed to be higher than $\delta^{13}C_{DIC}$ values (Figure 6.17). The offset of is ~0.35-0.4 ‰ for GeoB 2107 and ~0.35 ‰ for GeoB 2109.

Positive offsets between *Cibicidoides* and $\delta^{13}C_{DIC}$ values have been well documented in various ocean basins, as summarized by McCorkle et al. (1998). The largest positive offsets have been observed in core tops from 1 km to 3 km in the southeastern Indian Ocean (0.45 ‰, McCorkle et al., 1998), the upper northern Indian Ocean (0.3-0.4 ‰, Ahmed and Labeyrie, 1994) and the shallow northern subtropical western Atlantic (0.3 ‰, Slowey and Curry, 1995). In other ocean regions there does not appear to be an offset, such as in the shallow regions off the coast of Australia and Tasmania (Lynch-Stieglitz et al., 1994). In the southwest Atlantic, Oppo and

Horowitz (2000) report that *Cibicidoides* calcify with $\delta^{13}C$ values up to 0.4 ‰ higher than $\delta^{13}C_{DIC}$ in this region, consistent with the offset observed in cores GeoB 2107 and GeoB 2109 stated above.

Core top εNd values Fe-Mn leachates from GeoB cores 2107, 2104, 2109 and 2112 were compared by Carter (2009) with the closest seawater εNd profile, SAVE 302, from Jeandel et al., (1993). The core top εNd of GeoB 2107 and GeoB 2104 are both within 1 εNd of the modern seawater value at their respective depths (Figure 6.18).

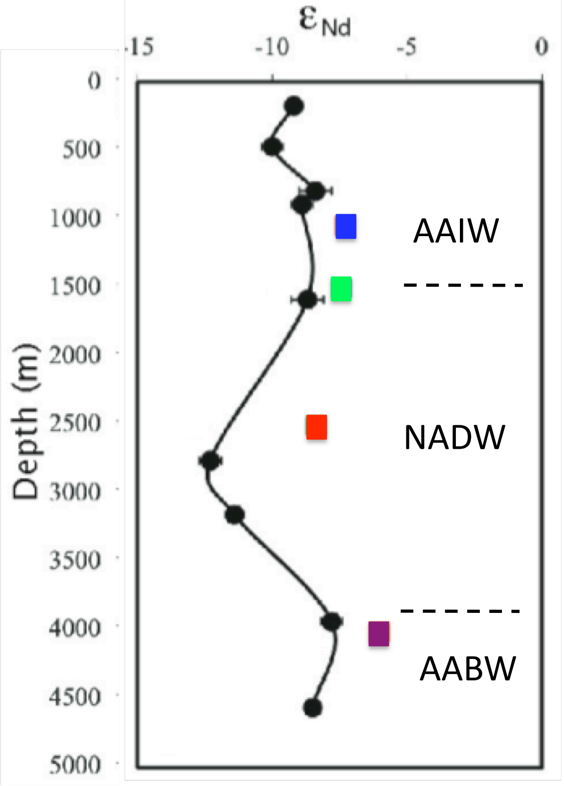

Figure 6.18: Seawater Nd profile from SAVE 302 (black line, Jeandel 1993) and core top Fe-Mn leachate values (closed squares). Core tops Fe-Mn from GeoB 2107 (blue), GeoB 2104 (green) and GeoB 2112 (purple) are close to modern seawater εNd and more radiogenic than modern seawater for GeoB 2109 (red). Error bars are within symbol size where not shown. Adapted from Carter (2010).

A core top value obtained by Pahnke et al. (2008) on core KNR159 from the Brazilian margin at 1268 m (εNd = -7.3 ± 0.14) is within analytical uncertainty of those obtained by Carter from 1045 m and 1503 m (GeoB 2107 = -7.29 ± 0.08; GeoB 2104 = -7.42 ± 0.06), all of which are directly influenced by AAIW. These results suggest that Nd from Fe-Mn leachates in intermediate depth cores are representative of modern seawater and can be used to reconstruct water mass histories at intermediate depths in the southwest Atlantic.

The sample from GeoB 2112 (4010 m) also has as εNd value within ~1 εNd of the water that bathes it today - AABW. However, this 'core top' sample produced a radiocarbon age of ~5 ka and therefore can not be compared to modern seawater values.

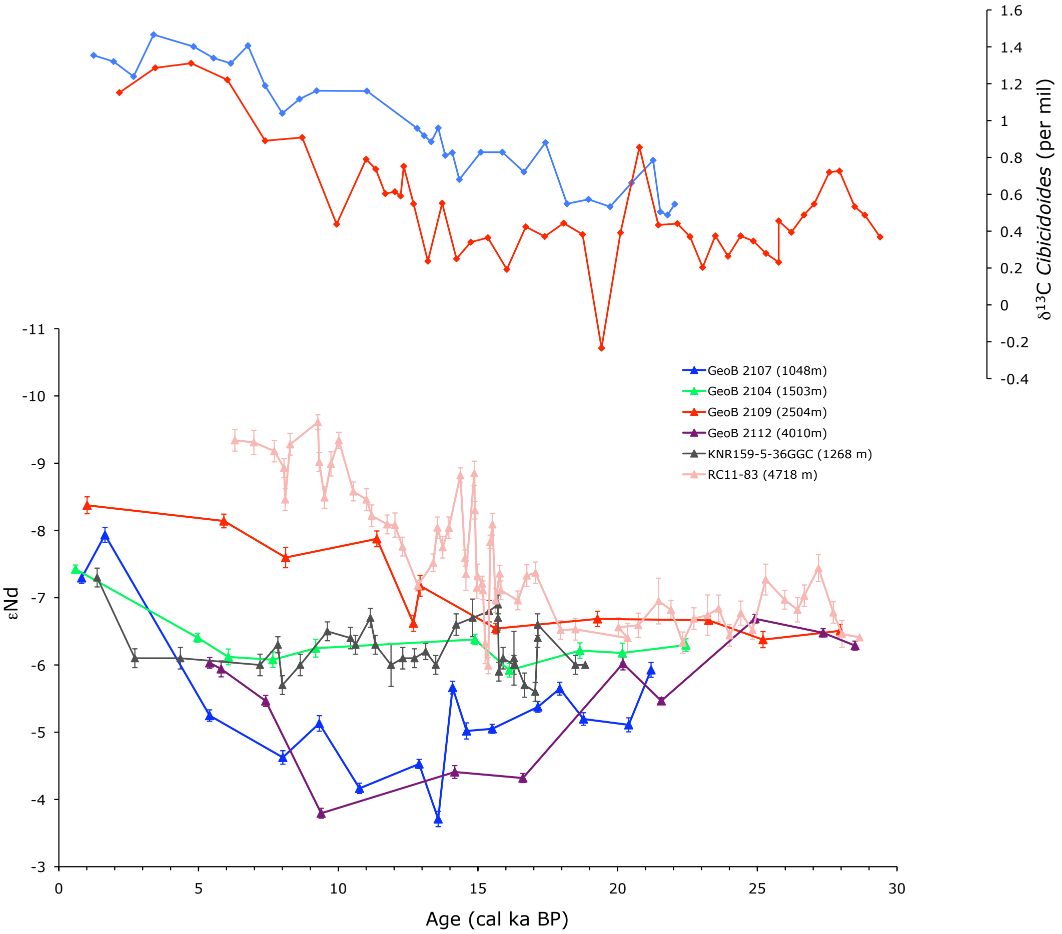

Figure 6.19: $\delta^{13}C$ and εNd data from GeoB cores 2107 (1048 m, blue), 2104 (1503 m, green), 2109 (2504 m, red) and 2112 (4010 m, purple). Also shown are εNd records from core KNR159-5-36GGC at 1258 m (black curve, Pahnke et al., 2008) and from core RC11-83 (4718 m) in the Cape basin (pink curve, Piotrowski et al 2005). Modern NADW εNd~-14, AABW εNd~-7 to -9, Pacific deep waters εNd~-4 (Frank, 2002). Nd values higher than -7 in GeoB 2107, GeoB 2112 – cores bathed by southern source water masses throughout the record, reflect an increase in the southern Nd end-member due to reduced influence of northern source waters.

The core top from GeoB 2109 located within modern day NADW is 4 εNd units higher than modern seawater at 2500 m and is therefore significantly more radiogenic than expected (core top εNd =-8.37; seawater εNd =-12.3 (Jeandel et al., 1993)). Carter (2009) suggests that contamination by a combination of Nd from volcanics and silicates may have overprinted the authigenic seawater values in this core.

Despite the possible contamination of Nd in GeoB 2109, downcore changes in εNd correlate well with $\delta^{13}C$, with both records indicating an increasing component of northern source water across the deglacial (Figure 6.19), suggesting that Nd may still be recording changes in relative contributions of northern and southern waters. Furthermore, the εNd record from GeoB 2109 shows some similarity to core RC11-83 (pink curve, Figure 6.19) from the Cape Basin (Piotrowski et al., 2004) before ~12 ka. Therefore, both the Nd and $\delta^{13}C$ data from GeoB 2109 will be used to interpret past changes in water mass geometry over this core site.

6.3.4 Interpretations of changes in water mass geometry at intermediate depths

The interpretation of down core εNd and $\delta^{13}C$ data from intermediate depth cores GeoB 2107 and GeoB 2104 is made difficult by the fact that these cores are currently located close to the transition zone from AAIW to underlying NADW in the modern ocean (Figure 3.3).

In order to help understand changes in water mass geometry at these depths, a valuable source of data is provided by Curry and Oppo (2005) who compiled $\delta^{13}C$ data from multiple cores along the Brazilian margin to assess glacial and Holocene water mass geometry in the southwestern Atlantic ocean. The Holocene and LGM profiles of $\delta^{13}C$ versus depth (Figure 6.20) show that the core of AAIW, indicated by relatively low $\delta^{13}C$ values in the profile, is observed at ~1500 m in the Holocene ($\delta^{13}C$ = ~1.0 ‰) and at approximately 1000 m ($\delta^{13}C$ = ~0.5 ‰) during the Glacial.

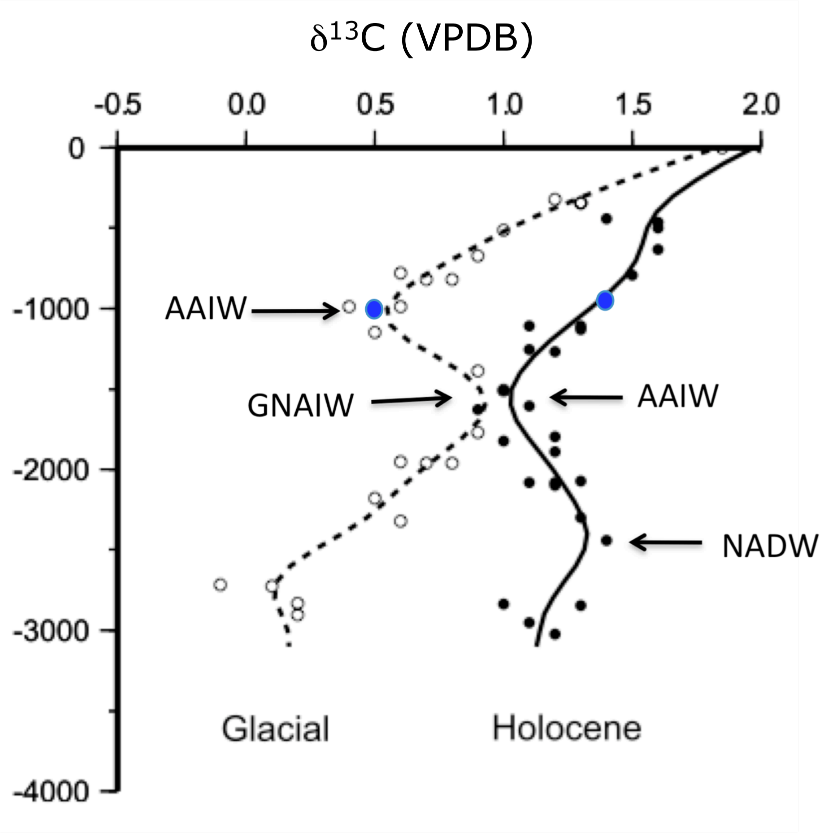

Figure 6.20: Holocene (solid line, solid symbols) and glacial (dashed line, open symbols) profiles of *Cibicidoides* and *Paulina* $\delta^{13}C$ values from a compilation of Brazilian margin cores. Surface values are provided by stable isotope measurements on *G. ruber*. Lines fit through the data produced with a spline function (adapted from Curry and Oppo, 2005). Blue circles mark the average Holocene (0-8 ka) and LGM (19-23 ka) $\delta^{13}C$ values from GeoB 2107.

Average $\delta^{13}C$ values for GeoB 2107 during the mid to late Holocene ($\delta^{13}C$ = 1.35 ‰ between 0-7 ka) and glacial ($\delta^{13}C$ = 0.55 ‰ between 19-23 ka) on *Cibicidoides* (Figure 6.19) are practically identical to the Curry and Oppo (2005) $\delta^{13}C$ data (Figure 6.20) at 1000 m for the Holocene ($\delta^{13}C$ = ~1.4 ‰) and in the Glacial ($\delta^{13}C$ = ~0.5 ‰). The ~0.9 ‰ difference in $\delta^{13}C$ between the Holocene and LGM is significantly greater than the mean whole ocean Holocene to glacial $\delta^{13}C$ depletion of 0.32 ‰ (Duplessy et al., 1988; Matsumoto and Lynch-Stieglitz, 1999; Oppo and Horowitz, 2000). The shift to more negative $\delta^{13}C$ values in excess of the mean whole ocean $\delta^{13}C$ change at the LGM can be explained by changes in the air sea exchange of surface waters that form AAIW. As discussed in section 2.7.1, modern AAIW has a distinctly positive $\delta^{13}C$ signature ($\delta^{13}C$ = ~1.5‰) due to prolonged exposure of source waters to the atmosphere in cold, windy regions of the Southern Ocean allowing dissolved carbon to exchange with heavier carbon in the atmosphere. During the last glacial, reduced ventilation of the Southern Ocean, due to increased sea ice (Moore et al., 2000, Stephen and Keeling 2000) and surface water stratification (Francois et al., 1997; Toggweiler, 2006) along with a reversal in the direction of CO_2 flux (e.g. Sigman and Boyle, 2000) all contributed to a reduced $\delta^{13}C$ air-sea signature in AAIW (Mook et al., 1974; Lynch-Stieglitz and Fairbanks, 1994; Lynch-Stieglitz et al., 1995).

The Curry and Oppo (2005) $\delta^{13}C$ data is also helpful for interpretation of the downcore Nd values from the shallowest core, GeoB 2107, which are more radiogenic than Nd values from GeoB 2104 from ~22 ka to ~5 ka (Figure 6.19). This is consistent with the fact that GeoB 2107 is located within modern day AAIW and, according to the $\delta^{13}C$ depth profiles in Figure 6.20, should not be seeing any local mixing with an underlying northern water mass at the LGM.

As discussed in section 2.7.2 of this thesis, variations in the southern Nd end-member are related to the relative input of northern versus southern sourced waters to the circumpolar Southern Ocean (Piotrowski et al., 2004, Pahnke et al., 2008). This suggests that lower Nd values observed in GeoB 2107, whilst still located within AAIW, reflect a greater contribution of northern source waters to the Southern Ocean during the late Holocene and to a lesser extent at the LGM.

The Nd record from GeoB 2104 at 1503 m contrasts with the shallower record from GeoB 2107, recording less radiogenic values at all points up until ~5 ka. The downcore Nd data set from GeoB 2104 is broadly similar to a published Nd record from core KNR159-5-36GGC (black curve, Figure 6.20) at 1258 m (Pahnke et al., 2008), also from the Brazilian margin (27.51°S, 46.47°W), which suggests that the same water mass was present at both 1500 m and 1250 m from the LGM to the present.

At a depth of ~1500 m, GeoB 2104 is located very close to the core of GNAIW (~1600 m) as defined by the Curry and Oppo (2005) glacial $\delta^{13}C$ depth plot (Figure 6.20) and should see a significantly greater component of GNAIW in the glacial. This possibly explains the observation that Nd values in GeoB 2104 are less radiogenic than GeoB 2107 at all points during the late glacial and deglacial, although values are within error of each other at ~21 ka, suggesting that GeoB 2107 was in close proximity to northern source waters at this time.

The similarity of $\delta^{13}C$ records between GeoB 2107 and GeoB 2104 on *Uvigerina* (Figure 6.12) may appear inconsistent with the Nd evidence that suggests GeoB 2107 is within AAIW for the duration of the 25 kyr record whereas GeoB 2104 is seeing a greater component of northern source waters during the glacial and deglacial. However, as discussed above, these records are from the same benthic species

Uvigerina peregrina that is strongly susceptible to changes in biological productivity (e.g. Lynch Stieglitz et al., 2003). Given the close geographic proximity of these two cores, it is possible that the $\delta^{13}C$ records on *Uvigerina* are reflecting changes in biological productivity rather than water mass distribution histories.

6.3.5 Interpretation of changes in deep water mass geometry

During the last glacial, deep water circulation in the South Atlantic was dominated by waters of southern origin (Figure 6.21, Curry and Oppo 2005). The Holocene and LGM profiles of $\delta^{13}C$ versus depth in Figure 6.20 show NADW, indicated by relatively high $\delta^{13}C$ values, was centered at 2500 m ($\delta^{13}C$ = ~1.4 ‰) during the Holocene but had shoaled to ~1600 m ($\delta^{13}C$ = ~0.9 ‰) during the Glacial (GNAIW).

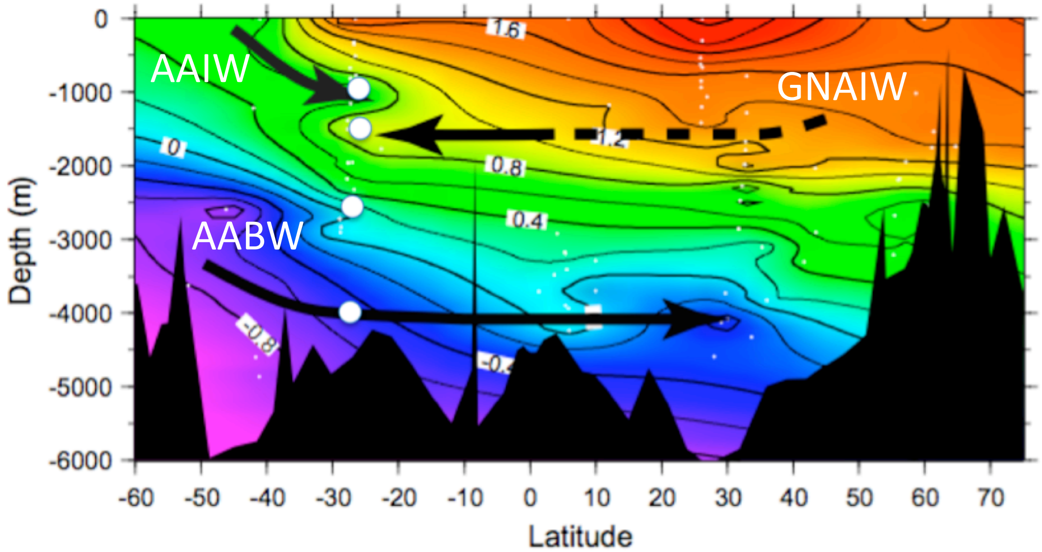

Figure 6.21: The distribution of $\delta^{13}C$ in the glacial western Atlantic. Black arrows are shown to represent the flow direction of AAIW, GNAIW and AABW. Adapted from Curry and Oppo (2005). White circle mark the locations of the four GeoB cores used in this study.

This change in water mass structure is reflected in the benthic $\delta^{13}C$ record of GeoB 2109 which shows an increase in $\delta^{13}C$ from 0.3 ‰ at the LGM to average values of

1.3 ‰ between 0-8 ka, in agreement with glacial and Holocene values compiled by Curry and Oppo (2005) at 2500 m. The ~1.0 ‰ difference in $\delta^{13}C$ between the Holocene and LGM, in excess of the mean ocean depletion of 0.32 ‰ (e.g. Duplessy et al., 1988), are consistent with the increased contribution of poorly ventilated southern component waters and reduced basin scale convection in the deep glacial Atlantic (e.g. Boyle and Keigwin 1987; Lynch Stieglitz et al., 2007)

The transition from dominant southern water flow in the glacial to northern waters in the Holocene is observed to begin at approximately 15 ka when $\delta^{13}C$ values of 0.24 ‰ begin to increase steeply until 6.2 ka where $\delta^{13}C$ values level off at 1.2 ‰ (Figure 6.20).

As already discussed, the fact that core top εNd values in GeoB 2109 do not match modern seawater means that interpretations of absolute εNd values from this downcore record must be made with caution. However, variations in the εNd of GeoB 2109, whist purely indicative rather than diagnostic of any paleoceanographic changes, may still be useful for examining the relative changes in contribution of northern versus southern sourced waters over the core site and are therefore discussed in this section.

The most radiogenic values in GeoB 2109 are observed during the glacial and early deglacial (averaging -6.5 ‰ between 28 ka and 16 ka). Similar glacial and early deglacial εNd values are observed in core RC11-83 (averaging -6.8 ‰ between 28 ka and 16 ka) form the Cape Basin (pink curve, Figure 6.20) of Piotrowski et al. (2005), consistent with a strong influence of southern source water flow in the South Atlantic at this time.

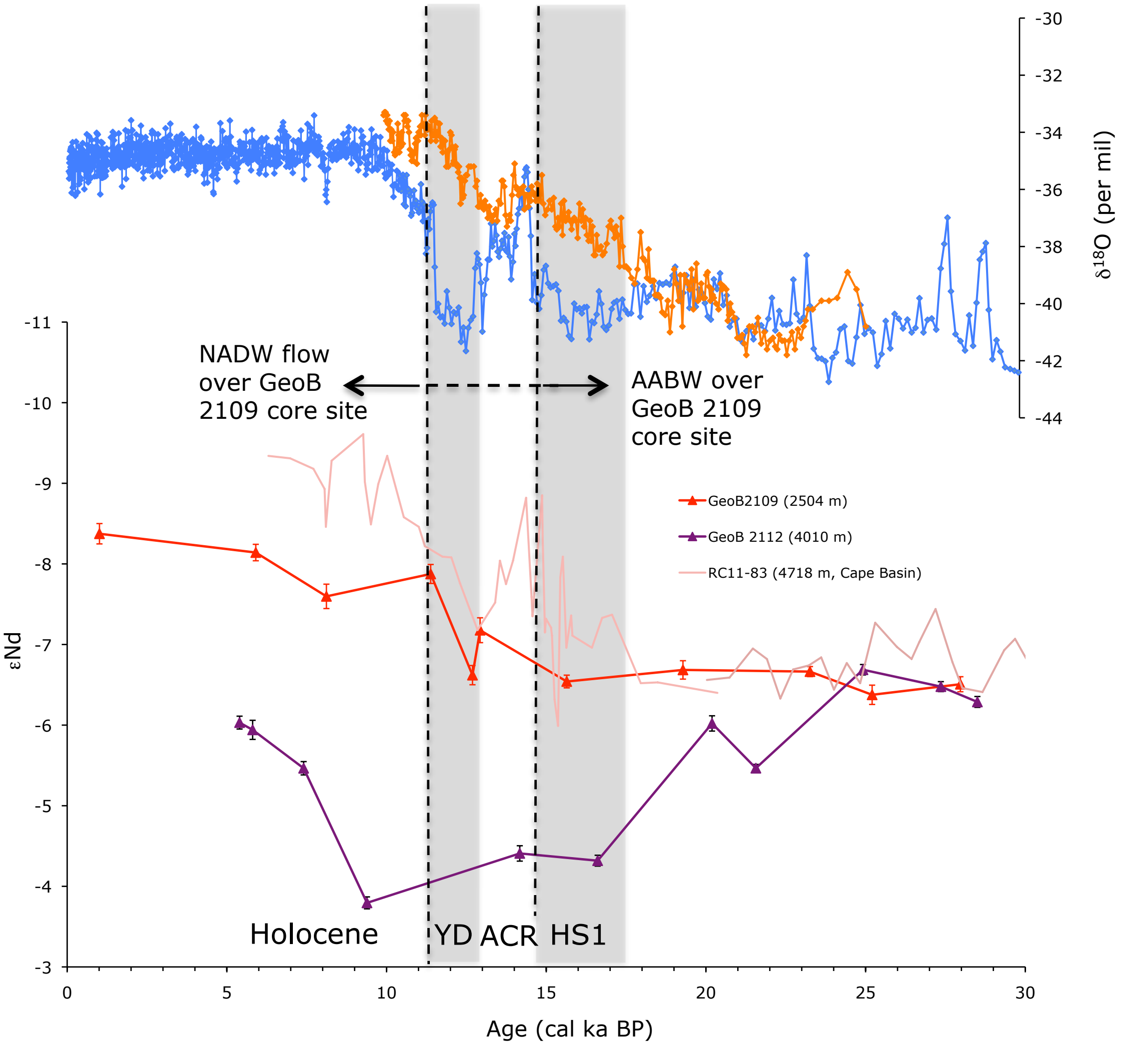

Figure 6.22: South Atlantic deep core Nd records showing the transition from AABW flow at mid depths in the South Atlantic during the early deglacial to NADW flow during the Holocene. Greenland ice core δ^{18}O (GISP, blue line) and Antarctica ice core δ^{18}O (Byrd, orange line) indicate periods of cooling in the north (HS1, YD, grey shaded bars) and in the south (ACR).

There is evidence from the Nd record of core RC11-83 (4718 m) in the southeast Atlantic that northern source waters may have penetrated to depth in the South Atlantic during the Antarctic Cold Reversal (ACR) following HS1, as indicated by an decrease in εNd to ~-9 at 14.5 ka (Figure 6.22). The similarity between Nd records of

RC11-83 and GeoB 2109 prior to ~12 ka suggests that northern source waters may also have been present at the core site of GeoB 2109 during the ACR, although a lack of Nd data for GeoB 2109 at this time means this is inconclusive.

It is noticeable that Nd values from RC11-83 in the Cape Basin (4718 m) are not consistent with those from GeoB 2112 at 4010 m in the Argentine Basin, which are significantly more radiogenic during the early deglacial and up to the mid Holocene. The more radiogenic Nd values of GeoB 2112 relative to RC11-83 indicates that southern sourced waters were present at depths of 4 km in the Argentine Basin whilst a stronger component of northern sourced waters occupied similar depths in the southeast Atlantic. Due to dissolution of carbonate at depths associated with these two cores, it is not possible to further assess the possible east-west water mass distribution gradient using $\delta^{13}C$.

The εNd profiles for GeoB 2112 and GeoB 2109 (Figure 6.23) show similar average εNd values of ~-6.5‰ at ~25 ka, suggesting that the same southern water mass (AABW) was filling the Atlantic from depths of 4000 m to at least 2500 m at this time. There is a strong increase of εNd at 4000 m beginning at ~20 ka, continuing through the deglacial and into the early Holocene, culminating in peak radiogenic εNd values of -3.8 ‰ at ~9 ka. This εNd value suggests that at this time AABW was comprised entirely of the Pacific end member, with a value close to εNd = -4 ‰ (Abouchami et al., 1997). The subsequent decrease in εNd to -6 ‰ in GeoB 2112 at ~5 ka suggests increasing influence of northern source waters during the early Holocene. This is consistent with modern day salinity profiles which show GeoB

2112 to be located close to the boundary between AABW and overlying NADW (Figure 3.3) in addition to the εNd and $\delta^{13}C$ data from GeoB 2109 (2500 m) which indicate increasing NADW in deep waters during the Holocene.

There is some evidence of a shift to more radiogenic values in both GeoB 2109 and the Cape Basin core of Piotrowski et al. (2005) at the onset of the Younger Dryas around 12 ka. This is consistent with a decrease in NADW input into the Southern Ocean at this time, in both the southwest Atlantic at GeoB 2109 and in the southeast Atlantic in the Cape Basin.

Following the Younger Dryas, an increase in northern component waters at 2500 m is indicated by a decrease in εNd to -7.9 ‰ at 11.3 ka, concurrent with a steep increase in $\delta^{13}C$ observed in GeoB 2109 (Figure 6.19). εNd values decrease slightly to -8.3 ‰ near core top, when $\delta^{13}C$ are observed to reach maximum values of 1.3 ‰, indicating the completed transition to a dominant flow of northern source waters at 2500 m in the Argentine Basin by the late Holocene.

A summary of the main differences in water mass geometry in the Argentine Basin between the LGM and the Holocene is given in Figure 6.23. Changes in depth of water mass boundaries are based mainly on interpretations of the $\delta^{13}C$ compilation data from Brazilian margin cores (Curry and Oppo, 2005, Figure 6.20) combined with εNd and $\delta^{13}C$ data from the four study cores.

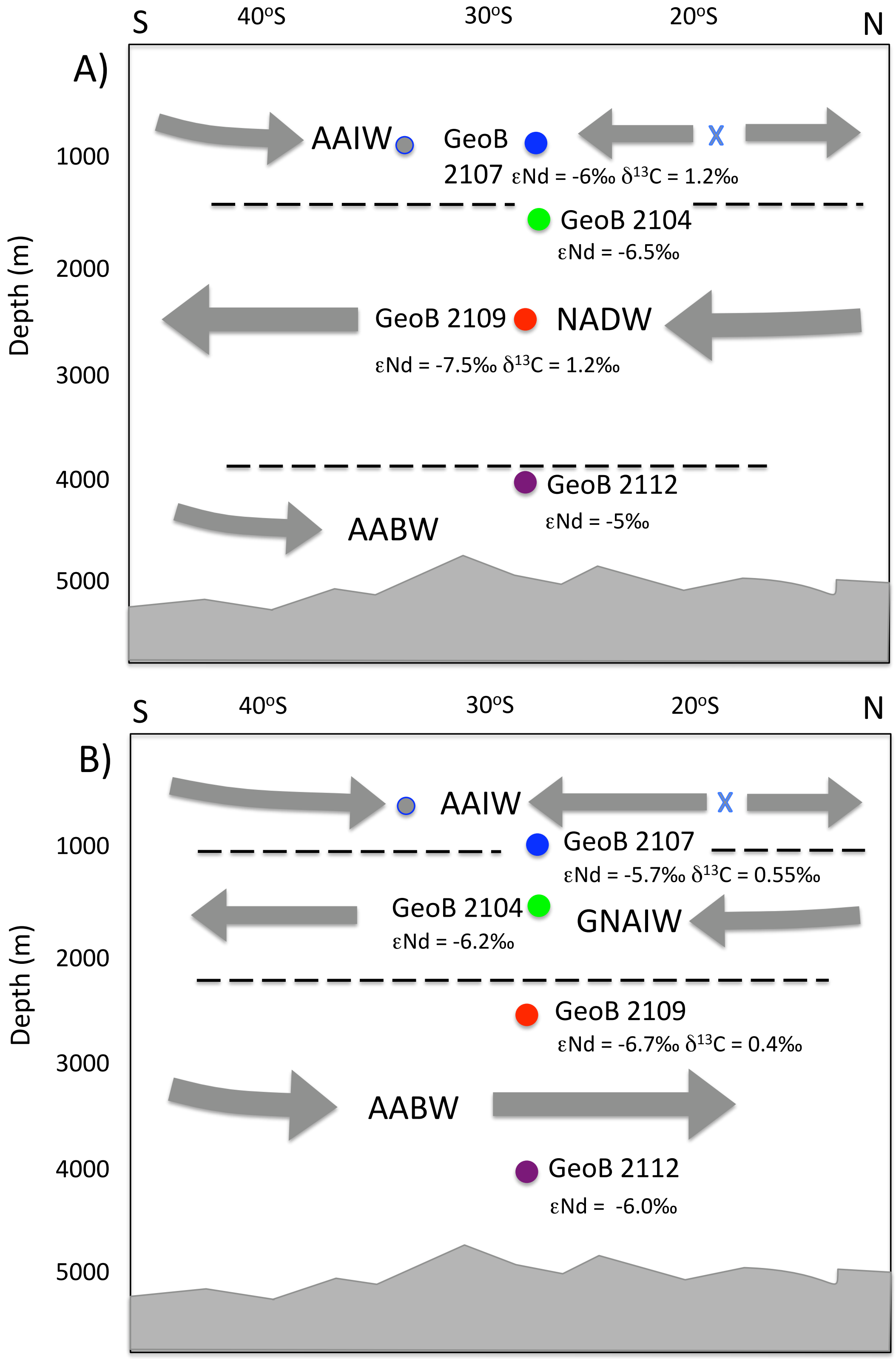

Figure 6.23: A cartoon to show water mass circulation in the southwest Atlantic for A) the Holocene and B) during the LGM. Average εNd and δ^{13}C values during these intervals are indicated by each core. Horizontal dashed lines indicate the approximate depths of water mass boundaries based on the compilation δ^{13}C data from Brazilian margin cores (Curry and Oppo 2005, Figure 6.20). The boundary between modern NADW and AABW is based on modern hydrolgraphic transects (Figure 3.3). A filled grey circle is used to represent eastward flow of AAIW and a blue X to represent westward flow of AAIW towards the continental margin before bifurcating into north and south flowing branches (as shown in Figure 3.2).

6.4 Conclusions

Lithogenic fluxes in Brazilian margin cores GeoB 2107 (1048 m), GeoB 2104 (1504 m) and GeoB 2109 (2504 m) appear to be significantly controlled by sea level. Maximum lithogenic fluxes are observed in the early deglacial when sea level was lowest and are observed to decrease in response to rising sea level across the deglacial up until flooding of the continental shelf at ~13 ka when lithogenic fluxes stabilize in all cores. A strong correlation between preserved vertical particle fluxes and lithogenic fluxes is observed across all cores, suggesting that particle flux is dominantly controlled by lithogenic inputs in this region, in turn reflecting the close proximity of these cores to the Brazilian continental shelf.

Biological productivity proxies opal and Ba/Ca suggest productivity was greater at the LGM than during the Holocene. This is consistent with observed increases in productivity north of the Antarctic polar front at the LGM (Kumar et al. 1993). A third proxy for past productivity, authigenic U, shows significant differences between cores and does not correlate well the Ba/Ca and opal data which suggests that authigenic U is not reflecting local changes in productivity and is more likely reflecting oxygen levels specific to the different water masses flowing over each core.

GeoB 2107 is located within modern day AAIW and, according to the $\delta^{13}C$ depth profiles in Figure 6.19, should not be seeing any local mixing with an underlying northern water mass at the LGM. At a depth of ~1500 m, GeoB 2104 should see a significantly greater component of GNAIW in the glacial, with Nd values in GeoB 2104 are less radiogenic than GeoB 2107 at all points during the late glacial and deglacial. This is consistent with GeoB 2104 being located very close to the core of GNAIW (~1600 m) at the LGM as defined by the Curry and Oppo glacial $\delta^{13}C$ depth plot (Figure 6.19).

At greater depths, water mass distribution at the LGM is very different to today, with dominant flow of AABW replacing northern source waters, which shallow to ~1600 m. Nd and $\delta^{13}C$ data suggest a switch from dominant southern to northern source water mass flow in the southwest Atlantic occurred in the late deglacial at approximately 11 ka, with the transition to modern values appearing to have occurred relatively late in the Holocene.

Ch 7: ^{231}Pa/^{230}Th data

7.1 Introduction

To date, the use of ^{231}Pa/^{230}Th sedimentary records to reconstruct past variation in the strength of AMOC have focused primarily on the North Atlantic, investigating the link between past NADW flow strength and climate variability (e.g. McManus et al. 2004, Gherardi et al. 2005). However, the use of water mass tracers such as δ^{13}C (e.g. e.g. Duplessy 1998; Curry and Oppo 2005) and εNd (e.g. Piotrowski et al., 2004) to reconstruct past water mass distribution in the Atlantic suggests ^{231}Pa/^{230}Th records from the North Atlantic may be strongly influenced by circulation of southern waters during cold climate intervals.

In this study, four sediment cores from the Argentine Basin spanning depths ranging from 1 to 4 km were selected for ^{231}Pa/^{230}Th analyses (as described in chapter 3) to assess past flow rates of southern source AAIW and AABW in addition to NADW far from it source, as identified using existing δ^{13}C and Nd data. ^{231}Pa/^{230}Th data records for each core were produced for the last ~25 kyrs, a time period encompassing the last deglaciation and the major abrupt climate changes associated with it.

Whilst this work will primarily investigate differences in the circulation state of these water masses between the Holocene and LGM, this research will also assess the possibility of a seesaw like response in southern water masses to changes in northern water mass flow on millennial time scales, where quality of age models and resolution of data allow for direct comparison between core records.

7.2 Data corrections

Analytical methods, described fully in chapter 4, were used to assess total ^{231}Pa and ^{230}Th concentrations on a total of 108 samples from the four Argentine Basin cores detailed in chapter 3.

Such Pa and Th concentrations in marine sediments consist of three components: isotopes scavenged from seawater, those supported by decay of isotope parents in detrital material, and those supported by the decay of authigenic U (Henderson and Anderson 2003). The use of Pa and Th as a proxy for past circulation is based on the scavenged component (i.e. the excess, or unsupported, fraction). Therefore, the influence of the other two components must be removed before interpretation:

$$(^{231}\mathrm{Pa})_{\mathrm{xs}} = (^{231}\mathrm{Pa})_{\mathrm{meas}} - (^{231}\mathrm{Pa})_{\mathrm{det}} - (^{231}\mathrm{Pa})_{\mathrm{auth}} \qquad (7.1)$$

$$(^{230}\mathrm{Th})_{\mathrm{xs}} = (^{230}\mathrm{Th})_{\mathrm{meas}} - (^{230}\mathrm{Th})_{\mathrm{det}} - (^{230}\mathrm{Th})_{\mathrm{auth}} \qquad (7.2)$$

Where (…) denotes activity and the subscripts

xs = excess (scavenged component)

meas = measured (total)

det = detrital (continental component)

auth = authigenic (insitu ingrowth from U)

The detrital component is derived from continental erosion and is transported to the ocean by aeolian and riverine inputs. This detrital material is old enough for the detrital Th and Pa to be in secular equilibrium with their radiodecay parent isotopes, ^{238}U and ^{235}U.

$$(^{230}\mathrm{Th})_{\mathrm{det}} = (^{238}\mathrm{U})_{\mathrm{det}} \tag{7.3}$$

$$(^{231}\mathrm{Pa})_{\mathrm{det}} = (^{235}\mathrm{U})_{\mathrm{det}} \tag{7.4}$$

Measured U concentrations can not be used directly to assess this component because of the presence of authigenic U. Instead, detrital (^{238}U) (and subsequently (^{230}Th)) is estimated from the (^{232}Th), which is assumed to be entirely of detrital origin. The detrital ^{238}U/^{232}Th ratio for the Argentine Basin was determined to be 0.5 (see Figure 6.7).

$$(^{230}\mathrm{Th})_{\mathrm{det}} = (^{232}\mathrm{Th})_{\mathrm{meas}} \left(\frac{(^{238}\mathrm{U})}{(^{232}\mathrm{Th})} \right)_{\mathrm{det}} \tag{7.5}$$

The activity of detrital ^{235}U (and subsequently ^{231}Pa) is estimated from the average natural ^{235}U/^{238}U activity ratio of 0.046.

$$(^{231}\mathrm{Pa})_{\mathrm{det}} = 0.046 \times (^{232}\mathrm{Th})_{\mathrm{meas}} \left(\frac{(^{238}\mathrm{U})}{(^{232}\mathrm{Th})} \right)_{\mathrm{det}} \tag{7.6}$$

Authigenic ^{231}Pa and ^{230}Th are derived from decay of ^{235}U and ^{234}U which have been incorporated into the sediment directly from seawater at or shortly after sedimentation (Anderson, 1982). This authigenic uranium is not old enough for Pa and Th to be in secular equilibrium meaning Pa and Th produced from authigenic U have to be calculated applying the law of radioactive decay:

$$(^{230}\mathrm{Th})_{\mathrm{auth}} = (^{234}\mathrm{U})_{\mathrm{auth}}\left(1 - e^{-\lambda_{230Th}t}\right) \tag{7.7}$$

$$(^{231}\mathrm{Pa})_{\mathrm{auth}} = (^{235}\mathrm{U})_{\mathrm{auth}}\left(1 - e^{-\lambda_{231Pa}t}\right) \tag{7.8}$$

Where λ is the decay constant specific to each isotope and t is the time elapsed since the emplacement of authigenic U, which is typically taken to be the time of sediment deposition.

The activities of ^{235}U and ^{234}U are calculated from ^{238}U which is more abundant and therefore more accurately quantified.

$$(^{238}\mathrm{U})_{\mathrm{auth}} = (^{238}\mathrm{U})_{\mathrm{meas}} - \left((^{238}\mathrm{U})_{\mathrm{det}}\right) \tag{7.9}$$

Because authigenic U is derived from seawater, it has an initial (^{234}U/^{238}U) = 1.146, equivalent to that dissolved in seawater (Robinson et al., 2004). Combining equations 7.7 and 7.9:

$$(^{230}\mathrm{Th})_{\mathrm{auth}} = 1.146\left((^{238}\mathrm{U})_{\mathrm{meas}} - (^{238}\mathrm{U})_{\mathrm{det}}\right)\left(1 - e^{-\lambda_{230Th}t}\right) \tag{7.10}$$

The authigenic component of ^{231}Pa can be calculated using the natural ^{235}U/^{238}U ratio of 0.046. Combining equations 7.8 and 7.9:

$$(^{231}\mathrm{Pa})_{\mathrm{auth}} = 0.046\left((^{238}\mathrm{U})_{\mathrm{meas}} - (^{238}\mathrm{U})_{\mathrm{det}}\right)\left(1 - e^{-\lambda_{231Pa}t}\right) \tag{7.11}$$

Substituting $^{238}U_{det}$ by 7.5 (into 7.10) and 7.6 (into 7.11) gives the final equations for the authigenic components of Th (7.12) and Pa (7.13):

$$(^{230}\mathrm{Th})_{\mathrm{auth}} = 1.146\left[(^{238}\mathrm{U})_{\mathrm{meas}} - (^{232}\mathrm{Th})_{\mathrm{meas}}\left(\frac{(^{238}\mathrm{U})}{(^{232}\mathrm{Th})}\right)_{\mathrm{det}}\right]\left(1 - e^{-\lambda_{230Th}t}\right) \tag{7.12}$$

$$(^{231}\mathrm{Pa})_{\mathrm{auth}} = 0.046\left[(^{238}\mathrm{U})_{\mathrm{meas}} - (^{232}\mathrm{Th})_{\mathrm{meas}}\left(\frac{(^{238}\mathrm{U})}{(^{232}\mathrm{Th})}\right)_{\mathrm{det}}\right]\left(1 - e^{-\lambda_{231Pa}t}\right) \tag{7.13}$$

Finally, the effect of radioactive decay since time of deposition must be corrected for to give the initial ^{230}Th and ^{231}Pa concentrations. This correction is given by:

$$(^{230}\mathrm{Th})_{\mathrm{xs,0}} = (^{230}\mathrm{Th})_{\mathrm{xs}} \times e^{\lambda_{230Th}t} \tag{7.14}$$

$$(^{231}\mathrm{Pa})_{\mathrm{xs,0}} = (^{231}\mathrm{Pa})_{\mathrm{xs}} \times e^{\lambda_{231Pa}t} \tag{7.15}$$

7.3. Results: Downcore ^{231}Pa/^{230}Th profiles

Downcore records of (^{231}Pa), (^{230}Th) and (^{231}Pa/^{230}Th)$_{xs,0}$ are presented separately by core together with opal flux and particle flux profiles. Also shown are scatter plots between opal flux, particle flux and ^{231}Pa/^{230}Th for each core. These data are discussed both individually by core and collectively in the next section For simplicity, (^{231}Pa/^{230}Th)$_{xs,0}$, (^{231}Pa) and (^{230}Th) will be referred to as ^{231}Pa/^{230}Th, ^{231}Pa and ^{230}Th respectively in the text of the remainder of this chapter.

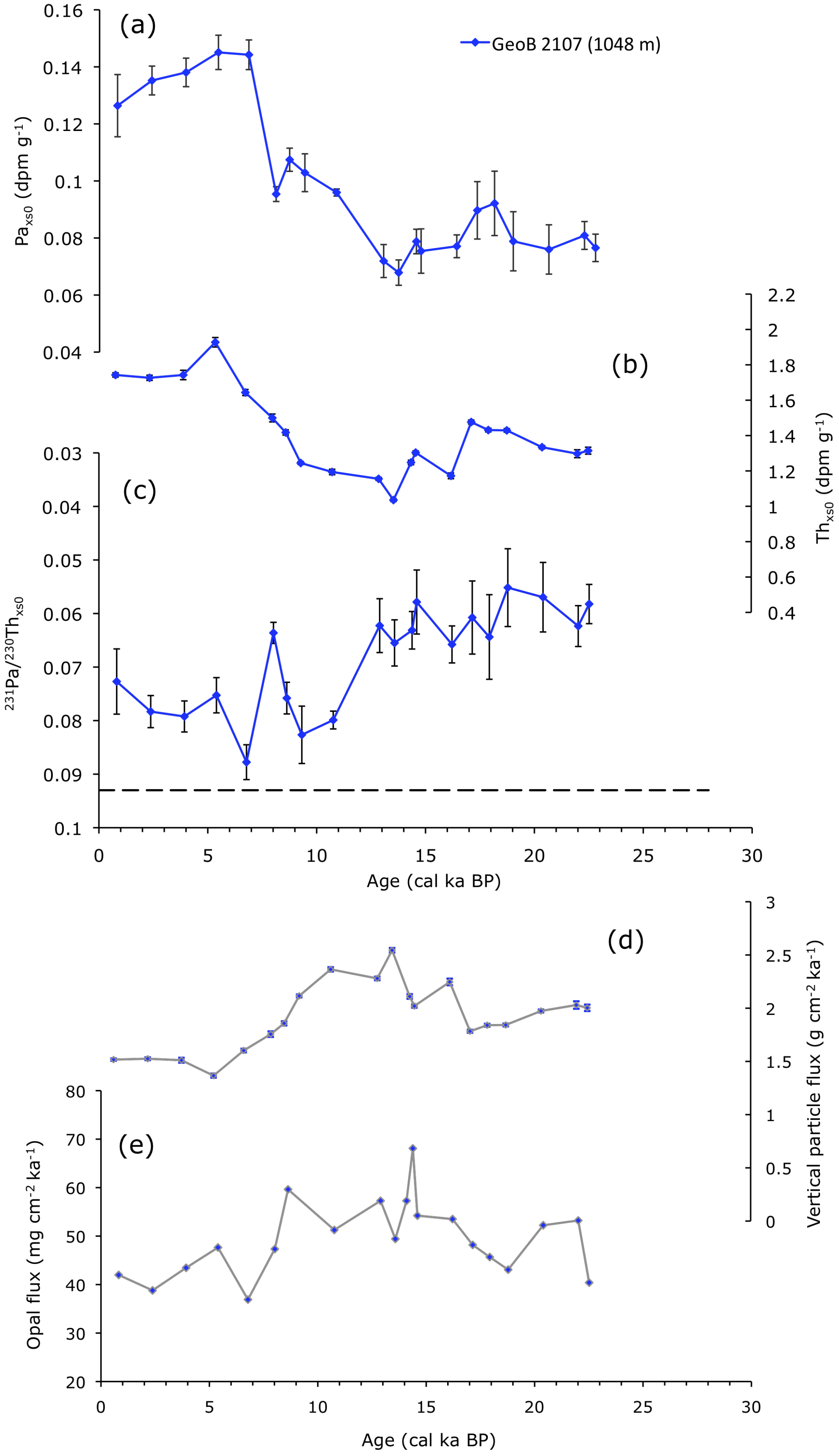

***Figure 7.1*: (a)** Pa$_{xs0}$, **(b)** Th$_{xs0}$, **(c)** ^{231}Pa/^{230}Th$_{xs0}$, **(d)** vertical particle flux and **(e)** opal flux profiles for GeoB 2107 (1048m). Errors are within symbol size where not shown. The horizontal dashed black line in **(c)** represents the natural ^{231}Pa/^{230}Th production ratio (0.093).

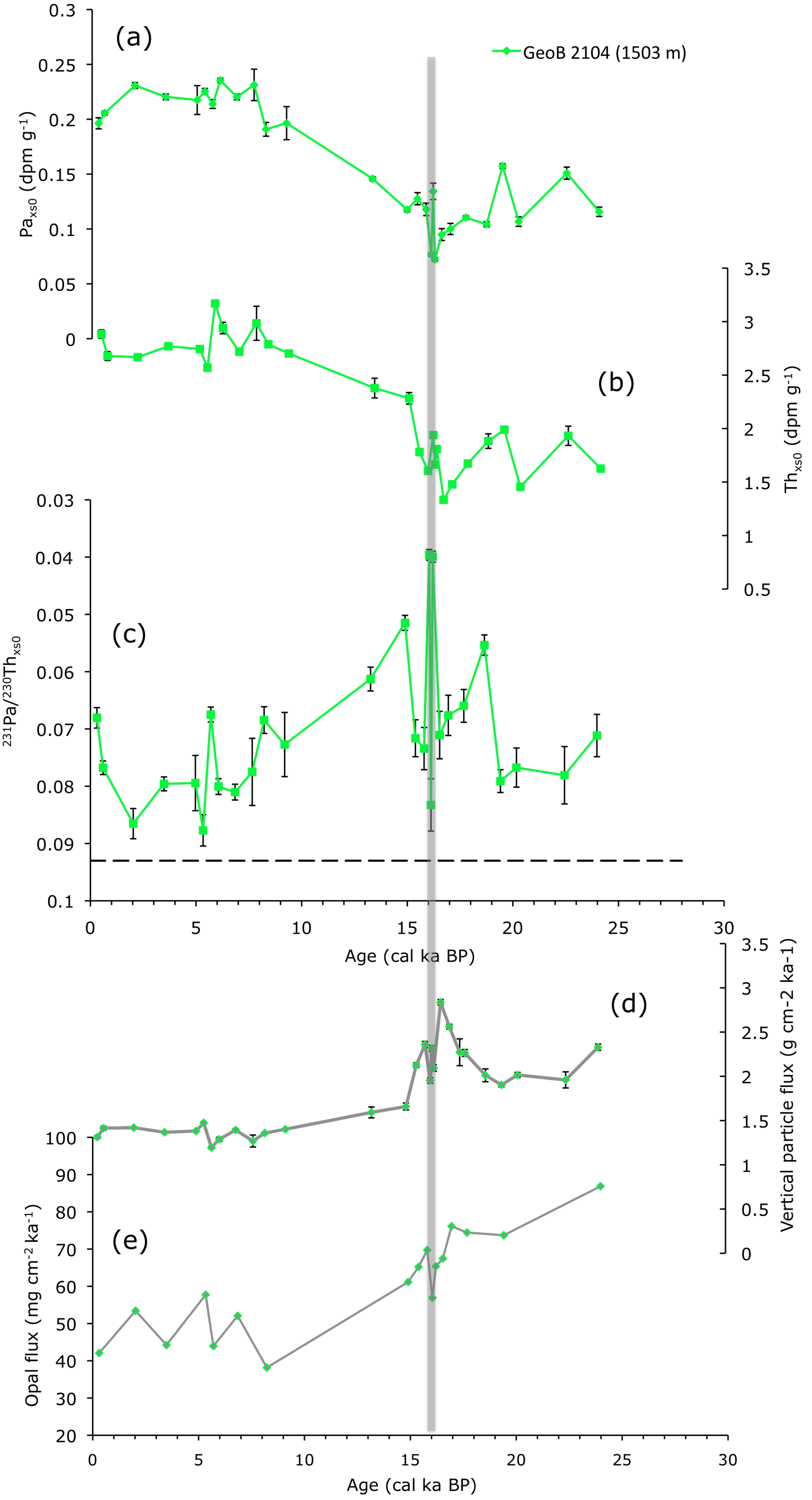

***Figure 7.2*: (a)** Pa_{xs0}, **(b)** Th_{xs0}, **(c)** $^{231}Pa/^{230}Th_{xs0}$, **(d)** vertical particle flux and **(e)** opal flux profiles for GeoB 2104 (1503 m). Errors are within symbol size where not shown. The horizontal dashed black line in **(c)** represents the natural $^{231}Pa/^{230}Th$ production ratio (0.093). The vertical grey shaded bar marks the approximate timing of possible turbidite activity in this core.

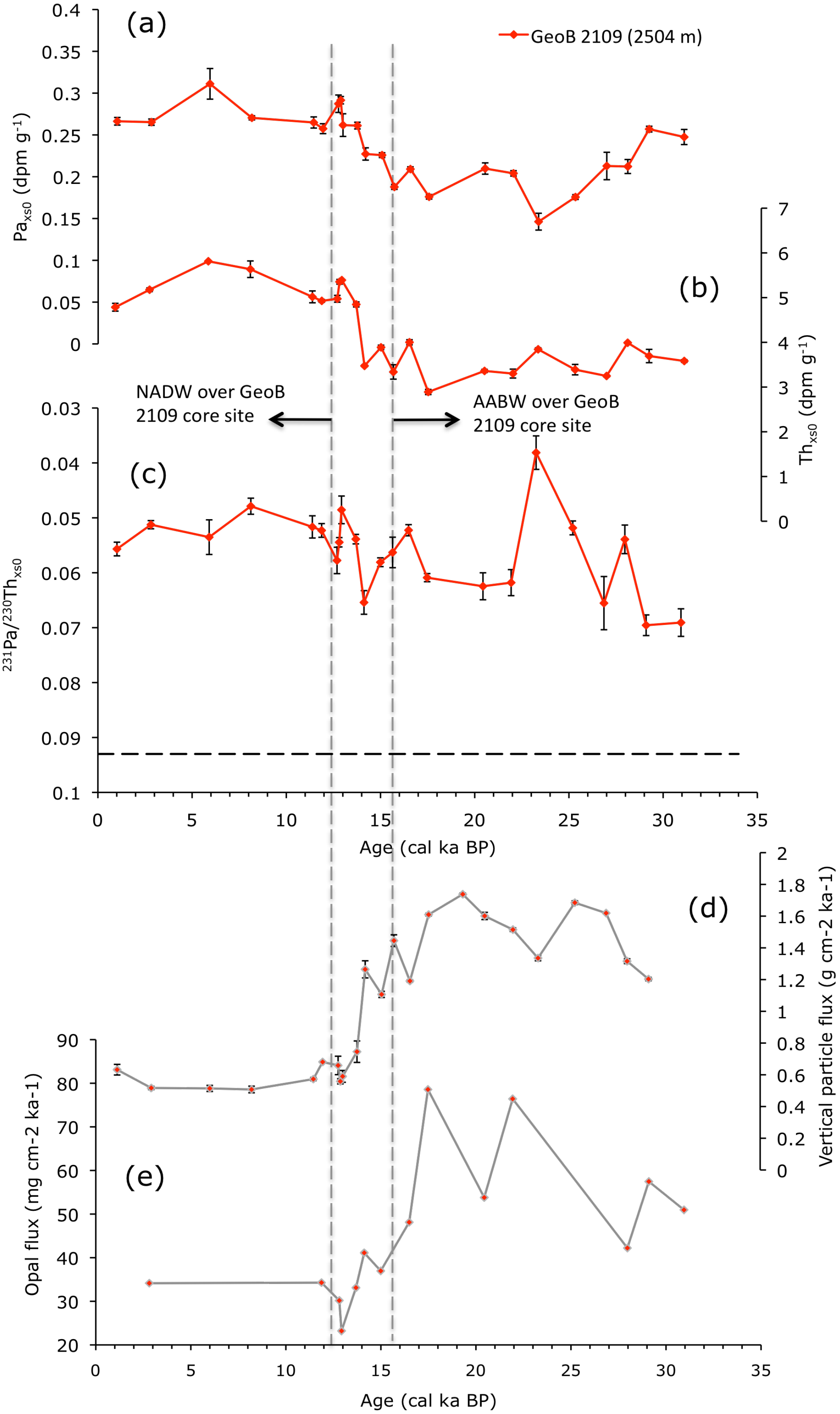

***Figure 7.3*: (a)** Pa$_{xs0}$, **(b)** Th$_{xs0}$, **(c)** ^{231}Pa/^{230}Th$_{xs0}$, **(d)** vertical particle flux and **(e)** opal flux profiles for GeoB 2109 (2504 m). Errors are within symbol size where not shown. The horizontal dashed black line in **(c)** represents the natural ^{231}Pa/^{230}Th production ratio (0.093).

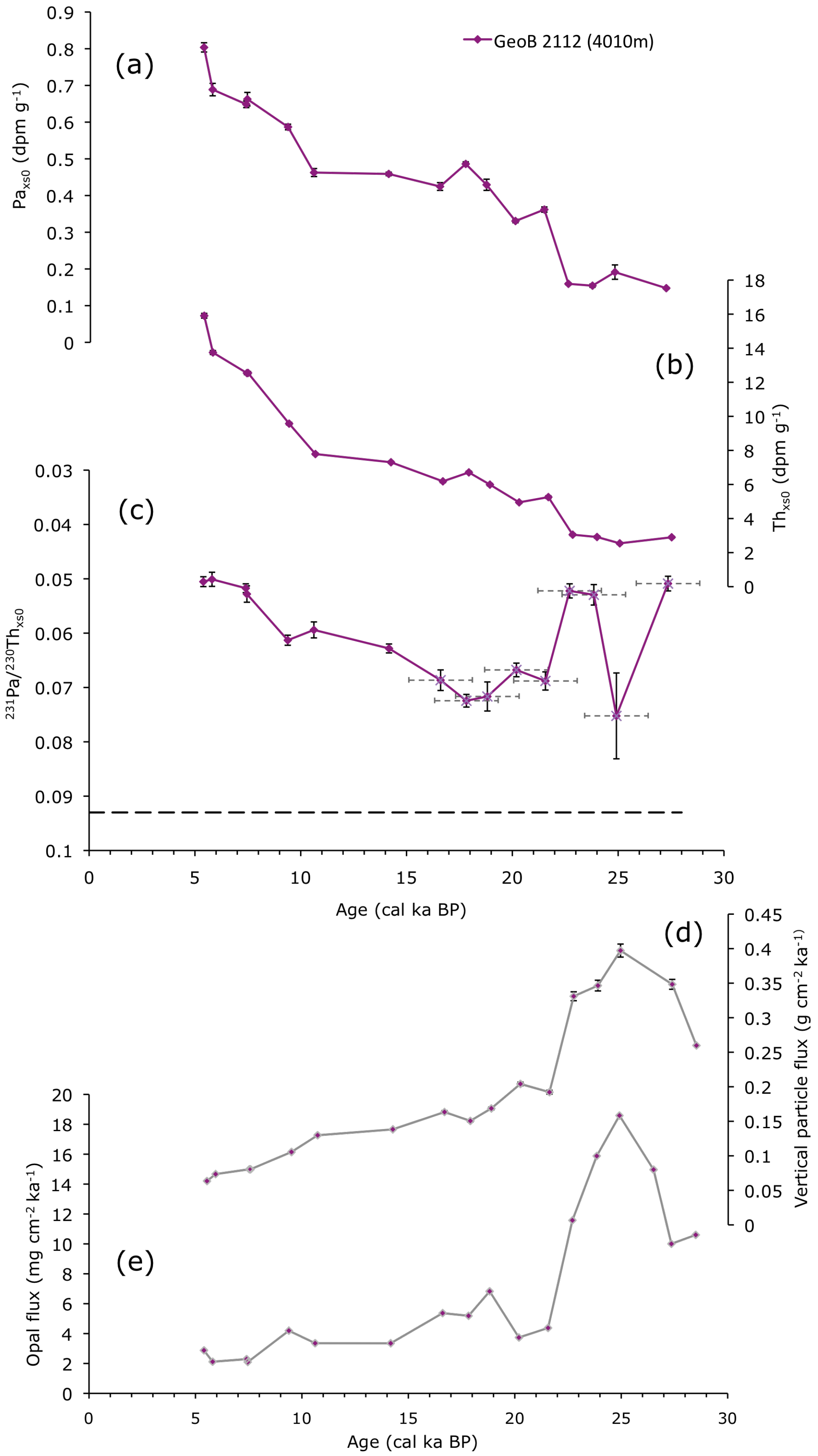

***Figure 7.4*: (a)** Pa$_{xs0}$, **(b)** Th$_{xs0}$, **(c)** ^{231}Pa/^{230}Th$_{xs0}$, **(d)** vertical particle flux and **(e)** opal flux profiles for GeoB 2112 (4010 m). Errors are within symbol size where not shown. The horizontal dashed black line in **(c)** represents the natural ^{231}Pa/^{230}Th production ratio (0.093). The grey dashed error bars in **(c)** show the estimated uncertaintiy on the GeoB 2112 age model as discussed in section 5.5

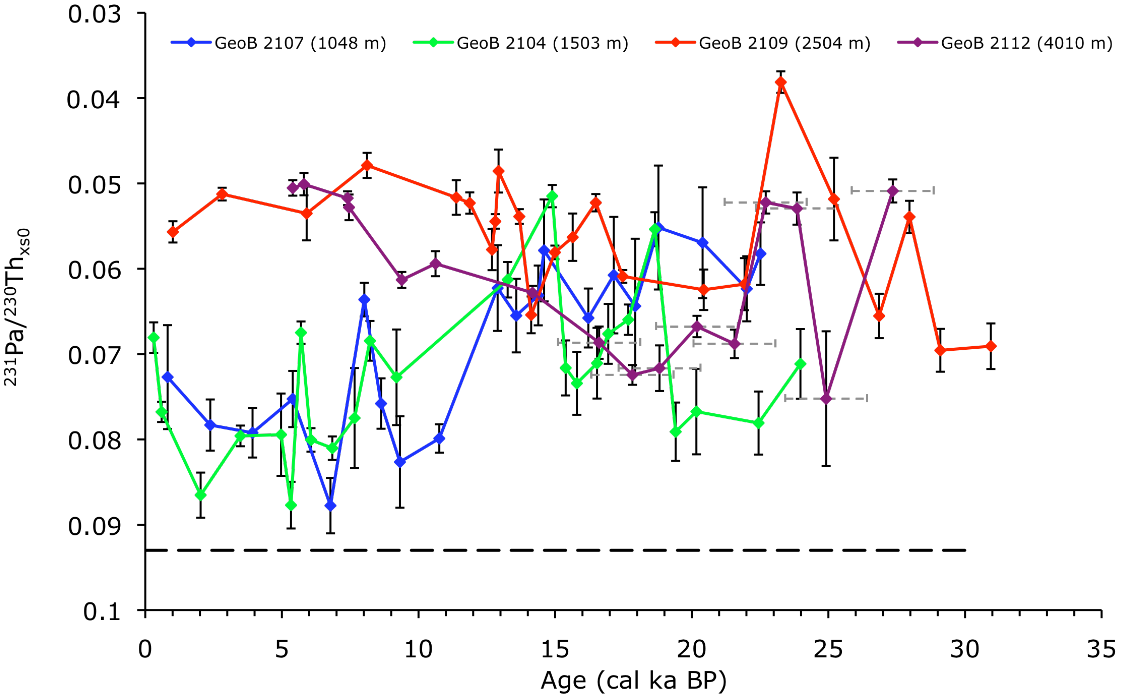

Figure 7.5: Combined ^{231}Pa/^{230}Th downcore records from GeoB 2107 (1048m), GeoB 2104 (1503m), GeoB 2109 (2504m) and GeoB 2112 (4010m). A horizontal dashed black line is used to indicate the natural ^{231}Pa/^{230}Th production ratio (0.093).

^{231}Pa/^{230}Th ratios in core GeoB 2107 (1048 m) are significantly lower at the LGM (averaging 0.059 ± 0.005, n =4 between 19-23 ka, Figure 7.1) than during the Holocene (averaging 0.078 ± 0.004, n= 8 between 0-10 ka). ^{231}Pa/^{230}Th ratios in this core remain low through most of the deglacial, showing little variation from an average of 0.064 between 17.9 ka and 12.9 ka. A large increase is observed in ^{231}Pa/^{230}Th from 0.063 to 0.082 between 12.9 ka and 10.8 ka. ^{231}Pa/^{230}Th ratios then remain above 0.07 during the Holocene with the exception of an isolated minimum of 0.064 at 8 ka.

In core GeoB 2104 (1503 m) ^{231}Pa/^{230}Th ratios are distinctly higher than in GeoB 2107 at the LGM, with average values of 0.078 ± 0.004, n = 4 in GeoB 2104 compared to 0.059 in GeoB 2107 ± 0.005, n =4 between 19 ka and 23 ka (Figures 7.2, 7.1). Large fluctuations in $^{231}Pa/^{230}Th$ are observed in GeoB 2104 at approximately 16.2-16.0 ka when $^{231}Pa/^{230}Th$ values fluctuate between 0.085 and 0.040. Similar fluctuations are also observed at this time in the particle flux and opal records of GeoB 2104 and may be the result of turbidite activity specific to core GeoB 2104. For this reason, these values are omitted from the $^{231}Pa/^{230}Th$ curve of GeoB 2104 in subsequent Figures. During the Holocene, $^{231}Pa/^{230}Th$ values in GeoB 2104 range between 0.07 and 0.09, a similar range of values seen in GeoB 2107 at this time.

$\delta^{13}C$ and εNd data (discussed in chapter 6) indicate a transition from southern to northern sourced waters flowing over the core site of GeoB 2109 (2504 m) beginning around 13 ka (section 6.3.3). Prior to this change, $^{231}Pa/^{230}Th$ values are higher, with the exception of a prominent peaks at ~23 ka ($^{231}Pa/^{230}Th$ = 0.04) and 16.5 ka ($^{231}Pa/^{230}Th$ = 0.052). $^{231}Pa/^{230}Th$ levels in GeoB 2109 (2504 m) remain stable throughout the Holocene, ranging between 0.055 and 0.048.

$^{231}Pa/^{230}Th$ ratios in core GeoB 2112 (4010 m) are similar to those observed in GeoB 2109 throughout the ~25 kyr record, most notably at 23.5 ka where a clear minimum in $^{231}Pa/^{230}Th$ is observed in both cores (Figure 7.5). $^{231}Pa/^{230}Th$ ratios in core GeoB 2112 decrease from ~0.07 at the LGM to ~0.06 at 10 ka. A further decrease in $^{231}Pa/^{230}Th$ is observed between 9.4 and 7.4 ka (from 0.061 to 0.051).

$^{231}Pa/^{230}Th$ values in GeoB 2107 show no significant correlation with either opal flux (r^2 = 0.16, Figure 7.6) or mass flux (r^2 = 0.10, Figure 7.7) with fluxes higher in the LGM when $^{231}Pa/^{230}Th$ are observed to decrease. A similarly poor correlation is observed in GeoB 2104 between ^{231}Pa/^{230}Th and opal ($r^2 = 0.032$) and particle fluxes ($r^2 = 0.080$).

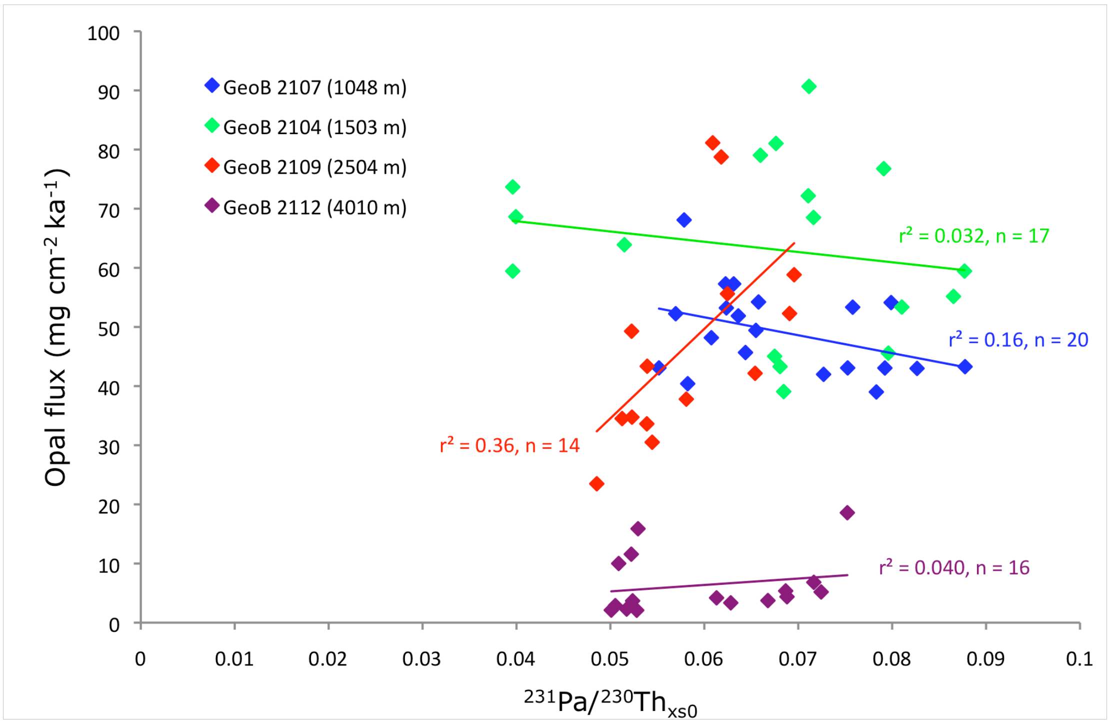

Figure 7.6: Plots to show the relationship between opal flux and ^{231}Pa/^{230}Th for cores GeoB 2107 (1048 m, blue), GeoB 2104 (1503 m, green), GeoB 2109 (2504 m, red) and GeoB 2112 (4010 m, purple).

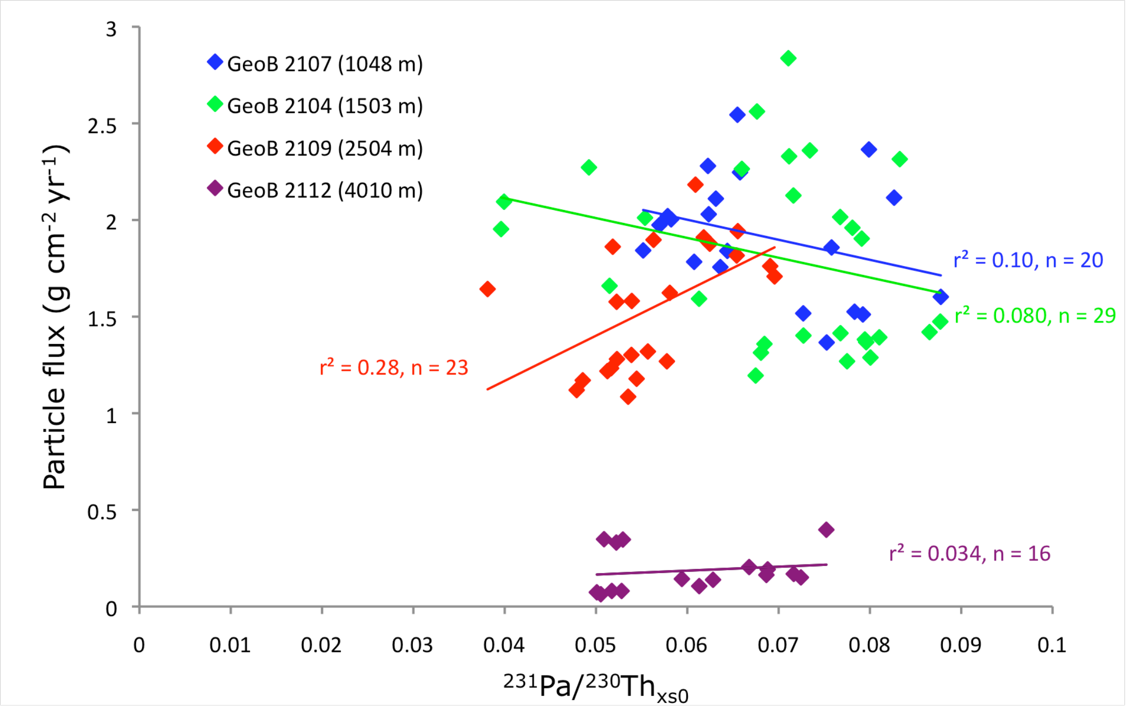

Figure 7.7: Plots to show the relationship between particle flux and ^{231}Pa/^{230}Th for cores GeoB 2107 (1048 m, blue), GeoB 2104 (1503 m, green), GeoB 2109 (2504 m, red) and GeoB 2112 (4010 m, purple).

There is a greater but still not highly significant correlation observed between $^{231}Pa/^{230}Th$ and both opal ($r^2 = 0.36$) and mass flux ($r^2 = 0.28$) in GeoB 2109 with $^{231}Pa/^{230}Th$ generally higher in the LGM when opal and particle fluxes reach maximum levels. However, individual peaks observed in downcore profiles of opal and particle fluxes do not correlate well with $^{231}Pa/^{230}Th$ records in GeoB 2109, which shows low $^{231}Pa/^{230}Th$ values close to peaks in opal at 22 ka and 17.5 ka. $^{231}Pa/^{230}Th$ values in GeoB 2112 show a poor correlation with both opal ($r^2 = 0.040$) and mass flux ($r^2 = 0.034$), although a peak in particle and opal fluxes are also observed to occur at a time when $^{231}Pa/^{230}Th$ values are near maximum levels at ~25 ka. The relationship between $^{231}Pa/^{230}Th$ and both particle ($r^2 = 0.033$, n = 89) and opal flux ($r^2 = 0.00014$, n = 67) for all combined samples is shown in Figure 7.8.

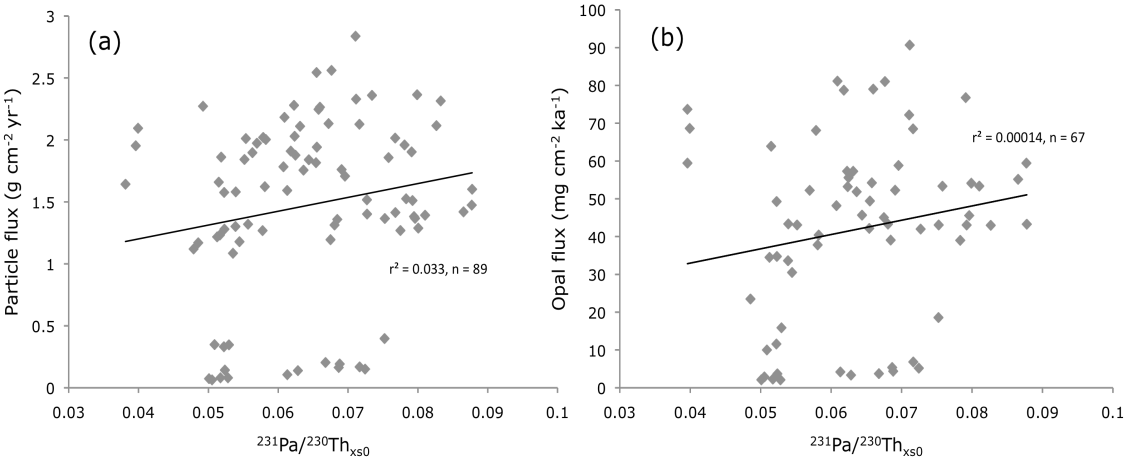

Figure 7.8: Plots to show the relationship between (a) particle flux and $^{231}Pa/^{230}Th$ and (b) opal flux and $^{231}Pa/^{230}Th$ for all combined samples from cores GeoB 2107, GeoB 2104, GeoB 2109 and GeoB 2112 in the Argentine Basin.

7.4 Discussion

7.4.1 Effect of opal and particle fluxes on $^{231}Pa/^{230}Th$

Protactinium is more readily scavenged by opal and in areas of high particle flux (see chapter 2). It is therefore expected that increases in particle flux or opal flux will correlate with increases in $^{231}Pa/^{230}Th$ if productivity, or the composition of scavenging particles, is responsible for the observed changes in $^{231}Pa/^{230}Th$.

Opal fluxes range from an average of ~60 mg cm^{-2} ka^{-1} in GeoB 2107 (1048 m) to an average of ~10 mg cm^{-2} ka^{-1} in GeoB 2112 (4010 m). These values are significantly lower than in regions where opal has been shown to have a strong correlation with $^{231}Pa/^{230}Th$ such as the Atlantic sector of the Southern Ocean where opal fluxes range between ~500 mg cm^{-2} ka^{-1} and 6000 mg cm^{-2} ka^{-1} over the last ~20 kyrs (Anderson et al. 2009, Figure 7.9).

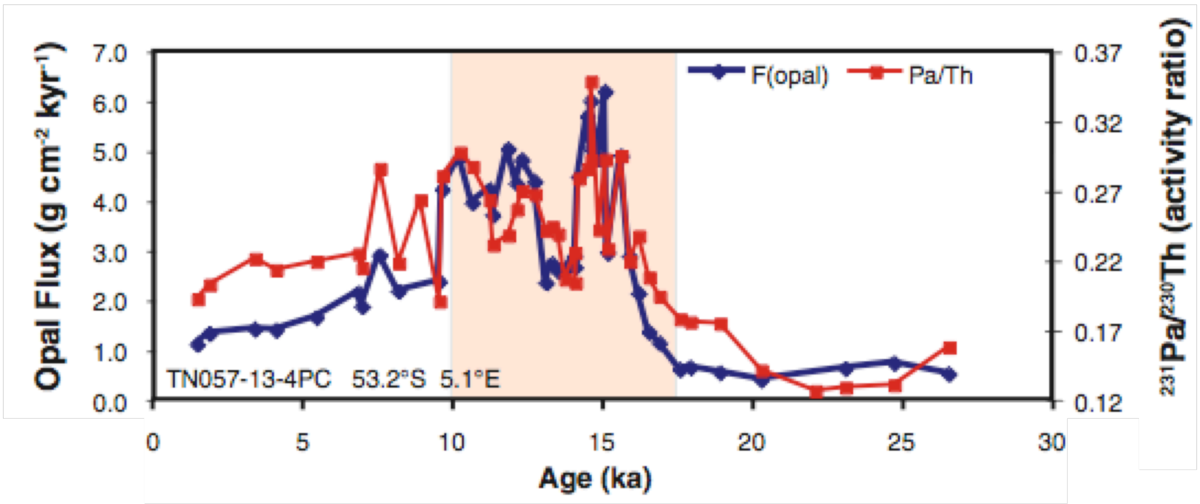

Figure 7.9: A strong correlation between opal flux and $^{231}Pa/^{230}Th$ in the Atlantic sector of the Southern Ocean (core TN057-13-4PC, 53.2° S, 5.1°E). Adapted from Anderson et al. (2009). Note Opal flux units are in g cm^{-2} kyr^{-1} as opposed to mg cm^{-2} kyr^{-1} for all Argentine Basin cores (Figures 7.1-7.4).

No significant correlation is observed between $^{231}Pa/^{230}Th$ and opal flux ($r^2 = 0.0001$, Figure 7.8) or between $^{231}Pa/^{230}Th$ and particle flux ($r^2 = 0.033$, Figure 7.8) in all combined samples from the four study cores, indicating that particle composition and flux have little effect on $^{231}Pa/^{230}Th$ in this location. This agrees with Niemann (2003) who measured the spatial distribution of $^{231}Pa/^{230}Th$ in surface sediments across the Argentine Basin and found that particle flux and opal flux have little correlation with $^{231}Pa/^{230}Th$ in sediments bathed by intermediate and deep water masses in this region. However, particle flux may have more influence on $^{231}Pa/^{230}Th$ further south where higher particle flux levels are observed in the Brazil Malvinas Confluence Zone (Niemann, 2003). This would result in greater scavenging of Pa from AAIW en route to the Argentine Basin, which may explain the lower concentrations of Pa observed in GeoB 2107 relative to all other cores from this study (Figures 7.1-7.4). Furthermore, enhanced scavenging of Pa in the BMCZ would most likely lead to reduced $^{231}Pa/^{230}Th$ ratios in each of the Argentine Basin study cores bathed by southern component water masses.

In the location of the cores studied here, the lack of apparent influence of local particle flux and opal flux suggests that changes due to ocean circulation are likely to explain much of the variability in $^{231}Pa/^{230}Th$.

7.4.2 Further discussion of authigenic U and sediment focusing factor

As discussed in section 6.3.2, downcore authigenic U records in GeoB cores show some similarities with opal flux, supporting a possible productivity control on authigenic U levels in the Argentine Basin. The $^{231}Pa/^{230}Th$ data presented in this chapter can be used to assess the possible relationship between authigenic U and circulation. Depleted oxygen levels associated with reduced ventilation of different water masses at the depths specific to each core would give rise to peaks in authigenic U and can be assessed by comparison with ^{231}Pa/^{230}Th records (Figure 7.10).

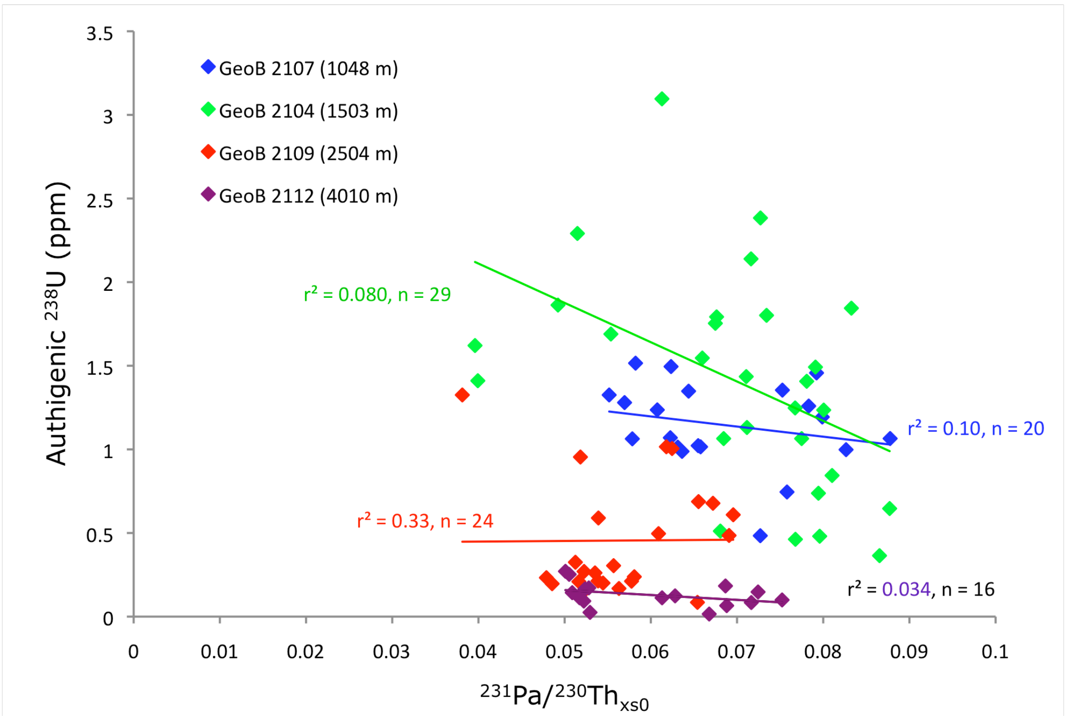

Figure 7.10: Correlation plots between authigenic U and ^{231}Pa/^{230}Th for cores GeoB 2107, GeoB 2104, GeoB 2109 and GeoB 2112, with r^2 values given to two significant figures for each core.

Figure 7.10 shows there is no significant relationship between authigenic U and ^{231}Pa/^{230}Th in any of the individual GeoB core records, or collectively across all samples (r^2 = 0.031, n = 89). Furthermore, where downcore authigenic U profiles (Figure 6.8) show distinct differences between two cores bathed by the same water mass ^{231}Pa/^{230}Th values (Figure 7.5) are observed to be very similar, which would not be expected if ventilation was controlling authigenic U levels in this region. For example, cores GeoB 2107 and GeoB 2104, bathed by AAIW during the deglacial show similar ^{231}Pa/^{230}Th values between 14-9 ka when authigenic U are observed to be significantly higher in GeoB 2104.

The absence of any evidence for a significant relationship between ^{231}Pa/^{230}Th and authigenic U suggests that changes in authigenic U are most likely due to productivity changes in the Argentine Basin, with some evidence for increased authigenic U levels corresponding to increases in opal flux as discussed in section 6.3.2.

Focusing factors are observed to be greater than 1 in all study cores for the last ~25 ka (Figures 6.3, 6.4) indicating a net flux of sediment into the locality of the GeoB core sites located on the continental slope of Brazilian margin.

Cores GeoB 2107 (1048 m) and GeoB 2104 (1503 m) show most variability in focusing factor downcore, possibly due to gravitational settling of fine material further up slope. This is consistent with the fact that turbidites are known to occur commonly along the upper South Brazilian continental slope (Kowsmann and de Ataide Costa, 1979).

There appears to be no clear or consistent co-variation between focusing factor and ^{231}Pa/^{230}Th (Figure 7.5) across all of the GeoB cores. Significant changes in ^{231}Pa/^{230}Th, such as in GeoB 2109 (from ~ 27 to 22 ka and from ~19 to 14 ka) occur when focusing factors are relatively stable. Additionally, significant changes in focusing factor in GeoB 2107 between 17-13 ka are observed to occur when ^{231}Pa/^{230}Th is stable. However, some similarities between ^{231}Pa/^{230}Th and focusing factor are observed, most notably in GeoB 2104 from ~24-19.5 ka, when relatively high ^{231}Pa/^{230}Th values are observed at the same time as a peak in focusing factor, suggesting that enhanced focusing factor may be due to reduced flow speed over GeoB 2104 at this time.

Average focusing factors in GeoB 2112 of ~10 during the Holocene and ~6 during the LGM, are relatively high in comparison to the shallower GeoB cores. This core is located within the margins of the Argentine Basin, where mudwaves are well documented (e.g. Jones, 1994), likely contributing greater sediment drift, and subsequently high and temporally variable focusing factors at this particular core site.

7.4.3 Effect of water mass on ^{231}Pa/^{230}Th records

A key question when interpreting sedimentary ^{231}Pa/^{230}Th ratios is whether they represent average flow conditions through the entire water column or just the bottom most water mass.

^{231}Pa/^{230}Th downcore profiles from the four Argentine Basin cores in this study (Figure 7.5) show distinct differences with depth, indicating that ^{231}Pa/^{230}Th ratios are set by the water mass immediately above the sediment, rather than averaging through the entire water column. Results from a model study by Thomas et al. (2006) suggest that sedimentary ^{231}Pa/^{230}Th values are set by waters within 1000 m from the sediment water interface. Comparison of ^{231}Pa/^{230}Th records from intermediate depth cores GeoB 2107 (1048 m) and GeoB 2104 (1504 m, Figure 7.11), located along the Brazilian continental slope at depths just 500 m apart, can help to improve on this estimate.

Modern day hydrographic transects combined with Nd data indicate that, during the Holocene, core GeoB 2107 remained within AAIW and core GeoB 2104 was bathed by NADW but located close to (within ~300 m) the boundary with AAIW (see chapter 6). Mean $^{231}Pa/^{230}Th$ values are identical between cores GeoB 2107 and GeoB 2104 during the Holocene (0-10 ka) when $^{231}Pa/^{230}Th$ in GeoB 2107 = 0.077 ± 0.004, n = 8 and in GeoB 2104 = 0.077 ± 0.003, n = 12, which suggests that both cores are reflecting the flow conditions of AAIW during this time.

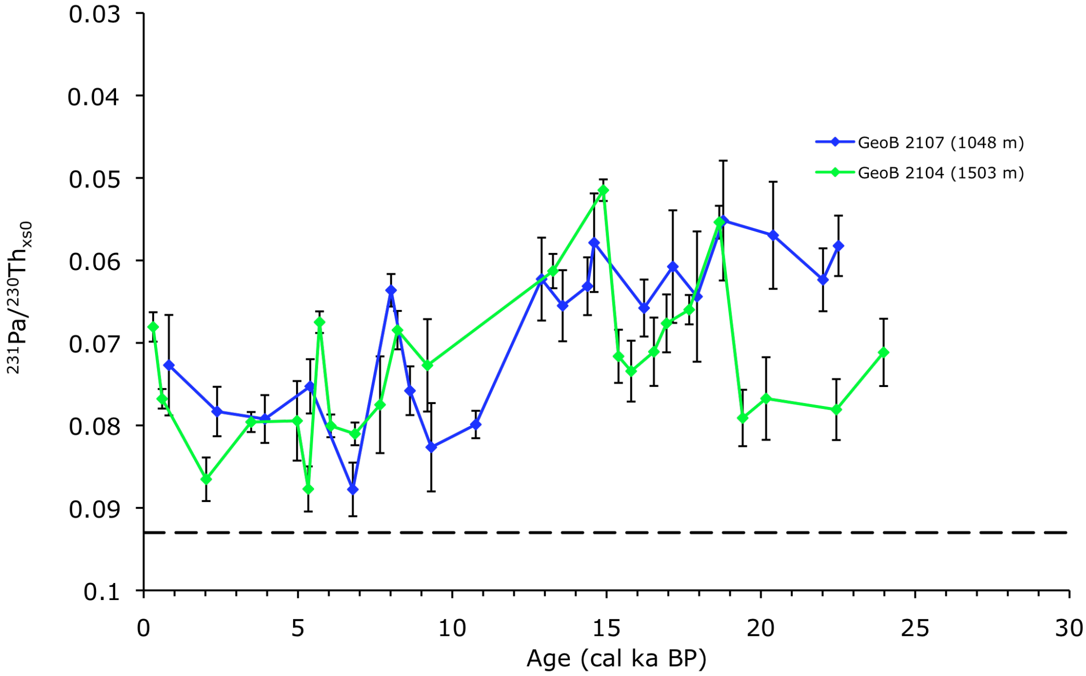

Figure 7.11: Downcore $^{231}Pa/^{230}Th$ ratios in cores GeoB 2107 (1048m) and GeoB 2104 (1503m). A horizontal dashed black line is used to indicate the natural $^{231}Pa/^{230}Th$ production ratio (0.093).

At the LGM, $\delta^{13}C$ data from the Brazilian margin (Curry and Oppo 2005, Figure 6.20) indicate that the core of northern source waters (GNAIW) had shoaled to 1500 m and that AAIW at the LGM was present at depths down to only ~1000 m, some 500 m above core GeoB 2104. Average $^{231}Pa/^{230}Th$ values in cores GeoB 2107 and

GeoB 2104 are noticeably different at the LGM (19-23 ka) when mean ^{231}Pa/^{230}Th in GeoB 2107 = 0.058 ± 0.005, n = 4 and in GeoB 2104 = 0.077 ± 0.004, n = 4. A plausible explanation for these differences is that, during the LGM, ^{231}Pa/^{230}Th values in GeoB 2107 continue to reflect circulation of AAIW at 1000 m but ^{231}Pa/^{230}Th values in GeoB 2104 mainly reflect flow of GNAIW at this time, with AAIW further above core GeoB 2104 at the LGM relative to the Holocene. Given that GeoB 2107 and GeoB 2104 are located at depths only 500 m apart but show distinct ^{231}Pa/^{230}Th values at the LGM, this finding suggests that sedimentary ^{231}Pa/^{230}Th ratios are set by waters within approximately 500 m of the sediment surface.

7.4.4 Glacial-interglacial circulation changes at intermediate depths: faster AAIW at the LGM?

Modern day salinity profiles (WOCE) and glacial δ^{13}C data from the Brazilian margin (Curry and Oppo, 2005) indicate that core GeoB 2107 (1048 m) was located within AAIW both today and at the last glacial maximum (section 6.3.3).

^{231}Pa/^{230}Th values in core GeoB 2107 (Figure 7.12) are significantly lower at the LGM (average ^{231}Pa/^{230}Th = 0.058 ± 0.005, n = 4) than during the Holocene (average ^{231}Pa/^{230}Th = 0.077 ± 0.004, n = 8). As discussed in section 7.4.1, should variations in opal flux or particle flux in the Argentine Basin be driving the observed changes in ^{231}Pa/^{230}Th we would expect these fluxes to be lower at the LGM relative to the Holocene. However, both opal and particle flux in GeoB 2107 show a slight increase from Holocene to LGM values (Figure 7.1).

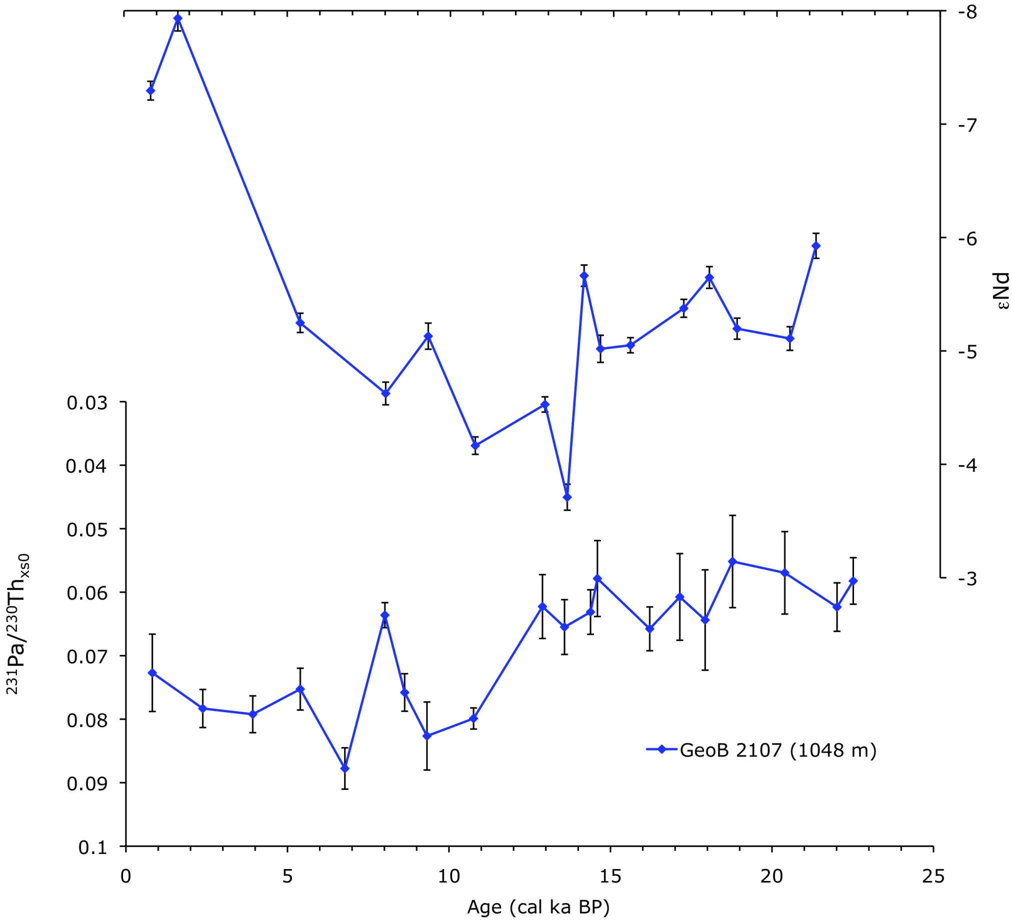

Figure 7.12: ^{231}Pa/^{230}Th and εNd records for intermediate depth core GeoB 2107 (1048 m). Nd data provided by Paul Carter at Bristol University.

An alternative explanation for lower ^{231}Pa/^{230}Th values in GeoB 2107 during the LGM is that opal and/or particle flux levels increase upstream of the GeoB 2107 core site at this time. Kumar et al. (1995) present evidence for a northward shift of the southern ocean opal belt at the LGM based on higher opal fluxes observed in sediments north of the Antarctic Polar Front during the LGM relative to the Holocene (Figure 7.13).

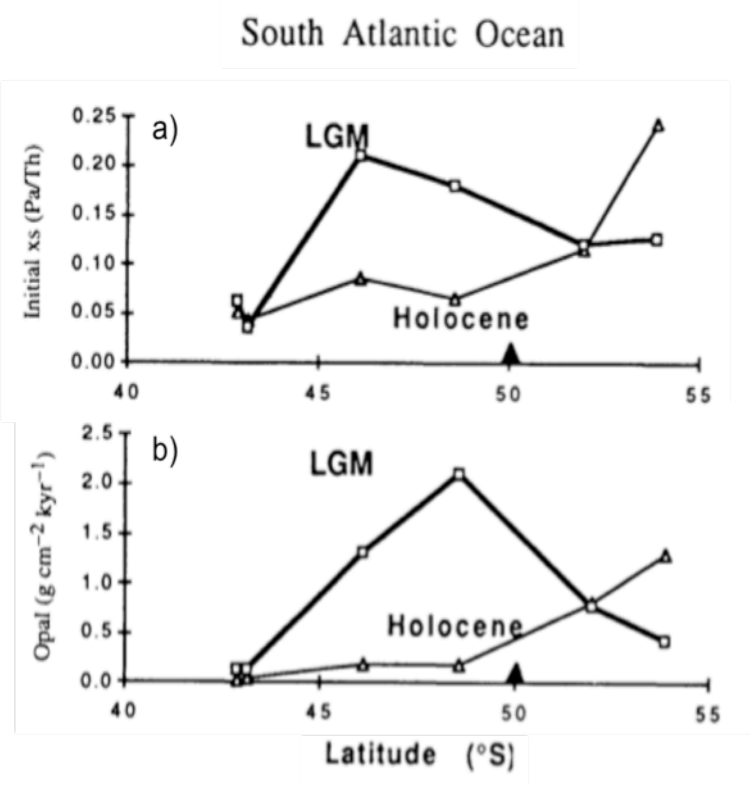

Figure 7.13: Average Holocene and LGM ^{231}Pa/^{230}Th ratios (a) and ^{230}Th normalized opal fluxes (b) from six sediment cores in the Atlantic sector of the Southern Ocean. Black filled triangle indicates the approximate latitude of the modern day Antarctic Polar Front. Adapted from Kumar et al. (1995).

As discussed in section 2.5, Pa and Th water column profiles for the southwest Indian Ocean, produced by Thomas et al. (2006), indicate that waters flowing from the Southern Ocean (AABW) had experienced Pa loss. This was attributed by Thomas et al. (2006) to scavenging of Pa as waters flow northwards through the opal belt at ~50°S. This finding suggests that scavenging of Pa from southern source waters passing through the opal belt would result in relatively low sedimentary ^{231}Pa/^{230}Th values immediately north of the opal belt at ~45°S during the LGM and at first sight offers a possible explanation for the lower ^{231}Pa/^{230}Th values in GeoB 2107 at the LGM even though GeoB 2107 is located significantly further north at 27°S.

However, the ^{231}Pa/^{230}Th record from GeoB 2112, a core bathed by AABW throughout the last 25 kyrs, shows higher ^{231}Pa/^{230}Th values at the LGM relative to the Holocene (i.e. the opposite change to GeoB 2107, Figure 7.5) and higher average LGM values relative to GeoB 2107. Given that both AABW and AAIW pass through the opal belt en route to the Argentine Basin from the south and should therefore be influenced by changes in upstream productivity in a similar manner, the inconsistencies between downcore $^{231}Pa/^{230}Th$ records of GeoB 2107 and GeoB 2112 suggest that upstream scavenging is not controlling $^{231}Pa/^{230}Th$ ratios in these sediments.

Lower $^{231}Pa/^{230}Th$ in GeoB 2107 at the LGM could also result from greater lateral advection of Pa associated with faster flow of AAIW. Greater production of AAIW at the LGM, as indicated by lower $Pa/^{230}Th$ values, may be due to stronger westerly winds over the Southern Ocean inducing unusually deep upwelling (Toggweiler and Samuels, 1995) and increased northward Ekman drift such that sub Antarctic surface waters, freshened by net precipitation, feed the formation of Antarctic Intermediate Water (Rickaby and Elderfield, 2005).

Other studies have provided evidence for higher production and northward expansion of AAIW at the LGM relative to today. Based on measurements of redox sensitive metals Re and Mn in sediments, Muratli et al. (2010) observed an increase in the depth range of well oxygenated waters off Chile at the LGM, interpreted as reflecting a glacial increase in production of oxygen rich AAIW.

Lynch-Stieglitz et al. (1994) examined glacial sediment $\delta^{18}O$ and $\delta^{13}C$ data from the southern continental margin of Australia in conjunction with $\delta^{18}O$ and $\delta^{13}C$ data from sediments in the North Indian and Southern Ocean to infer a reduced contribution to glacial AAIW of North Indian Ocean Intermediate Water relative to Antarctic Surface Waters, indicating that AAIW in the glacial was cooler, less saline and better ventilated than AAIW today. This paleoceanographic evidence is in agreement with several modeling studies which predict greater formation of AAIW during the glacial (e.g. Ganopolski et al., 1998; Liu et al., 2002; Meissner et al., 2005).

An increase in production of AAIW during abrupt cooling events in the north Atlantic during the deglacial (HS1, YD) is suggested by Rickaby and Elderfield (2005) who observed the characteristic chemical signature of AAIW (based coupled benthic Cd/Ca and $\delta^{13}C$ data) in sediments from the high latitudes of the North Atlantic, and also by Pahnke et al. (2008) who observed an increase in Nd isotope values in intermediate depth cores from the tropical and South Atlantic during HS1 and the YD. In addition, Pahnke and Zahn (2005) suggest AAIW in the Pacific was enhanced during northern hemisphere stadials based on comparisons between benthic $\delta^{13}C$ data in sediments from the southwest Pacific and the North Atlantic. However, evidence for increase in circulation rate of AAIW during HS1 and the YD is not seen in the $^{231}Pa/^{230}Th$ record of GeoB 2107. A model study investigating the sensitivity of $^{231}Pa/^{230}Th$ to changes in circulation state by Rae (2007) found that $^{231}Pa/^{230}Th$ values are less sensitive to change at high circulation states due to increased lateral advection of ^{230}Th with ^{231}Pa. The absence of any significant change to $^{231}Pa/^{230}Th$ in GeoB 2107 during HS1 and the YD (Figure 7.11) may therefore be due to low sensitivity of $^{231}Pa/^{230}Th$ to increases in circulation when the circulation rate of AAIW is already high during the deglacial, as indicated by mean deglacial $^{231}Pa/^{230}Th$ values of 0.063 ± 0.005, n = 7.

Given the lack of evidence for either a local or upstream scavenging control on ^{231}Pa/^{230}Th in core GeoB 2107, the ^{231}Pa/^{230}Th data from this core can best be explained by faster flow of AAIW during the LGM and deglacial relative to the Holocene, consistent with evidence from various peleoceanographic studies discussed above.

7.4.5. LGM to Holocene changes in deep water mass geometry and circulation in the Argentine Basin.

At the LGM both GeoB 2109 (2504 m) and GeoB 2112 (4010 m) were bathed by southern source waters (i.e. AABW) as indicated by Nd isotope data (section 6.3.3). ^{231}Pa/^{230}Th values in GeoB 2109 average 0.062 ± 0.04, n = 2 at the LGM compared to 0.052 ± 0.002, n = 4 during the Holocene (Figure 7.14).

A similar LGM to Holocene change in ^{231}Pa/^{230}Th is observed in GeoB 2112 (4010 m) where average ^{231}Pa/^{230}Th values decrease from 0.069 ± 0.001, n = 3 at the LGM to 0.053 ± 0.001, n = 5 for the Holocene. Given the weak correlation between both opal and particle fluxes with ^{231}Pa/^{230}Th for these cores as discussed above (Figure 7.8), these higher ^{231}Pa/^{230}Th values are inferred to reflect weaker circulation of southern sourced waters at depths greater than 2500 m at the LGM relative to flow of NADW during the Holocene (average Holocene ^{231}Pa/^{230}Th in core GGC5 from the North Atlantic = 0.055 ± 0.02, n = 10).

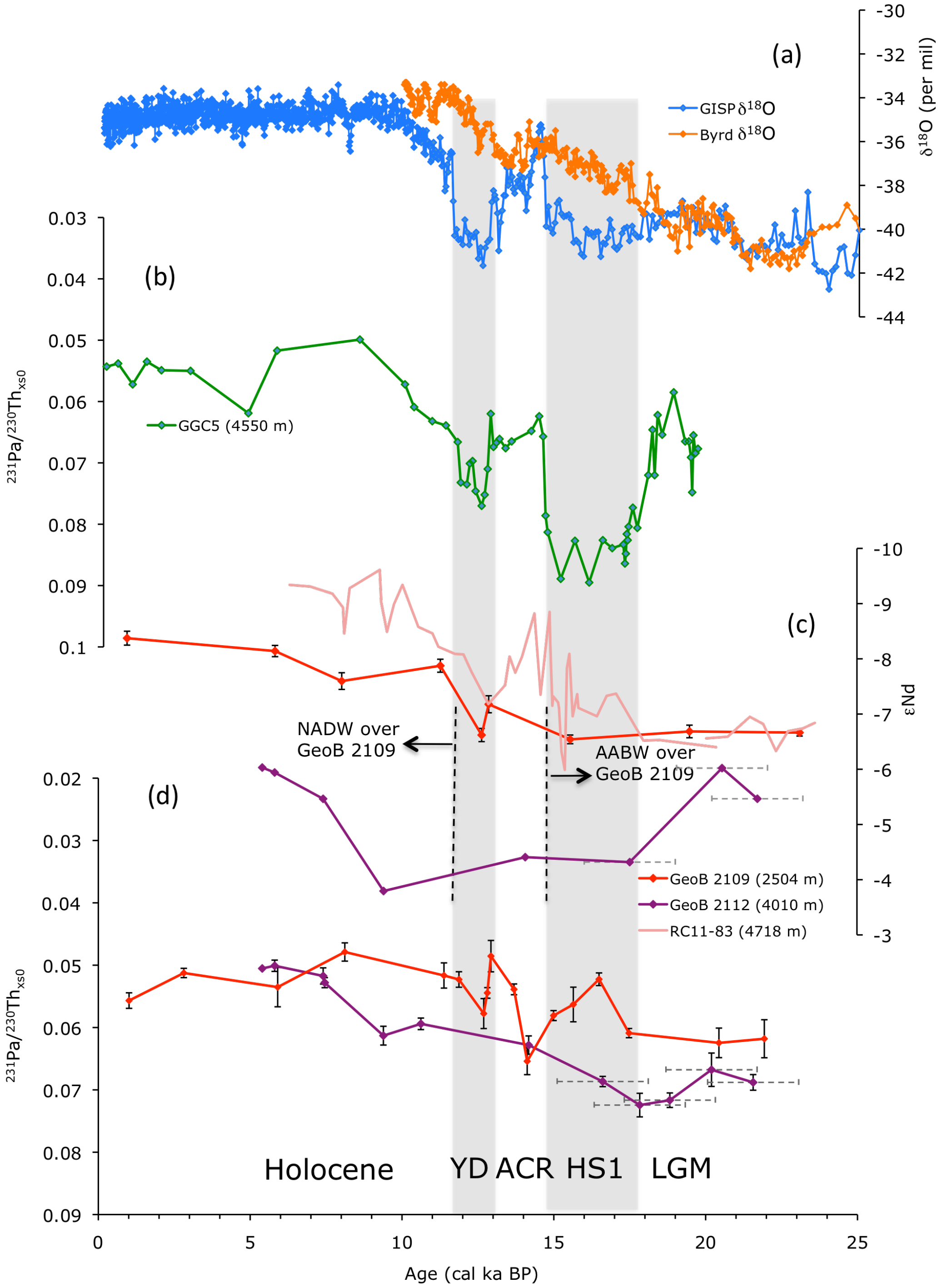

Figure 7.14: Changes in deep water mass geometry and circulation in the Argentine Basin since the LGM inferred from ^{231}Pa/^{230}Th and Nd records. **(a)** Ice core δ^{18}O data from Greenland (GISP, blue line) and Antarctica (Byrd, orange line). **(b)** ^{231}Pa/^{230}Th data from core GGC5 from the Bermuda Rise in the North Atlantic (4550m, light green, McManus et al. 2004). **(c)** Nd records from cores GeoB 2109 (2504 m, red) and GeoB 2112 (4010 m, purple) in the Argentine Basin and from core RC11-83 in the Cape Basin (4718m, pink line, Piotrowski et al. 2005). **(d)** ^{231}Pa/^{230}Th data from GeoB 2109 (2504 m, red) and GeoB 2112 (4010 m, purple). Grey shaded vertical bars represent periods of cooling over Greenland (HS1, YD). The horizontal error bars in **(c)** and **(d)** are the estimated age uncertainty associated with GeoB 2112 samples prior to ~16 ka, as discussed in section 5.5.

Although ^{231}Pa/^{230}Th values in GeoB 2109 and GeoB 2112 are higher at the LGM relative to the Holocene, they are still significantly below the production ratio (0.093) indicating that whilst deep ocean circulation in the Atlantic was reduced at the LGM, northward flow of AABW was far from completely sluggish.

During HS1, a time of significant cooling over Greenland, constant or lower Nd values in GeoB 2109 and GeoB 2112 indicate the continued presence of AABW at depths greater than 2500 m in the Argentine Basin. At this time ^{231}Pa/^{230}Th values are observed to decrease in GeoB 2109, indicating enhanced lateral export of Pa associated with as an increase in production of AABW. Changes in ^{231}Pa/^{230}Th in cores bathed by AABW in relation to abrupt cooling episodes in the north are discussed in section 7.4.7.

As discussed in chapter 6 (section 6.3.3), Nd values in core RC11-83 (4718 m) from the Cape Basin are observed to decrease following HS1, indicating a stronger influence of northern source waters (i.e. NADW) in the South Atlantic during the ACR (at ~14 ka). This is supported by a recent study of Barker et al. (2010) who observed significantly younger than modern ^{14}C ventilation ages in core TNO57-21 from the deep South Atlantic Ocean (TNO57-21; 41.1^{o}S, 7.8^{o}E, 4981 m) during the ACR, consistent with an increased presence of well ventilated northern source waters. ^{231}Pa/^{230}Th values in GeoB 2109 and GeoB 2112 are observed to reach ~0.065 at this time (Figure 7.14), values almost identical to those observed in core GGC5 (4550 m) from the Bermuda Rise at this time (= ~0.064 at 14 ka). Similar ^{231}Pa/^{230}Th values are also observed between core GGC5 and cores GeoB 2109 and GeoB 2112 in the Holocene, when NADW was present at depths greater than 2500 m in the south

Atlantic, supporting the possibility that northern source waters were present at great depths in Argentine Basin during the ACR. Nd values in GeoB 2109 during the Younger Dryas are the same as prior to 15 ka, indicating the return to a dominant flow of AABW at mid depths in the Argentine Basin. This is in agreement with Nd data from GeoB 2107, which shows a sharp increase from 5.5 ‰ during the ACR to maximum values of -3.8‰ at the start of the YD (Figure 7.12) reflecting a reduced contribution of northern source waters to the south during the Younger Dryas.

A decrease in εNd from -6.6 ‰ at 12.6 ka to -7.9 ‰ at 11.4 ka together with increasing δ^{13}C values in GeoB 2109 following the Younger Dryas indicate a greater contribution of southward flowing NADW at 2500 m during the late deglacial (Figure 7.14). This is consistent with the core of northern source waters in this region deepening from ~1600 m at the LGM to 2500 m in the Holocene as discussed in chapter 6 (Figure 6.20, section 6.3.3).

^{231}Pa/^{230}Th and Nd values in GeoB 2109 (2500 m) remain relatively uniform (^{231}Pa/^{230}Th = 0.048-0.055, εNd = -7.6 ‰ to -8.4 ‰) throughout the Holocene indicating the continued presence of vigorous and well ventilated NADW. Average Holocene ^{231}Pa/^{230}Th values in GeoB 2109 (0.052 ± 0.002, n = 4) are surprisingly low given the expected export of Pa with NADW from the North Atlantic, where average Holocene ^{231}Pa/^{230}Th values of 0.055 ± 0.02, n = 10 are observed in core GGC5 from the Bermuda Rise (McManus et al. 2004). The lower than expected Holocene ^{231}Pa/^{230}Th values in GeoB 2109 may be due to removal of Pa from NADW by boundary scavenging as this water mass flows south as a deep western boundary current along the continental margin of north America en route to the Argentine Basin.

^{231}Pa/^{230}Th values in GeoB 2112, a core that has remained within AABW throughout the last ~25 kyr, are similar to those at 2500 m in the mid Holocene (~0.050 between ~7.5 and 5.5 ka). Given that GeoB 2109 is bathed by NADW throughout the Holocene, the similarity in ^{231}Pa/^{230}Th values between these two cores suggest that ^{231}Pa/^{230}Th values in GeoB 2112 may be reflecting flow of NADW above AABW in the water column. This is consistent with the modern day location of GeoB 2112 being close to the boundary between AABW and NADW in the water column (Figure 3.3, chapter 3). The decrease in GeoB 2112 ^{231}Pa/^{230}Th between 9.4 and 7.4 ka (from 0.061 to 0.051) is observed to coincide with a decrease in εNd (-6.6 ‰ to -7.9 ‰). This suggests that the presence of NADW in the Argentine Basin at 4000 m may not have been established until ~7.5 ka at 4000 m, some 3-4 kyr after NADW is observed at 2500 m in GeoB 2109. However, the low data resolution in the early Holocene of GeoB 2112 m means it is not possible to accurately assess the timing of a transition from northward flow of AABW to southward flow of NADW at 4000 m in the Argentine Basin.

7.4.6 Glacial-interglacial circulation changes inferred from ^{231}Pa/^{230}Th time slice profiles: Comparison with North Atlantic ^{231}Pa/^{230}Th records

Gherardi et al., (2009) compared ^{231}Pa/^{230}Th records from multiple cores between ~1700 m and 4500 m in the North Atlantic in order in order to investigate the evolution of the geometry and rate of formation of deep waters in the North Atlantic for the last 20,000 years. Analysis of ^{231}Pa/^{230}Th records from the four Argentine Basin cores between ~1000 m and 4000 m in this work allows for a similar study to be made for the South Atlantic and directly assess the relationship between shallow and deep water circulation on glacial-interglacial timescales between hemispheres.

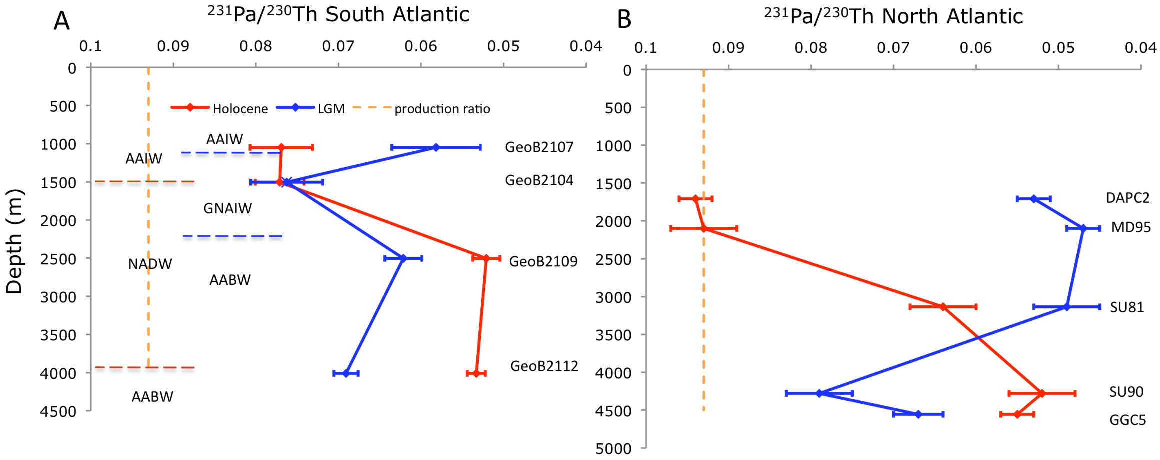

Figure 7.15: Sedimentary ^{231}Pa/^{230}Th time slices versus water depth from (A) Argentine Basin sediments and (B) North Atlantic sediments (Gherardi et al., 2009). A vertical orange dashed line is used to show the ^{231}Pa/^{230}Th production ratio (0.093). Approximate depths of water mass boundaries for the Holocene (red) and LGM (blue) in the southwest Atlantic are based on δ^{13}C data from Brazilian margin cores as described in chapter 6, (section 6.2.3, figure 6.21). The ^{231}Pa/^{230}Th scale is inverted in order to show strong MOC on the right-hand side and a reduced MOC on the left-hand side of each figure.

During the Holocene, intermediate depth cores GeoB 2107 (1048 m) and GeoB 2104 (1503 m) in the South Atlantic (Figure 7.15, A) record high average ^{231}Pa/^{230}Th values (GeoB 2107 = 0.077 ± 0.004, n = 8, GeoB 2104 = 0.077 ± 0.003, n = 12). ^{231}Pa/^{230}Th values are significantly lower at greater depths, averaging 0.052 ± 0.004, n

= 4 in GeoB 2109 (2504 m) and 0.053 ± 0.001, n = 5 in GeoB 2112 (4010 m). A similar ^{231}Pa/^{230}Th depth profile is observed in North Atlantic sediments during the Holocene (Figure 7.15, B) where high ^{231}Pa/^{230}Th values at or in excess of the production ratio are observed at intermediate depths down to ~2200 m and decrease to progressively lower values are at greater depths (~0.065 at ~3000 m, ~0.055, 4500 m). Should variations in ^{231}Pa/^{230}Th values mainly reflect changes in circulation in the location of these cores, these results indicate that both the north and South Atlantic were dominated by vigorous flow of NADW at great depths during the Holocene, with relatively weak overturning of intermediate waters above.

The Holocene pattern of Atlantic circulation described above appears to have been very different during the glacial. At the LGM, low ^{231}Pa/^{230}Th values (0.058 ± 0.005, n = 5) are observed at 1000 m depth in the south Atlantic whilst even lower values are observed at ~1500 m and at 2200 m in the North Atlantic (~0.053, 0.045) indicating vigorous flow of AAIW and GNAIW respectively. ^{231}Pa/^{230}Th values of 0.076 ± 0.004, n = 5 observed in GeoB 2104 (1504 m), located within the core of GNAIW in the South Atlantic at the LGM, are not consistent with lower ^{231}Pa/^{230}Th values of ~0.053 (core DAPC2, 1709 m) observed at similar depths in the North Atlantic. This may be due to the scavenging of excess Pa exported with rapid flow of GNAIW far from its source. In contrast to the low ^{231}Pa/^{230}Th values at intermediate depths, relatively high ^{231}Pa/^{230}Th values are observed in both the south and north Atlantic at depths greater than 4 km during the LGM, with GeoB 2112 averaging ^{231}Pa/^{230}Th values of 0.069 ± 0.001, n = 3 and North Atlantic records at 4.3 km (core SU90) and 4.5 km (core GGC5) depth averaging LGM ^{231}Pa/^{230}Th values of 0.079 and 0.067

respectively. These higher ^{231}Pa/^{230}Th values at depth are consistent with the increased presence of a relatively sluggish and poorly ventilated AABW throughout the Atlantic basin at this time (e.g. Marchitto et al., 2002; Curry and Oppo, 2005).

The observation of rapid circulation at intermediate depths during the LGM relative to weaker overturning of deep waters is consistent with the requirement that at least one water mass is rapidly renewed in order to maintain the distinct vertical structure of water masses seen in nutrient proxies at the LGM (Curry and Oppo 2005), that would otherwise be erased by wind and tidal mixing (Wunsch, 2003).

North and south Atlantic records differ at mid depths during the LGM where in the north low ^{231}Pa/^{230}Th values (0.049) similar to those observed at intermediate depths are seen at 3000 m (core SU81), where as in the South Atlantic GeoB 2109 (2500 m) shows average LGM ^{231}Pa/^{230}Th values of 0.064, closer to deep water ^{231}Pa/^{230}Th values. A possible explanation for these differences is that rapid overturning may have extended down to mid depths in the North Atlantic at the LGM but only reached intermediate depths in the South Atlantic, consistent with the core of northern source waters in the Argentine Basin deepening from ~1600 m at the LGM to ~2500 m in the Holocene (Curry and Oppo, 2005, Figure 6.20).

The lack of any significant north-south gradient in deep water (AABW or NADW) ^{231}Pa/^{230}Th values during either the LGM or the Holocene is surprising. During the LGM the difference in ^{231}Pa/^{230}Th values between core GGC5 (0.067) from the deep northwest Atlantic and core GeoB 2112 (0.069), both bathed by AABW, is 0.002. In the Holocene, the difference in ^{231}Pa/^{230}Th values between core GGC5 (0.055) and core GeoB 2109 (0.052), both bathed by NADW is 0.003. A significant gradient in ^{231}Pa/^{230}Th between hemispheres might have been expected given the export of Pa with southward flowing NADW to the Southern Ocean during the Holocene and export of Pa with northward flowing AABW to the North Atlantic during the LGM. As discussed in section 7.4.5, the lower than expected north-south ^{231}Pa/^{230}Th gradient may be due to removal of Pa from NADW and AABW by boundary scavenging as these water masses flow along the continental margin of North America as a deep western boundary current.

7.4.7. Rapid flow of SCW during abrupt circulation changes in the North Atlantic: evidence for a bipolar seesaw?

Distinctly low ^{231}Pa/^{230}Th values are observed in GeoB 2109 and GeoB 2112 at ~23.5 ka and also at 16.5 ka in GeoB 2109 (Figure 7.16). Unfortunately, no samples were measured around 16.5 ka in GeoB 2112 due to the lower sedimentation rate of this core. These lower ^{231}Pa/^{230}Th values suggest increased flow of southern source AABW during these intervals, given the lack of local opal and particle flux control on ^{231}Pa/^{230}Th in the Argentine Basin as discussed above.

Opposite signals of high ^{231}Pa/^{230}Th values are observed in North Atlantic sediment records during HS2 (core ODP1063, Lippold et al., 2009) and HS1 (core GGC5, McManus et al., 2004), suggesting a possible bipolar seesaw relationship between deepwater circulation changes in the north and the South Atlantic on abrupt timescales.

A comparison of these abrupt changes in ^{231}Pa/^{230}Th values in the north and south, together with oxygen isotope data from Greenland and Antarctica, allows for some assessment of the relative timing of circulation changes between northern and southern water masses (Figure 7.16). However, it is acknowledged that higher data resolution of cores GeoB 2109 and GeoB 2112 would be required to make an accurate assessment of the relative timing of changes in ^{231}Pa/^{230}Th values between hemispheres on millennial timescales.

Figure 7.16 shows that during HS2 and HS1, increasing ^{231}Pa/^{230}Th values in North Atlantic sediment cores coincided with colder temperatures as indicated by a decrease in δ^{18}O in Greenland ice cores.

There is some evidence for a similar relationship but of opposite signal between ^{231}Pa/^{230}Th in Argentine Basin sediments and δ^{18}O data from Antarctica ice cores. During HS1 and toward the end of HS2, peaks of low ^{231}Pa/^{230}Th values are observed to occur during or soon after periods of increasing oxygen isotope values, suggesting a possible link between warming in the south and increased circulation of AABW.

^{231}Pa/^{230}Th values in GeoB 2109 and GeoB 2112 are noticeably lower toward the end of HS2 than during the LGM, with minimum values of 0.038 observed in GeoB 2109 at ~23.5 ka and a minimum of 0.052 at ~23 ka in GeoB 2112. There is a disagreement in ^{231}Pa/^{230}Th values between the two cores at ~25 ka when ^{231}Pa/^{230}Th values are observed to reach 0.075 in GeoB 2112. This maximum ^{231}Pa/^{230}Th value is observed to coincide with a maximum in particle flux and opal flux (Figure 7.4). However, similarly high particle and opal fluxes are also observed at 23 ka in GeoB 2112 when ^{231}Pa/^{230}Th values are at minimum levels, inconsistent with a productivity or opal flux control on ^{231}Pa/^{230}Th values. Given the large estimated age uncertainty of the GeoB

2112 age model (± 1500 years) it is possible that the sample at ~25 ka in GeoB 2112 (Figure 7.16) may have a true age closer to 26.5 ka, a time when similarly high ^{231}Pa/^{230}Th values are observed in GeoB 2109.

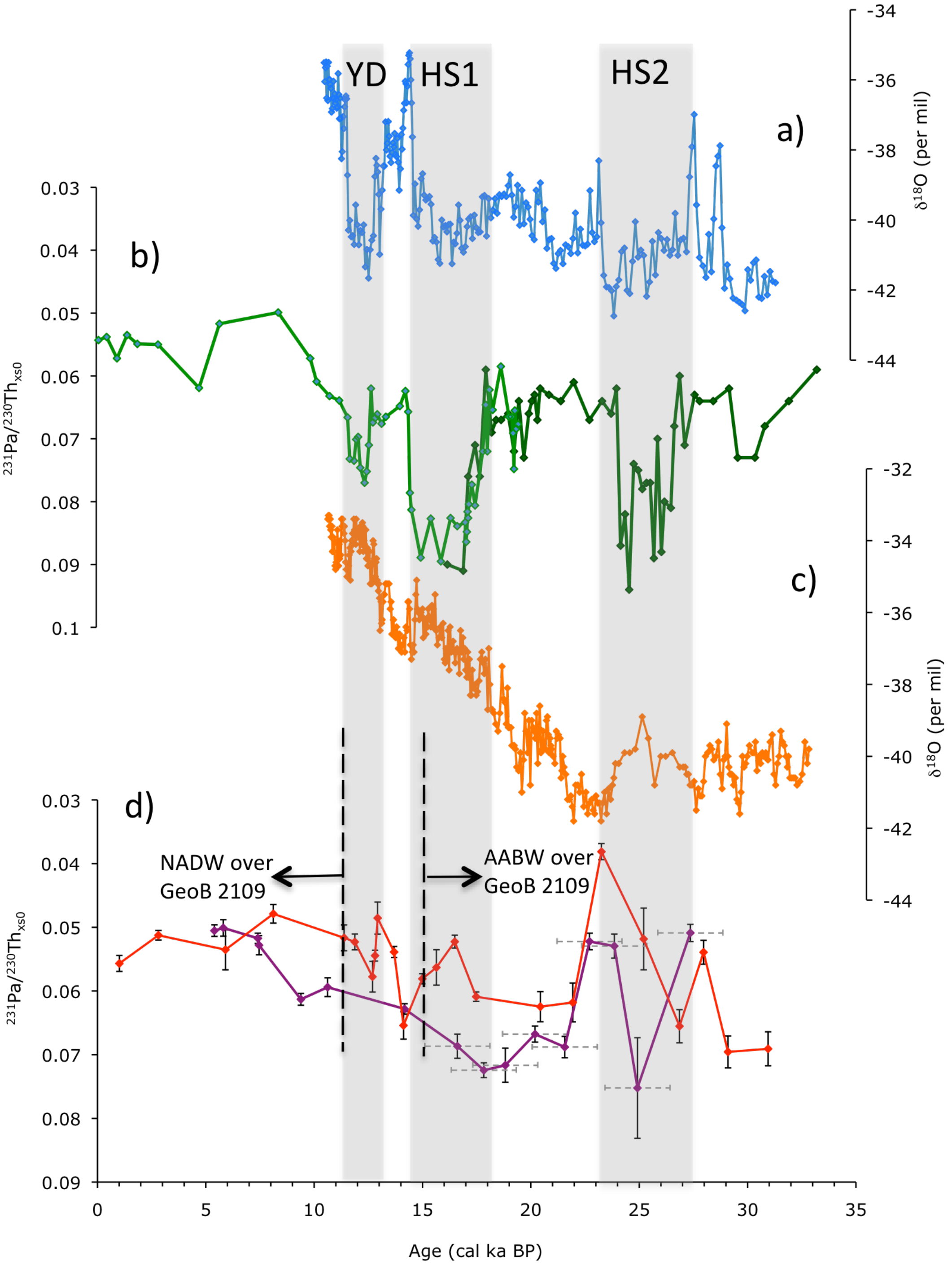

Figure 7.16: A direct comparison between ^{231}Pa/^{230}Th records from the North and South Atlantic, together with a) Greenland (GISP, blue) and c) Antarctica (Byrd, orange) δ^{18}O records. North Atlantic ^{231}Pa/^{230}Th records (b) are from cores GGC5 (light green, 33°42’ N, 57°33 W’, depth 4584 m, McManus et al., 2004) and ODP1063 (dark green, 33°41 N, 57°37 W’ 4550 m, Lippold et al., 2009). South Atlantic ^{231}Pa/^{230}Th records (d) are from cores GeoB 2109 (red, 2504 m) and GeoB 2112 (purple, 4010 m). A vertical dashed black line is used to indicate the transition from southern to northern source waters flowing over the core site of GeoB 2109 in southwest Atlantic.

The low ^{231}Pa/^{230}Th data resolution of GeoB 2109 and GeoB 2112 around the time of H2 make it difficult to accurately assess the relative timing of changes in ^{231}Pa/^{230}Th and temperature in the Southern Hemisphere. Although further data in required to improve assessment of millennial scale changes in ^{231}Pa/^{230}Th at this time, the minimum peaks in ^{231}Pa/^{230}Th seen in GeoB 2109 and GeoB 2112 around 23.5 ka (Figure 7.16) are observed to lag a peak in oxygen at ~25 ka seen in the Byrd ice core record from Antarctica. This apparent time lag is in contrast to the near synchronous relationship between ^{231}Pa/^{230}Th and oxygen observed in the north (core ODP1083, Lippold et al. 2009) at the beginning of HS2.

A possible mechanism consistent with these observations is one in which deep water formation of NADW/GNAIW is first inhibited due to freshwater inputs from the North American ice sheet. Heat previously transported northward to the high latitudes of the North Atlantic via surface currents is then redistributed from the tropics to the south, leading to cooling over Greenland and warming over Antarctica. Evidence of warming in the South Atlantic during abrupt intervals of northern hemisphere cooling is presented by Barker et al. (2009) who observed a sharp decline in the percentage of polar species of planktonic foraminifera in core TNO57-21 (4981 m) from the southeast Atlantic (41.1 S, 7.8 E) during HS1 and HS2. Subsequent reduction of sea ice cover around Antarctica (Gersonde et al., 2005) together with a poleward shift in the westerlies (Toggweiler et al., 2006) would in turn lead to greater wind induced upwelling and a progressive increase in deep overturning of the Southern Ocean. This is consistent with the physical requirement that global rates of deep water formation must balance global deep upwelling (Munk and Wunsch, 1998). Enhanced deep overturning in the Southern Ocean and increased production of AABW would consequently lead to greater lateral export of Pa with AABW to the North Atlantic, resulting in lower ^{231}Pa/^{230}Th in the sediments of GeoB 2109 and GeoB 2112.

Changes in ^{231}Pa/^{230}Th appear more synchronous between hemispheres during HS1 in comparison to HS2, with minimum ^{231}Pa/^{230}Th values in GeoB 2109 at 16.5 ka occurring at the same time as maximum ^{231}Pa/^{230}Th values in the north (core GGC5), offering further support for a strong link between northern and southern hemisphere deep water formation on abrupt timescales.

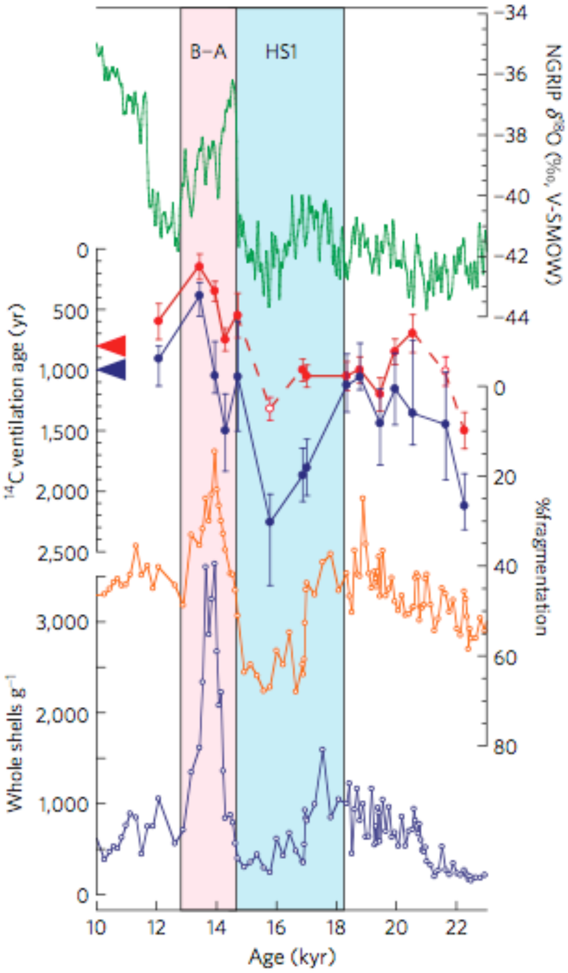

Figure 7.17: Deglacial radiocarbon and carbonate preservation in core TN057-21 (4981 m, 41.1°S, 7.1°E) from the deep southeastern Atlantic (Barker et al., 2010). ^{14}C ventilation ages are plotted as benthic-planktic age differences (red) and using a projection age method (blue). Increased carbonate dissolution is observed to occur within HS1 (blue rectangle), consistent with a greater contribution of relatively corrosive AABW; enhanced preservation occurs during the B-A (pink rectangle).

The interpretation of enhanced formation of AABW during periods of northern hemisphere cooling in the deglacial are supported by recent findings by Barker et al.

(2010) who observed a significant increase in the ^{14}C ventilation age in core TNO57-21 (4981 m) from the deep South Atlantic during HS1 (Figure 7.17), reflecting an increased penetration of southern source deep waters into the Atlantic Ocean, rich in aged carbon from deep waters of the Southern Ocean. This is consistent with observations of depletions in ^{14}C in intermediate waters in the eastern North Pacific during HS1 and YD by Marchitto et al. (2007). The redistribution of carbon from the abyss to the upper ocean and atmosphere in connection with enhanced deep overturning in the Southern Ocean is also reflected by atmospheric CO_2 concentrations which are observed to increase rapidly during the YD and HS1 (Marchitto et al. 2007).

Conclusions

In the Argentine Basin, opal fluxes are significantly lower than in other ocean regions, such as the Southern Ocean, where opal has been shown to have a strong correlation with sedimentary ^{231}Pa/^{230}Th. Neither opal nor particle fluxes were found to have a significant correlation with ^{231}Pa/^{230}Th in the study cores from the Argentine Basin, suggesting that changes in ocean circulation in this region are likely to explain much of the variability in ^{231}Pa/^{230}Th.

The four study cores, located over a depth range of 1-4 km in the Argentine Basin, show distinct downcore ^{231}Pa/^{230}Th records for the last ~25 kyrs, indicating that ^{231}Pa/^{230}Th in sediment is set by flow of the bottom most water mass in the water column. More specifically, ^{231}Pa/^{230}Th ratios are likely to be set by waters within approximately 500 m of the sediment surface, given the disparity in records between cores GeoB 2107 and GeoB 2104 at the LGM, located within different water masses just 500 m apart in the water column.

GeoB 2107 (1048 m), a core bathed in AAIW throughout out the last 25 kyrs, shows significantly lower ^{231}Pa/^{230}Th values in the LGM relative to the Holocene. This observation is best explained by faster flow of AAIW at the LGM consistent with both paleoceanographic and modeling observations of indicating increased production and extent of AAIW in the glacial.

At greater depths, ^{231}Pa/^{230}Th values in GeoB 2109 and GeoB 2112 (4010 m) at the LGM are relatively high in comparison to the Holocene, yet remain significantly below the production ratio, suggesting that AABW production was far from completely sluggish at this time. A transformation from southern to northern source waters flowing over GeoB 2109 (2504m) in the late deglacial, as indicated by εNd and δ^{13}C data, is observed to coincide with a decrease in ^{231}Pa/^{230}Th values indicating the replacement of AABW with more vigorous NADW at 2500 m in the South Atlantic.

A comparison of average Holocene and LGM ^{231}Pa/^{230}Th values in the four GeoB study cores with existing North Atlantic ^{231}Pa/^{230}Th records points to the operation of two contrasting modes of ocean circulation in the Atlantic during the LGM and the Holocene. At the LGM, lower ^{231}Pa/^{230}Th values in intermediate depth cores, observed in both the South and North Atlantic, suggest rapid renewal of intermediate depth water masses AAIW and GNAIW whilst less vigorous flow of AABW, indicated by higher ^{231}Pa/^{230}Th values, floods the entire Atlantic basin at greater depths. In contrast, during the Holocene relatively high ^{231}Pa/^{230}Th values at intermediate depths indicate weaker production of intermediate waters in comparison to a more vigorous flow of NADW below.

On millennial timescales, there is evidence for increasing formation of AABW in the Argentine Basin during Heinrich Stadials 1 and 2 and the Younger Dryas, when ^{231}Pa/^{230}Th values are observed to increase in Argentine Basin deep core records. Minimum ^{231}Pa/^{230}Th values in the south occur whilst maximum ^{231}Pa/^{230}Th are observed in deep North Atlantic, suggesting a possible inverse coupling of deep water production between hemispheres. During HS2, a significant delay between warming in Antarctica and minimum ^{231}Pa/^{230}Th values in deep cores from the Argentine Basin suggest that perturbations in deep water production of NADW/GNAIW, possibly related to meltwater discharges from the North American ice sheet, are responsible for driving reorganizations in deep water mass circulation in both hemispheres of the Atlantic Ocean.

Chapter 8: Summary and Conclusions

Southern source water masses are a major component of the global ocean conveyor and are responsible for the storage and distribution of huge quantities of heat and carbon. Understanding variations in the past rate of circulation of these water masses is therefore of critical importance for assessing the influence of ocean circulation on Earth's climate. To investigate the circulation rates and distribution histories of southern source waters in the southwest Atlantic for the past ~25 kyrs, four sediment cores from the Argentine Basin were analysed for $^{231}Pa/^{230}Th$, $\delta^{13}C$ and εNd data. Located over a depth range of 1-4 km, these cores were selected to sample modern day AAIW and AABW in addition to NADW far from its source, allowing for direct comparison of past circulation rates of northern and southern source waters on millennial as well as glacial-interglacial timescales.

The potential influence of composition and flux of scavenging particles on $^{231}Pa/^{230}Th$ of were assessed by measuring biogenic silica and evaluating past changes in particle flux by ^{230}Th normalization. Total particulate fluxes are found to correlate well with lithogenic inputs (average r^2 =0.729), which in turn are observed to be strongly controlled by sea level, with reduced sea levels at the LGM shifting sediment deposition to the shelf break and increasing sediment fluxes at intermediate depths. However, particle fluxes show a weak correlation with $^{231}Pa/^{230}Th$ across all four study cores (average r^2 =0.035).

Opal fluxes in the Argentine Basin were found to be low in comparison to other ocean regions where biological productivity has been observed to show a strong control on sediment ^{231}Pa/^{230}Th (e.g. Anderson et al., 2009). ^{230}Th normalized opal fluxes are observed to show a weak correlation with ^{231}Pa/^{230}Th across all core samples in the Argentine Basin (average r^2 =0.068). Given the lack of a local control of both opal and particle fluxes on ^{231}Pa/^{230}Th, changes in ^{231}Pa/^{230}Th in the study area are inferred to mainly reflect lateral advection of Pa related to changes in circulation.

Opal fluxes and additional productivity proxies authigenic U and Cd/Ca, although inconsistent, suggest that productivity in the Argentine Basin was greatest at the LGM. Local changes in productivity can not explain the disparity in authigenic U records between cores given their close proximity to one another. Instead, authigenic U profiles are more likely to reflect the distinct oxygen concentrations of the different water masses bathing each core site.

Downcore ^{231}Pa/^{230}Th records from the four study cores show distinct differences with depth, indicating that ^{231}Pa/^{230}Th in sediments are reflective of flow conditions in the bottom most water mass rather than representing average flow conditions over the entire water column. This is most clear from the distinctly different downcore ^{231}Pa/^{230}Th profiles of GeoB 2107 (1048 m) and GeoB 2112 (4010 m), located within AAIW and AABW respectively, which can not easily be explained by changes in particle flux or composition.

On glacial to interglacial timescales, significantly lower ^{231}Pa/^{230}Th values are observed in the shallowest core, GeoB 2107 (1048 m), bathed by AAIW throughout the last 25 kyrs. Given the lack of evidence for a local or far field control on

^{231}Pa/^{230}Th ratios, these data are best be explained by an increase in AAIW circulation at the LGM, consistent with paleoceanographic and modeling evidence of a more prominent mass of AAIW during glacial times. Evidence for faster AAIW during the abrupt northern hemisphere cooling events of the deglacial (HS1, YD), as suggested by recent studies (e.g. Pahnke et al. 2008), is not seen here, although this may be due to ^{231}Pa/^{230}Th values being less sensitive to change when flow rates are already high, as indicated by continuously low ^{231}Pa/^{230}Th values in GeoB 2107 across the deglacial.

Comparison of average Holocene and LGM ^{231}Pa/^{230}Th values from Argentine Basin cores with average time slice ^{231}Pa/^{230}Th records from North Atlantic sediments compiled by Gherardi et al. (2009) indicate that vigorous circulation occurred at intermediate depths in both the north and South Atlantic during the LGM, with less rapid circulation taking place at greater depths. This glacial pattern of circulation is observed to have reversed in the Holocene, when lower ^{231}Pa/^{230}Th values are observed at greater depths in both hemispheres suggesting the operation of two distinctly different modes of circulation in the Atlantic on glacial-interglacial timescales. A transformation between these two modes of circulation is observed in the South Atlantic from ^{231}Pa/^{230}Th, δ^{13}C and εNd data in core GeoB 2109 (2504 m), with moderate flow of AABW during the LGM replaced by a more vigorous flow of NADW at great depths during the Holocene.

On millennial timescales, significant changes in ^{231}Pa/^{230}Th are observed in deep cores GeoB 2109 and GeoB 2112 between the late glacial and Holocene, providing some evidence for enhanced AABW formation during northern hemisphere stadials.

The low ^{231}Pa/^{230}Th values observed in the deep southwest Atlantic during HS2, HS1 and the YD are observed to contrast with maximum ^{231}Pa/^{230}Th values in North Atlantic sediments, suggesting a close inverse coupling of deep water formation between hemispheres. The shifts to lower ^{231}Pa/^{230}Th in GeoB 2109 and GeoB 2112 can not be easily explained by opal or particle flux data and are therefore interpreted to reflect greater lateral advection of Pa away from these core sites due to enhanced AABW formation. This is consistent with several studies which show evidence for a strong presence of southern sourced waters in the North Atlantic during northern hemisphere stadials (e.g. Skinner and Shackleton, 2005, Robinson et al., 2004, Roberts et al., 2009).

The observation of high ^{231}Pa/^{230}Th values in North Atlantic sediments during abrupt cooling over Greenland has previously been interpreted as reflecting a decrease in Pa export to the south due to reduced NADW formation (McManus et al., 2004). However, given that ^{231}Pa/^{230}Th data from Argentine Basin cores in this study indicate that ^{231}Pa/^{230}Th is set by the bottom most water mass, combined with evidence for enhanced flow of AABW into the North Atlantic during northern hemisphere stadials, a logical explanation for the high ^{231}Pa/^{230}Th values in deep North Atlantic sediments is that they reflect export of Pa with AABW from the south to the north as opposed to reduced export of Pa to the south with northern source waters. This is supported by recent work on North Atlantic sediments by Roberts et al. (2009) who observed increases in ^{231}Pa/^{230}Th to maximum values during the YD and HS1 to be synchronous with increases in Nd in core GGC5 from the Bermuda Rise, indicating that changes in $^{231}Pa/^{230}Th$ values in the north are directly related to an increase in contribution of southern sourced waters.

The replacement of northern sourced waters with AABW during northern hemisphere stadials may also explain the strong correlation observed between diatom abundance and $^{231}Pa/^{230}Th$ values in North Atlantic records during HS2 and HS1 (Lippold et al. 2009). The increase in diatom abundance may reflect a change in the silica concentration of ocean water (Keigwin and Boyle, 2008) and is consistent with a northward penetration of silica rich southern source waters during these intervals, fuelling the production of diatoms which scavenge excess Pa exported to the north with AABW, possibly accounting for the high $^{231}Pa/^{230}Th$ ratios during these intervals.

Comparison of $^{231}Pa/^{230}Th$ and ice core $\delta^{18}O$ records in both hemispheres indicate that, whilst $^{231}Pa/^{230}Th$ and $\delta^{18}O$ changes in the north were of a synchronous nature during HS2 and HS1, $^{231}Pa/^{230}Th$ changes in the south lagged behind Antarctic temperature during HS2. This suggests that perturbations to deep ocean circulation in the Southern Ocean may have originated in the North Atlantic, possibly due to meltwater inputs triggering a reduction in deep water formation and subsequent redistribution of heat to the south. This in turn could lead to progressive renewal of deep water formation in the south through increased wind strengths and associated wind induced upwelling in the Southern Ocean. This proposed mechanism is consistent with climate records being out of phase between hemispheres throughout the last glacial in which warming in Antarctica was observed to occur on average ~1500 years after abrupt cooling in Greenland (Blunier and Brook, 2001).

Results from this study indicate a dynamic link between deep water production in the south and the north, on both glacial-interglacial and abrupt timescales. This has strong implications for Earth's climate given the capability of deep waters in the southern hemisphere to redistribute vast quantities of heat and carbon around the oceans and into the Earth's atmosphere.

Additional paleocirculation records from the South Atlantic are needed to build on these results, particularly with regard to assessing changes in deep water circulation rates between hemispheres on abrupt timescales. Future studies should ideally focus on high sedimentation rate cores located at mid depths (~2000-3000 m), so as to contain enough carbonate needed to produce a suitable age model for assessment of changes on abrupt timescales, but deep enough to record changes in the circulation and distribution of northern and southern sourced deep water masses. From the cores used in this study, further work to improve the resolution of ^{231}Pa/^{230}Th and Nd data in core GeoB 2109 around the abrupt climate events of the late glacial and deglacial will help to constrain the timing and magnitude of changes in the circulation of northern and southern water masses and cement the evidence presented here for a bipolar seesaw relationship in deep water production between hemispheres.

Bibliography

Abouchami, W., Goldstein, S.L, Gazer, S.J.G, Eisenhauer, A., and Mangini, A. (1997). “Secular changes of lead and neodymium in central Pacific seawater recorded by a Fe-Mn crust.” Geochimica et Cosmochimica Acta, **61**: 3957-3974.

Adkins, J. F., Cheng, H., Boyle., E.A., Druffel, E.R.M., and Edwards, R.L. (1998). "Deep-Sea Coral Evidence for Rapid Change in Ventilation of the Deep North Atlantic 15,400 Years Ago." Science **280**: 725-728.

Ahmed, S.M., and Labeyrie, L.D. (1994). "Glacial to Interglacial Holocene $\delta^{13}C$ variations in intermediate depth water masses of the north Indian Ocean." Geo-Marine Letters **14**: 26-40.

Anderson, R. F. (1982). "Concentration, vertical flux, and remineralisation of particulate uranium in seawater." Geochimica et Cosmochimica Acta **46**: 1293-1299.

Anderson, R. F., Ali, S., Bradtmiller, L. I., Nielsen, S.H.H., Fleisher, M.Q., Anderson, B.E., and Burckle, L.H. (2009). "Wind-driven upwelling in the Southern Ocean and the deglacial rise in atmospheric CO_2." Science **323**: 1443–1448.

Anderson, R. F., Bacon, M.P., and Brewer, P.G. (1983). "Removal of ^{230}Th and ^{231}Pa at ocean margins." Earth and Planetary Science Letters **66**: 73-90.

Arz, H.W., Patzold, J., and Wefer, G. (1998). "Correlated millenial-scale changes in surface hydrography and terrigenous sediment yield inferred from last glacial marine deposits off northeastern Brazil." Quaternary Research **50**: 157-166.

Arz, H.W., Patzold, J., and Wefer, G. (1999). "The deglacial history of the western tropical Atlantic as inferred from high resolution stable isotope records off northeastern Brazil." Earth and Planetary Science Letters **167**: 105-117.

Bacon, M. P. and Anderson, R.F. (1982). "Distribution of thorium isotopes between dissolved and particulate forms in the deep sea." Journal of Geophysical Research **87** (C3).

Bard, E. (1988). "Correction of accelerator mass spectrometry ^{14}C ages measured in planktic foraminifera: Paleoceanographic implications." Paleoceanography **3**: 635-645

Barker, S., Knorr, G., Vautravers, M.J., Diz, P. and Skinner L.C. (2010). "Extreme deepening of the Atlantic overturning circulation during deglaciation." Nature Geoscience **3**: 567-571

Blunier, T., and Brook, E.J. (2001). "Timing of millennial-scale climate change in Antarctica and Greenland during the last glacial period". Science **291**, 109-112.

Boebel, O., Schmid, C., Podesta, G., and Zenk, J. (1999). "Intermediate water in the Brazil-Malvinas Confluence Zone: a Lagranian view." Journal of Geophysical Research **104** (9): 21,063-21,082

Bopp, C.J., Lundstorm, C., Johnson, T., and Glesner, J.J.G. (2009) "Variations in ^{238}U/^{235}U in Uranium ore deposits: Isotopic signatures of the U reduction processes" Geology **37** (7): 611-614.

Boyle, E. A. and Keigwin, L. (1987). "North Atlantic thermohaline circulation during the past 20,000 years linked to high-latitude surface temperature." Nature **330**: 35-40.

Boyle, E. A. (1986). "Paired Cd and $\delta^{13}C$ data from benthic foraminifera: implication for ocean circulation, phosphorous and atmospheric CO_2." Geochimica et Cosmochima Acta **50**: 265-276.

Bradtmiller, L. I., Anderson, R.F., Fleisher, M.Q., and Burckle, L.H (2009). "Comparing glacial and Holocene opal fluxes in the Pacific sector of the Southern Ocean." Paleoceanography **24** 2214, doi: 10.1029/2008PA001693.

Broecker, W. S. (2004). "The role of the ocean in climate; yesterday, today and tomorrow." Eldigio Press, Columbia University, USA.

Broecker, W. S. (1991). "The great conveyor belt." Oceanography **4**: 79-89.

Broecker, W. S., and Maier-Reimer, E. (1992). "The influence of air-sea exchange on the carbon isotope distribution in the sea." Global Biogeochemical Cycles **6**: 315-320.

Broecker, W. S. (1994). "Massive iceberg discharges as triggers for global climate change." Nature **372**: 1582-1588.

Broecker, W. S. (1997). "Thermohaline circulation, the achilles heel of our climate system: will man made CO_2 upset the current balance?" Science **278**: 421-424.

Broecker, W. S. (1998). "Paleocean circulation during the last deglaciation: A bipolar seesaw." Paleoceanography **13** (2): 119-121.

Broecker, W.S., and Maier-Reimer, E. (1992). "The influence of air-sea exchange on the carbon isotope distribution in the sea." Global Biogeochemical Cycles **6** (3): 315-320.

Carter, P (2009). "Testing the bipolar seesaw with Nd isotopes in the Argentine Basin" Ph.D thesis chapter 6. Bristol University.

Chase, Z., Anderson, R.F., Fleisher, M.Q., and Kubik, P.W. (2002). "The influence of particle composition and particle flux on scavenging of Th, Pa and Be in the ocean." Earth and Planetary Science Letters **204** (1-2): 215-229.

Chase, Z. and Anderson, R.F. (2004). Comment on "On the importance of opal, carbonate and lithogenic clays in scavenging and fractionation Th, Pa and Be in the ocean" by Luo, S. and Ku, T.L. Earth and Planetary Science Letters **220** 213-222.

Chiang, J.C.H., Biasutti, M., and Battisti D.S. (2003). "Sensitivity of the Atlantic Intertropical Convergence Zone to Last Glacial Maximum boundary conditions." Paleoceanography **18** (4): DOI 10.1029/2003PA000916.

Chen, J.H., Edwards, R.L., and Wasserburg, G.J. (1986). "^{238}U, ^{234}U and ^{232}Th in seawater." Earth and Planetary Science Letters **80**: 241-251.

Chiu, T.C., Fairbanks, R.G., Mortlock, R.A., and Bloom, A.L. (2005). "Extending the radiocarbon calibration beyond 26,000 years before present using fossil coral records." Quaternary Science Reviews **24**: 1797-1808

Choi, M.S, Francois, R., Sims, K., Bacon, M.P., Brown-Leger, S., Fleer, A.P., Ball, L., Schneider, D., and Pichat, S. (2001). "Rapid determination of ^{230}Th and ^{231}Pa in seawater by desolvated micro-nebulization inductively coupled magnetic sector mass spectrometry". Marine Chemistry **76**: 99-112

Clark, P. U., Pisias, G.N., Stocker, T.F., Weaver, A.J. (2002). "The role of the thermohaline circulation in abrupt climate change." Nature **415** (6874): 863-869.

Cochran, J. K. (1992). "The oceanic chemistry of the uranium and thorium series nuclides." Uranium-series disequilibrium: Applications to earth, marine, and environmental sciences. Clarendon: 334–395.

Colling, A., Brown, E., Park, D., Phillips, J., Rothery, D., and Wright, J. (2001). "Ocean Circulation". The Open University, Oceanography Series. Butterworth Heinemann.

Coplen, T. P. (1996). Editorial. "More uncertainty than necessary." Paleoceanography **11:** 369-370.

Curry, W. B., N.J. Shackleton et al., (1998). "Changes in the $\delta^{13}C$ distribution of deep water $\sum CO_2$ between the last glaciation and the Holocene." Paleoceanography **3** (3): 117-121.

Curry, W. B., Duplessy, J.B., Labyrie, L.D., and D. W. Oppo (2005). "Glacial water mass geometry and the distribution of $\delta^{13}C$ and CO_2 in the western Atlantic Ocean." Paleoceanography **20**: doi10.1029/2004PA001021.

Dansgaard, W. (1993). "Evidence for general instability of past climate from a 250-kyr ice core record." Nature **364**: 218-220.

DePaolo, D.J., and Wasserburg. G.J. (1976). "Nd isotopic variations and petrogenetic models." Geophyscial Research Letters **3**: 249-252.

Dunk R.M., Jenkins W.J., and Mills, R.A. (2002). "A re-evaluation of the oceanic uranium budget." Chemical Geology. **190**: 45-67.

Duplessy, J. C., Shackleton, N.J., Matthews,.R.K., Prell, W., Ruddiman, W.F., Caralp, M., and Hendy, C. (1984). "^{13}C record of benthic foraminifera in the last interglacial ocean: implications for the carbon cycle and the global deep water circulation." Quaternary Research **21**: 225-243.

Duplessy, J. C., Shackleton, N.J., Fairbanks, R.G., Labeyrie, L., Oppo, D., and Kallel, N (1988). "Deep water source variations during the last climatic cycle and their impact on the global deep water circulation." Paleoceanography **3** (3): 343-360.

Edwards, R. L., Chen, J.H., and Wasserburg, G.J. (1986). "^{238}U-^{234}U ^{230}Th-^{232}Th systematics and the precise measurement of time over the past 500,000 years." Earth and Planetary Science Letters **81**: 175-192.

Elderfield, H., Upstill-Goddard, R., and Sholkovitz, E.R. (1990). "The rare earth elements in rivers, estuaries, and coastal seas and their significance to the composition of ocean waters." Geochimica et Cosmochimica Acta **54** (4): 971-991.

Elliot, M., Labeyrie, L., and Duplessy, J.C (2002). "Changes in North Atlantic deep-water formation associated with the Daansgaard-Oeschger temperature oscillations (60-10 ka)." Quaternary Science Reviews **21** (10): 1153-1165.

Fairbanks, R. G. and E. Bard (1990). "The age and origin of the younger Dryas climate event in Greenland ice cores." Paleoceanography **5**(6): 937-948.

Fairbanks, R. G., Mortlock, R.A., Chiu, T.C., Cao, L., Kaplan, A., Guilderson, T.P., Fairbanks, T.W., Bloom, A.L., Grootes, P.M., and Nadeau, M.J (2005). "Radiocarbon calibration curve spanning 10,000 to 50,000 years BP based on paired ^{230}Th/^{234}U/^{238}U and ^{14}C dates on pristine corals." Quaternary Science Reviews **25**: 1781-1796.

Frank, M. (2002) "Radiogenic isotopes: Tracers of past ocean circulation and erosional input." Reviews of Geophysics **40**.

Francois, R., Altabet, M.A., Yu, E., Sigman, D.M., Bacon, M.P., Frank, M., Bohrmann, G., Bareille, G., and Labeyrie, L.D. (1997). "Contribution of Southern Ocean surface-water stratification to low atmospheric CO_2 concentrations during the last glacial period." Nature **389**: 929-934.

Ganachaud, A. and C. Wunsch (2000). "Improved estimates of global ocean circulation, heat transport and mixing from hydrographic data." Nature **408** (6811): 453-7.

Ganopolski, A. and Rahmstorf, S. (2001). "Rapid changes of glacial climate simulated in a coupled climate model." Nature **409**: 153-158.

Ganopolski, A., Rahmstorf, S., Petoukhov, V., and Claussen, M. (1998). "Simulation of modern and glacial climates with a coupled global model of intermediate complexity." Nature **391**: 351-356.

Garabato, A.C.N., Jullion, L., Stevens, D.P., Heywood, K.J., and King, B.A. (2009). "Variability of Subantarctic Mode Water and Antarctic Intermediate Water in the Drake Passage during the late twentieth and early twenty-first centuries." Journal of Climate **22** (13): 3661-3668.

Gherardi, J. M., Labeyrie, L., McManus, J.F., Francois, R., Skinner, L.C., and Cortijo, E. (2005). "Evidence from the Northeastern Atlantic basin for variability in the rate of the meridional overturning circulation through the last deglaciation [rapid communication]." Earth and Planetary Science Letters **240** (3-4): 710-723.

Gherardi, J. M., Labeyrie, L., Nave, S., Francois,. R., McManus, J.F., and Cortijo., E. (2009). "Glacial-interglacial circulation changes inferred from Pa/Th sedimentary records in the North Atlantic region." Paleoceanography **24** 2204, doi: 10.1029/2008PA001696.

Goldstein, S.J., and Jacobsen, S.B. (1988). "Nd and Sr isotopic systematics of river water suspended material: implications for crustal evolution." Earth and Planetary Science Letters **87** (3): 249-265.

Goldstein, S. J., Zylerberg, D., Pahnke, K., Hemming, S.R., and Van der Flierdt, T. (2007). "Quantifying changes in the global thermohaline circulation." A circum-Antarctic perspective. Paper presented at U.S. Geological Survey and The National Academies.

Gordan, A.L. (1996). "Comment on the South Atlantic's role in the global circulation." The South Atlantic: present and past circulation. Berlin, Srpinger-Verlag.

Guilderson, T. P., L. Burckle, et al. (2000). "Late Pleistocene sea level variations derived from the Argentine Shelf." Geochemistry, Geophysics, Geosystems **1**: 1-15.

Gutjahr, M., Frank, M., Stirling, C.H., Klemm, V., Van der Flierdt, T., and Halliday, A.N. (2007). "Reliable extraction of a deepwater trace metal isotope signal from Fe-Mn oxyhydroxide coatings of marine sediments." Chemical Geology **242**: 351-370.

Hall, I.R., McCave, N., Shackleton, N.J., Weedon, G., and Harris, S.E. (2001). "Intensified deep Pacific inflow and circulation in Pleistocene glacial times." Nature **412**: 809-812.

Hall, I.R., Moran, S., Zahn, R., Knutz., Shen, C.C., and Edwards. R.L (2006). "Accelerated drawdown of meridional overtunring in the late-glacial Atlantic triggered by transient pre-H event freshwater perturbation." Geophysical Research Letters, **33**, LL6616, doi: 10.1029/2006GL026239.

Heil, G. (2006). "Abrupt Climate Shifts in the Western Tropical to Subtropical Atlantic region during the Last Glacial." PhD thesis, University of Bremen.

Hemming, S. R. (2004). "Heinrich events: massive late Pleistocene detritus layers of the North Atlantic and their global climate imprint." Reviews of Geophysics **42** (1).

Henderson, G. M. and R. F. Anderson (2003). "The U-series Toolbox for Paleoceanography." Reviews in Mineralogy and Geochemistry **52** (1): 493-531.

Henderson, G. M., Heinze, C., Anderson, R.F., and Winguth, A.M.E. (1999). "Global distribution of the ^{230}Th flux to ocean sediments constrained by GCM modelling-implications for the use of the ^{231}Pa/^{230}Th ratio as a paleoproductivity proxy." Deep Sea Research Part I: Oceanographic Research Papers **46** (11): 1861-1893.

Henderson, G. M. and E. Maier-Reimer (2002). "Advection and removal of ^{210}Pb and stable Pb isotopes in the oceans. A GCM study." Geochimica et Cosmochimica Acta **66**: 257-272.

Hoefs, J. (2003). "Stable Isotope Geochemistry" Springer, Berlin

Jacobsen, S.B., and Wasserburg, G.J. (1980). "Sm-nd isotopic composition of chondrites." Earth and Planetary Science Letters **50**: 139-155.

Jones, G.A. (1994). "Holocene climate and deep ocean circulation changes: evidence from accelerator mass spectrometer radiocarbon dated Argentine Basin (SW Atlantic) mudwaves." Paleoceanography **9** (6): 1001-1016.

Keeling, R. F. and B. B. Stephens (2001). "Antarctic sea ice and the control of Pleistocene climate instability." Paleoceanography **16** (1): 112-131.

Keigwin, L. D. and E. A. Boyle (2008). "Did North Atlantic overturning halt 17,000 years ago?" Paleoceanography **16** PA1101, doi: 10.1029/2007PA001500.

Koroleff, F. (1983). "Determination of Silicon" In: Methods of seawater analysis 2nd ed. Edited by K. Grasshoff, K. Kremling and M.Ehrhardt. Verlag Chemie, Weinheim: 174-183.

Kowsmann, R.O., and de Ataide Costa. (1979). "Sedimentação quaternária da margem continental brasiliera e das áreas oceanicas adjacentes." In: Rechonhecimento global da margem continental brasiliera projecto REMAC edited by L.A.M de Mello, 55 pp. Petrobas, Rio de Jániero.

Kroopnick, P.M (1985). " The distribution of $\delta^{13}C$ in the world oceans." Deep Sea Research Part I **32**: 57-84.

Kuhlbrodt, T., Griesel, A., Montoya, M., Levermann, A., Hofmann., M., and Rahmstorf, S. (2007). " On the driving processes of the Atlantic Meridional Oveturning Circulation." Reviews of Geophysics **95** doi: 10.1029/2004RG000166.

Kumar, N., Anderson, R.F., Mortlock, R.A., Froelich, P.N., Kubik, P., Dittrich-Hannen, B., and Suter, M (1995). "Increased biological productivity and export production in the glacial Southern Ocean." Nature **378** (6558): 675-680.

Kumar, N., Gwiazda, R., Anderson, R.F., and Froelich, P.N (1993). "^{231}Pa/^{230}Th ratios in sediments as a proxy for past changes in Southern Ocean productivity." Nature **362** (6415): 45-48.

Langmuir, D. (1978). "Uranium solution mineral equilibria at low temperatures with applications to sedimentary ore deposits." Geochimica et Cosmochimica Acta **42** (6): 547-569.

Lao, Y., Anderson., R.F., Broecker, W.S., Hofmann, H.J., and Wolfi, W. (1993). "Particulate fluxes of Th, Pa and Be in the northeastern Pacific Ocean." Geochimica et Cosmochimica Acta **57**: 205-217.

Lippold, J., Grutzner, J., Winter, D., Lahaye, Y., Mangini, A., and Christl, L. (2009). "Does sedimentary ^{231}Pa/^{230}Th from the Bermuda Rise monitor past Atlantic meridional overturning circulation?" Geophysical Research Letters, **36**: L12601, doi: 10.1029/2009GL038068.

Lisiecki, L.E., and Raymo, M.E. (2005). "A Plio-Pleistocene stack of 57 globally distributed benthic δ^{18}O records." Paleoceanography **20**: DOI:10.1029/ 2004PA001071

Liu, Z., Shin, S., Otto-Bliesner, B., Kutzbach, J.E., Brady, E.C., and Lee, D. (2002). "Tropical cooling at the last glacial maximum and extratropical ocean ventilation." Geophysical Research Letters **29**: 1409.

Luo, S. and T. L. Ku (1999). "Oceanic ^{231}Pa/^{230}Th ratio influenced by particle composition and remineralization." Earth and Planetary Science Letters **220**: 201-211.

Luo, S. and T. L. Ku (2004). "On the importance of opal, carbonate and lithogenic clays in scavenging and fractionating ^{230}Th, ^{231}Pa and ^{10}Be in the oceans." Earth and Planetary Science Letters **167** (3): 183-195.

Lutjeharms, J.R.E. (1985). "Location of frontal systems between Africa and Antarctica: some preliminary results." Deep sea research. Part A. Oceanographic research papers **32** (12): 1499-1509.

Lyle, M., Mitchell, N., Mix, A., Martinez, J.I., and Paytan, A. (2005). "Do geochemical estimates of sediment focussing pass the sediment test in the equatorial Pacific?" Paleoceanography **20**: PA1005.

Lynch-Stieglitz, J., Adkins, J.F., Curry, W.B., Dokken, T., Hall, I.R., Herguera, J.C., Hirschi, J.J., Ivanova, E.V., Kissel, C., Marchal, O., Marchitto, T.M., McCave, I.N., McManus, J.F., Mulitza, S., Ninnemann, U., Peeters, F., Yu, E., and Zahm, R. (2007). "Atlantic Meridional Overturning Circulation During the Last Glacial Maximum." Science **316** (5821): 66.

Lynch-Stieglitz, J., Curry, W.B., Oppo, D.W., Charles, C.D., and Munson, J. (2006). "Meridional overturning circulation in the South Atlantic at the last glacial maximum." Geochemistry Geophysics Geosystems **7**: Q10N03.

Lynch-Stieglitz, J., and Fairbanks, R.G. (1994). "Glacial-interglacial history of Antarctic intermediate water: Relative strengths of Antarctic versus Indian Ocean sources." Paleoceanography **9** (1): 7-30.

Lynch-Stieglitz, J., Stocker, T.F., Broecker, W.S., and Fairbanks, R.G. (1995). "The influence of air-sea exchange on the isotopic composition of oceanic carbon: Observations and modelling." Global Biogeochem. Cycles **9** (4): 653–665.

Lynch-Stieglitz, J. (2003). "Tracers of past ocean circulation." In: Treatise on Geochemistry (eds. K. Turkikian and H.D.Holland) **6**: The Ocean and Marine Geochemistry. Elsevier.

Maamaatuaiahutapu, K., Provost, C., Andrie, C., and Vigan, X. (1999), "Origin and ages of mode waters in the Brazil-Malvinas Confluence region during austral winter 1994." Journal of Geophysical Research **104** (C9): 21051-21061.

Mackensen A., Hubberton, H.W., Bickert, T., and Fischer, G. (1993). "The $\delta\ ^{13}C$ in benthic foraminferal tests of Fontbotia weuellerstorfi relative to the $\delta\ ^{13}C$ of dissolved inorganic carbon in the Southern Ocean deep water: implications for Glacial ocean circulation models." Paleoceanography **8**: 587-591.

Marchal, O., François, R., Stocker, T.F., and Joos, F. (2000). "Ocean thermohaline circulation and sedimentary $^{231}Pa/^{230}Th$ ratio." Paleoceanography **15** (6): 625-641.

Marchitto, T. M. and W. S. Broecker (2006). "Deep water mass geometry in the glacial Atlantic Ocean: A review of constraints from the paleonutrient proxy Cd/Ca." Geochemistry Geophysics Geosystems **7** (12): QI2003, doi:10.1029/2006GC001323.

Marchitto, T. M., Oppo, D.W., and Curry W.B. (2002). "Paired benthic foraminiferal Cd/Ca and Zn/Ca evidence for a greatly increased presence of Southern Ocean Water in the glacial North Atlantic." Paleoceanography **17** (3): 1038.

Marchitto, T.M., Lehman, S.J., Ortiz, J.D., Fluckiger, J., and Van Green, A. (2007). "Marine radiocarbon evidence for the mechanism of deglacial atmospheric CO_2 rise." Science **316**: 1456-1459.

Mason, A.J and G.M Henderson (2010)."Correction of multi-collector-ICP-MS instrumental biases in high precision uranium-thorium chronology. International Journal of Mass Spectrometry **295** (1-2): 26-35.

Matsumoto, K., and Lynch-Stieglitz, J. (1999). "Similar glacial and Holocene deep water circulation inferred from southeast Pacific benthic foraminiferal carbon isotope composition." Paleoceanography **14**: 149-163.

McCartney, M.S. (1977). "Subantarctic Mode Water." In: A Voyage of Discovery. Edited by M. Angel. Deep Sea Research **24**: 103-119

McCave, I. N., Manighetti, B., and Beveridge N.A.S (2004). "Circulation in the glacial North Atlantic inferred from grain-size measurements." Nature **374**: 149-153.

McCave, I. N. and I. R. Hall (2006). "Size sorting in marine muds: Processes, pitfalls, and prospects for paleoflow-speed proxies." Geochemistry Geophysics Geosystems **7** (10): doi 10.1029/2006GC001284

McClaren, J. W., Beauchemin, D., and Berman, S.S. (1987). "Application of isotope dilution inductively coupled mass spectrometry to the analysis of marine sediments." Analytical Chemistry **59** (4): 610-613

McCorkle, D.C., Heggie, D.T., and Veeh, H.H. (1998). "Glacial and Holocene stable isotope distributions in the southeastern Indian Ocean." Paleoceanography **13**: 20-34

McManus, J. F., Francois, R., Gherardi, J.M., Keigwin, L.D., and Brown-Leger, S. (2004). "Collapse and rapid resumption of Atlantic meridional circulation linked to deglacial climate changes." Nature **248**: 834-837.

Meissner, K. J., Galbraith, E., and Volker, C. (2005). "Denitrification under glacial and deglacial conditions: A physical approach." Paleoceanography **20**: PA3001.

Mook, W.G., Bommerson, J.C., and Staverman, W.H. (1974). "Carbon isotope fractionation between dissolved bicarbonate and gaseous carbon dioxide" Earth and Planetary Science Letters **22**: 169-176.

Moore, J. K., Abbott, M. R., Richman, J., and Nelson, D. (2000). "The Southern Ocean at the last glacial maximum: A strong sink for atmospheric carbon dioxide." Global Biogeochemical Cycles **14** (1): 455-476.

Moran, S. B., Shen, C.C., Weinstein, S.E., Hettinger, L.H., Hoff, J.H., Edmonds, H.N., and Edwards R.L (2001). "Constraints on deep water age and particle flux in the Equatorial and South Atlantic Ocean based on seawater ^{231}Pa and ^{230}Th data." Geophysical Research Letters **28** (18): 3437-3440.

Mortlock, R.A and P.N. Froelich (1989). "A simple method for the rapid determination of biogenic opal in pelagic marine sediments." Deep Sea Research **36** (9): 1415-1426.

Muratli, J. M., Chase, Z., Mix, A.C., and McManus, J. (2010). "Increased glacial-age ventilation of the Chilean margin by Antarctic Intermediate Water." Nature Geoscience **3**: 23-26.

Munk, W. and C. Wunsch (1998). "Abyssal recipes II: energetics of tidal and wind mixing." Deep Sea Research Part I: Oceanographic Research Papers **45** (12): 1977-2010.

Niemann, S. (2003). "Pa and Th at the southeast South American continental margin." PhD thesis, Freie Universitat Berlin.

Oppo, D. W. and M. Horowitz (2000). "Glacial deep water geometry: South Atlantic benthic foraminiferal Cd/Ca and δ^{13}C evidence." Paleoceanography **15** (2): 147-160.

Osborne, N.S., Stimson, H.F., and Ginnings, D.C. (1939). "Measurements of heat capacity and heat of vaporization of water in the range 0 to 100°C." Journal of Research of the National Bureau of Standards **23**: 197-260.

Pahnke, K., Zahn, R., Elderfield, H., and Schulz, M. (2003). "340,000-Year Centennial-Scale Marine Record of Southern Hemisphere Climatic Oscillation." Science **301**: 948-952.

Pahnke, K., and Zahn, R. (2005). "Southern hemisphere water mass conversion linked with North Atlantic climate variability" Science **307**: 1741-1746.

Pahnke, K., Goldstein, S.L., and Hemming, S.R. (2008). "Abrupt changes in Antarctic Intermediate Water circulation over the past 25,000 years" Nature Geoscience **1**: 870-874.

Parish, T.R. (1988). "Surface winds over the Antarctic continent - a review." Reviews of geophysics and space physics **26**: 169-180.

Park, R., and Epstein, S. (1960). "Carbon isotope fractionation during photosynthesis" Geochimca et Cosmochimicha Acta **21**: 110-126.

Piepgras, D.J., and Wasserburg, G.J. (1987). "Rare-earth element transport in the western north Atlantic inferred from Nd isotopic observations." Geochimica et Cosmochimica Acta **51**: 1257-1271.

Piotrowski, A. M., Goldstein, S.L., Hemming, S., and Fairbanks, R. (2004). "Intensification and variability of ocean thermohaline circulation through the last deglaciation." Earth and Planetary Science Letters **225** (1-2): 205-220.

Potts, P.J. (1987). "A handbook of silicate rock analysis." Blackie Academic and Professional, London.

Rae, J.W.B (2007). "Testing the Bipolar Seesaw with Protactinium and Thorium Isotopes in the SW Atlantic." M.A thesis. University of Oxford

Rahmstorf, S. (2000). "The Thermohaline Ocean Circulation: A System with Dangerous Thresholds?" Climatic Change **46** (3): 247-256.

Rahmstorf, S. (2002). "Ocean circulation and climate during the past 120,000 years." Nature **419**: 207-214.

Rahmstorf, S. (2006). "Thermohaline Ocean Circulation." In: Encyclopaedia of Quaternary Sciences, Edited by S.A. Elias. Elevier, Amsterdam

Regelous, M., Turner, S.P., Elliot, T.R., Rostami, K and Hawkesworth, C.J. (2004). "Measurement of Femtogram Quantities of Protactinium in Silicate Rock Samples by Multicollector Inductively Coupled Plasma Mass Spectrometry." Analytical Chemistry **76**: 3584-3589.

Reid, J. L. (1994). "On the total geostrophic Circulation of the North Atlantic ocean: Flow patterns, tracers and transports." Progress in Oceanography.**33**: 1-92

Reid, J. L. (1989). "On the total geostrophic circulation of the South Atlantic ocean: Flow patterns, tracers and transports." Progress in Oceanography **23**: 149-244

Reid, J. L., Nowlin Jr, W.D., Patzert, W.C. (1977). "On the Characteristics and Circulation of the Southwestern Atlantic Ocean." Journal of Physical Oceanography **7** (1): 62-91.

Roberts, N. L., Piotrowski, A.M., McManus., J., and Keigwin, L. (2009). "Synchronous deglacial overturning and water mass source changes." Science **327**: 75-77.

Robinson, L. F., Adkins, J.F., Keigwin, L.D., Southon, J., Fernandez, D. P., Wang, S.L and Scheirer, D.S. (2005). "Radiocarbon Variability in the Western North Atlantic During the Last Deglaciation." Science **310** (5753): 1469-1473.

Robinson, L. F., G. M. Henderson, et al. (2004). "Climate control of riverine and seawater uranium isotope ratios." Science **305**: 851-854.

Robinson, L. F., Henderson, G.M, Hall, L., and Matthews, I. (2002). "U-Th dating of marine isotope stage 7 in Bahamas slope sediments." Earth and Planetary Science Letters **196** (3-4): 175-187.

Rutberg, R.L., Hemming, S.R., and Goldstein S.L., (1998)."Evidence for decreased NADW during glacial stages 2 and 4 from Nd isotopes in Southern Ocean sediments." Mineralogical Magazine **62** (A): 1304-5

Sabine, C.L., Feely, R.A., Gruber, N., Key, R.M., Kitack, L., Bullister, J.L., Wanninkhoff, R., Wong, C.S., Wallace, D.W.R., Tilbrook, B., Millero, F.J., Peng, T.H.Kozyr,A., Ono,T., and Rios, A.F. (2004). "The oceanic sink for anthropogenic CO_2." Nature **305**: 357-361.

Sarnthein, M., Winn, K., Jung, S.J.A., Duplessy, J.C., Labeyrie, L., Erlenkeuser, H., and Ganssen, G. (1994). "Changes in east Atlantic deepwater circulation over the last 30,000 years: Eight time slice reconstructions." Paleoceanography **9** (2): 209-268.

Schobbenhaus, C., Campos, D.A., Derzw, G.R and Asmus H.E. (1995) Geological Map of Brazil, Brazilian Geological Survey, Rio de Janiero.

Scholten, J.C., Fietzke, J., Mangini, A., Stoffers, P., Rixen, T., Gaye-Haake, B., Blanz, T., Ramaswamy, T., Sirocko, F., Schulz.H., and Ittekkot, V. (2005). "Radionuclide fluxes in the Arabian Sea: the role of particle composition." Earth and Planetary Science Letters **230**: 319-337.

Scholten, J.C., Fietzke, J., Mangini, A., Garbe-Schonberg, C.D., Eisenhauer, A., Schneider, R., andStoffers, P. (2008). "Advection and scavenging: effects on ^{230}Th and ^{231}Pa distribution off southwest Africa." Earth and Planetary Science Letters **271**: 159-169.

Shackleton, N.J., Hall, M.E., and Vincent, E. (2000). "Phase relationships between millennial scale events 64,000-24,000 years ago." Paleoceanography **15**: 565-569.

Siddall, M., Henderson, G.M., Edwards, N.R., Frank, M., Muller, S.A., Stocker, T.F., and Joos, F. (2005). "^{231}Pa/^{230}Th fractionation by ocean transport, biogenic particle flux and particle type." Earth and Planetary Science Letters **237** (1): 135-155.

Siddall, M., Stocker, T.F., Henderson, G.M., Joos, F., Frank, M., Edwards, N.R., Ritz, S.P., and Muller, S.A. (2007). "Modelling the relationship between ^{231}Pa/^{230}Th distribution in North Atlantic sediment and Atlantic meridional overturning circulation." Paleoceanography **22**: doi10.1029/2006PA001358.

Sigman, D.M., and Boyle, E.A. (2000). "Glacial-interglacial variations in atmospheric carbon dioxide." Nature **407**: 859-869.

Skinner, L.C. and N.J.Shackleton (2004). "Rapid transient changes in northeast Atlantic deep water ventilation across Termination I." Paleoceanography **19**: PA2005.

Slowey, N.C., and Curry, W.B. (1995). "Glacial-interglacial differences in circulation and carbon cycling within the upper western Atlantic." Paleoceanography **10**: 715-732.

Stephens, B. B. and R. F. Keeling (2000). "The influence of Antarctic sea ice on glacial-interglacial CO 2 variations." Nature **404** (6774): 171-174.

Stirling, C.H., Haliday, A.N., and Porcell, D. (2005). "In search of live CM-247 in the early solar system " Geochemica et Cosmochimca Acta **69** (4): 1059-1071.

Stocker, T. F. (1998). "The seesaw effect." Science (Washington, D. C.) **282** (5386): 61-62.

Stocker, T. F. and S. J. Johnsen (2003). "A minimum thermodynamic model for the bipolar seesaw." Paleoceanography **18** (4): 1087.

Stommel, H. (1961). "Thermohaline convection with two stable regimes of flow." Tellus **13** (2): 224-230.

Stramma, L. and M. England (1999). "On the water masses and mean circulation of the South Atlantic Ocean." Journal of Geophysical Research-Oceans **104** (C9): 20,863.

Stuvier, M and Grootes, P.M. (2000). "GISP2 oxygen isotope ratios." Quaternary Research **53**: 227-283.

Stuvier, M and Polach, H.A (1997). "Discussion: Reporting of ^{14}C data." Radiocarbon **19**: 355-363.

Sugden, D.E., McCulloch, R.D., Bory, A.J.M., and Hein, A.S. (2009). "Influence of Patagonian glaciers on Antarctic dust deposition during the last glacial period." Nature Geoscience **2**: 281-285.

Talley, L.D (2003). "Shallow, intermediate and deep overturning components of the global heat budget." Journal of Physical Oceanography **33**: 530-560.

Thomas, A. L. (2006) "Variations in past and present ocean circulation assessed with U-series nuclides." D.Phil thesis, University of Oxford.

Thomas, A. L., Henderson, G.M., and Robinson, L.F. (2006). "Interpretation of the ^{231}Pa/^{230}Th paleocirculation proxy: New water-column measurements from the southwest Indian Ocean." Earth and Planetary Science Letters **241** (3-4): 493-504.

Thomas, A. L., Henderson, G.M., and McCave, I.N (2007). "Constant bottom water flow into the Indian Ocean for the past 140 ka indicated by sediment ^{231}Pa/^{230}Th." Paleoceanography **21** doi:10.1029/2007PA001415.

Thomas, A. L., Henderson, G.M., Deschamps, P., Yokoyama, Y., Mason, A.J., Bard, E., Hamelin, B., Durand, N., and Camoin, G. (2009). "Penultimate deglacial sea-level timing from U/Th dating of Tahitian Corals." Science 324: 1186-1189.

Toggweiler, J. R., Russell, J.L., Carson, S.R. (2006). "The Mid-Latitude Westerlies, Atmospheric CO_2, and Climate Change during the Ice Ages." Paleoceanography **21** (2).

Toggweiler, J. R., and B. Samuels. (1995). "The Effect of the Drake Passage on the global thermohaline." Deep Sea Research part I **42**: 477-500.

Tsuchiya, M. (1989). "Circulation of the Antarctic Intermediate Water in the North Atlantic Ocean." Journal of marine research **47**: 747-755.

Usman, K. and T. D. MacMahon (2000). "Determination of the half-life of ^{233}Pa." Applied Radiation and Isotopes **52** (3): 585-9.

Van de Flierdt, T., Robinson, L.F., Adkins, J.F., Hemming, S>R., and Goldstein, S.L. (2006). "Temporal stability of the neodymium isotope signature of the Holocene to glacial North Atlantic." Paleoceanography **21**.

Wang, X., Auler, A.S., Edwards, R.L., Cheng, H., Cristalli, P.S., Smart, P.L., Richards, D.A and Shen, C.C. (2004). "Wet periods in northeastern Brazil over the past 210 kyr linked to distant climate anomalies." Nature **432**: 740-743.

Wang, X., Auler, A.S., Edwards, R.L., Cheng, H., An, Z.S., Wu, J.Y., Shen, C.C., and Dorale, J.A. (2001). "A high resolution absolute-dated Late Pleistocene monsson record from Hulu Cave, China." Science **294**: 2345-2348.

Warren, B. A. (1981). "Deep circulation of the world ocean." Evolution of Physical Oceanography pages 6-42. MIT press, Cambridge (Massachusetts).

Warren, B. A. (1983). "Why is no deep water formed in the North Pacific?" Journal of Marine Research **41** (2): 327-347.

Wunsch, C. (2003). "Determining paleoceanographic circulations, with emphasis on the Last Glacial Maximum." Quaternary Science Reviews **22**: 371–385.

You, Y. (2001). "Quantitative estimate of Antarctic Intermediate Water contributions from the Drake Passage and the Southwest Indian Ocean to the South Atlanitc." Journal of Geophysical Research **107**: 10.1029.

Yu, E. F., Francois, R., and Bacon, M.P (1996). "Similar rates of modern and last-glacial ocean thermohaline circulation inferred from radiochemical data." Nature **379** (6567): 689-694.

Appendix: Data tables

GeoB 2107 (1048 m)

Sample	Run	Depth (cm)	Age (yr)	$(^{231}Pa)_{xs0}$ (dpm/g)	2.S.E	$(^{230}Th)_{xs0}$ (dpm/g)	2.S.E	$(^{231}Pa/^{230}Th)_{xs0}$ (dpm/g)	2.S.E	Mass flux (g cm^{-2} ka^{-1})	2.S.E	Opal flux (mg cm^{-2} ka^{-1})
A1	4	1	817	0.123	0.005	1.635	0.014	0.075	0.003	1.611	0.014	47.153
A1 JR	JR3	1	817	0.129	0.017	1.851	0.010	0.070	0.009	1.423	0.008	41.314
A3	4	11.3	2379	0.135	0.005	1.727	0.015	0.078	0.003	1.525	0.013	40.908
A5	4	21.5	3926	0.138	0.005	1.743	0.027	0.079	0.003	1.511	0.023	45.138
A7	7	31.2	5397	0.145	0.006	1.928	0.027	0.075	0.003	1.366	0.019	45.086
A9	4	41.5	6778	0.144	0.005	1.644	0.017	0.088	0.003	1.602	0.017	45.273
A11	7	51	8016	0.095	0.003	1.500	0.022	0.064	0.002	1.756	0.026	54.235
A12	4	55.7	8629	0.107	0.004	1.417	0.015	0.076	0.003	1.858	0.019	64.333
A12r	7	55.7	8629	0.099	0.005	1.915	0.035	0.052	0.003	1.375	0.025	47.774
A13 JR	JR3	61	9319	0.103	0.007	1.245	0.008	0.083	0.005	2.115	0.014	45.170
A14	7	66.1	10761	0.081	0.002	1.114	0.009	0.073	0.002	2.365	0.020	56.635
A14r	12	66.1	10761	0.111	0.001	1.275	0.021	0.087	0.002	2.514	0.018	56.635
A15 JR	JR3	71.7	12895	0.072	0.006	1.155	0.008	0.062	0.005	2.280	0.017	60.218
A16	4	76.5	13577	0.064	0.003	1.014	0.010	0.063	0.003	2.493	0.016	53.300
A16 JR	JR3	76.5	13577	0.072	0.006	1.056	0.007	0.068	0.006	2.596	0.027	50.988
A18*	12	86.2	14094	0.048	0.002	-26.935	-41.706	-0.002	-0.006	-	-	-
A19r	6	91.6	14382	0.079	0.004	1.248	0.013	0.063	0.004	2.110	0.022	73.885
A20 JR	JR3	95.6	14595	0.075	0.008	1.304	0.010	0.058	0.006	2.020	0.015	57.450
A23	4	110.5	16215	0.077	0.004	1.172	0.016	0.066	0.004	2.247	0.031	57.388
A24 JR	JR3	116.2	17146	0.090	0.010	1.477	0.011	0.061	0.007	1.784	0.014	50.898
A25 JR	JR3	121	17930	0.092	0.011	1.431	0.010	0.064	0.008	1.840	0.013	48.489
A26 JR	JR3	126.2	18779	0.079	0.010	1.429	0.010	0.055	0.007	1.842	0.013	45.733
A28 JR	JR3	136.1	20396	0.076	0.009	1.334	0.009	0.057	0.006	1.974	0.014	55.464
A30	4	146	22013	0.081	0.005	1.297	0.022	0.062	0.004	2.030	0.035	57.081
A31	4	151.2	22515	0.077	0.005	1.314	0.020	0.058	0.004	2.003	0.030	43.361

Table 7.1: ^{231}Pa and ^{230}Th, corrected for lithogenic and authigenic components, (^{231}Pa/^{230}Th$_{xs}$)0, ^{230}Th normalized sediment flux and opal flux data for all samples from core GeoB 2107. ‘A’ denotes samples are from core GeoB 2107 and ‘r’ denotes replica measurements. An average of all replicated sample measurements was used for final data plots**.** ‘JR’ denotes samples measured by James Rae who worked exclusively on core GeoB 2107 for his masters thesis (J. Rae, 2007). * Sample A18 from run 12 was omitted from final data plots due negative read outs in the Th data.

GeoB 2107 (1048 m)

Sample	**Run**	**Depth** (cm)	**Age** (yr)	**(^{232}Th)** (dpm/g)	2.S.E	**(^{230}Th)** (dpm/g)	2.S.E	**(^{231}Pa)** (dpm/g)	2.S.E	**(^{238}U)** (dpm/g)	2.S.E	**δ^{234}U**	2.S.E	**^{238}U/^{232}Th**	2.S.E
A1	4	1	817	2.198	0.010	2.721	0.013	0.172	0.004	1.434	0.0000	-3.686	1.841	0.652	0.003
A1 JR	JR3	1	817	2.146	0.004	2.910	0.010	0.177	0.016	1.460	0.0005	-22.010	7.088	0.680	0.001
A3	4	11.3	2379	2.009	0.007	2.717	0.014	0.177	0.004	1.944	0.0000	40.239	1.841	0.968	0.003
A5	4	21.5	3926	2.016	0.011	2.733	0.025	0.177	0.004	2.095	0.0000	50.696	1.841	1.039	0.005
A7	7	31.2	5397	2.045	0.007	2.857	0.025	0.181	0.005	2.033	0.0000	40.872	5.707	0.994	0.003
A9	4	41.5	6778	1.822	0.005	2.510	0.016	0.172	0.004	1.706	0.0000	35.735	1.841	0.936	0.003
A11	7	51	8016	1.650	0.009	2.278	0.020	0.124	0.002	1.562	0.0000	29.561	5.707	0.947	0.005
A12	4	55.7	8629	1.686	0.005	2.210	0.013	0.133	0.003	1.497	0.0000	34.791	1.841	0.888	0.003
A12r	7	55.7	8629	2.427	0.014	3.023	0.032	0.142	0.004	1.672	0.0000	26.540	5.707	0.689	0.004
A13 JR	JR3	61	9319	1.521	0.004	1.973	0.007	0.126	0.005	1.505	0.0004	29.032	7.088	0.990	0.002
A14	7	66.1	10761	1.254	0.004	1.747	0.008	0.103	0.001	1.662	0.0000	40.062	5.707	1.326	0.004
A14r	12	66.1	10761	1.444	0.020	1.877	0.032	0.128	0.001	1.467	0.0000	47.873	1.473	1.016	0.014
A15 JR	JR3	71.7	12895	1.432	0.003	1.844	0.007	0.096	0.004	1.514	0.0004	27.480	7.088	1.057	0.002
A16	4	76.5	13577	1.392	0.005	1.696	0.009	0.089	0.002	1.477	0.0000	38.490	1.841	1.061	0.004
A16 JR	JR3	76.5	13577	1.358	0.004	1.711	0.006	0.094	0.004	1.424	0.0004	36.406	7.088	1.049	0.003
A18*	12	86.2	14094	-3.460	2.749	-25.403	-39.335	0.000	0.000	1.973	0.0001	38.960	1.473	-0.570	-0.453
A19r	6	91.6	14382	2.144	0.009	2.166	0.010	0.117	0.003	1.828	0.0000	25.235	1.048	0.853	0.004
A20 JR	JR3	95.6	14595	1.868	0.005	2.188	0.008	0.108	0.006	1.727	0.0008	20.084	7.088	0.925	0.003
A23	4	110.5	16215	2.030	0.005	2.145	0.014	0.112	0.003	1.772	0.0000	21.643	1.841	0.873	0.002
A24 JR	JR3	116.2	17146	2.018	0.009	2.424	0.009	0.122	0.007	1.932	0.0006	33.796	7.088	0.957	0.004
A25 JR	JR3	121	17930	2.127	0.009	2.452	0.008	0.127	0.008	2.069	0.0006	8.636	7.088	0.973	0.004
A26 JR	JR3	126.2	18779	2.132	0.007	2.448	0.008	0.117	0.007	2.055	0.0004	19.134	7.088	0.964	0.003
A28 JR	JR3	136.1	20396	1.997	0.004	2.291	0.007	0.111	0.006	1.954	0.0007	34.365	7.088	0.978	0.002
A30	4	146	22013	2.266	0.008	2.426	0.018	0.122	0.003	2.249	0.0001	38.308	1.841	0.992	0.004
A31	4	151.2	22515	2.313	0.009	2.467	0.015	0.120	0.003	2.287	0.0001	34.531	1.841	0.989	0.004

Table 7.2: Corrected activities of isotopes used in lithogenic and authigenic correction for GeoB 2107 samples. 'JR' denotes samples measured by James Rae who worked exclusively on core GeoB 2107 for his masters thesis (J. Rae, 2007). * Sample A18 from run 12 was omitted from final data plots due negative read outs in the Th data.

GeoB 2104 (1503 m)

Sample	**Run**	**Depth** (cm)	**Age** (yr)	**(^{231}Pa)$_{xs0}$** (dpm/g)	2.S.E	**(^{230}Th)$_{xs0}$** (dpm/g)	2.S.E	**(^{231}Pa/^{230}Th)$_{xs0}$** (dpm/g)	2.S.E	**Mass flux** (g cm^{-2} ka^{-1})	2.S.E	**Opal flux** (mg cm^{-2} ka^{-1})
B0	11	0.5	307	0.196	0.005	2.884	0.039	0.068	0.002	1.313	0.018	43.299
B1	2	1.55	598	0.206	0.002	2.678	0.041	0.077	0.001	1.414	0.022	-
B2	5	6.5	2026	0.231	0.003	2.668	0.021	0.087	0.003	1.420	0.011	55.163
B3	8	11.6	3483	0.220	0.003	2.769	0.026	0.080	0.001	1.368	0.013	45.573
B4	1	16.5	4969	0.209	0.015	2.830	0.034	0.074	0.006	1.338	0.016	-
B4r	7	16.5	4969	0.226	0.011	2.658	0.022	0.085	0.004	1.425	0.012	-
B5	5	21.5	5334	0.225	0.003	2.569	0.023	0.088	0.003	1.474	0.013	59.442
B6	11	26.7	5699	0.214	0.004	3.169	0.039	0.067	0.002	1.195	0.015	45.039
B7	2	31.55	6064	0.235	0.002	2.940	0.053	0.080	0.002	1.288	0.023	-
B8	8	36.5	6846	0.220	0.003	2.719	0.033	0.081	0.001	1.393	0.017	53.367
B9	1	41.5	7660	0.231	0.014	2.985	0.159	0.077	0.006	1.269	0.068	-
B10	6	47	8223	0.191	0.006	2.788	0.023	0.068	0.002	1.359	0.011	39.072
B12	1	56.5	9195	0.196	0.015	2.702	0.018	0.073	0.006	1.402	0.009	-
B14	2	67.5	13262	0.146	0.002	2.379	0.092	0.061	0.002	1.592	0.062	-
B16	2	76.7	14894	0.118	0.002	2.283	0.054	0.051	0.001	1.659	0.039	63.809
B17	6	82.3	15386	0.128	0.006	1.781	0.022	0.072	0.003	2.127	0.026	68.518
B18	5	87.5	15795	0.118	0.006	1.605	0.023	0.073	0.004	2.360	0.034	73.674
B18.5	11	90.5	16041	0.077	0.002	1.939	0.032	0.040	0.001	1.953	0.032	59.446
B19	1	91.5	16123	0.119	0.013	1.876	0.011	0.063	0.007	2.610	0.055	-
B19r	2	91.5	16123	0.150	0.002	1.451	0.030	0.103	0.003	2.019	0.012	-
B19.5	11	92.7	16205	0.072	0.002	1.808	0.032	0.040	0.001	2.094	0.038	68.636
B20	5	96.7	16533	0.095	0.005	1.335	0.015	0.071	0.004	2.837	0.031	72.146
B21	6	101.7	16943	0.100	0.005	1.479	0.016	0.068	0.004	2.561	0.027	81.039
B22	2	107.5	17435	0.082	0.002	1.667	0.111	0.049	0.003	2.272	0.152	-
B23	8	111.6	17677	0.110	0.002	1.673	0.028	0.066	0.002	2.264	0.039	79.030
B25	2	121.5	18652	0.104	0.002	1.883	0.068	0.055	0.002	2.011	0.073	-
B26	6	126.5	19410	0.157	0.004	1.990	0.024	0.079	0.003	1.904	0.023	76.766
B27	1	131.5	20169	0.091	0.009	1.032	0.009	0.089	0.008	3.672	0.032	-
B27r	8	131.5	20169	0.122	0.002	1.879	0.027	0.065	0.002	2.015	0.029	-
B30	2	146.3	22445	0.151	0.005	1.933	0.090	0.078	0.004	1.960	0.091	-
B32	5	156.6	23977	0.116	0.006	1.626	0.025	0.071	0.004	2.330	0.036	90.675

Table 7.3: ^{231}Pa and ^{230}Th, corrected for lithogenic and authigenic components, (^{231}Pa/^{230}Th$_{xs}$)0, ^{230}Th normalized sediment flux and opal flux data for all samples from core GeoB 2104.

GeoB 2104 (1503 m)

Sample	Run	Depth (cm)	Age (yr)	(^{232}Th) (dpm/g)	2.S.E	(^{230}Th) (dpm/g)	2.S.E	(^{231}Pa) (dpm/g)	2.S.E	(^{238}U) (dpm/g)	2.S.E	δ^{234}U	2.S.E	^{238}U/^{232}Th	2.S.E
B0	11	0.5	307	2.125	0.016	3.938	0.038	0.244	0.005	1.444	0.0000	-6.230	1.455	0.680	0.002
B1	2	1.55	598	2.399	0.019	3.865	0.040	0.258	0.002	1.545	0.0002	-3.271	12.200	0.644	0.004
B2	5	6.5	2026	2.158	0.007	3.697	0.021	0.271	0.006	1.351	0.0000	12.510	4.270	0.626	0.002
B3	8	11.6	3483	2.079	0.009	3.722	0.031	0.254	0.003	1.398	0.0000	0.829	5.707	0.673	0.003
B4	1	16.5	4969	1.991	0.009	3.733	0.033	0.237	0.014	1.649	0.0002	5.441	2.100	0.828	0.003
B4r	7	16.5	4969	1.997	0.007	3.561	0.020	0.252	0.010	1.446	0.0000	-1.077	5.707	0.724	0.003
B5	5	21.5	5334	1.878	0.009	3.412	0.022	0.247	0.006	1.421	0.0000	26.757	4.270	0.757	0.004
B6	11	26.7	5699	1.917	0.013	4.043	0.037	0.241	0.004	2.267	0.0001	59.950	1.455	1.183	0.003
B7	2	31.55	6064	2.028	0.016	3.852	0.050	0.259	0.002	1.935	0.0002	40.857	12.200	0.954	0.006
B8	8	36.5	6846	1.787	0.010	3.492	0.031	0.236	0.002	1.523	0.0000	29.261	5.707	0.852	0.005
B9	1	41.5	7660	1.763	0.006	3.726	0.149	0.243	0.012	1.676	0.0003	40.198	2.100	0.950	0.002
B10	6	47	8223	1.739	0.006	3.504	0.021	0.205	0.005	1.455	0.0000	20.404	1.048	0.837	0.003
B12	1	56.5	9195	1.746	0.004	3.521	0.017	0.216	0.012	2.652	0.0009	78.357	2.100	1.518	0.003
B14	2	67.5	13262	2.056	0.014	3.437	0.081	0.183	0.001	3.338	0.0004	79.067	12.200	1.623	0.009
B16	2	76.7	14894	2.449	0.021	3.465	0.046	0.163	0.001	2.934	0.0004	50.039	12.200	1.198	0.008
B17	6	82.3	15386	2.196	0.007	2.884	0.019	0.163	0.004	2.694	0.0001	53.694	1.048	1.227	0.004
B18	5	87.5	15795	2.180	0.008	2.686	0.020	0.152	0.004	2.434	0.0000	59.209	4.270	1.116	0.004
B18.5	11	90.5	16041	2.001	0.013	2.864	0.027	0.117	0.001	2.210	0.0001	37.934	1.455	1.104	0.003
B19	1	91.5	16123	2.326	0.003	3.017	0.010	0.158	0.009	2.664	0.0004	43.744	2.100	1.145	0.001
B19r	2	91.5	16123	2.155	0.022	2.526	0.024	0.173	0.001	2.329	0.0003	35.880	12.200	1.080	0.009
B19.5	11	92.7	16205	2.100	0.014	2.775	0.027	0.114	0.001	2.103	0.0001	34.085	1.455	1.001	0.003
B20	5	96.7	16533	2.216	0.007	2.427	0.012	0.132	0.004	2.179	0.0000	43.820	4.270	0.983	0.003
B21	6	101.7	16943	2.299	0.008	2.635	0.013	0.141	0.004	2.487	0.0001	36.740	1.048	1.082	0.004
B22	2	107.5	17435	2.477	0.019	2.894	0.094	0.133	0.001	2.628	0.0003	33.567	12.200	1.061	0.007
B23	8	111.6	17677	2.436	0.011	2.837	0.024	0.148	0.002	2.371	0.0001	26.751	5.707	0.974	0.004
B25	2	121.5	18652	2.730	0.028	3.179	0.055	0.152	0.001	2.626	0.0003	26.191	12.200	0.962	0.008
B26	6	126.5	19410	2.208	0.011	2.977	0.019	0.172	0.004	2.217	0.0001	37.110	1.048	1.004	0.005
B27	1	131.5	20169	1.406	0.002	1.708	0.007	0.104	0.006	1.469	0.0002	-24.483	2.100	1.045	0.001
B27r	8	131.5	20169	2.475	0.011	3.011	0.021	0.154	0.002	2.333	0.0001	27.303	5.707	0.943	0.004
B30	2	146.3	22445	3.054	0.111	3.323	0.046	0.182	0.001	2.577	0.0003	14.698	12.200	0.844	0.025
B32	5	156.6	23977	2.585	0.011	2.788	0.019	0.145	0.004	2.136	0.0000	43.883	4.270	0.658	0.003

Table 7.4: Corrected activities of isotopes used in lithogenic and authigenic correction for GeoB 2104 samples. 'B' denotes samples are from core GeoB 2104 and 'r' denotes replica measurements. An average of all replica sample measurements was used for final data plots. Samples B22 (run 2) and B27 (run 1) were omitted from final data plots due to low Pa concentrations (table 7.3) for B22 and low Th, U concentrations in B27.

GeoB 2109 (2504 m)

Sample	**Run**	**Depth** (cm)	**Age** (yr)	**(^{231}Pa)$_{xs0}$** (dpm/g)	2.S.E	**(^{230}Th)$_{xs0}$** (dpm/g)	2.S.E	**(^{231}Pa/^{230}Th)$_{xs0}$** (dpm/g)	2.S.E	**Mass flux** (g cm^{-2} ka^{-1})	2.S.E	**Opal flux** (mg cm^{-2} ka^{-1})
E1	3	1	1011	0.270	0.182	4.928	0.158	0.055	0.037	1.280	0.033	-
E1r	5	1	1011	0.262	0.007	4.638	0.034	0.057	0.002	1.361	0.010	-
E1rr	12	1	1011	0.267	0.002	4.789	0.069	0.056	0.001	1.318	0.019	-
E1.5	11	4.5	2814	0.265	0.004	5.177	0.042	0.051	0.001	1.218	0.010	34.510
E3	1	10.5	5906	0.311	0.018	5.813	0.015	0.054	0.003	1.086	0.003	-
E4	3	15.5	8117	0.273	0.003	5.574	0.286	0.049	0.003	1.132	0.058	-
E4r	12	15.5	8117	0.268	0.002	5.696	0.084	0.047	0.001	1.108	0.016	-
E5	1	20.5	11382	0.263	0.015	5.115	0.012	0.052	0.003	1.234	0.068	-
E5r	3	20.5	11382	0.244	0.003	4.919	0.254	0.050	0.003	1.283	0.054	-
E5rr	12	20.5	11382	0.287	0.002	5.333	0.088	0.054	0.001	1.183	0.019	-
E6	5	23.7	11875	0.237	0.007	4.974	0.029	0.048	0.001	1.268	0.007	34.748
E6r	8	23.7	11875	0.278	0.005	4.881	0.032	0.057	0.001	1.292	0.008	-
E7	3	29.3	12691	0.287	0.003	4.944	0.108	0.058	0.001	1.276	0.023	-
E7r	7	29.3	12691	0.288	0.018	5.004	0.044	0.058	0.004	1.261	0.011	-
E7.5	11	31.5	12810	0.292	0.004	5.354	0.053	0.054	0.001	1.179	0.012	30.510
E8	1	34	12929	0.262	0.014	5.391	0.016	0.049	0.003	1.170	0.003	23.484
E8.5	11	37.5	13689	0.261	0.004	4.847	0.056	0.054	0.001	1.302	0.015	33.614
E9	5	39.5	14123	0.227	0.007	3.474	0.020	0.065	0.002	1.816	0.011	42.166
E9.5	11	43.5	14991	0.226	0.003	3.888	0.049	0.058	0.001	1.623	0.021	37.792
E10	3	46.5	15642	0.197	0.003	3.537	0.114	0.056	0.002	1.784	0.047	-
E10r	12	46.5	15642	0.179	0.003	3.139	0.208	0.057	0.004	2.010	0.133	-
E10.5	11	49.5	16488	0.209	0.003	4.002	0.057	0.052	0.001	1.577	0.023	49.280
E11	5	53	17475	0.176	0.007	2.890	0.035	0.061	0.002	2.183	0.026	81.136
E12	3	59.4	19281	0.144	0.004	3.282	0.112	0.044	0.002	1.921	0.054	-
E12r	12	59.4	19281	0.244	0.003	2.692	0.086	0.091	0.003	2.343	0.075	-
E13	6	63.5	20437	0.212	0.008	3.296	0.036	0.064	0.003	1.914	0.021	55.609
E13r	7	63.5	20437	0.207	0.012	3.426	0.031	0.061	0.004	1.841	0.017	-
E14	8	68.8	21932	0.204	0.003	3.301	0.034	0.062	0.001	1.910	0.020	78.742
E15	3	73.5	23258	0.138	0.003	3.948	0.140	0.035	0.001	1.598	0.046	-
E15r	12	73.5	23258	0.154	0.003	3.740	0.093	0.041	0.001	1.687	0.042	-
E17	1	83.5	25204	0.176	0.016	3.390	0.021	0.052	0.005	1.862	0.011	-
E18	6	92	26859	0.213	0.008	3.248	0.019	0.066	0.003	1.942	0.012	-
E19	3	97.7	27968	0.212	0.003	3.936	0.149	0.054	0.002	1.603	0.049	43.360
E19r	12	97.7	27968	0.047	0.002	4.046	0.105	0.012	0.001	1.559	0.040	-
E20	6	103.5	29097	0.257	0.009	3.694	0.030	0.070	0.003	1.708	0.014	58.830
E22	6	113	30946	0.247	0.009	3.583	0.034	0.069	0.003	1.761	0.017	52.273

Table 7.5: ^{231}Pa and ^{230}Th, corrected for lithogenic and authigenic components, (^{231}Pa/^{230}Th$_{xs}$)0. ^{230}Th normalized sediment flux and opal flux data for all samples from core GeoB 2109. 'E' denotes samples are from core GeoB 2109 and 'r' denotes replica measurements. An average of all replica sample measurements was used for final data plots. Sample E19r (run 12) was omitted from final data plots due to low Pa concentrations. Samples E12 (run 3) and E12r (run 12) were omitted from final data plots due to the poor reproducibility of this sample.

GeoB 2109 (2504 m)

Sample	**Run**	**Depth** (cm)	**Age** (yr)	**(^{232}Th)** (dpm/g)	2.S.E	**(^{230}Th)** (dpm/g)	2.S.E	**(^{231}Pa)** (dpm/g)	2.S.E	**(^{238}U)** (dpm/g)	2.S.E	**δ^{234}U**	2.S.E	**^{238}U/^{232}Th**	2.S.E
E1	3	1	1011	1.593	0.010	5.682	0.156	0.301	0.179	1.044	0.0002	11.680	12.030	0.655	0.003
E1r	5	1	1011	1.471	0.006	5.333	0.033	0.291	0.007	0.939	0.0000	9.132	4.270	0.638	0.002
E1rr	12	1	1011	1.500	0.013	5.495	0.069	0.296	0.002	0.982	0.0000	12.474	1.473	0.654	0.006
E1.5	11	4.5	2814	1.347	0.007	5.725	0.040	0.282	0.004	0.916	0.0000	12.740	1.455	0.680	0.001
E3	1	10.5	5906	1.503	0.003	6.270	0.014	0.310	0.016	0.947	0.0001	9.791	2.100	0.630	0.001
E4	3	15.5	8117	1.505	0.011	5.942	0.266	0.266	0.002	0.939	0.0002	11.549	12.030	0.624	0.004
E4r	12	15.5	8117	1.370	0.013	5.973	0.078	0.257	0.002	0.845	0.0000	11.717	1.473	0.617	0.006
E5	1	20.5	11382	1.392	0.003	5.322	0.010	0.241	0.012	0.853	0.0001	-1.750	2.100	0.613	0.001
E5r	3	20.5	11382	1.389	0.022	5.146	0.228	0.226	0.002	0.864	0.0001	-6.665	12.030	0.622	0.008
E5rr	12	20.5	11382	1.567	0.013	5.589	0.079	0.263	0.002	0.925	0.0000	1.612	1.473	0.590	0.005
E6	5	23.7	11875	1.692	0.004	5.319	0.026	0.224	0.006	0.944	0.0000	-19.107	4.270	0.558	0.001
E6r	8	23.7	11875	1.683	0.006	5.235	0.028	0.256	0.004	0.975	0.0001	-17.335	5.707	0.579	0.002
E7	3	29.3	12691	1.604	0.009	5.223	0.096	0.258	0.002	0.958	0.0002	-18.066	12.030	0.597	0.003
E7r	7	29.3	12691	1.694	0.007	5.322	0.039	0.261	0.014	1.007	0.0001	-22.139	5.707	0.594	0.002
E7.5	11	31.5	12810	1.505	0.010	5.533	0.047	0.259	0.003	0.902	0.0000	-20.724	1.455	0.600	0.002
E8	1	34	12929	1.600	0.002	5.608	0.014	0.238	0.010	0.947	0.0001	-29.006	2.100	0.592	0.001
E8.5	11	37.5	13689	1.818	0.013	5.207	0.049	0.239	0.003	1.068	0.0000	-37.440	1.455	0.588	0.002
E9	5	39.5	14123	2.209	0.008	4.166	0.017	0.220	0.005	1.168	0.0000	-48.923	4.270	0.529	0.002
E9.5	11	43.5	14991	2.164	0.013	4.497	0.042	0.216	0.002	1.260	0.0000	-47.987	1.455	0.582	0.001
E10	3	46.5	15642	2.683	0.018	4.428	0.099	0.205	0.002	1.487	0.0002	-44.076	12.030	0.554	0.003
E10r	12	46.5	15642	2.183	0.069	3.812	0.177	0.180	0.001	1.197	0.0000	-44.444	1.473	0.548	0.017
E10.5	11	49.5	16488	2.398	0.018	4.672	0.049	0.205	0.002	1.401	0.0000	-44.789	1.455	0.584	0.002
E11	5	53	17475	2.340	0.010	3.695	0.029	0.181	0.005	1.540	0.0000	-2.662	4.270	0.658	0.003
E12	3	59.4	19281	2.612	0.013	4.160	0.094	0.164	0.002	1.863	0.0001	-1.025	12.030	0.713	0.003
E12r	12	59.4	19281	2.566	0.034	3.539	0.070	0.228	0.002	1.738	0.0001	-1.247	1.473	0.677	0.009
E13	6	63.5	20437	2.762	0.012	4.264	0.029	0.214	0.005	2.150	0.0001	7.464	1.048	0.778	0.003
E13r	7	63.5	20437	2.650	0.010	4.309	0.025	0.207	0.008	2.056	0.0001	4.432	5.707	0.776	0.003
E14	8	68.8	21932	2.517	0.011	4.116	0.028	0.199	0.002	2.016	0.0002	12.445	5.707	1.067	0.003
E15	3	73.5	23258	2.670	0.014	4.756	0.113	0.165	0.002	2.385	0.0002	27.909	12.030	0.893	0.004
E15r	12	73.5	23258	2.495	0.029	4.270	0.074	0.168	0.001	2.176	0.0001	28.386	1.473	0.872	0.010
E17	1	83.5	25204	2.872	0.006	4.294	0.016	0.183	0.010	2.148	0.0003	12.567	2.100	0.748	0.001
E18	6	92	26859	2.646	0.009	3.990	0.014	0.192	0.005	1.836	0.0000	-9.839	1.048	0.694	0.002
E19	3	97.7	27968	2.694	0.011	4.498	0.115	0.188	0.002	1.755	0.0002	-59.530	12.030	0.651	0.002
E19r	12	97.7	27968	2.588	0.035	4.426	0.079	0.095	0.001	1.767	0.0001	-0.195	1.473	0.683	0.009
E20	6	103.5	29097	2.236	0.008	4.069	0.022	0.200	0.005	1.572	0.0000	-5.201	1.048	0.703	0.003
E22	6	113	30946	2.348	0.009	3.975	0.025	0.191	0.005	1.536	0.0000	-16.919	1.048	0.654	0.003

Table 7.6: Corrected activities of isotopes used in lithogenic and authigenic correction for GeoB 2109 samples.

GeoB 2112 (4010 m)

Sample	**Run**	**Depth** (cm)	**Age** (yr)	**(^{231}Pa)$_{xs0}$** (dpm/g)	2.S.E	**(^{230}Th)$_{xs0}$** (dpm/g)	2.S.E	**(^{231}Pa/^{230}Th)$_{xs0}$** (dpm/g)	2.S.E	**Mass flux** (g cm^{-2} ka^{-1})	2.S.E	**Opal flux** (mg cm^{-2} ka^{-1})
F1	9	0.5	5398	0.804	0.013	15.906	0.139	0.051	0.001	0.064	0.001	2.877
F2	10	2	5807	0.689	0.017	13.749	0.114	0.050	0.001	0.074	0.001	2.118
F3	9	3.5	7404	0.649	0.009	12.539	0.087	0.052	0.001	0.081	0.001	2.292
F4	10	4.8	7456	0.663	0.018	12.548	0.083	0.053	0.002	0.081	0.001	2.095
F5	9	6.7	9387	0.587	0.008	9.572	0.074	0.061	0.001	0.106	0.001	4.194
F6	10	7.9	10622	0.463	0.011	7.788	0.061	0.059	0.001	0.130	0.001	3.356
F7	9	9.5	14171	0.459	0.005	7.305	0.059	0.063	0.001	0.138	0.001	3.351
F8	10	11.1	16610	0.425	0.011	6.184	0.073	0.069	0.002	0.163	0.002	5.369
F9	9	12.7	17829	0.486	0.006	6.709	0.072	0.072	0.001	0.151	0.002	5.188
F10	10	14	18820	0.429	0.015	5.991	0.069	0.072	0.003	0.169	0.002	6.825
F11	9	15.8	20192	0.331	0.005	4.950	0.059	0.067	0.001	0.204	0.003	3.737
F12	10	17.6	21564	0.362	0.007	5.259	0.075	0.069	0.002	0.192	0.003	4.377
F13	9	19.1	22707	0.159	0.002	3.053	0.059	0.052	0.001	0.331	0.006	11.578
F14	10	20.6	23851	0.154	0.004	2.916	0.065	0.053	0.002	0.347	0.008	15.882
F15	9	22	24918	0.191	0.020	2.544	0.060	0.075	0.008	0.397	0.009	18.585
F16	10	24.1	26518	0.019	0.003	1.396	0.050	0.013	0.002	0.724	0.026	14.968
F17	9	25.2	27357	0.148	0.002	2.901	0.060	0.051	0.001	0.348	0.007	10.004
F18	10	26.7	28500	0.085	0.006	3.891	0.099	0.022	0.002	0.260	0.007	10.602

Table 7.7: ^{231}Pa and ^{230}Th, corrected for lithogenic and authigenic components, (^{231}Pa/^{230}Th$_{xs}$)0, ^{230}Th normalized sediment flux and opal flux data for all samples from core GeoB 2112. Samples F16 (run 2) and F18 (run 1) were omitted from final data plots due to very high U concentrations in these samples and low Pa concentrations after correcting for authigenic components.

GeoB 2112 (4010 m)

Sample	**Run**	**Depth** (cm)	**Age** (yr)	**(^{232}Th)** (dpm/g)	2.S.E	**(^{230}Th)** (dpm/g)	2.S.E	**(^{231}Pa)** (dpm/g)	2.S.E	**(^{238}U)** (dpm/g)	2.S.E	**δ^{234}U**	2.S.E	**^{238}U/^{232}Th**	2.S.E
F1	9	0.5	5398	1.914	0.015	16.096	0.132	0.762	0.011	1.146	0.0002	-27.137	1.023	0.598	0.002
F2	10	2	5807	1.906	0.011	13.971	0.108	0.653	0.015	1.136	0.0000	-35.508	2.255	0.596	0.001
F3	9	3.5	7404	1.874	0.011	12.662	0.077	0.598	0.008	1.037	0.0000	-42.005	1.023	0.553	0.001
F4	10	4.8	7456	1.806	0.009	12.614	0.032	0.607	0.016	1.013	0.0000	-47.007	2.255	0.561	0.001
F5	9	6.7	9387	2.001	0.012	9.791	0.055	0.528	0.006	1.084	0.0000	-53.654	1.023	0.542	0.001
F6	10	7.9	10622	2.081	0.010	8.099	0.022	0.418	0.009	1.143	0.0000	-65.051	2.255	0.549	0.001
F7	9	9.5	14171	2.302	0.012	7.579	0.062	0.394	0.003	1.244	0.0000	-61.480	1.023	0.540	0.001
F8	10	11.1	16610	2.412	0.017	6.516	0.025	0.355	0.007	1.319	0.0000	-74.797	2.255	0.547	0.002
F9	9	12.7	17829	2.388	0.016	6.911	0.057	0.390	0.004	1.304	0.0000	-76.018	1.023	0.546	0.002
F10	10	14	18820	2.568	0.016	6.312	0.023	0.347	0.010	1.321	0.0000	-78.256	2.255	0.514	0.001
F11	9	15.8	20192	2.702	0.016	5.468	0.061	0.278	0.003	1.363	0.0000	-83.677	1.023	0.504	0.001
F12	10	17.6	21564	2.652	0.018	5.626	0.061	0.290	0.004	1.349	0.0000	-85.581	2.255	0.508	0.001
F13	9	19.1	22707	2.707	0.026	3.848	0.046	0.162	0.001	1.423	0.0000	-82.324	1.023	0.526	0.002
F14	10	20.6	23851	2.795	0.026	3.718	0.051	0.157	0.003	1.388	0.0000	-96.188	2.255	0.497	0.002
F15	9	22	24918	2.570	0.028	3.327	0.046	0.173	0.012	1.359	0.0000	-71.127	1.023	0.529	0.002
F16	10	24.1	26518	2.120	0.018	3.059	0.038	0.133	0.002	4.800	0.0001	100.337	2.255	2.264	0.008
F17	9	25.2	27357	2.681	0.020	3.626	0.045	0.147	0.001	1.447	0.0000	-74.471	1.023	0.540	0.002
F18	10	26.7	28500	3.834	0.040	5.258	0.073	0.163	0.003	3.339	0.0001	13.765	2.255	0.871	0.004

Table 7.8: Corrected activities of isotopes used in lithogenic and authigenic correction for GeoB 2112 samples. 'F' denotes samples are from core GeoB 2112 and 'r' denotes replica measurements. An average of all replica sample measurements was used for final data plots. Samples F16 (run 2) and F18 (run 1) were omitted from final data plots due to very high U concentrations in these samples and low Pa concentrations after correcting for authigenic components.